MASARYK UNIVERSITY
Faculty of Science
Department of Physical Electronics

Preparation of nanostructured hard protective coatings by magnetron sputtering

Habilitation thesis
Scientific field: Plasma physics

Mgr. Pavel Souček, Ph.D.

Brno 2017

I would like to thank all my colleagues present and the past, local as well as from abroad. A special thanks are dedicated to my family.

Abstract:

The presented habilitation work called *Preparation of nanostructured hard protective coatings by magnetron sputtering* summarises and comments on the results acquired during my work at the Department of Physical Electronics at the Faculty of Science of the Masaryk University and also on the results gained in collaboration with colleagues from the University of Groningen, PLATIT a.s. (formerly PIVOT a.s.), Institute of Physics of Materials and Institute of Nuclear Physics of the ASCR, Institut des Matériaux Jean Rouxel Nantes and INP Greifswald. Ten papers providing a comprehensive view of the preparation and analysis of magnetron sputtered hard titanium and carbon-based nanocomposite coatings and next-generation prospective molybdenum–boron–carbon coatings are chosen to be presented in this work. Titanium and carbon-based coatings are shown as an example of presently used coatings designed for maximum hardness. First, the deposition process as such was studied in detail. The behaviour of the plasma parameters on the set deposition conditions was understood. Similarities and differences to classical reactive magnetron sputtering were identified. Large series of nanocomposite nc-TiC/a-C:H coatings were deposited and studied from different angles. The relationships between the deposition parameters, the structure of the coatings and their mechanical properties were described. Superhard coatings were deposited. Molybdenum–boron–carbon-based coatings are presented as an example of next-generation protective coatings still in their early stages of development. These coatings are not superhard as it was realised by the industry that the highest hardness does not necessarily mean the best performance. The next generation of protective coatings sacrifices some of the hardness but gains moderate ductility instead.

Contents

Chapter 1

Introduction

The presented habilitation work called *Preparation of nanostructured hard protective coatings by magnetron sputtering* summarizes and comments on the results acquired during my work at the Department of Physical Electronics at the Faculty of Science of the Masaryk University and also on the results gained in collaboration with colleagues from other departments from Czech Republic and abroad. I have participated in all the work presented in this work with special focus on deposition and chemical and structural analyses of nanocomposite and nanolaminate protective coatings.

The core of the presented habilitation work is divided into two mutually independent sections. The first section deals with nanocomposites composed of nanocrystalline titanium carbide grains embedded in an amorphous hydrogenated carbon matrix (nc-TiC/a-C:H). These coatings are relatively well known in the world and publications in the literature can be found since the 1980s (see Fig.1.1, where the works published till the early phases of our study are shown). This type of coatings has been in the focus of researchers due to high hardness reaching the superhard region, simultaneous low coefficient of friction and wear and also for its biocompatibility. The second section is focussed on a different type of coatings. During the last several years, it was realized that optimizing coatings for maximum hardness does not yield the best results for real life applications. This is because superhard coatings generally exhibit one common downside — brittelnes. If a crack is formed, it rapidly propagates. This to a premature failure of the coating and of the coated tool as a whole. Recently, in 2009 a group of unusually stiff and ductile hard coatings was proposed based on theoretical calculations by the group of prof. Schneider from Aachen University. Differ-

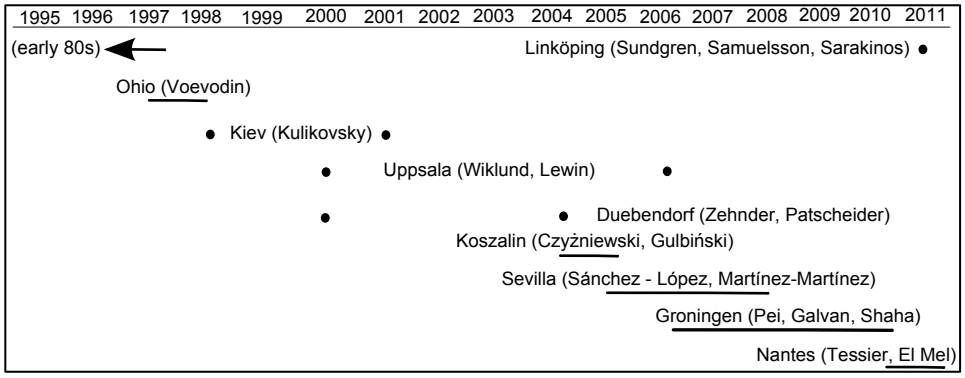

Figure 1.1: The first reports on preparation of nc-TiC/a-C:H coatings.

ent combinations of metal-, boron- and carbon-based materials in a Me_2BC structure were studied by ab initio calculations. These materials owe their unique combination of high hardness and enhanced ductility to their inherently nanolaminated microstructure. They exhibit high aspect ratio unit cell that is similar to MAX phases with alternating planes containing stiff carbidic and boridic bonds with high degree of ionicity providing the high stiffness and hardness, while metallic bonds provide moderate ductility. So far only few papers numbering in single digits are available on this material. Such coatings could serve as the next generation of protective coatings for applications where current protective coatings fail and therefore were in the focus of our latest research.

The individual chapters contain commentaries of published works that are in the attachment. As all of the attached papers present a complete work by themselves, I commented also on the facts that are not usually not widely discussed in published papers like the motivation and encountered problems. The most important results obtained during my work are naturally also included. The list of references consists of only the works in the attachment as all of them contain numerous references more than adequately describing the studied field.

Chapter 2

Study of nanocomposite nc-TiC/a-C:H coatings prepared by a hybrid PVD-PECVD process

2.1 Introduction

The first chapter describes the first type of the studied coatings — nc-TiC/a-C:H coatings. It is divided into two sections. This first section is primarily focused on the study of the behaviour of the deposition process and the plasma parameters. This section is built around the first two attached papers [1] and [2]. In many cases, a study focused on coating deposition is focused only on the influence of a set deposition parameters such as the flow of the buffer and reactive gasses or power supplied to the targets on the properties of the deposited coatings. Although this approach might be to a certain limit valid, it omits the study of the plasma that is just taken as a "black box" supplying the film forming atoms. Such an approach led to an inevitable confusion in the literature. While some call the process of sputtering titanium target in argon/acetylene gas mixture *reactive magnetron sputtering*, some call it *hybrid PVD-PECVD process*. Paper [1] is focused on showing that these are not the same and on proving that only one of these options is correct. Paper [2] is based on linking the deposition parameters with the processes in the volume of the chamber and on the sputtered target.

These consequently influence the properties of the deposited coatings. The findings published in this work will be later used for successful up-scaling of the process to an industrial configuration.

The second section is primarily focused on the deposited coatings. A method allowing for analysis of the mechanical properties and composition of the coatings with in-depth resolution with then available equipment was presented first and in-depth homogeneity of the coatings was studied [3]. Once uniformity of the coatings was established, the surface morphology, adhesion, structure and mechanical properties of coatings prepared in relatively mild conditions suitable for heat sensitive substrates such as steel was described [4]. Next, the study was extended to analyses of coatings made in harsher conditions with enhanced ion bombardment during the coating growth [5]. Carbon-based coatings generally exhibit a low coefficient of friction and wear, however these parameters are evaluated from a steady state of the measurement and the often unstable initial part of the measurement is generally omitted. A study was undertaken to assess the applicability of this method for short-term repeating applications such as drilling, milling, etc. [6]. Then further concepts possibly extending the applicability of the nc-TiC/a-C:H coatings were followed. After recent acquirement of a HiPIMS source, the effects of the HiPIMS use were investigated. HiPIMS and DCMS deposited coatings were compared and the key coating parameters leading to significant hardness increase influenced by HiPIMS were pinpointed [7]. Lastly, the concept of doping of the coatings with weak carbide forming elements to alter the structure of the coatings was investigated [8].

2.2 Process characterization

2.2.1 Reactive magnetron sputtering or a hybrid PVD-PECVD process

Magnetron sputtering is a classical physical vapour deposition (PVD) method of preparation of coatings studied and used since the 1980s. The basic physical principle of sputtering is knocking out of atoms from a cathode (also called target) by incident energetic particles supplied by a plasma ignited between the cathode and the grounded walls of the chamber. The plasma is held in the vicinity of the target by a magnetic field.

Reactive magnetron sputtering involves adding a reactive gas into the

chamber during magnetron sputtering. The present reactive gas can react with the material of the target and, depending on the amount of the present reactive gas, the process can progress in two different modes. If the amount of the reactive gas is low the target remains nearly clean, the pressure in the chamber is generally low, the intensity of the optical emission lines corresponding to target material and the deposition rate are high. This is the so-called metallic mode. As the reactive gas flow increases, the material of the targets reacts with the target more and when a particular gas flow is reached, the racetrack i.e. the working area of the target, is nearly instantly covered by products of reaction of the target material and the reactive gas. For example, TiN is formed if titanium target is sputtered in argon/nitrogen mixture and TiO_2 is formed if oxygen is used instead of nitrogen. The process is rapidly shifted into the so-called compound (also referred to as poisoned mode). In this mode the pressure is significantly higher as all the nitrogen able to react with the material in the chamber has already reacted and the excess gas is adding to the Ar background pressure. The intensity of the target material lines in the optical emission spectra drops as the resulting compound is sputtered instead of the target material. The compounds formed on the target also typically show lower sputter yield resulting in much-decreased deposition rate. The lower sputter yield, meaning that it is more difficult to sputter this compound than the original material, also signifies that if we want to shift back to the metallic mode, we need to decrease the reactive gas flow to a significantly lower value than where the transition from metallic mode to poisoned mode occurred. This behaviour called hysteresis is a hallmark of the classical reactive magnetron sputtering[1]

Similarities and differences between processes where oxygen and acetylene are used under otherwise identical conditions with a focus on the Ti line intensities were studied in paper [1]. A sputtering system with a relatively large 20 cm in diameter Ti target and moderate pumping speed of $0.04\,\mathrm{m^3 s^{-1}}$ was used to ensure the occurrence of hysteresis. The process with oxygen exhibited a hysteresis behaviour as is typically observed. However, the process with acetylene behaves differently. No hysteresis is observed in our work. The Ti line intensity for every acetylene flow during the flow increase matches the one measured during the acetylene flow decrease.

[1]The hysteresis can be suppressed by very high pumping speeds and/or by using very small targets, but it is generally observed for standard deposition systems.

An effort was made to model the experimentally observed lack of hysteresis. The standard Berg's model assuming that the reactive gas atoms from dissociated from e.g. nitrogen or oxygen can react only with the surface of the titanium target and forms a single layer of the reacted nitride or oxide is modified. An assumption that carbon atoms can not only react with titanium but also together and form a thicker carbon layer on the target and the chamber walls is added. This assumption agrees with the experiments, where we observe that if the process is stopped after the highest acetylene flow is reached and the chamber is opened, the target including the racetrack is covered by thick black residue. It is found out that indeed this assumption does lead to suppression of hysteresis. It is furthermore possible to estimate the degree of dissociation of acetylene in the chamber. This is found to be 20 – 50 %.

Therefore, magnetron sputtering of titanium in argon/acetylene atmosphere does not principally exhibit hysteresis. Thus, designating the studied process reactive magnetron sputtering is not entirely justified and can lead to certain misunderstanding. A more correct way would be to label the process as a hybrid PVD-PECVD process as it combines elements typical for PVD, i.e. sputtering of titanium target, and for PECVD, i.e. use of plasma to dissociate a precursor gas in the volume and formation of thick films formed from the precursor elements.

2.2.2 The link between the process parameters and coating properties

The effort to link the processes taking place inside the chamber during the deposition and the properties of the coatings follows [2]. The cathode voltage and current (in constant power mode), the total pressure, argon, titanium and hydrogen optical emission lines are measured for different acetylene flows. Coatings are furthermore deposited at selected acetylene flows. All of the studied parameters are found to be evolving continuously, however, in a non-monotonous manner. The behaviour of the observed parameters is found out to be governed by the processes on the target. The target after each deposition was imaged and areas with different apparent colours were assigned to their respective phases (Ti — metallic grey, TiC — dull grey, C — black). The relative coverage of the racetrack by different phases derived from pixel counting of the target images was used to of understand

the process dynamics.

For low acetylene flows the voltage increases due to the formation of TiC layer on the surface of the racetrack on the target. The TiC layer is formed at the expense of Ti, and the relative concentration of Ti in the plasma decreases accordingly, while the H concentration increases due to acetylene fragmentation in the plasma volume. The border between the low and medium range of acetylene flows is identified by a local maximum of the cathode voltage and an according minimum of the cathode current. The medium range of acetylene flows is characterised by a slight decrease of the cathode voltage. This is probably due to formation of sub-stoichiometric TiC on the racetrack. The cathode voltage decreases with increasing stoichiometry of the TiC compound with acetylene flow increase. Ti concentration in the plasma is still decreasing and hydrogen concentration continues to increase. Stoichiometric TiC coatings are deposited in this zone. The border between the medium and the high range of acetylene flows is more distinct and is characterised by a local minimum of the cathode voltage, an according local maximum of the current and maxima in the hydrogen line and argon line emissions. The hardest coatings are always deposited at this border. For high acetylene flows the target voltage rapidly increases due to rapid penetration of the carbon layer into the target racetrack. The Ti concentration in plasma further decreases but H concentration remains slightly decreasing.

The knowledge of the process behaviour later proves to be pivotal in our work for successful up-scaling of the process on an industrial scale. This upsacling is performed on a setup with a central cylindrical rotating cathode supplied by PLATIT. The process analysis methods are limited to monitoring the cathode voltage and current and the total pressure as these are already a part of the industrial deposition apparatus. The behaviour of these parameters is found to be similar to that observed in the laboratory scale device with a planar target. The only difference is in the process changes being more sudden. This is due to different geometries. The magnetic field configuration in our laboratory scale device with planar target allows for a slow gradual growth of the TiC or C phases on the non-sputtered part of the target and their gradual penetration into the target racetrack leading to slower gradual evolution of the cathode voltage. The cylindrical target and its magnetic field configuration in the industrial device are optimized for much higher target utilization ($\gtrsim 85\,\%$ compared to $\sim 15\,\%$ for planar

target). This setup leads to the fact that virtually the whole cathode acts as the racetrack. Therefore, the TiC or C layers can not gradually penetrate from the non-sputtered parts of the target and the whole target undergoes the change of the surface state nearly instantaneously. A robust automatic algorithm for production of hard nc-TiC/a-C:H coatings is developed based on the sudden evolution of the cathode voltage and the total pressure allowing for a repeatable and reliable deposition of hard nc-TiC/a-C:H coatings independently on the chamber and target history.

2.3 Deposition and analyses of nc-TiC/a-C:H coatings

2.3.1 Analysis of coatings with in-depth resolution

One of the first obstacles reached with analyses of the deposited coatings was how to check the homogeneity of the coating with in-depth resolution [3]. The deposition process in our case is always reaching a steady state typically for the first fifteen minutes. Then, for the rest of the process (typically 45 minutes), the process parameters are sufficiently stable. It is desirable to find out if the evolution of the coating parameters follows the evolution of the deposition process.

Figure 2.1a shows the standard way of measurement of mechanical properties of coatings. If information from a deeper part of the coating is required, a higher load is applied. This, however, increases the affected coating volume not only to the deeper parts of the coating, but also to the sides. Moreover, another problem arises when a hard coating on a soft substrate is measured. It is known that the soft substrate is already under plastic strain before the lower part of the coating is affected. Therefore, the data from the bottom part of the coating cannot be reliably extracted.

An alternate method is proposed in our work (see Fig. 2.1b). An abrasion of a spherical crater on a calotest machine is performed first. Then measurements with a constant load over the calotte with equidistant steps follow. Determination of the indent distance from the calotte centre gives the thickness of the film at the given position[2]. This way it is possible to mea-

[2]Measurement on a metallographic cut is also possible. It was, however, found out that as shallow angle cuts are needed, machine polishing was not precise enough. Handmade cuts seemed adequate, but careful measurements of their profile revealed that they were

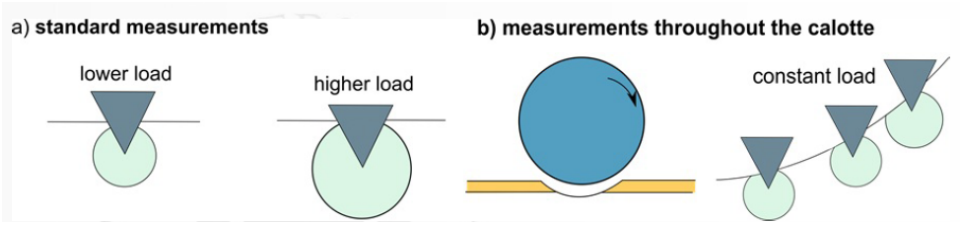

Figure 2.1: Comparison of a) standard and b) proposed measurements of deeper parts of the coating.

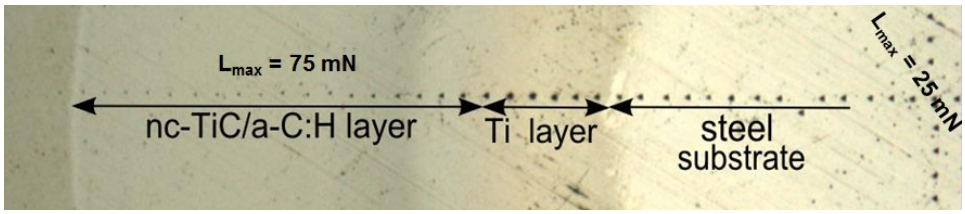

Figure 2.2: Residual indents on a calotte after measurement of mechanical properties.

sure mechanical properties from deeper parts of the coatings more directly, efficiently and exactly. An example of a realised measurement of mechanical properties on a calotte is presented in Fig. 2.2.

Furthermore, our calculations show that as the plastically influenced volume of the coating is similar to that producing the X-ray signal in EDX, it is possible to directly compare the mechanical properties and chemical composition derived by EDX. We conclude that using the presented method, it is possible to confirm that the chemical composition, as well as the mechanical properties, attain stable values during the early phase of the deposition where the process is reaching the equilibrium. Then, the composition and the hardness and Young's modulus remain stable.

not linear. This made a recalculation of the distance to the depth imprecise. Machine made calotes were found out to be the optimal solution as either analytical equation or an imaging on a confocal microscope and approximating of the profile with a parabola are simple and give good results.

2.3.2 Analyses of nc-TiC/a-C:H coatings prepared at low ion bombardment

Once the homogeneity of the coatings was established, the analysis of the properties of the coatings as a function of the reactive gas flow began [4]. The first series of coatings is deposited using the so-called well-balanced magnetic field configuration. It is known that this configuration allows for strong plasma confinement in the vicinity of the target providing relatively dense plasma close to the target. The shape of the magnetic field lines does not allow for a significant release of ions from the plasma towards the growing coating limiting its ion bombardment and energy influx.

The deposition process in our work needed to be optimised at the start of the series to ensure sufficient adhesion. The adhesion of the coating to the selected substrate must be high enough for reliable nanoindentation measurements as well as for future applications, where adhesion of the coating to the coated tool is one of the critical parameters determining a successful coating.

Argon ion etch cleaning of the substrates is performed first for 35 min to ensure a clean substrate surface. When the intended coating is deposited directly onto the substrate, the adhesion is not high enough. This is illustrated by significant delamination around the residual crater after a Rockwell adhesion test according to DIN CEN/TS 1071-18 standards with 1500 N load shown in Fig. 2.3a. Therefore a pure titanium adhesion layer is deposited for three minutes. This corresponds to the adhesion layer thickness of ~ 700 nm. The time of the interlayer deposition is selected as a minimum needed for the setting of all the parameters used during the deposition. This includes the setting of a manual matching box of the RF bias and manual logging of the pressure, cathode voltage and current and arcing occurrence. Also, the required acetylene flow is slowly gradually set during the last minute as the older mass flow controller tends to open too much and to poison the process if it is operated too quickly. The residual crater after the Rockwell test of a coating with the adhesion interlayer is shown in Fig. 2.3b. The adhesion of the coating with the adhesion layer is good in the HF0 – HF1 grade. Despite the adhesion layer is relatively thick, its thickness is not further optimised as the deposited coatings exhibit good adhesion.

After the deposition of the titanium interlayer, the deposition of the nc-TiC/a-C:H coating follows. The acetylene flow during the deposition directly

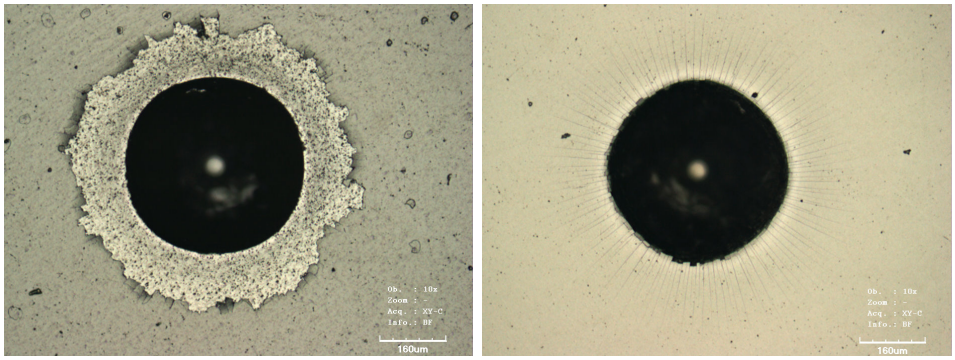

Figure 2.3: Comparison of adhesion of coatings without (left) and with (right) adhesion promoting titanium interlayer.

determining the carbon and titanium content is identified as the critical parameter influencing the structure and the mechanical properties of the deposited coatings in our work. XRD proves the presence of TiC grains of sizes ranging from several tens of nm to several nm depending on the carbon content in the coating. No Ti peaks are detected in the XRD patterns even when the Ti/C ratio is > 1 indicating that substoichiometric TiC is formed rather than Ti. The highest hardness and Young's modulus of 46 GPa and 415 GPa, respectively, are reached for the Ti/C ratio of $\sim 3/4$. This sample has a dense columnar structure with elongated TiC grains ~ 15 nm wide. This sample also exhibits the most pronounced preferential (111) orientation of the grains.

2.3.3 Analyses of the sensitivity of the nc-TiC/a-C:H coatings properties to the level ion bombardment controlled by the applied magnetic field

This study was motivated by the drastically different mechanical properties of nc-TiC/a-C:H coatings with identical chemical composition reported by various authors. These differences are illustrated in Fig. 2.4. The deposition temperatures are typically $\lesssim 300\,^{\circ}\mathrm{C}$, which is significantly lower than the melting temperature of titanium (3067°C) and also lower than the temperature, at which the carbon matrix starts to deteriorate (350 – 400 °C). The deposition temperature, therefore, isn't a key factor for these differences. This indicates that the differences in the ion flux should be the culprit. A comparison of the levels of the ion flux between the published

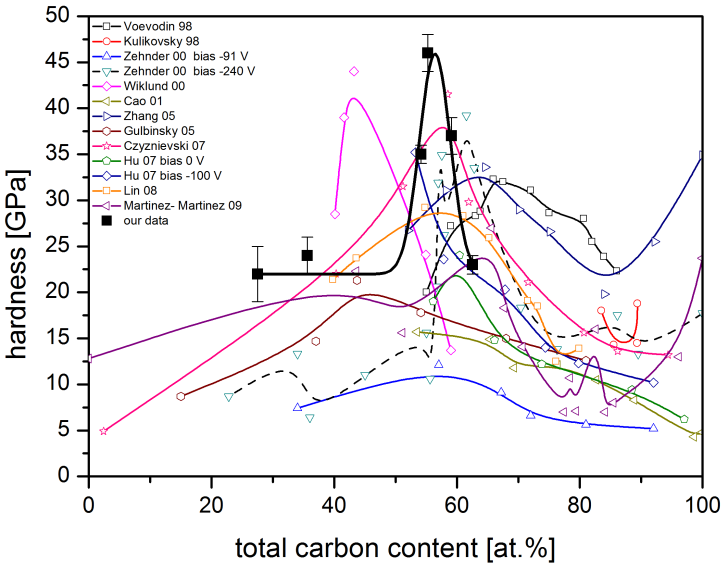

Figure 2.4: Different hardnesses of nc-TiC/a-C:H coatings reported by different authors.

works is however nigh impossible. This is because not all the experimental details are always presented in the published papers (e.g. substrate bias voltage, magnetic field configuration, target size and target to substrate distance). All of the presented parameters might suggest high levels of ion flux, but the only unreported parameter can completely alter this expectation. For instance, the distance of 100 — 150 mm between the substrate and 2 or 3-inch magnetron targets quite common in research systems results in very low plasma densities at the substrate even for highly unbalanced magnetrons. Therefore, the paper aims to single out the effect of the ion flux is a single apparatus [5].

Two series of coatings are deposited. One with a lower ion flux and one with a higher level of ion flux. The lower flux of ions is assured by using a well balanced magnetic field in the magnetron. Use of the well-balanced configuration results in saturated ion current on the substrate of $0.3\,\mathrm{mA/cm^2}$ corresponding to the ion flux of $1.87{\cdot}10^{15}\,\mathrm{cm^2 s^{-1}}$. An unbalanced magnetic field[3] is used for depositions with higher ion flux. This configuration results in the saturated ion current of $2.1\,\mathrm{mA/cm^2}$ corresponding to the ion flux of $1.31{\cdot}10^{16}\,\mathrm{cm^2 s^{-1}}$. Thus, the number of impinging ions was increased seven

[3]Newly manufactured and retrofitted to the existing Alcatel system by Gencoa.

times.

The structure of the coatings is, somewhat surprisingly, not significantly affected by the different levels of the ion flux. Also, the maximal values of the hardness and elastic modulus are nearly identical. However, their evolutions are slightly shifted to different C/Ti ratios. Therefore, different acetylene fluxes are needed in both cases to achieve the highest hardness.

2.3.4 Investigation of the tribological properties of nc-TiC/a-C:H coatings in short-term repeating applications

It has been previously shown by others as well as in our work that carbon-based coatings can achieve a very low coefficient of friction (CoF) of < 0.1 together with low wear rate. These works show that the CoF exhibits a typical 3 zone behaviour — TiC, transition and C phase governed zones. The first zone is characterised by high CoF > 0.25 and high counterpart wear. This is due to low carbon content, relatively high hardness and also high roughness of the coating. This leads to significant energy dissipation in the wear of the ball resulting in high CoF. The transition zone already exhibits lower CoF. However, the value of the CoF is not stable. This is due to periodical formation and destruction of a carbon-rich transfer layer effectively insulating the coating and the counterpart leading to a three body interaction. The periodical destruction of the transfer layer is caused by a low amount of very hard sharp debris from the coating. The carbon governed zone is characterised by low and stable CoF of ~ 0.1. The carbon-rich transfer layer is fully formed, and the wear of the counterpart is low.

All of these tests focus on the long-term evolution of the wear and friction of the sliding couple, and the so-called running-in stage i.e. the often unstable initial phase of the sliding contact between fresh, unworn surfaces is rarely studied and is typically omitted. The omitting of the running-in period is justifiable if the tested sample is designed for applications where the same parts are in constant contact. A car engine is such an example. On the other hand, there are applications where the coating gets periodically in contact with a new counterpart. The examples would be drilling, milling or forming. If there is a transfer film created between the contact surfaces of a drill and one hole, this transfer film does not play a role in drilling another hole. What coefficient of friction would better describe such applications — the one measured in the running-in period or the one measured after? The

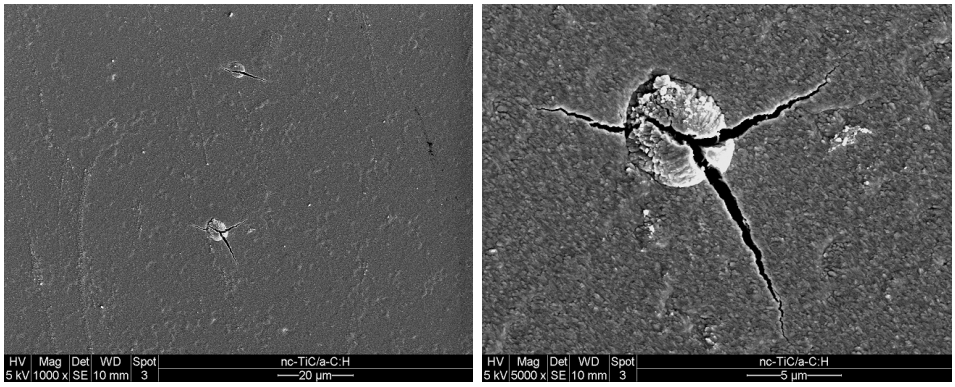

Figure 2.5: Examples of cracked pincushions.

running-in stage was studied in detail in both continuous and interrupted tribotests in paper [6].

A nc-TiC/a-C:H coating prepared in an industrial apparatus with carbon content of ~ 90 at.% was chosen for this testing as the high carbon content enables the creation of the transfer layer. These tests were carried out at ambient temperature as we have already shown that the coatings oxidise during high-temperature tests in air and various TiO_2 phases are formed. Also the growth defects in the coatings tend to crack at high temperatures even without mechanical stresses (see Fig. 2.5). Such cracking leads to a premature failure of the coatings.

In our work the usually long-term continuous tests are divided into shorter runs. The wear track on the coating as well as the wear scar on the counterpart are imaged after each run. The coefficient of friction (CoF) measurements reveal that the CoF is initially high for the first several runs but remains constant and low for later runs. The roughness of the coating is found to be the main factor in determining the CoF behaviour. The initial high CoF is caused by high initial roughness of the coating leading to slow or no formation of the carbon rich transfer layer crucial for low CoF. After the roughness of the hard coating decreases to a certain value, the transfer layer can form fast and the resulting CoF is low and stable. Roughness of the softer steel counterpart and any possible oxidation of the wear track are found out to be of little influence. Therefore, although the standard CoF analysis procedure involving quantification of the value of the CoF measured in the steady state region after the running-in period does not exactly describe the initial use of the coated tool, it is relevant even for descrip-

tion of the most of the lifetime of coatings enduring short-term repeating applications such as those found in machining.

2.3.5 Properties of nc-TiC/a-C:H coatings prepared employing High Power Impulse Magnetron Sputtering

High Power Impulse Magnetron Sputtering, HiPIMS for short, is a variant of magnetron sputtering, where the power to the cathode is supplied in very short and very intense pulses with an extended off-time between them. The power pulse is typically tens, or a few hundreds of microseconds long and the duty cycle is usually around one or two percent. It has been reported that this technique generally produces plasma two orders of magnitude denser than in the case of DC magnetron sputtering, which leads to significant ionisation of the sputtered species. The ionisation of the sputtered species routinely reaches more than 50 % in HiPIMS, whilst it is in the order of few percent in the case of DCMS. It is also known that the ion current to on the substrate in the pulse and directly after the pulse is significantly enhanced. This increased ion and energy flux together with deposition from ions instead of neutrals have been shown to alter the structure and overall properties of different types of coatings. Therefore, this method is used to study the effect of its use on nc-TiC/a-C:H coatings [7].

One of the main drawbacks of HiPIMS is a lower deposition rate than for corresponding coatings prepared by DCMS. This is also observed in our work. However, the deposition rate of coatings prepared by DCMS decreases at higher acetylene flows, while the deposition rate of coatings prepared by HiPIMS increases. The reduction of the deposition rate in the DCMS case can be explained by a lower flux of titanium from the target due to the racetrack being covered by carbon residue. The effect of lower titanium sputtering rate is probably not sufficiently compensated by the increase of carbon flux on the coating. The increase in the deposition rate at high acetylene fluxes with HiPIMS can be explained by enhanced flux of carbon because of expected higher level of acetylene dissociation in the denser HiPIMS plasma, as it is known that dissociation of molecular gasses such as oxygen and nitrogen is considerably higher in HiPIMS compared to DCMS. Moreover, it has been shown in the literature that acetylene gets more dissociated in denser plasmas (RF compared to DC) again justifying the assumption of higher level of acetylene dissociation in HiPIMS.

Different dynamics on the target were observed in our work for both plasma excitation methods. Targets imaged after the deposition revealed that when DCMS deposition of coatings with high carbon content results in the racetrack being nearly fully covered with a black residue, depositions of corresponding coatings with HiPIMS lead to much cleaner target probably due to Ti ion backattraction. This has a rather unexpected result. The cleaner surface of the target even at processes leading to deposition of coatings with carbon content higher than 90 at.% allow for a wider range of reliably deposited coatings while using HiPIMS. In comparison, the DCMS depositions do not allow for arc-free deposition of coatings with carbon content $\gtrsim$ 70 at.% in our setup.

Two sets of coatings are deposited by DCMS and HiPIMS at the same mean power, pressure and temperature. DCMS deposited coatings are prepared with a self-bias of -100 V and HiPIMS coatings are made at floating potential. HiPIMS deposited coatings exhibit structure refinement caused by the enhanced ion bombarbment — grains of similar size as in DCMS are of better stoichiometry and are separated by a lower amount of the a-C:H matrix leading to closer grain-to-grain distance. This is attributed to the higher ion and energy flux inherent to the HiPIMS process. This structure refinement leads to higher hardness, elastic modulus, as well as the H/E and H^3/E^2 ratios of the HiPIMS deposited coatings.

The effect of the bias for HiPIMS deposited coatings is also tested for several samples to have direct comparison with the biased DCMS deposited coatings prepared with -100 V bias. Use of HiPIMS together with RF bias proved to be technically challenging. Although the substrate holder and the power source are separated by two capacities in the standard matchbox, the power source is not hard enough. A large number of positive ions generated by HiPIMS imping the substrate holder and lower the voltage generated by the power source. When the voltage is $\sim$ 120 V before the pulse, it starts to decrease at the onset of the pulse. It steadily declines during the pulse, and also for approximately 250 microseconds after the pulse as the remaining ions generated in the plasma travel to the substrate. Then, the voltage begins to rise to its pre-pulse value. This behaviour is illustrated by measurements plotted in Fig. 2.6. Therefore, the use of the second HiPIMS channel or addition of a large capacitor to the circuit in case of using the substrate bias would be needed for the experiments to attain a stable bias value.

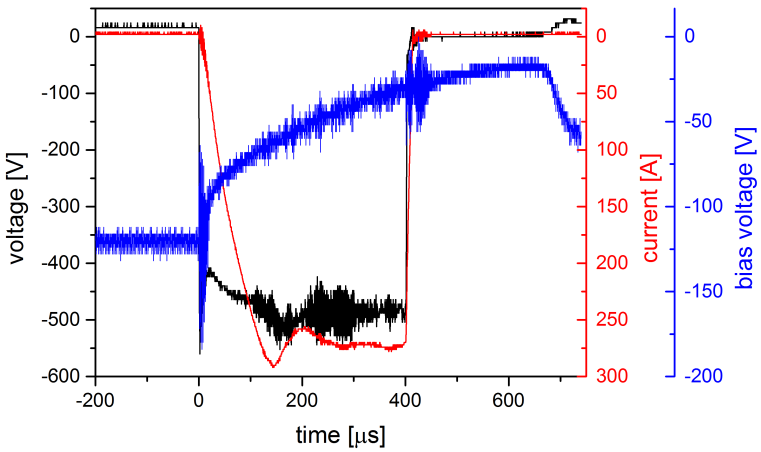

Figure 2.6: The evolution of the discharge voltage, discharge current and bias voltage during the HiPIMS pulse.

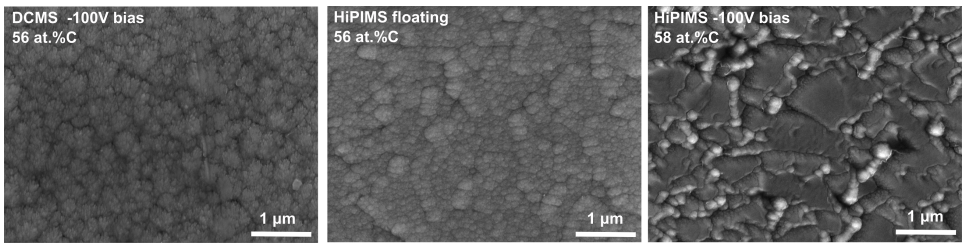

Figure 2.7: Comparison of surface morphologies of coatings with similar carbon content prepared using DCMS with bias (left), HIPIMS without bias (centre) and HiPIMS with bias (right).

The comparison of the surface morphologies of coatings with similar carbon content prepared using bias and DCMS (left), no bias and HIPIMS (centre) and HiPIMS with bias (right) is shown in Fig. 2.7. While the shift from the use of DCMS with the bias to HiPIMS without bias results in some surface refinement, the addition of bias to HiPIMS leads to a very strong change of the surface structure. The surface exhibits occurrence of local melting possibly due to local thermal spikes generated by the energetic ion bombardment. Also, the TiC grain strain doubled, and the hardness was reduced by half. Therefore, use of -100 V bias proved to be severely detrimental to the properties of the deposited coatings. However, lower levels of bias should be tried as well. This is planned for a future experiment.

2.3.6 The effect of nickel doping on the properties of of nc-Ti(:Ni)C/a-C:H coatings

The next part of our work is motivated by the works of prof. Ulf Jansson and dr. Erik Lewin from the Uppsala University. They theoretically predicted that the use of doping of the nc-TiC/a-C:H coatings by a weak carbide forming element could, in particular conditions, lead to the formation of a metastable TiXC phase, where the doping element X is incorporated in the grain. The incorporation of the doping element into the grain should change the coating microstructure such as the grain size, stoichiometry or the average grain separation. Such changes in the microstructure could lead to (favourable) changes in the mechanical properties. The metastable grains might also favour release of carbon from the grain to the matrix under stress and the coating could exhibit self-lubrication.

The same deposition conditions (i.e. power to the target, pressure, bias) are used in our work to have direct comparison with previously deposited undoped samples to isolate the effect of the doping. Zinc, copper and nickel are initially tested. The first idea is to change the level of doping by placing metal pellets on a pure titanium target. Zinc and copper are proved to be unsuitable due to the high temperature of the target during the deposition. The copper pellets are mostly thawed, zinc pellets first melt and then evaporate. Nickel as the doping element is thus chosen in our work [8]. The work with nickel pellets is complicated because of ferromagneticity of nickel and placement of the pellets in a strong magnetic field on the cathode. Thus, in the end, the coatings are prepared by sputtering of an alloy TiNi target in an atmosphere containing acetylene. The amount of the metals supplied from the sputtering of the TiNi target steadily decreases with increased acetylene flow (and hence the carbon content of the coating) due to the used deposition process. This results in a gradual decrease of the effect of the doping with increasing carbon content. It is concluded that nickel is successfully incorporated into the grains as no diffractions corresponding to Ti are observed and the cubic TiC lattice parameter of the doped coatings is higher than that measured in coatings prepared without nickel. A change in the microstructure of the coatings is observed as expected. Nickel addition primarily leads to grain size decrease due to the suspected formation of lattice defects induced by nickel incorporation into the grains. Lower mean grain separation is also observed. The change in the microstructure leads to

somewhat enhanced hardness if the carbon content is $\lesssim 45\,\mathrm{at.\%}$. However, it is strongly reduced if the carbon content is higher.

Therefore, Ni doping does not lead to deposition of coatings with higher maximal hardness. However, nickel is incorporated to the grains, and self-lubricity of the coatings can still be achieved. This can be a subject of subsequent tests.

Chapter 3

Nanostructured Mo-B-C coatings prepared by magnetron co-sputtering

3.1 Introduction

The second section is devoted to the deposition and analysis of a different type of nanostructured coatings containing molybdenum, boron and carbon. The work on this type of coatings is inspired by the works of the group of professor Jochen Schneider from Aachen University on the Mo_2BC coatings.

Mo_2BC in a bulk form was in the centre of focus of studies before, but it was rather for its superconducting properties and not the mechanical properties. Mo_2BC in the form of a thin film is first synthesised in Aachen in 2009. They also calculated, that the elemental cell of crystalline Mo_2BC combining layers with high and low electron density intrinsically exhibits high hardness and stiffness coupled with enhanced ductility. This would be very advantageous for demanding applications in the industry, where the current generation of although hard, but often brittle protective coatings fails. The presented method of the synthesis on crystalline Mo_2BC coatings has one drawback. Substrate temperature $\gtrsim 800\,^\circ\mathrm{C}$ is needed to obtain crystalline coating when DC is used for the plasma excitation. This temperature is decreased down to $\sim 400\,^\circ\mathrm{C}$ when HiPIMS is used. HiPIMS is, however, still an expensive technology with many free parameters not wholly suitable for an easy mass industrial use. Therefore, we use mid-frequency pulsed DC

plasma excitation to enhance the energy flow to the substrate compared to DC sputtering to lower the crystallisation temperature. We also studied if a fully crystalline coating with a precise chemical composition is even needed to achieve hard and crack resistant coatings. This is described in paper [9]. The second paper discussed in this chapter and the last in this work [10] is focused on the changes of the structure and the mechanical properties of the coatings with increasing annealing temperature.

3.2 Synthesis of Mo-B-C coatings using pulsed-DC and their analysis

The first step in the deposition of Mo-B-C coatings is to establish what pulsing frequency and duty cycle should be used to maximise the ion flux on the substrate to in turn maximise the energy flow on the growing coating to promote its crystallinity. This is tested by a simple planar Langmuir probe placed on the substrate holder and DC-biased to -100 V to reach the saturated ion current. The pulsing frequency is varied from 0 kHz (i.e. DC) to 350 kHz. Duty cycles of 65 % and 85 % are tested for each frequency. The dependency of the ion flux on the pulsing frequency for both duty cycles is plotted in Fig. 3.1. Increased pulsing frequency results in an increase of the ion current. Also, the lower duty cycle shows a higher ion current. This is understandable as the power was always the same, it is concentrated in a shorter part of the pulse in case of the lower duty cycle. This results in a denser plasma leading to higher ionisation of the argon as well as, to a certain extent, of the sputtered species. Moreover, the literature search revealed that not only the ion number increases with higher pulsing frequency. Also, the ion energy distribution significantly broadens, and three different energy populations are present. This results in yet higher energy flow to the substrate. Therefore, conditions with the highest ion current are chosen for the depositions in our work — 350 kHz pulsing frequency with 65 % duty cycle. Three targets are usually sputtered – molybdenum, carbon and B_4C. The pulsed DC output is connected to the carbon target as the vast majority of the ions are argon ions and the highest power is always supplied to the carbon target because of its low sputter yield. Several depositions are carried out from a single compound Mo_2BC target connected to the pulsed DC power supply.

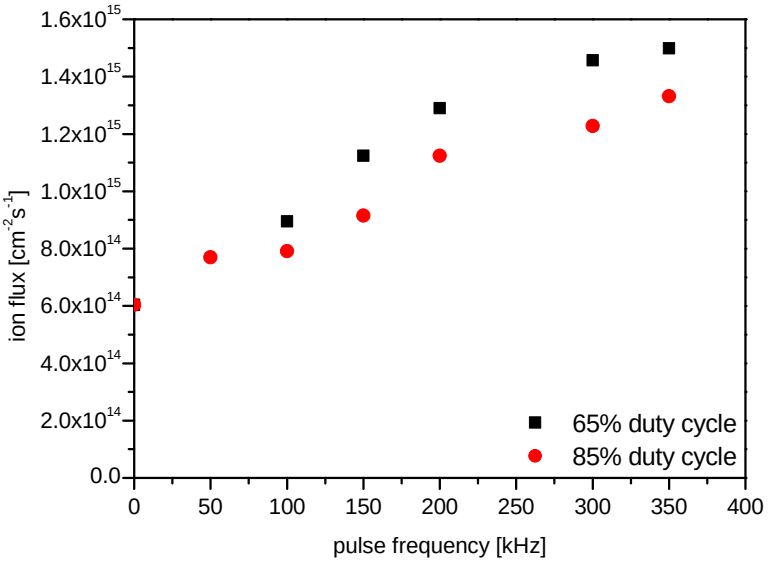

Figure 3.1: The ion flux as a function of the pulsing frequency and the duty cycle.

Once the pulsing conditions are established, the depositions begin. Coatings with different microstructures are prepared by varying the coating composition, deposition temperature and bias. The microstructure of the coatings is observed, and the crystallinity is first evaluated by X-ray diffraction and later by transmission electron microscopy with selected area electron diffraction. Coatings with three different types of microstructure are prepared.

The first type of coatings exhibits a small broad diffraction peak centred at $\sim 38^\circ$ (samples A1 and A2 in paper [9]). Dark field transmission electron microscope (TEM) micrograph reveals only short-range ordering in the coating, which was confirmed by SAED (see Fig. 3.2a). These near-amorphous coatings exhibit the hardness of ~ 20 GPa and elastic modulus of ~ 280 GPa. The fracture resistance is tested by indentation with the load of 1 N. This load ensures that the Berkovich tip indents the sample to a maximum depth exceeding the coating thickness. No crack formation is detected on the load/displacement curves or the surface of the coating in the area of the residual indent as is shown in Fig. 3.2b. This implied that obtaining fully crystalline Mo_2BC coating is not a strict condition for achieving hard and fracture resistance coatings. Even the chemical composition of 50 at.%

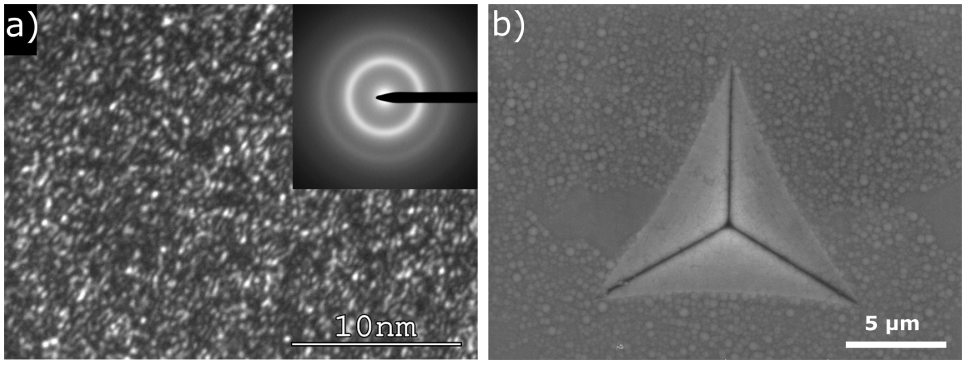

Figure 3.2: Near amorphous Mo-B-C coatings. a) TEM b) residual indent.

of Mo, 25 at.% of B and 25 at.% C is not necessary as similar deformation behaviour is observed even when the composition is varied.

Samples labelled as C in paper [9] are later divided into two subgroups. Only sample C2 from this article falls into the first subgroup. The first subgroup exhibits chemical composition approximately corresponding to Mo_2BC. The X-ray diffractograms have a more pronounced narrower asymmetrical diffraction peak centred at $\sim 41^\circ$. This peak can be deconvoluted into two partially overlapping peaks. The base broad peak resembled the one seen in the near-amorphous coatings. The second one is narrower indicating the presence of another phase with a higher level of crystallinity. The position of the sharp peak is close to the reference value for (111) and (080) Mo_2BC diffractions. A bright field TEM image with the corresponding SEAD pattern presented in Fig. 3.3a shows a fine columnar microstructure throughout the whole thickness. The SAED pattern is composed of several diffuse rings with a strong texture. These are indexed as corresponding to Mo_2BC phase. The individual crystallite size is estimated using the Scherrer equation from the sharp peak of the XRD to be ~ 4 nm. The small size of the crystallites also explains the lack of other diffraction peaks in the X-ray diffractograms. Due to the relatively large size of the elemental cell, each crystallite is composed of only a few elemental cells. Therefore, only a very limited periodicity makes the appearance of weaker diffraction peaks highly unlikely. In conclusion, this subgroup of coatings is composed of Mo_2BC nanocrystallites in a Mo-B-C matrix in a nanocomposite fashion. The hardness of such samples is higher ~ 31 GPa probably owing to the nanocomposite structure. TEM micrograph of a lamella cut from the area of the residual indentation im-

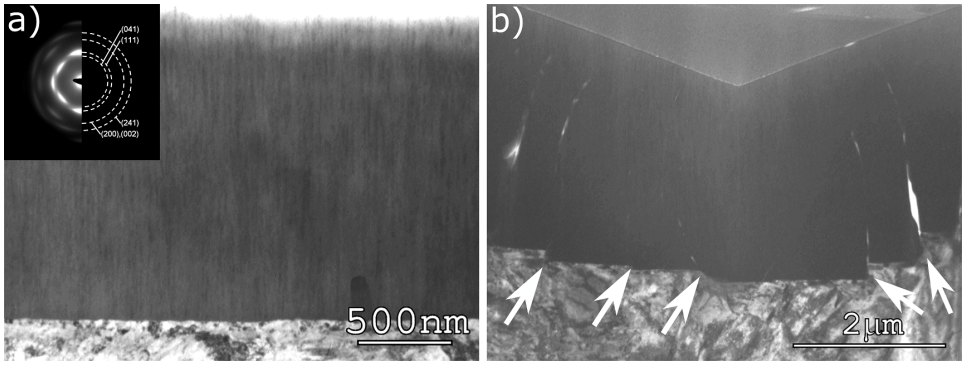

Figure 3.3: Nanocomposite Mo-B-C coating. a) TEM b) cross-section view of a residual indent.

print in the coating prepared on the high-speed steel substrate is presented in Fig. 3.3b. The high-speed steel substrate shears in several places under the severe stresses induced by the high-load indentation tests (indicated by the white arrows). The adhesion of the coating to the substrate proves to be higher than the internal cohesion and cracks originate from the coating/substrate interface, specifically from the places of the substrate failure. However, the cracks stop propagating in the volume of the coating and do not reach its surface. This strongly implies excellent fracture resistance of the nanocomposite coatings.

The last subgroup is characterised by a strong excess of molybdenum in the coating typically caused by application of bias during the deposition, as the application of bias cause enhanced re-sputtering of the lighter elements. Samples C1 and C3 belong to this group. The X-ray diffractograms exhibit a similarly broad base peak as the first two groups indicating the presence of a amorphous Mo-B-C pahse. However, another yet harper peak is superimposed and is shifted to the one seen in the nanocomposite group. The presence of this peak sharp together with a small peak at $\sim 59°$ indicates the presence of crystalline Mo phase. This is confirmed by the electron diffraction pattern presented in Fig. 3.4a. The TEM figure also revealed that the coating is predominantly crystalline. The size of the Mo crystallites calculated by the Scherrer equation was $\sim 6\,\mathrm{nm}$. Therefore, these coatings are prevalently nanocrystalline with lower amount of an amorphous phase. They exhibit the hardness of $\sim 21\,\mathrm{GPa}$, but the elastic modulus is higher than that of the near-amorphous coatings. A lamella from the area under the

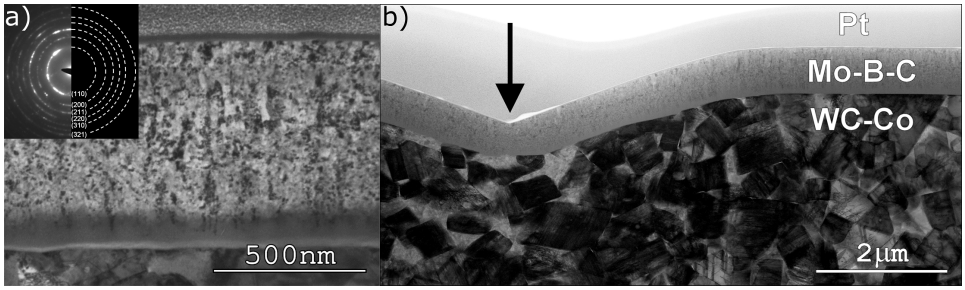

Figure 3.4: Nanocrystalline Mo-B-C coating. a) TEM b) cross-section view of a residual indent.

residual indentation imprint is shown in Fig. 3.4b. The cermet substrate is significantly deformed, and the coating complies. Despite this large deformation, the coating exhibits good adhesion and no delamination under the imprint is observed. Furthermore, no cracks are detected in the bulk of the coating. The fully plastic deformation response even under such severe deformation without the presence of cracking in the coating proves high fracture resistance of the prevalently nanocrystalline coatings.

In summary not only the predicted crystalline Mo_2BC coatings exhibit high hardness coupled with enhanced ductility. All of the prepared amorphous, nanocomposite, as well as prevalently nanocrystalline coatings, show hardness higher than 20 GPa with no cracks in the area of residual imprints after high-load tests. State of the art protective coatings such as TiN, TiAlN or TiB_2 tested in the same manner fail and exhibit severe cracking. Cracks in the bulk of deposited coatings are detected only if the substrate itself shears. If the substrate is plastically deformed without shearing, the coating complies, and no cracks in the bulk of the coating are detected. Such material can pave the way to next generation of protective coatings for the most demanding applications where deformation of the coated workpiece is involved.

3.3 Thermal stability of the Mo-B-C coatings

The last paper covered in this work is focused on the study of the changes in the structure and mechanical properties of the Mo-B-C coatings induced by annealing of the sample. This is important to obtain the value of the crystallization temperature, to identify the crytalline phase or phases and

to understand the changes of the mechanical properties once it is reached. An amorphous sample in the as-deposited state with the composition close to Mo_2BC was chosen for this study as the changes in the structure should be the most pronounced. Samples deposited on high-speed steel were tested up to 600°C and samples deposited on tungsten carbide-cobalt cermet up to 1000°C.

The microstructure is evaluated by XRD. No significant changes of the X-ray diffractogram up to 900°C are observed. Diffraction peaks corresponding to Mo2C phase appear when the coating is annealed to 1000°C. These results would indicate that the mechanical properties would not change up to 900°C.

This is not the case. The as-deposited coatings on both substrates exhibit the hardness of ~ 20 GPa. The annealing to 500°C and 600°C leads to a distinct increase to ~ 24 GPa in case of coatings on the high-speed steel substrate and ~ 23 GPa in case of coatings on the cermet substrate. The small difference between the substrates can be explained by different coefficients of thermal expansion of both substrates generating higher thermal stress in case of the steel substrate. The same explanation cannot be used to account for the difference between the as-deposited coating and the coating annealed to 500°C. The load/displacement curves can shed some light on this problem. Whereas the load/displacement curve in the case of the as-deposited coating is smooth, the same curve in the case of the sample annealed at 500°C exhibits several pop-ins typical for crystalline materials. Therefore, even though the annealing temperature is relatively low, the areas of the short-range ordering serve as seeds for crystallite growth. The size of the crystallites is probably in the range of 1 – 2 nm, which is too small for the X-ray diffraction to produce distinct peaks. The hardness of the coating further increases to ~ 31 GPa after annealing to 1000°C probably due to the formation of Mo_2C.

The fracture resistance is tested in the same manner as is described in the previous section. The as-deposited coating do not exhibit any cracks in or around the residual indentation imprint. Small picture-frame cracks in the imprint are observed when the coating is annealed to 600°C. A distinct cracks more than 5 µm long cracks from the corners of the imprint are seen when the sample is annealed to 1000°C. Therefore, the hardness of the deposited coating can be enhanced by post-deposition annealing, however, this hardness increase is at the cost of fracture resistance decrease.

Bibliography

[1] T. Schmidtová, P. Souček, P. Vašina, *Study of hybrid PVD–PECVD process of Ti sputtering in argon and acetylene*, Surf. Coat. Technol. 205 (2011) S299–S302

[2] T. Schmidtová, P. Souček, V. Kudrle, P. Vašina, *Non-monotonous evolution of hybrid PVD–PECVD process characteristics on hydrocarbon supply*, Surf. Coat. Technol. 232 (2013) 283–289

[3] P. Vašina, P. Souček, T. Schmidtová, M. Eliáš, V. Buršíková, M. Jílek, M. Jílek jr., J. Schäfer, J. Buršík, *Depth profile analyses of nc-TiC/a-C:H coating prepared by balanced magnetron sputtering*, Surf. Coat. Technol. 205 (2011) S53–S56

[4] P. Souček, T. Schmidtová, L. Zábranský, V. Buršíková, P. Vašina, O. Caha, M. Jílek, A.A. El Mel, P.Y. Tessier, J. Schäfer, J. Buršík, V. Peřina, R. Mikšová, *Evaluation of composition, mechanical properties and structure of nc-TiC/a-C:H coatings prepared by balanced magnetron sputtering*, Surf. Coat. Technol. 211 (2012) 111–116

[5] P. Souček, T. Schmidtová, L. Zábranský, V. Buršíková, P. Vašina, O. Caha, J. Buršík, V. Peřina, R. Mikšová, Y.T. Pei, J.Th.M. De Hosson, *On the control of deposition process for enhanced mechanical properties of nc-TiC/a-C:H coatings with DC magnetron sputtering at low or high ion flux*, Surf. Coat. Technol. 255 (2014) 8–14

[6] R. Žemlička, P. Souček, P. Vogl, M. Jílek, V. Buršíková, P. Vašina, Y.T. Pei, *On the significance of running-in of hard nc-TiC/a-C:H coating for short-term repeating machining*, urf. Coat. Technol. 315 (2017) 17–23

[7] P. Souček, J. Daniel, J. Hnilica, K. Bernátová, L. Zábranský, V. Buršíková, M. Stupavská, P. Vašina, *Superhard nanocomposite nc-TiC/a-C:H coatings: The effect of HiPIMSon coating microstructure and mechanical properties*, Surf. Coat. Technol. 311 (2017) 257–267

[8] J. Daniel, P. Souček, K. Bernátová, L. Zábranský, M. Stupavská, V. Buršíková, P. Vašina, *Investigation of the Influence of Ni Doping on the Structure and Hardness of Ti-Ni-C Coatings*, J. Nanomater. 2017 (2017) 6368927

[9] L. Zábranský, V. Buršíková, P. Souček, P. Vašina, J. Buršík, *On the study of the mechanical properties of Mo-B-C coatings*, Eur. Phys. J. Appl. Phys. 75 (2016) 24716(7pp)

[10] L. Zábranský, V. Buršíková, P. Souček, P. Vašina, J. Dugáček, P. Sťahel, J. Buršík, M. Svoboda, V. Peřina, *Thermal stability of hard nanocomposite Mo-B-C coatings*, Vacuum 138 (2017) 199–204

Author's publications not discussed in this work

[11] J. Daniel, P. Souček, L. Zábranský, V. Buršíková, M. Stupavská, P. Vašina, *On the effect of the substrate to target position on the properties of titanium carbide/carbon coatings*, Surf. Coat. Technol *in press*, doi: 10.1016/j.surfcoat.2017.06.076

[12] M. Kotilainen, R. Krumpolec, D. Franta, P. Souček, T. Homola, D.C. Cameron, P. Vuoristo, *Hafnium oxide thin films as a barrier against copper diffusion in solar absorbers*, Sol. Energ. Mat. Sol. C. 166 (2017) 140–146

[13] R. Žemlička, M. Jílek, P. Vogl, J. Šrámek, P. Souček, V. Buršíková, P. Vašina, *Principles and practice of an automatic process control for the deposition of hard nc-TiC/a-C:H coatings by hybrid PVD-PECVD under industrial conditions*, Surf. Coat. Technol. 304 (2016) 9–15

[14] J. Buršík, V. Buršíková, P. Souček, L. Zábranský, P. Vašina, *Nanostructured Mo-B-C coatings*, Rom. Rep. Phys. 68 (2016) 1069–1075

[15] T. Homola, V. Buršíková, T.V. Ivanova, P. Souček, P.S. Maydannik, D.C. Cameron, J.M. Lackner, *Mechanical properties of atomic layer deposited Al_2O_3/ZnO nanolaminates*, Surf. Coat. Technol. 284 (2015) 198–205

[16] L. Zábranský, V. Buršíková, J. Daniel, P. Souček, P. Vašina, J. Dugáček, P. Šťahel, O. Caha, J. Buršík, V. Peřina, *Comparative analysis of thermal stability of two different nc-TiC/a-C:H coatings*, Surf. Coat. Technol. 267 (2015) 32–39

[17] P. Souček, T. Schmidtová, V. Buršíková, P. Vašina, Y.T. Pei, J.Th.M. De Hosson, O. Caha, V. Peřina, T. Mikšová, P. Malinský, *Tribological properties of nc-TiC/a-C:H coatings prepared by magnetron sputtering at low and high ion bombardment of the growing film*, Surf. Coat. Technol. 241 (2014) 64–73

[18] A.A. El Mel, E- Gautron, F. Christien, B. Angleraud, A. Granier, P. Souček, P. Vašina, V. Buršíková, M. Takashima, N. Ohtake, H. Akasuka, T. Suzuki, P.Y. Tessier, *Titanium carbide/carbon nanocomposite hard coatings: A comparative study between various chemical analysis tools*, Surf. Coat. Technol. 256 (2014) 41–46

[19] R. Žemlička, M. Jílek, P. Vogl, P. Souček, V. Buršíková, J. Buršík, P. Vašina, *Understanding of hybrid PVD–PECVD process with the aim of growing hard nc-TiC/a-C:H coatings using industrial devices with a rotating cylindrical magnetron*, Surf. Coat. Technol. 255 (2014) 118–123

[20] L. Zábranský, V. Buršíková, P. Souček, P. Vašina, T. Gardelka, P. Sťahel, O. Caha, V. Pečina, J. Buršík, *Study of the thermal dependence of mechanical properties, chemical composition and structure of nanocomposite TiC/a-C:H coatings (Reprinted from Surface & Coatings Technology, vol 242, pg 62-67, 2014)*, Surf. Coat. Technol. 255 (2014) 158–163

[21] J. Šperka, P. Souček, J.J.W.A. Van Loon, A. Dowson, C. Schwartz, J. Krause, Y. Butenko, G. Kroesen, V. Kudrle, *Hypergravity synthesis of graphitic carbon nanomaterial in glide arc plasma*, Mater. Res. Bull 54 (2014) 61–65

[22] L. Zábranský, V. Buršíková, P. Souček, P. Vašina, T. Gardelka, P. Sťahel, O. Caha, V. Pečina, J. Buršík, *Study of the thermal dependence of mechanical properties, chemical composition and structure of nanocomposite TiC/a-C:H coatings*, Surf. Coat. Technol. 242 (2014) 62–67

[23] J. Šperka, P. Souček, J.J.W.A. Van Loon, A. Dowson, C. Schwartz, J. Krause, Y. Butenko, G. Kroesen, V. Kudrle, *Hypergravity effects on glide arc plasma*, Eur. Phys. J. D. 67 (2013) 261

[24] F. Amato, N.R. Panyala, P. Vašina, P. Souček, J. Havel, *Laser desorption ionisation quadrupole ion trap time-of-flight mass spectrometry of titanium-carbon thin films*, Rapid Commun. Mass Spectrom. 27 (2013) 1196–1202

[25] L. Zábranský, V. Buršíková, J. Buršík, P. Vašina, P. Souček, O. Caha, M. Jílek, V. Peřina, *Study of the indentation response og nanocomposite n-TiC/a-C:H coatings*, Chemické listy 106 (2012) S1508–S1511

[26] M. Eliáš, P. Souček, P. Vašina, *Influence of N_2 and CH_4 on deposition rate of boron based thin films prepared by magnetron sputtering*, Chemické listy 102 (2008) S1506-S1509

Attached commented publications

Surface & Coatings Technology 205 (2011) S299–S302

Contents lists available at ScienceDirect

Surface & Coatings Technology

journal homepage: www.elsevier.com/locate/surfcoat

Study of hybrid PVD–PECVD process of Ti sputtering in argon and acetylene

Tereza Schmidtová [a,*], Pavel Souček [a], Petr Vašina [a], Jan Schäfer [b]

[a] Department of Physical Electronics, Faculty of Science, Masaryk University, Kotlářská 2, CZ-61137, Brno, Czech Republic
[b] INP Greifswald e.V., Felix-Haussdorff-Str.2, D-17489, Greifswald, Germany

ARTICLE INFO

Article history:
Received 10 September 2010
Accepted in revised form 16 February 2011
Available online 26 February 2011

Keywords:
Hybrid PVD–PECVD process
Reactive magnetron sputtering
Hysteresis
Modelling

ABSTRACT

Hybrid PVD–PECVD process of target sputtering in hydrocarbon containing atmosphere combines aspects of both conventional reactive magnetron sputtering (PVD) and plasma enhanced chemical vapour deposition (PECVD). Such process is being typically used for deposition of metal carbides embedded in hydrogenated carbon matrix. Compared to the conventional co-sputtering of metal and carbon targets, in the hybrid deposition process the source of the carbon is dissociated hydrocarbon vapour in plasma. The aim of this paper is to study the extent of similarities or differences between this hybrid process and the conventional reactive magnetron sputtering. We have chosen the sputtering of titanium target in acetylene containing atmosphere as a representative of the hybrid processes. We focused on experimental measurements of the hybrid PVD–PECVD process behaviour, the time necessary for the process to achieve steady-state conditions and basic modelling of the process.

1. Introduction

Hybrid deposition processes [1–3] combine various techniques for deposition of thin films. Hybrid PVD–PECVD process of a target sputtering in a hydrocarbon containing atmosphere combines aspects of both conventional reactive magnetron sputtering (PVD) and plasma enhanced chemical vapour deposition (PECVD) [4–6]. Such hybrid processes are being used for synthesis of metal carbon nanocomposite layered structures [7–10]. The source of the carbon in the hybrid PVD–PECVD process is dissociated hydrocarbon vapour and not the carbon target as in co-sputtering experiments. The main research in this field is focused on the study of properties of deposited material and the process features are often neglected.

Adding acetylene in the hybrid process is very like adding oxygen or nitrogen into the conventional reactive magnetron sputtering and therefore there is a rightful question of similarity or difference between these two processes. Reactive magnetron sputter deposition in oxygen/nitrogen containing atmosphere is widely used for deposition of various materials. In general, reactive magnetron sputtering controlled by a supply flow of the reactive gas suffers with undesirable hysteresis behaviour. In a certain range of reactive gas supply there exist two modes of operation: the so-called metal mode and the compound mode [11].

The aim of this paper is an experimental study of the behaviour of hybrid PVD–PECVD process and basic modification of the current model for the reactive magnetron sputtering [12] to involve aspects of the studied hybrid PVD–PECVD process. We present the experimental measurements of the hybrid process behaviour and discuss the time necessary to achieve steady-state conditions during this process and report on the hybrid process modelling using the approach of Berg model [12].

2. Experimental configuration

Measurements were done on the commercial magnetron sputtering system Alcatel SCM 650 — the experimental set-up drawing can be found at [13]. A titanium target (purity 99.99%) 20 cm in diameter was sputtered downwards being mounted on a well balanced magnetron head. The distance between the target and substrate was 7 cm. The argon flow was kept constant at 20 sccm for all experiments. For the study of the hybrid PVD–PECVD process acetylene gas was used. For comparison with the conventional reactive magnetron sputtering we have chosen oxygen and nitrogen. The gas inlet position was located below the substrate holder [13] however the pump entry covered both the region bellow and above the substrate holder. Thus the amount of gas entering the zone between the target and the substrate was lower than total measured supply. Plasma was ignited by a RF generator at 900 W. We had chosen the RF discharge on purpose in order to eliminate the arcing caused by a formation of dielectric carbon rich layer on the target surface.

The non-invasive widely used technique of optical emission spectroscopy was used as the diagnostic tool. Jobin-Yvon Triax 320 and Avantes SD2000 spectrometers were used.

3. Results

Argon and titanium lines were always present in optical emission spectra. For the reactive sputtering in oxygen also the oxygen line at

* Corresponding author.
E-mail address: dorian@physics.muni.cz (T. Schmidtová).

0257-8972/$ – see front matter © 2011 Elsevier B.V. All rights reserved.
doi:10.1016/j.surfcoat.2011.02.047

777 nm was observed. In the case of hybrid sputtering with acetylene only very weak lines of atomic carbon at 248 nm and molecular band of CH radical at 431 nm were observed together with stronger atomic hydrogen lines H_α, H_β depending on the acetylene supply.

For both reactive sputtering and hybrid process we chose the Ti line at 365 nm and studied its evolution on oxygen, nitrogen or acetylene flow. The measured data were normalised to reach 100% of Ti line intensity for no supply of oxygen, nitrogen or acetylene and clean target. In Fig. 1 are shown the measured dependencies of Ti line intensity on oxygen and acetylene flow. Each point corresponds to steady-state conditions that were reached after setting of the desired gas flow. The starting point for increasing flows was the clean target and for decreasing flows the target poisoned by a high amount of gas.

The hysteresis region for oxygen case (upper graph) is wide because of a difference between titanium sputtering yield from the cleaned part of the target and from the poisoned part of the target (TiO_2). The transition between the metal and the compound mode is given by newly generated process conditions in the whole reactor when a critical reactive gas flow is reached. On the other hand the hybrid process of titanium sputtering in argon and acetylene behave differently than reactive magnetron sputtering (lower graph). Ti line intensity is decreasing and increasing linearly on the amount of acetylene flow. Clearly no hysteresis is observed despite that the sputtering yields of TiC [14] and C [15] are lower than of Ti [14,15].

In the hybrid PVD–PECVD process the addition of hydrocarbon gas into argon sputtering of metal target results in formation of carbon rich layers on the target surface as well as on all other reactor surfaces. Depending on experimental conditions, we have observed black, thick carbon rich rings surrounding the racetrack area of the target. Apart from the racetrack the target was all covered by carbon rich layer.

In the reactive magnetron sputtering the only option how to getter oxygen from the volume is a reaction at the target surface or with sputtered titanium atoms at the substrate area. In the hybrid process the acetylene dissociation takes place in magnetised plasma and carbon and carbon fragments diffuse to reactor surfaces and attach. These thick carbon rich layers on all reactor surfaces can store a large amount of carbon to such an extent that in the volume the presence of carbon containing radicals could be minimal, as was experimentally observed. Therefore the hysteresis behaviour would be strongly suppressed.

Another important issue during conventional reactive sputtering is the ability of the process to readily respond to changes. New steady-state conditions are achieved usually very fast after the change of the gas flow. This is a key problem for the process control in general [16,17]. The ability of the hybrid process to absorb carbon in already carbon rich layers can lead to significant time prolongation of achieving the steady-state conditions or can even cause a time drift of the deposition process itself as carbon rich layers grow thicker and thicker.

In Fig. 2 are shown the time evolutions of the Ti line intensity for oxygen, nitrogen and acetylene. If 8 sccm of oxygen, nitrogen or acetylene is added into the reactor, the steady-state conditions are reached within 1 min. For the case of oxygen and nitrogen the transition from the metal to the compound mode occurs in very short time. If lower flow than that corresponding to the transition is set, the steady-state conditions are attained within several minutes. However for lower flow of acetylene the characteristic time is prolonged up to tens of minutes as can be seen in lower graph of Fig. 2. These characteristic times have to be taken into account during depositions because until the steady-state conditions are reached the coating composition can vary.

Since the hybrid PVD–PECVD process does not show the hysteresis region, there is no reason to intentionally poison the target before the deposition to operate it in the mode similar to the compound mode of the reactive magnetron sputtering. Nevertheless, it would be useful to know the characteristic times in this case. The target was at first intentionally fully poisoned by a high amount of oxygen, nitrogen or acetylene applied for the period of 3 min and the desired flow was set after that. We observed that the reactive sputtering achieves the steady-state in minutes, however the hybrid PVD–PECVD process

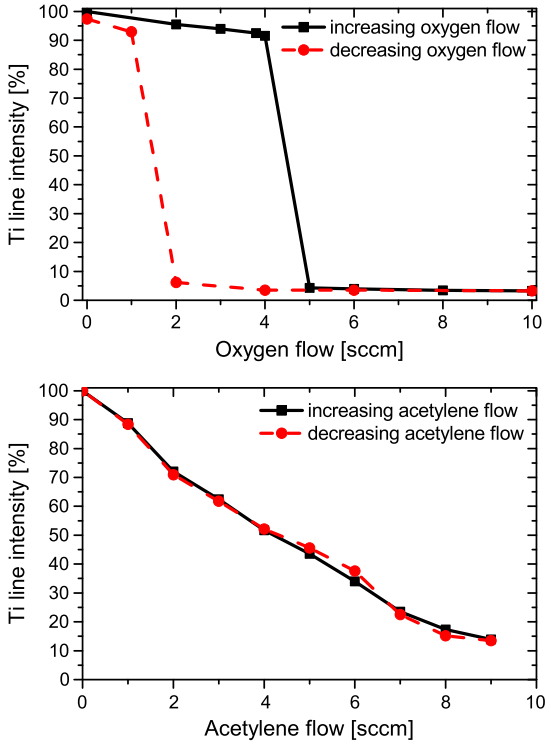

Fig. 1. Hysteresis behaviour of Ti line intensity on oxygen flow for conventional reactive magnetron sputtering (upper graph) and linear dependency of Ti line intensity on the acetylene flow for the hybrid process.

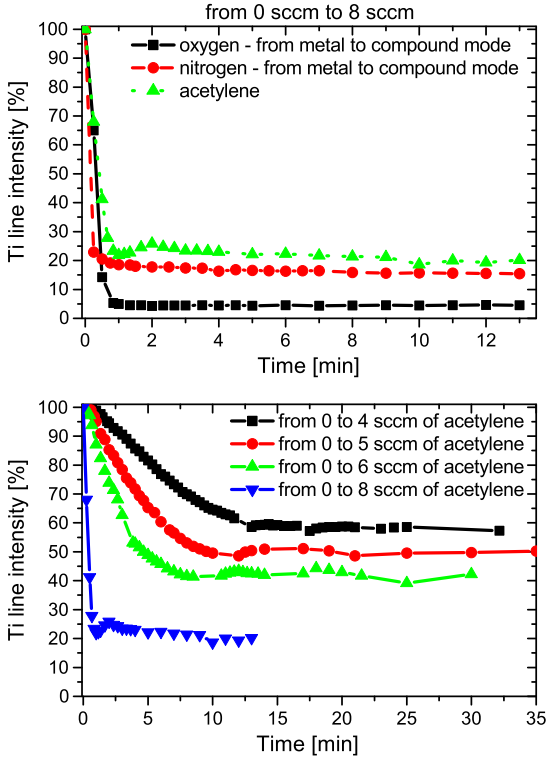

Fig. 2. Time evolution of Ti line intensity for oxygen, nitrogen and acetylene (upper graph) and for different acetylene flows (lower graph).

reaches the steady-state in the order of tens of minutes. This is caused by the formation of thin compound layers of TiN, TiO_2 on the target that are quickly out-sputtered compared to the thick carbon rich layers formed during the 3 min of the target poisoning. If we let the target to poison longer than 3 min, the times of achieving the steady-state conditions of the PVD–PECVD process will be prolonged.

4. Hybrid process modelling

The hybrid process behaviour has been modelled for the steady-state conditions using essentials of Berg model [12] which is widely used for modelling of hysteresis behaviour of reactive magnetron sputtering. Shortly, the Berg model is based on a description of the target poisoning using an equation of balance between formation and out-sputtering of the poisoned part of the target in steady-state conditions. Another balance equation is written for the substrate. Fluxes of metallic and compound species towards the substrate are given by percentage size of poisoned part of the target multiplied by corresponding sputtering yields. The reactive gas supply either contributes to the formation of compounds at target and substrate or leads to increase of reactive gas partial pressure. The surplus of the reactive gas is pumped out from the system by a pump of given pumping speed.

If we approach the hybrid process as conventional reactive sputtering as in Berg model where the C can react with Ti exclusively, forming TiC in a monolayer only, due to difference in sputtering yields of Ti [14,15] and TiC [14] the hysteresis would occur as a result of reduced supply of metal. However the observed behaviour of hybrid process was different.

For the purpose of basic modelling of the hybrid PVD–PECVD process the assumption of thick carbon layer forming on all surfaces was included into Berg model. We assumed total C_2H_2 dissociation only into C and H described by a dissociation degree. We then presumed the total carbon consumption on all surfaces in contrast to the Berg assumption of reactive gas consumption only on the clean parts of the target and the substrate where titanium is exposed. The assumption of the total carbon consumption at the target and the substrate enabled the formation of thick carbon layers, in other words the carbon fragments were allowed to attach also to already formed carbon layers.

The equations expressing these ideas were compiled as in Berg model. Our algorithm steps follow the equation order in given paper [12]. Following model parameters were used. The target area 0.03 m^2 and the pumping speed 0.04 $m^3\ s^{-1}$ were experimentally measured. The current corresponding to argon ion flux towards the cathode 0.5 A was deduced from reactive magnetron sputtering behaviour for the same discharge power. The substrate area of 0.3 m^2 was estimated from reactor geometry. Sputtering yields of Ti 0.2 and C 0.03 were taken from literature [15] for 200eV of Ar^+ that corresponds to RF self-bias measured in our experiment. We assumed gas temperature 300 K. According to literature [18], the hydrogen content in a-C:H matrix of n-TiC/a-C:H film is typically ~10%. Low hydrogen content in formed carbon rich layers facilitates the attachment of carbon fragments and further growth [19,20]. In our model, the sticking coefficients of carbon were kept one for simplicity. Further, if the sticking coefficient of C on C was decreased by 20%, the overall difference in model output was not more than 15% for higher flows of acetylene and even much lower for lower flows.

In Fig. 3 the observed behaviour of the hybrid PVD–PECVD process is plotted and it is compared to hybrid process simulations for different dissociation degrees. We assumed that the modelled sputtered Ti flux corresponds to the measured Ti line intensity. Clearly, no hysteresis was modelled. The shape of the modelled dependency is mainly influenced by the dissociation degree, the discharge current, the available consumption area and the pumping speed. The best experimental fit is for 25% dissociation degree. However, the dissociation degree of C_2H_2 in the discharge zone is higher due to the distant gas inlet that caused reduced amount of acetylene actually entering the discharge region.

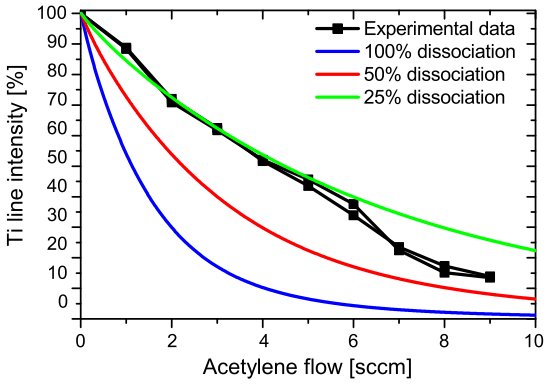

Fig. 3. Experimental Ti line intensity and modelled flux of sputtered Ti atoms on acetylene flow for different dissociation degrees of C_2H_2.

5. Conclusions

The hybrid PVD–PECVD process is unlike the conventional reactive magnetron sputtering. We have experimentally observed differences between the hysteresis behaviour of the conventional reactive magnetron sputtering of titanium target in oxygen/nitrogen containing atmosphere and the hybrid PVD–PECVD process of titanium target sputtering in argon and acetylene. No hysteresis region for the hybrid sputtering was found. This is an interesting fact from the industrial point of view because the hybrid process does not require any process control which is vital during conventional reactive magnetron deposition.

We presume forming of thick hydrogenated carbon rich layers from hydrocarbon radicals on all surfaces close to the electrode where the dissociation of acetylene takes place. Depositing coating is thus created not only by sputtering of titanium and carbon from the target surface but also by plasma induced polymerisation of hydrocarbon radicals directly at the substrate.

We have discussed the characteristic time needed for the hybrid process to achieve the steady-state conditions with findings that for higher amount of added acetylene the faster the steady-state conditions are reached. For higher flows the steady-state conditions are reached in within 1 min but for lower flows the time prolongs even to tens of minutes. The hybrid process behaviour has been basically modelled for the steady-state conditions using essentials of Berg model. The leading assumption of growing of thick carbon rich layers on surfaces caused the hysteresis suppression in the model.

Acknowledgements

This work has been supported by GACR 104/09/H080, 202/08/P038 and MSM contracts 0021622411 and OP R&DI CZ.1.05/2.1.00/03.0086. Pavel Souček acknowledges as a holder of Brno PhD Talent Financial Aid.

References

[1] J.P. Celis, D. Drees, M.Z. Huq, P.Q. Wu, M. De Bonte, Surf. Coat. Technol. 113 (1999) 165.
[2] A. Matthews, A. Leyland, Surf. Coat. Technol. 71 (1995) 88.
[3] A. Daniel, T. Duguet, T. Belmonte, Appl. Surf. Sci. 253 (2007) 9323.
[4] J.T. Harnack, F. Thieme, C. Benndorf, Surf. Coat. Technol. 39 (40) (1989) 285.
[5] J.T. Harnack, C. Benndorf, Mater. Sci. Eng. A140 (1991) 764.
[6] C. Benndorf, T.J. Harnack, U. Fell, Surf. Coat. Technol. 48 (1993) 345.
[7] Y.T. Pei, D. Galvan, J.Th.M. De Hosson, A. Cavaleiro, Surf. Coat. Technol. 198 (2005) 44.
[8] P.Y. Tessier, R. Issaoui, E. Luais, M. Boujtita, A. Granier, B. Angleraud, Solid State Sci. 11 (2009) 1824.

[9] W. Kulisch, P. Colpo, F. Rossi, D.V. Shtansky, E.A. Levashov, Surf. Coat. Technol. 118–119 (2004) 714.
[10] W. Gulbinski, S. Mathur, H. Shen, T. Suszko, A. Gilewicz, B. Warcholinski, Appl. Surf. Sci. 239 (2005) 302.
[11] S. Berg, H.-O. Blom, T. Larsson, C. Nender, J. Vac. Sci. Technol. A 5 (1987) 202.
[12] S. Berg, T. Nyberg, Thin Solid Films 476 (2005) 215.
[13] M. Eliáš, P. Souček, P. Vašina, Chem. Listy 102 (16) (2008) 1506.
[14] O.A. Fouad, A.K. Rumaiz, S.I. Shah, Thin Solid Films 517 (2009) 5689.
[15] Y. Yamamura, H. Tawara, Acad. Press 62 (1996) 149.
[16] T. Kubart, O. Kappertz, T. Nyberg, S. Berg, Thin Solid Films 515 (2006) 421.
[17] B. Bellido-González, B. Daniel, J. Counsell, D. Monaghan, Thin Solid Films 502 (2006) 34.
[18] A. Czyżniewski, W. Prechtl, J. Mater. Process. Technol. 157–158 (2004) 274.
[19] W. Jacob, Thin Solid Films 326 (1998) 1.
[20] M. Eckert, E. Neyts, A. Bogaerts, Chem. Vap. Deposition 14 (2008) 213.

Surface & Coatings Technology 232 (2013) 283–289

Contents lists available at ScienceDirect

Surface & Coatings Technology

journal homepage: www.elsevier.com/locate/surfcoat

Non-monotonous evolution of hybrid PVD–PECVD process characteristics on hydrocarbon supply

T. Schmidtová, P. Souček, V. Kudrle, P. Vašina *

Department of Physical Electronics, Kotlářská 2, Masaryk University, 61137 Brno, Czech Republic

ARTICLE INFO

Article history:
Received 25 February 2013
Accepted in revised form 13 May 2013
Available online 21 May 2013

Keywords:
Magnetron sputtering
Diagnostics of deposition process
Nanocomposites
Metal–carbon coatings

ABSTRACT

Hybrid PVD–PECVD process of titanium sputtering in argon and acetylene atmosphere combines aspects of both conventional techniques: sputtering of titanium target (PVD) and acetylene as a source of carbon (PECVD). This process can be used for preparation of metal carbon nanocomposites (MeC/C(:H)) or DLC layers doped with metal (DLC:Me). The aim of this paper is to describe and understand elementary processes influencing the hybrid PVD–PECVD process. A non-monotonous dependence of cathode voltage and current, total pressure and spectral line intensities on acetylene supply flow is reported. Explanation of non-monotonous evolutions through the analysis of the target state correlating the process characteristics with properties of coatings prepared by this process is proposed.

1. Introduction

Hybrid deposition systems combine more than one deposition technique [1]. These techniques are mutually independent and they are being used often in separate deposition chambers [1–4]. An overview of various deposition systems can be found in [2]. The sputtering of a metal target in a mixture of an inert gas and a hydrocarbon gas can be classified as a hybrid process combining PVD and PECVD techniques [5–8]. The source of carbon in the hybrid PVD–PECVD process is dissociated hydrocarbon vapour.

Hybrid PVD–PECVD process is being used for synthesis of metal hydrogenated carbon nanocomposite (MeC/C(:H)) [6,8–13] layers or DLC layers doped with metal (DLC:Me) [14–17]. For example nc-WC/a-C:H [18–21] or nc-TiC/a-C:H [9,22–24] are reported to have good mechanical and tribological properties combining high hardness, good toughness with low friction coefficient and wear which makes these materials industrially attractive for different applications. For the specific case of the titanium target sputtering in hydrocarbon containing atmosphere there exits variety of papers that are focused on the influence of process parameters on properties of deposited coating [8,25–29]. Process features are often omitted.

Hybrid PVD–PECVD process has been previously compared to the conventional reactive magnetron sputtering [30]. Even though the addition of the hydrocarbon is very similar to the adding of oxygen or nitrogen as a reactive gas in reactive sputtering, it was found [30] that hysteresis behaviour typical for reactive magnetron sputtering described by Berg model [31] was completely suppressed during hybrid PVD–PECVD process. Therefore, the hybrid PVD–PECVD depositions do not require complex feedback control. The absence of the hysteresis region was explained [30] by the capability of surfaces to be covered by thick carbon rich layers. In these thick carbon rich layers the carbon can be bound mutually in contrary to metal oxides/nitrides formation on surfaces during classical reactive magnetron sputtering where oxygen/nitrogen can be bound only to the metal. Nevertheless the target covering by these carbon rich layers during the hybrid PVD–PECVD process is still similar to the target poisoning by a reactive gas because it prevents the sputtering of the metal. So for description of both processes the phrases 'target poisoning' and 'target cleaning' can be understood and used.

The aim of this paper is to describe and understand elementary processes influencing the hybrid PVD–PECVD process governing the properties of the deposited coatings. We report a non-monotonous dependence of cathode voltage and current, total pressure and spectral line intensities on acetylene supply flow. We report on the dependence of the chemical composition and mechanical properties of the coatings on the acetylene flow. We provide an explanation of non-monotonous dependences through the analysis of the target state. The role of RF bias on the substrate and magnetron DC power on the process characteristics is also discussed.

2. Experimental configuration

Experimental measurements were done on semi-industrial magnetron sputtering system Alcatel SCM 650. Experimental setup drawing is shown in Fig. 1. A titanium target (purity 99.99%) 20 cm in diameter was mounted on a well balanced magnetron head, sputtering-up geometry was used. The magnetron plasma was well localized near the target, it does not extent to the substrate. The target-to-substrate distance was 7 cm. The chamber was pumped by turbomolecular pump

* Corresponding author: Tel.: +420 549 496 479.
E-mail address: vasina@physics.muni.cz (P. Vašina).

0257-8972/$ – see front matter © 2013 Elsevier B.V. All rights reserved.
http://dx.doi.org/10.1016/j.surfcoat.2013.05.014

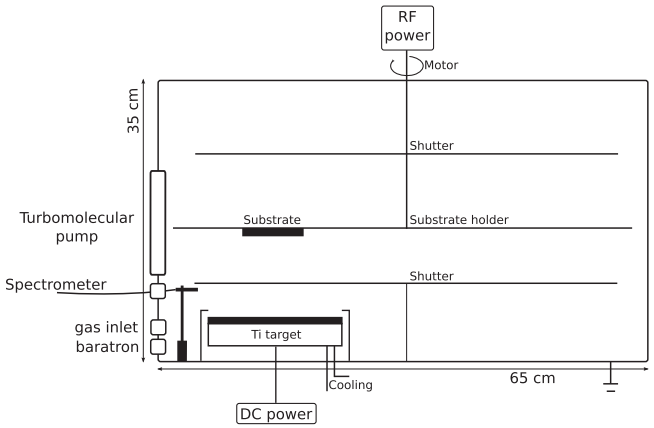

Fig. 1. Drawing of the experimental setup.

(700 l s^{-1}) backed by Roots pump. The base pressure was typically 10^{-4} Pa. During the deposition the pump was throttled to the pumping speed of 40 l s^{-1}. The argon (purity 99.999%) flow was kept constant at 20 sccm for all experiments. The typical working pressure was around 1 Pa.

For the study of the hybrid PVD–PECVD process acetylene (purity 99.6%) was used as carbon source. The acetylene flow ranged from 0 to 16 sccm. Magnetized plasma was ignited by DC power (1 kW or 2 kW) combined with or without RF substrate bias (225 W ~ −100 V). To enable comparison of the deposition process and deposited coating properties, the values of DC power, RF bias and supply flows of Ar and C_2H_2 were selected to correspond to values used in paper [23,24] where properties of deposited n-TiC/a-C:H coatings were studied in details. The DC generator was operated in constant power mode. Prior to each experiment, the target was thoroughly cleaned both mechanically and by Ar bombardment until the discharge voltage typical for pure Ti target was reached.

Spectrometer Avantes SD2000 was used as a diagnostic tool. Atomic spectral lines of titanium at 365 nm, argon at 420 nm and hydrogen at 656 nm were chosen for the study. There were no lines attributed to carbon or other fragments of acetylene in observed spectral range of 250–670 nm. Discharge parameters used for electrical diagnostics were the target voltage and the discharge current. The total pressure in the vacuum chamber was also recorded using MKS Baratron.

The depositions were carried out for 45 min at constant acetylene flow on high speed steel (HSS) and cermet tungsten carbide (WC) substrates. The DC power to the magnetron was set at the desired value and the substrate bias was −100 V. Chemical composition of the coatings was determined by Rutherford backscattering (RBS) and elastic recoil detection analysis (ERDA) methods using a Van de Graaff generator and TANDETRON with linear electrostatic accelerators. Fischerscope H100 depth sensing indenter equipped with a Berkovich tip was used to study the indentation response of the coating samples. The hardness and the indentation modulus were evaluated using the standard procedure proposed by Oliver and Pharr [32]. The EDX measurements were performed on JEOL JSM 6460 with Inca Energy EDX detector at 20 kV acceleration voltage.

For the study of the target state the following experimental settings were used. The depositions for various C_2H_2 flows were performed at conditions described in [23,24]. Target photo-documentation was done after each opening of the vacuum chamber. In order to quantify the target state on the evolution on the acetylene supply the pixel counting for target areas of interest were done for each taken photograph. The pixel counting determined the relative amount of studied parts. The pixel count was done at the racetrack part only, because the racetrack, the target erosion zone, plays the key role for the magnetron discharge. For the EDX (Energy-dispersive X-ray spectroscopy) study of the target racetrack coverage by Ti–C phases, Ti square samples (1 cm × 1 cm) were used and placed on the racetrack zone. One edge of Ti sample was placed in the racetrack centre and the other at the racetrack outer edge.

3. Results and discussion

3.1. Process characteristics

Typical overall hybrid PVD–PECVD process characteristics are given in Fig. 2. There are shown the dependences of cathode voltage and discharge current together with total pressure and spectral emission line intensities on the acetylene supply flow for 2 kW DC power applied on the magnetron target with −100 V RF bias.

Before measurement of each point, the target was thoroughly cleaned by Ar bombardment without the presence of acetylene to ensure the same target conditions and to eliminate the influence of previous measurements. The cleaning of the target covered by thick carbon rich layers takes long time [30]. The steady-state conditions of the hybrid PVD–PECVD process are reached in order of tens of minutes after acetylene injection. In Fig. 2 the full black square points denote the measured values with increasing acetylene flows — on the way from the clean target. When measuring with the decreasing acetylene flows, the cleaned target was exposed for 3 min to 30 sccm of C_2H_2 for full poisoning. The Fig. 2 the hollow red circle points denote measured values with decreasing acetylene flows — on the way from the poisoned target.

Fig. 2 demonstrates that the hybrid PVD–PECVD process does not exhibit hysteresis behaviour. The electrical characteristics in Fig. 2(a) and (b) are non-monotonous; a certain local minimum in voltage and local maximum in discharge current evolutions is observed. The discharge voltage and current are increasing and decreasing respectively while the DC generator was operated in constant power mode meaning that the current and voltage dependencies are inverted. There is also no rapid evolution of total pressure in the chamber with acetylene flow, see Fig. 2(c). The pressure is increasing with increasing acetylene flow almost linearly.

Dependence on acetylene supply flow of hydrogen, titanium and argon emission lines given by optical emission spectra are shown in Fig. 2(d)–(f). In Fig. 2(d) the non-monotonous evolution of hydrogen alpha line is plotted. It is increasing rapidly with increasing acetylene flow but for higher flows it is sharply decreasing, a maximum of hydrogen line intensity is observed for certain acetylene supply flow. The evolution of titanium emission line in Fig. 2(e) is different, it is almost linear. Looking at the argon emission line, see Fig. 2(f), its intensity is slightly decreasing, increasing and then decreasing as acetylene flow increases.

From the general overview of presented data, one can conclude that there exist three distinctive zones in which studied parameters evolve in a characteristic way. For 2 kW DC power applied on the magnetron target there is zone I from 0 to approximately 6 sccm of C_2H_2, zone II approximately from 6 to 12 sccm of C_2H_2 and zone III for higher flows than 12 sccm of C_2H_2.

The zone I is characterized by the increasing discharge voltage, pressure and hydrogen emission intensity and by the increase in discharge current, titanium emission intensity and slight decrease in argon emission. The zone II is characterized by the increase in discharge current, pressure, hydrogen emission intensity and slight increase in argon emission together with decreasing discharge voltage and titanium emission. In the zone III again the increase in the target voltage together with the slight increase in the total pressure can be observed, the decreasing values of the discharge current, titanium, hydrogen and argon is characteristic. Summarizing overview of each parameter evolutions within three defined zones is given in Table 1.

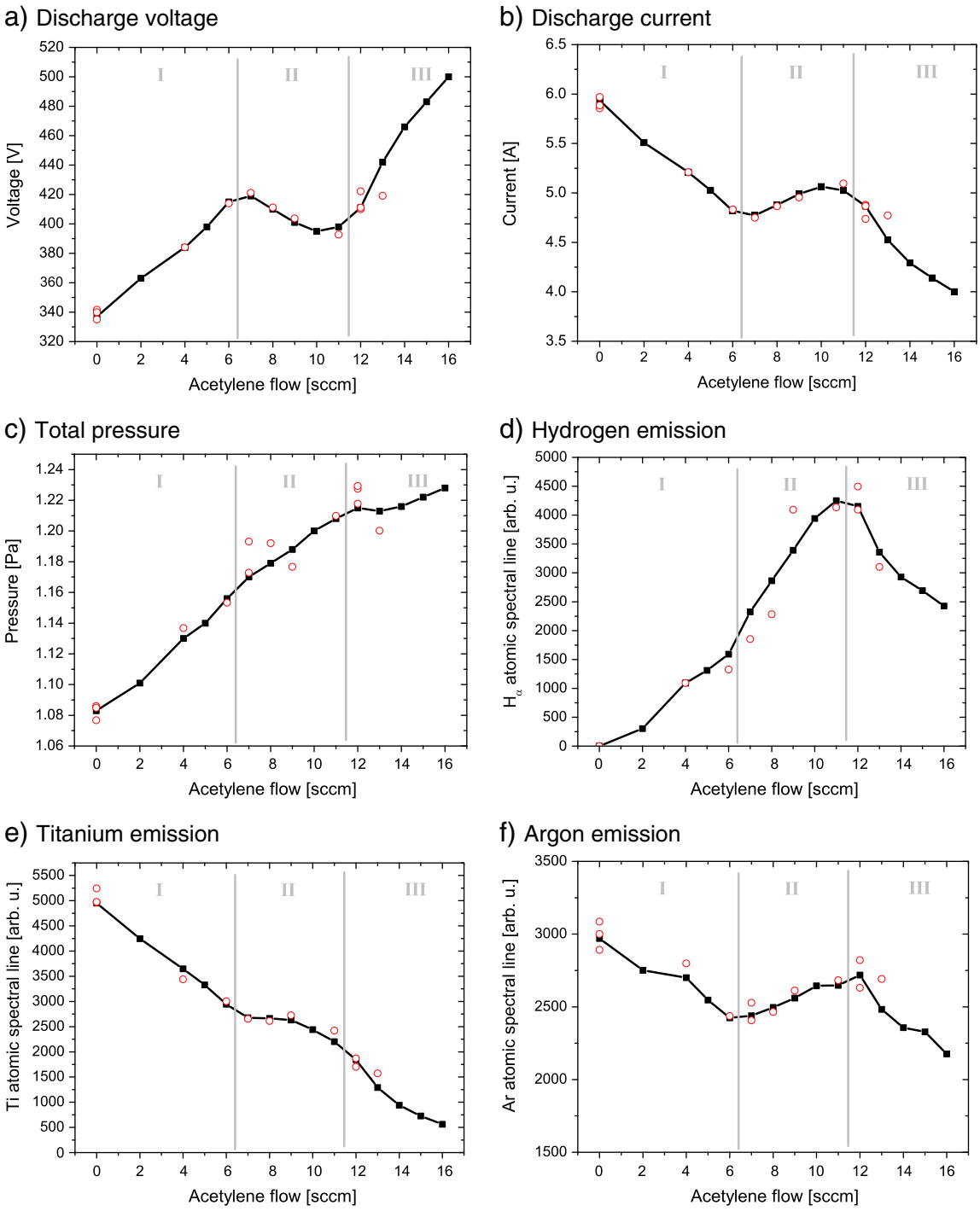

Fig. 2. Dependences of discharge voltage, discharge current, total pressure and spectral emission lines on acetylene flow. Black full square points are values obtained with increasing acetylene flow – on the way from clean target and red hollow circular points are values obtained with decreasing acetylene flow – on the way from poisoned target.

Table 1
Summarizing overview of each parameter evolutions within zones I–III.

	Voltage (current)	Spectral intensity			Relative density		
		H	Ti	Ar	H	Ti	Ar
Zone I	↗ (↘)	↗	↘	↘	↗	↗	→
Zone II	↘ (↗)	↗	↗	↗	↗	↘	→
Zone III	↗ (↘)	↘	↘	↘	→	↗	→

3.2. Film properties

A set of coatings was prepared using this hybrid PVD–PECVD process at acetylene flows of 8–14 sccm (i.e. in zones II and III) and analysed [24]. The chemical composition of the coatings behaves more monotonously as can be seen in Fig. 3. Titanium content decreases while carbon content increases with higher acetylene flow. Hydrogen content remains stable <10% and also the oxygen contamination remains low for the whole deposition range. The stoichiometric composition where

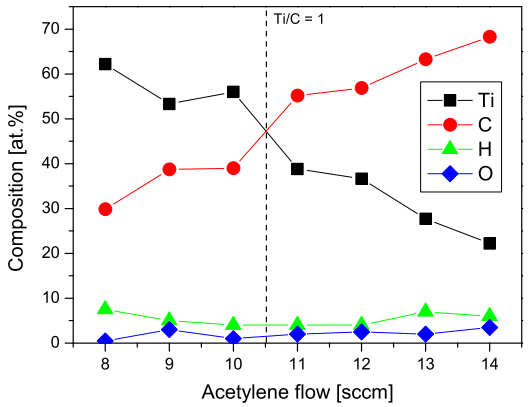

Fig. 3. Chemical composition of nc-TiC/a-C:H coatings depending on acetylene flow during deposition.

Ti/C = 1 was achieved for acetylene flow of ~10.5 sccm, which belongs to aforementioned zone II.

The mechanical properties show a distinct peak at acetylene flow of 12 sccm (see Fig. 4). At this point the hardness reaches 46 ± 2 GPa and Young's modulus 414 ± 7 GPa. The mechanical properties decrease with both lower and higher acetylene flows. The flow of 12 sccm lies on the border between zones II and III.

More detailed study of the properties of the thin films deposited by the hybrid PVD–PECVD process including evolution of the deposition rate, residual stress, microstructure, etc. with acetylene supply was presented in the associated paper [24].

3.3. The state of the target

For reactive magnetron sputtering, it was reported that the electrical characteristics are related to the state of the target; the target poisoning by a compound of different coefficient of secondary electron emission from the original target material results in a change in the target voltage [33]. In classical reactive magnetron sputtering the cathode voltage decreases/increases monotonously with the partial pressure of the reactive gas as there is a monotonous and continuous coverage of the target surface by a compound. However the electrical characteristics in Fig. 2(a) and (b) have distinctive evolution on the acetylene flow. A characteristic local minimum (maximum) in voltage (current) evolution is observed. As the pressure is evolving in Fig. 2(c) only a little its influence on the electrical characteristics should be negligible and the presence of the local minimum (maximum) should be related to the evolution of the state of the target in a different way during hybrid PVD–PECVD process than during classical reactive magnetron sputtering.

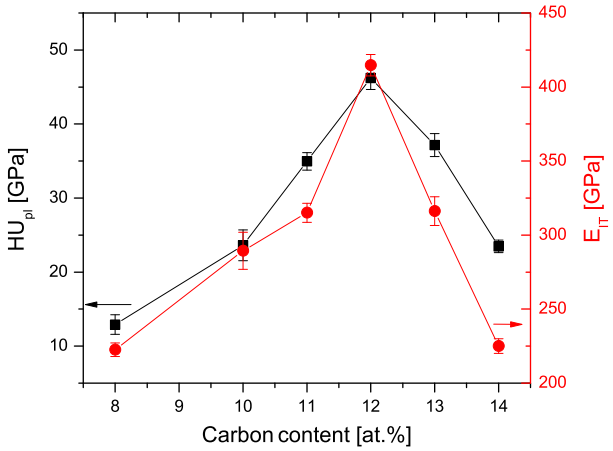

Fig. 4. Mechanical properties of nc-TiC/a-C:H coatings depending on acetylene flow during deposition.

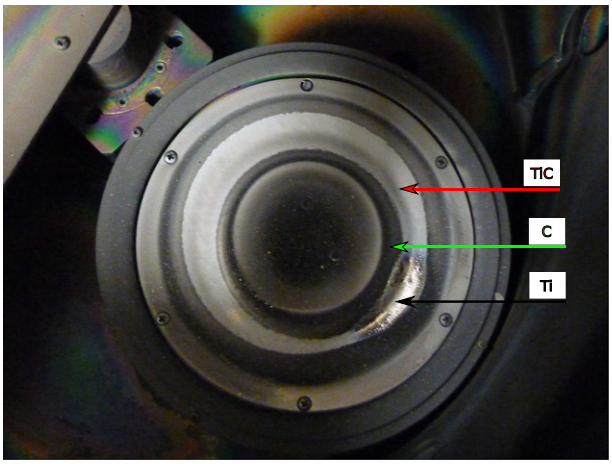

Fig. 5. Photograph of the target after sputtering by 2 kW DC power with RF substrate bias −100 V for 12 sccm of acetylene at steady-state conditions. Along the racetrack region three differently 'coloured' regions are visible. The pure metallic region is denoted as Ti, the grey as TiC and black as a-C.

For hybrid PVD–PECVD process a target surface photography is shown in Fig. 5. The target was covered by three differently 'coloured' regions. The following can be distinguished: a metallic region, a black region, and a grey region. The metallic region is of the same colour as the original titanium target, so it is denoted as titanium (Ti). The black layer which was easily removable by hand or an abrasive resembles the soots and so it is denoted as carbon (C). The grey region which is matt, compact and very difficult to remove by an abrasive is a transition between the metallic and black regions. It is similarly coloured to titanium carbide so this region is denoted as titanium carbide (TiC).

It was of interest to see the target surface changes after sputtering in the same conditions for various acetylene flows. In Fig. 6 are shown photographs of three target halves for selected 3, 9 and 13 sccm of acetylene flows. For better visualization the target racetrack is delimited by red highlights. For 3 sccm of C_2H_2 the target racetrack was mostly Ti, for 9 sccm of C_2H_2 the target was mainly grey — mainly TiC and for 13 sccm of C_2H_2 the racetrack was carbon rich with black and grey regions. Clearly some evolution of the target state with the acetylene flow is visible.

Calculation of the relative target racetrack coverage by Ti, TiC and C parts as was done by the pixel counts as described in the experimental section. In Fig. 7 shown are racetrack coverage percentages

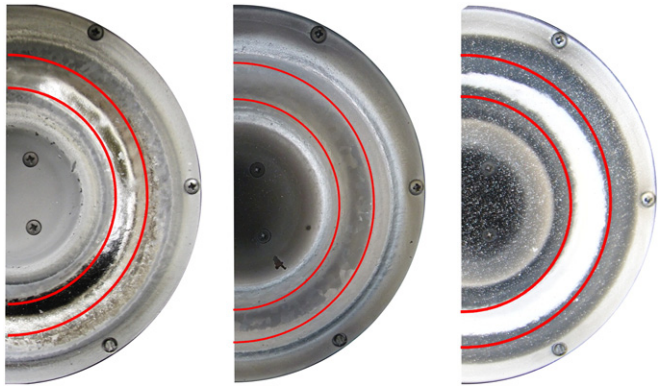

Fig. 6. Photographs of three selected target halves for 3, 9 and 13 sccm of acetylene after achievement of steady-state conditions during deposition. The target racetrack region is highlighted.

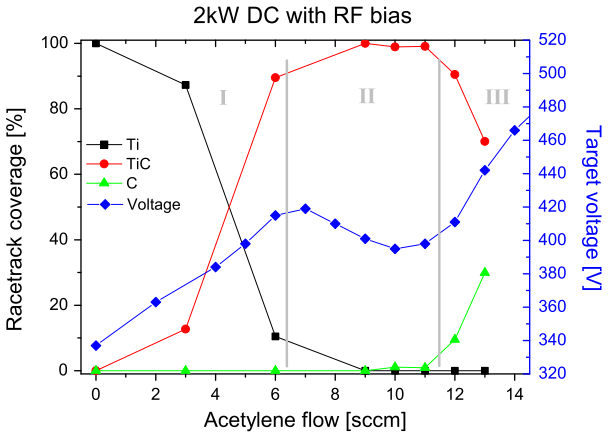

Fig. 7. Racetrack coverage by Ti, TiC and C on acetylene supply. Voltage characteristics with three zones behaviour is correlated with plotted racetrack coverage.

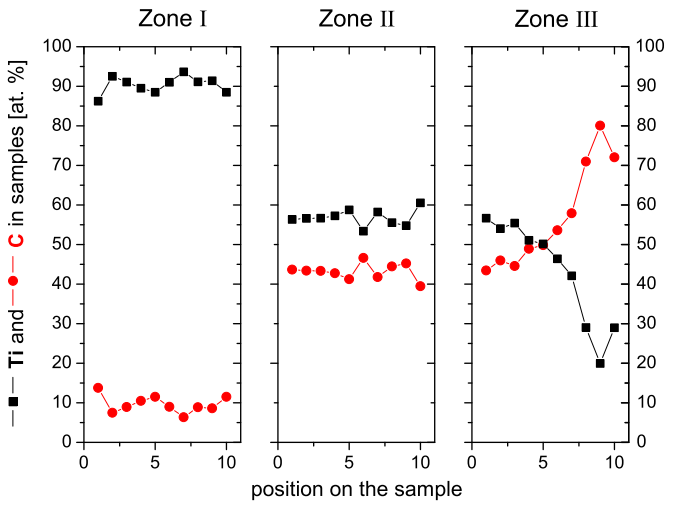

Fig. 8. EDX analysis of three Ti square samples (1 cm × 1 cm) placed in the target racetrack during the deposition at different acetylene flows. Position 0 marks the racetrack centre, position 11 marks the racetrack outer edge.

for the three studied parts and the results are also correlated with the three zone behaviour of voltage characteristics.

In the zone I from 0 to approximately 6 sccm of C_2H_2 Ti regions are diminishing on behalf of TiC regions, the racetrack is titanium rich. In the zone II approximately from 6 to 12 sccm of C_2H_2 the racetrack is composed mainly by TiC region. For higher flows of C_2H_2 in the zone III the TiC parts are overtaken by C, the racetrack becomes carbon rich. Combining information from discharge voltage characteristics with the racetrack coverage we can conclude that the voltage increase in the zone I is connected with the creation of TiC on the target racetrack. In the zone II, the voltage slightly decreases with acetylene inflow (by about 5%) and the voltage local minimum is observed at 11 sccm of acetylene supply. In the zone II, mainly the presence of the grey colour TiC was detected in the racetrack region (see Fig. 7) leading us to a conclusion that the voltage decrease should be related with the evolution of TiC Invoking the phase diagram of Ti–C [34,35], we suppose the voltage decrease to be caused by the evolution of the TiC stoichiometry in the racetrack region from the substoichiometric TiC (at 6 sccm of C_2H_2) to stoichiometric TiC (around 11 sccm of C_2H_2). The rapid voltage increase with higher acetylene flows in the zone III is clearly related to the carbon formation in the racetrack. Its composition is therefore carbon rich TiC/C. Therefore increasing of the acetylene supply flow results in continuous phase change from Ti-rich Ti/TiC (zone I) to mainly single phase TiC (zone II) and finally to carbon-rich TiC/C(zone III). The evolution of the target state is similar to phase changes in the growing TiC/C films with increase carbon content as can be found for example in [10,35].

For the better understanding of the racetrack coverage by Ti–C phases the analysis was performed on the Ti square samples placed on the cathode surface. The results for the three studied zones of acetylene flows are shown in Fig. 8. Note that the EDX method gathers the information from approximately 1 C_2H_2 volume of the top layer of the analysed material. As the thickness of the target layer which has been modified by the process is unknown and probably varies with acetylene supplies, only qualitative information of Ti and C compositions can be derived. From Fig. 8 the racetrack homogeneity is clearly observed. For low acetylene flows in the zone I the Ti/C ratio is very high and approaching the zone II the Ti and C abundances become equal. In the zone III where the amorphous carbon enters the racetrack region a clear evolution of composition is seen from racetrack centre to its edge where Ti/C ratio is reversed.

In our case, the maximal hardness of 46 ± 2 GPa and indentation modulus of 415 ± 7 GPa were measured for coatings with 55 at.% C deposited at the conditions close to the frontiers between zones II and III, where the target surface is covered by stoichiometric TiC. According to the generic design concept [36,37], this high hardness is based on the combination of the absence of dislocation activity in the small TiC nanocrystals and blocking of a-C:H grain boundary sliding by the formation of a strong interface between the two phases. Thus, the coatings with maximal hardness should show certain excess of carbon over titanium to form nanocomposite structure. In hybrid PVD–PECVD process, both the target and the substrate are being exposed to the flux of carbonaceous species originating from acetylene dissociations. Simultaneously to target poisoning, the target is being sputter cleaned providing additional flux of carbon atoms on the substrate. Similarly to reactive magnetron sputtering [31], higher relative amount of carbon could be expected to be found in the growing film than at the target surface which has been experimentally proved for sputtering of Ti in mixture of Ar and CH_4 [25]. In our experimental configuration, deposition process at conditions between zones II and III caused the optimal conditions for the growth of the nc-TiC/a-C:H with the maximal hardness. Depending on the experimental conditions, such as the magnetron head design and position of argon and acetylene gas inlet, the conditions to deposit coatings with maximal hardness could be slightly shifted, however they should be expected to be located always close to the frontiers between the zones II and III, where the target is covered by TiC and coating composition is slightly overstoichiometric with respect to carbon.

3.4. Relative evolution of concentrations of Ar, H and Ti in plasma

Assuming direct excitation of a ground state particle by an electron impact, the intensity of a spectral line depends on the concentration of electrons in the plasma bulk, concentration of ground state particles and excitation rate which is a factor proportional to overlap of excitation cross section and electron energy distribution function (EEDF). The flux of ions to the sheath edge is proportional to the ion density (which is equal to the electron density in the plasma) times the ion acoustic velocity, typically with a factor of 0.6 according to Bohm presheath diffusion criterion [38]. The ions are then accelerated by the sheath potential and bombard the cathode/target surface causing secondary electron emission and sputtering. Thus, the evolution of the concentration of electrons in the plasma is reflected by the discharge current. Assuming that electron energy distribution function, i.e. excitation rate and ion acoustic velocity does not depend on C_2H_2 supply, ratio of the atomic line intensities and discharge current provides the evolution of the ground state particle densities in plasma.

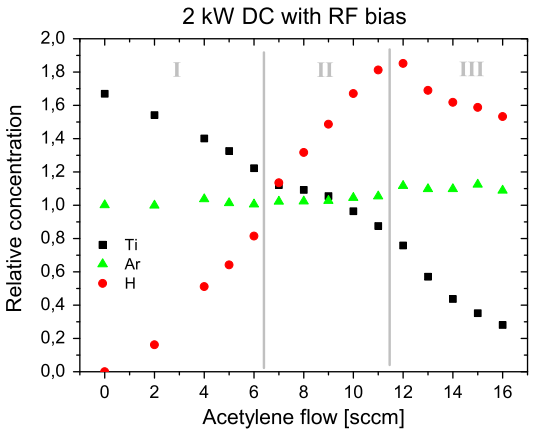

Fig. 9. Dependence of the relative concentrations of Ti, Ar and H in plasma on acetylene supply.

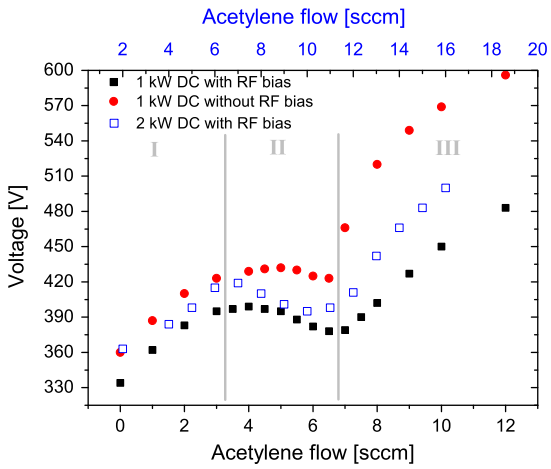

Fig. 10. Voltage characteristics on the acetylene supply flow for 1 kW DC with and without applied RF bias (225 W ~ −100 V).

The evolution of the relative concentrations of Ar, H and Ti in plasma volume is plotted in Fig. 9 together with marked zones I, II and III. The comparison of evolutions of the relative concentrations with other process parameters can be found in Table 1. Despite that the Ar line intensity evolves with C_2H_2 flow the calculated Ar concentrations are constant for all zones supporting the hypotheses on EEDF and ion acoustic velocity to be independent on C_2H_2 supply. Decrease of Ar line intensity in zone I, increase in zone II and decrease in zone III that follow the evolution of the discharge current perfectly (compare Fig. 2(b) and (f)) is caused by evolution of the plasma density and not by the evolution of the buffer gas concentration with the acetylene supply. The titanium concentration is decreasing almost linearly though all zones showing that by increasing the C_2H_2 flow the amount of sputtering Ti is decreasing linearly without any rapid transition.

The hydrogen concentration is increasing in zones I and II and despite that the well pronounced maximum of hydrogen line intensity was observed at the frontiers between the zones II and III, in the zone III the hydrogen concentration is not increasing anymore but it stays rather independent on C_2H_2 supply. The decrease of hydrogen emission in the zone III (see Fig. 2(d)) is not caused by decrease of hydrogen atom concentration (see Fig. 9) but should be related to the steep decrease of discharge current (i.e. plasma density) linked with a steep increase in the discharge voltage to maintain the discharge (see Fig. 2(a)) while the generator was operating in the constant power mode. For high amount of acetylene in the volume it is difficult to estimate the extent of the volume reactions of acetylene fragments. The constant hydrogen atom density in the zone III could be caused by two opposite effects that act simultaneously — an increase of acetylene supply is followed by the reduced ability of the plasma to dissociate acetylene molecules and produce hydrogen atoms due to lower plasma density (lower discharge current, higher voltage to sustain plasma). It is therefore possible that the production of atomic hydrogen is constant or even decreasing with the acetylene supply in the zone III. Other possible explanation for constant hydrogen atom concentration with acetylene supply could be that the substrate film is growing with high content of carbon matrix where significant amount hydrogen could be stored. However the film analysis in the acetylene in the range between 9 and 14 sccm showed, that the hydrogen content in the films is constant around 5% [23,24].

3.5. Influence of magnetron power and substrate bias

The effect of DC power applied on the magnetron target on the hybrid PVD–PECVD process evolution on acetylene supply was studied. By lowering the applied DC power from 2 kW to 1 kW the general trends (three zones behaviour) observed at electrical characteristics Fig. 2(a), (b) and Fig. 7 are preserved, see Fig. 10. The three zones are only shifted towards lower acetylene flows, as applying half power on the magnetron target shifts the boundaries of three zones roughly to half the acetylene flows.

The effect of applying RF bias to the substrate can also be seen in Fig. 10. Substrate bias of −100 V was set by 225 W RF power which was a quarter of the 1 kW DC power applied on the magnetron target. Such relatively high RF power applied on the substrate could be influencing the evolution of hybrid PVD–PECVD process on acetylene supply. Fig. 10 demonstrates that the three zones of the target state and entire process characteristics are not shifted with respect to C_2H_2 flow providing only negligible influence of RF plasma near the substrate on the evolution of the trends of deposition process characteristics.

4. Conclusions

The hybrid PVD–PECVD process of titanium sputtering in argon and acetylene atmosphere does not show the hysteresis behaviour. The absence of hysteresis region avoids process stability problems met in conventional reactive magnetron sputtering making the hybrid PVD–PECVD process relatively easy to control. Three distinctive zones were identified in the process evolution with the acetylene supply.

For the low range of acetylene flows (zone I) the voltage is increasing due to TiC formation on the surface of the target racetrack at the expense of Ti and the relative concentration of Ti in plasma is decreasing while the H concentration is increasing due to acetylene fragmentation in plasma volume. For medium range of acetylene flows (zone II) the target voltage stops increasing or it is slightly decreased. The racetrack is covered mainly by TiC. Ti concentration in plasma phase is still decreasing and hydrogen concentration continues to increase. Stoichiometric TiC coatings are being deposited at this zone. For high acetylene flows (zone III) the target voltage is rapidly increasing, the carbon layers start to penetrate into the target racetrack and the composition of the racetrack surface becomes carbon rich. The Ti concentration in plasma phase is still decreasing but H concentration is not evolving further, it remains more or less constant. On the border of zones II and III the nc-TiC/a-C:H coatings with highest hardness and Young's modulus were prepared. For the studied range of acetylene supply the Ar concentration remains the same.

Reduction of the power applied on the target keeps the three zone behaviour of the process. It shifts zone boundaries towards lower acetylene flows. Halving the magnetron power shifts the boundaries to half of the acetylene flows. RF bias does not significantly influence

the hybrid PVD–PECVD process characteristics. By varying the RF bias for constant magnetron power desired self-bias on the substrate can be set without modifying the overall process behaviour.

Acknowledgement

This research has been supported by Czech Science Foundation contract 104/09/H080 and 205/12/0407 and R&D centre for low-cost plasma and nanotechnology surface modifications CZ.1.05/2.1.00/03.0086 funded by European Regional Development Fund. Pavel Souek acknowledges the Brno City Municipality as holder of Brno PhD Talent Financial Aid. The authors would like to acknowledge Dr. V. Peřina from the Nuclear Physics Institute of the ASCR for RBS measurements and Dr. J. Buršík from the Institute of Physics of Materials of the ASCR for EDX measurements.

References

[1] D.M. Mattox, The Foundations of Vaccum Coating Technology, William Andrew Publishing, 2003. , (ISBN 1-800-932-7045).
[2] J.P. Celis, D. Drees, M.Z. Huq, P.Q. Wu, M. De Bonte, Surf. Coat. Technol. 113 (1999) 165.
[3] A. Matthews, A. Leyland, Surf. Coat. Technol. 71 (1995) 88.
[4] A. Daniel, T. Duguet, T. Belmonte, Appl. Surf. Sci. 253 (2007) 9323.
[5] J.T. Harnack, F. Thieme, C. Benndorf, Surf. Coat. Technol. 39 (40) (1989) 285.
[6] J.T. Harnack, C. Benndorf, Mater. Sci. Eng. A140 (1991) 764.
[7] C. Benndorf, T.J. Harnack, U. Fell, Surf. Coat. Technol. 48 (1993) 345.
[8] P.Y. Tessier, R. Issaoui, E. Luias, M. Boujtita, A. Granier, B. Angleraud, Solid State Sci. 11 (2009) 1824.
[9] Y.T. Pei, D. Galvan, J.Th.M. De Hosson, A. Cavaleiro, Surf. Coat. Technol. 198 (2005) 44.
[10] W. Gulbinski, S. Mathus, H. Shen, T. Suszko, A. Gilewicz, B. Warcholinski, Appl. Surf. Sci. 239 (2005) 302.
[11] W. Kulisch, P. Colpo, F. Rossi, D.V. Shtansky, E.A. Levashov, Surf. Coat. Technol. 118–119 (2004) 714.
[12] T. Ghodselahi, M.A. Vesaghi, A. Shafiekhani, A. Baradaran, A. Karimi, Z. Mobini, Surf. Sci. Technol. 202 (2008) 2731.
[13] J. Bruckner, T. Mantyla, Surf. Coat. Technol. 59 (1993) 166.
[14] C. Donnet, Surf. Coat. Technol. 100–101 (1998) 180.
[15] B. Oral, K.-H. Ernst, C.J. Schmutz, Diamond Relat. Mater. 5 (1996) 932.
[16] N. Yao, A.G. Evans, C.V. Cooper, Surf. Coat. Technol. 179 (2004) 306.
[17] G. Ma, S. Gong, G. Lin, L. Zhang, G. Sun, Appl. Surf. Sci. 258 (2012) 3045.
[18] S. Zhou, L. Wang, S.C. Xang, Q. Xue, Appl. Surf. Sci. 257 (2011) 6971.
[19] S.J. Park, K.-R. Lee, D.-H. Ko, K.Y. Eun, Diamond Relat. Mater. 11 (2002) 1747.
[20] A. Czyzniewski, Thin Solid Films 433 (2003) 180.
[21] C. Rebholtz, J.M. Schneider, H. Ziegele, B. Rahle, A. Leyland, A. Matthews, Vacuum 49 (1998) 265.
[22] Y. Wang, X. Zhang, X. Wu, H. Zhang, X. Zhang, Appl. Surf. Sci. 254 (2008) 5085.
[23] P. Vasina, P. Soucek, T. Schmidtova, M. Elias, V. Bursikova, M. Jilek, M. Jilek Jr., J. Schafer, J. Bursik, Surf. Sci. Technol. 205 (2011) S53.
[24] P. Soucek, T. Schmidtova, L. Zabransky, V. Bursikova, P. Vasina, O. Caha, M. Jilek, A. El Mel, P.Y. Tessier, J. Schafer, J. Bursik, V. Perina, R. Miksova, Surf. Coat. Technol. 211 (2012) 111.
[25] J.-E. Sundgren, B.-O. Johansson, S.-E. Karlsson, Thin Solid Films 105 (1983) 353.
[26] J.-E. Sundgren, B.-O. Johansson, S.-E. Karlsson, H.T.G. Hentzell, Thin Solid Films 105 (1983) 367.
[27] J.-E. Sundgren, B.-O. Johansson, H.T.G. Hentzell, S.-E. Karlsson, Thin Solid Films 105 (1983) 385.
[28] O.A. Fouad, A.K. Rumaiz, S.I. Shah, Thin solid Films 517 (2009) 5689.
[29] V.Yu. Kulikovsky, F. Fendrych, L. Jastrabik, D. Chvostova, Surf. Coat. Technol. 91 (1997) 122.
[30] T. Schmidtova, P. Soucek, P. Vasina, J. Schafer, Surf. Coat. Technol. 205 (2011) S299.
[31] S. Berg, T. Nyberg, Thin Solid Films 476 (2005) 215.
[32] W.C. Oliver, G.M. Pharr, J. Mater. Res. 19 (2004) 3.
[33] D. Depla, G. Buyle, J. Haemer, R. DeGryse, Surf. Coat. Technol. 200 (2006) 4329.
[34] K. Frisk, Calphad 27 (2003) 367.
[35] D.A. Andersson, P.A. Korzhavyi, B. Johansson, Calphad 32 (2008) 543.
[36] S. Veprek, S. Reiprich, Thin Solid Films 268 (1995) 64.
[37] S. Veprek, J. Vac. Sci. Technol. A 17 (1999) 2401.
[38] D. Bohm, in: A. Guthrie, R.K. Wakerling (Eds.), McGraw-Hill, New York, 1949, p. 77.

Surface & Coatings Technology 205 (2011) S53–S56

Contents lists available at ScienceDirect

Surface & Coatings Technology

journal homepage: www.elsevier.com/locate/surfcoat

Depth profile analyses of nc-TiC/a-C:H coating prepared by balanced magnetron sputtering

Petr Vašina [a], Pavel Souček [a,*], Tereza Schmidtová [a], Marek Eliáš [a], Vilma Buršíková [a], Mojmír Jílek [b], Mojmír Jílek Jr. [b], Jan Schäfer [c], Jiří Buršík [d]

[a] Department of Physical Electronics, Faculty of Science, Masaryk University, Kotlářská 2, CZ-61137, Brno, Czech Republic
[b] SHM Šumperk, Průmyslová 3020/3, CZ-787 01, Šumperk, Czech Republic
[c] INP Greifswald e.V., Felix-Hausdorff-Str. 2, D-17489, Greifswald, Germany
[d] Institute of Physics of Materials, Academy of Sciences of the Czech Republic, Žižkova 22, CZ-61662, Brno, Czech Republic

ARTICLE INFO

Available online 18 February 2011

Keywords:
Composite
Mechanical properties
Magnetron
Carbon
Titanium

ABSTRACT

Nanocrystalline titanium carbide embedded in an hydrogenated amorphous carbon matrix (nc-TiC/a-C:H) shows high hardness and Young's modulus together with low wear and low friction coefficient. In this paper, we report on the preparation of well adherent nc-TiC/a-C:H coatings ~5 μm thick on stainless steel substrates using a well balanced magnetic field configuration and only very low power RF bias on the substrate. Hardness and Young's modulus of these coatings are 43 GPa and 380 GPa, respectively. The mechanical properties – hardness and Young's modulus – measured from the coating's top reach the values obtained at optimized experiments where the unbalanced magnetic field configuration was used. A simple method of depth profiling suitable for evaluation of mechanical properties of several micrometers thick coatings is developed and employed. The paper reports on the depth profile analyses of the coating hardness, Young's modulus, composition and morphology.

1. Introduction

Nanocomposite materials consisting of nanocrystalline titanium carbide embedded in (hydrogenated) amorphous carbon matrix – nc-TiC/a-C(:H) show interesting mechanical properties such as high hardness and fracture toughness combined with low friction and wear. Typically n-TiC/a-C(:H) coatings show maximum hardness up to 40 GPa, reduced Young's modulus up to 300 GPa [1], low friction coefficient [2,3] around 0.1 and wear rate below [4] $2{\cdot}10^{-7}$ mm^3/Nm. A usually reported considerable deficiency of these coatings is the insufficient adhesion to the substrates, which is often improved by using either Cr [5,6], Ti [7] or graded adhesion promoting layer [6,8]. These materials are usually produced either by the co-sputtering of titanium and graphite targets [2,5,9–11] or by the sputtering of the titanium target in a hydrocarbon containing environment [1,3,5,8,12]. While depositing nc-TiC/a-C(:H) films, most of the authors use either the unbalanced [1], the close field unbalanced [5,8] magnetic field configuration or the IPVD concept [3,12] (Ionized PVD – deposition flux contains significant amount of ionized sputtered species [13]) which results in very high ion bombardment of the growing film during the deposition. The typical coating thickness ranges from several hundreds of nm up to 3 μm.

In our experiment the sputtering of the titanium target in a hydrocarbon (acetylene) containing environment was performed using the well balanced magnetic field configured magnetron and a low power RF substrate bias (~0.03 W/cm^2) in order to prepare nc-TiC/a-C:H coatings at much lower ion bombardment. The goal was to reduce internal stress in the coating and prepare well adherent and hard thin films with a thickness of at least 5 μm on Si and stainless steel substrates. As the ion bombardment was reduced, the coating was heated much more slowly during the deposition and the mechanical properties, coating morphology or the composition could have evolved relatively slowly with the coating thickness. In this paper we report the depth profile analyses of coatings ~5 μm thick prepared at the conditions where the studied mechanical properties – hardness and Young's modulus – measured from the coating top reach the results obtained at experiments where the unbalanced or even the close field unbalanced magnetic field configuration was used.

2. Experimental

The deposition of nc-TiC/a-C:H was performed using an industrial sputtering system Alcatel SCM 650. A well balanced sputtering source was mounted by Ti (20 cm in diameter, purity 99.99%) target and was powered by a DC generator. Si and polished steel substrates were placed on a rotary biasable (RF 13.56 MHz) substrate holder located 6.5 cm from the Ti target. Prior to each experiment the chamber was evacuated by a turbomolecular pump backed by a Roots pump to the

* Corresponding author. Tel.: +420 549 49 3062.
E-mail address: soucek@physics.muni.cz (P. Souček).

0257-8972/$ – see front matter © 2011 Elsevier B.V. All rights reserved.
doi:10.1016/j.surfcoat.2011.02.038

base pressure in the order of 10^{-4} Pa. The position of the Ar and C_2H_2 gas inlet was located between the target and the substrate at 2 cm distance from the Ti target.

Si (111) and polished steel samples were chemically cleaned before being inserted into the deposition chamber. In order to always ensure the same target condition prior to each deposition, the target was cleaned (mechanically by an abrading agent followed by sputtering to shutter) until the carbon layer from previous experiments was fully removed. Several hours later, after cooling down of the chamber, both the target and the substrates separated by the shutter were always cleaned for 35 min to reach always the same temperature conditions [14] at the deposition chamber prior to the deposition process. The cleaning was performed at the following conditions: 4 Pa of Ar, 1 kW DC, 500 W RF. The deposition procedure then proceeded by the setting of the following parameters: 20 sccm of Ar, pressure ~1.2 Pa, 2 kW DC, 200 W RF (bias −100 V). Then the shutter was opened and a 3 min deposition of pure titanium adhesion promoting layer ~700 nm thick was performed. Then 10 sccm of acetylene gas was introduced and the deposition of the nc-TiC/a-C:H coating started. After 45 min the discharge and every gas supply was turned off and the samples were cooled down under vacuum for several hours.

The thicknesses of both the nc-TiC/a-C:H and the adhesion promoting titanium layer were determined by the means of a Calotest equipment (Platit CT50). A Rockwell C-scale diamond-tipped indenter from Meopta was used to evaluate the adhesion of the coating according to German standard DIN CEN/TS 1071-8. Indentation tests were performed using a Fischerscope H100 depth sensing indentation tester equipped with a Berkovich indenter. The applied load varied in the range from 10 to 1000 mN. The accuracy of the depth measurement was about ±2 nm. The correct function of the measuring equipment was verified on certificated (DKD Dortmund) BK7 standard. From the load–penetration curves it is possible to determine the material resistance against plastic deformation $HU_{\mathrm{pl}} = \frac{L_{max}}{A_t}$, (so called plastic hardness), where A_t is the area of the remained indentation print created by irreversible deformation under maximum load L_{max}, and the reduced elastic modulus $E^* = \frac{E}{1-\nu^2}$, where ν is the Poisson's ratio and E is the Young's modulus. The reduced elastic modulus was evaluated using the standard procedure proposed by Oliver and Pharr [15]. The hardness HU_{pl} and Young's modulus E values obtained for on fused silica using the above described method were 9.5 GPa and 72.6 GPa, respectively. The films were tested by means of both, the common method of testing provided for several different indentation depths (i.e. several different applied loads in the range from 10 to 1000 mN) and the method of testing the sample in the abraded dimple from the calotest (calotte) along its diameter with equidistant steps using applied loads of 10, 20 and 75 mN. The distance between two indents was chosen so, that it was in each case at least three times larger, than the estimated radius of plastically deformed zone. The first method enabled us to map the indentation response from increasing volume of coating material from near surface almost up to film-substrate interface. The second method gave us information about indentation response of different parts of coatings bulk carried out at the same testing conditions. The vertical structure of samples deposited on Si substrate was analyzed by a field-emission Scanning Electron Microscope JEOL JSM-7500Fa, which employs a field-emission gun, a semi-in lens conical objective lens and a secondary electron in lens detector, enabling to perform image at a maximum specified resolution of 1.0 nm without the use of a conductive coating. Operating voltage of the SEM device was 2 kV. The film composition was studied using a scanning electron microscope JEOL JSM 6460 equipped with an Inca Energy (Oxford Instruments) analyser. EDX spectra collected in the SEM were evaluated using standard ZAF corrections (referring to the three effects: atomic number Z, absorption A and fluorescence F) [16]. Raman measurements were performed using the Jobin-Yvon T64000 system with laser operating at 532 nm. X-ray diffraction was performed using a setup for X-ray reflectometry and diffraction with high collimation.

3. Results and discussions

According to the literature [1,2,5,6,8,11], mechanical properties of the nanocomposite nc-TiC/a-C:H coatings depend strongly on the carbon content in the deposited coating. Typically n-TiC/a-C:H coatings show maximum of the hardness at Ti/C composition ratio around 2/3 [1]. Recently Martínez-Martínez et al. [11] pointed out the importance of relative amount of nc-TiC and a-C phases on mechanical properties as it was shown that the highest hardness (27 GPa in their particular case) was obtained at the relative amount of a-C phase about 40%, which is slightly higher than the previous mentioned Ti/C composition ratio of 2/3.

In order to optimize our deposition process to reach the maximal hardness of the coating, a set of samples deposited at various acetylene flow rate was prepared and analysed using the nanoindentation test. The hardness and Young's modulus of the coating prepared at 10 sccm of C_2H_2 were determined from indentation tests as (43 ± 2) GPa and (380 ± 10) GPa, respectively and were found satisfactory and these samples were chosen for further research. The hardness and Young's modulus of the samples were constant within the experimental errors for indentation loads from 20 to 75 mN, which correspond to maximum indentation depths from 150 to 410 nm. Nanocomposite character of the coating was confirmed using X-ray diffraction and Raman measurement. The size of the TiC nanocrystallites was estimated to be ~9 nm from X-ray diffraction using the Scherer formula and the presence of D and G peaks at Raman signal revealed the amorphous carbon phase.

The adhesion of the coating deposited on the stainless steel sample was tested using the Rockwell C-scale diamond-tipped indenter and the coating prepared on the Si sample was broken along the vertical crystal plane of silicon in order to reveal the coating morphology by SEM. The results from Rockwell-C tests show (Fig. 1) only fine radial cracks in the indentation area without delamination in the vicinity of the crater – typical disruption pattern which can be related to the HF 1 adhesion strength quality according to German standard DIN CEN/TS 1071-8 proving very good adhesion of the coating system to the polished steel substrates. The applied load was 1500 N. The cross section SEM image (Fig. 2) demonstrates two structural phases of the coating deposited on Si samples. The thickness of the coating is ~5 μm. The Ti layer (700 ± 100 nm) is characterized with a fine vertical texture, where the mean elementary length of the columns is approximately 100 nm in the imaged fracture area. The n-TiC/a-C:H

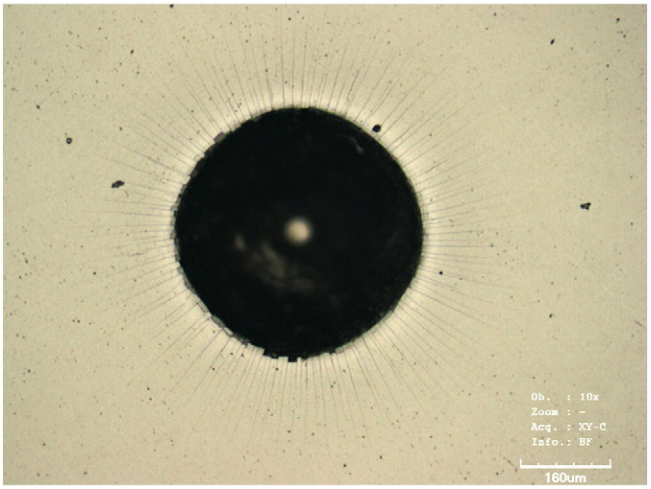

Fig. 1. Residual Rockwell adhesion test crater with fine cracks around its perimeter signalizing good adhesion of the coating system to the polished steel substrate.

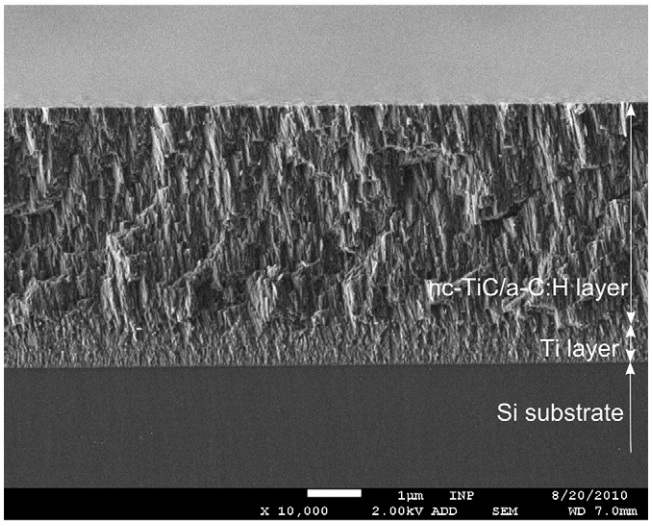

Fig. 2. SEM cross section image with visible columnar structure of the coating on Si substrate.

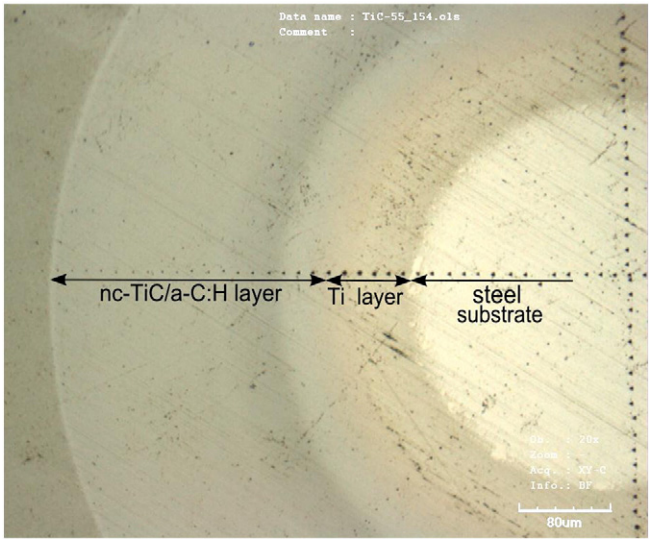

Fig. 3. The sets of 75 mN (horizontal and vertical direction) and 20 mN (visible at angles of approximately 45° from previous directions) residual indentation marks in the calotte. The more distinct residual indents correspond to areas with the lowest hardness and vice versa.

structure shows more massive columns running through the whole coating thickness very similar to those reported in the previously mentioned research [3,5,6,8]. The bottom Ti adhesive layer gradually merges with the n-TiC/a-C:H coating so no sharp interface exists between the two layers. The total thickness, Ti adhesion layer and the n-TiC/a-C:H layer thicknesses were estimated to be 5.6 μm, 0.7 μm and 4.9 μm, respectively.

The coating deposited on the stainless steel sample was studied by means of the Calotest where a ball of a known diameter is rotated against the coating surface and the addition of the abrasive slurry causes a spherically-shaped crater that is abraded through the coating and into the substrate. Subsequent inspection of the calotte with optical microscopy revealed the projected surfaces of the abraded coating and substrate sections as well as an interface between the Ti adhesive layer and the n-TiC/a-C:H coating. The thickness of the whole system was determined to be 6.2 μm: the thicknesses of the Ti adhesion layer and the n-TiC/a-C:H coating were 0.7 μm and 5.5 μm, respectively.

Moreover, the Calotest crater enabled the study of the thickness dependence of the indentation response of the coating by indenting the sample in the calotte along its diameter with equidistant steps. The experiment was performed at three different loads – 75, 20 and 10 mN. The indent distance from the calotte centre gives the film thickness at the measured position. In Fig. 3 the sets of 75 mN (horizontal and vertical direction) and 20 mN (visible at angles of approximately 45° from previous directions) indents are shown. The set of 10 mN indents is only scarcely visible. It is evident that the indents become deepest at the positions where the influence of the titanium layer dominates. The hardness and Young's modulus of Ti adhesive layer are substantially lower than hardness and Young's modulus of both the n-TiC/a-C:H coating and the stainless steel substrate. Indentation tests at lower loads, for example at 10 mN, give information about smaller volumes of the tested material, therefore using such load enabled to study the structure response of the sample. On the other hand, the fact that these tests sensed the structure response of deposited material caused higher scattering in the measured values (see Fig. 4). Moreover, the results obtained by measurements on the top or near to the sample surface at 10 mN are more influenced with the surface structure (e.g. roughness). The elastic deformation zone is much larger than that of the plastic deformation. Therefore the influence of the underlying titanium layer appeared sooner on Young's modulus dependence than on the dependence of the hardness. Fig. 4 also shows, that either the changes in the coating hardness or more probably the substantial influence of the titanium coated steel substrate on the measured hardness appeared when the n-TiC/a-C:H coating thickness decreased to approximately 0.75 μm. This value is in very good accordance with the plastic zone radius (radius of irreversibly deformed coating

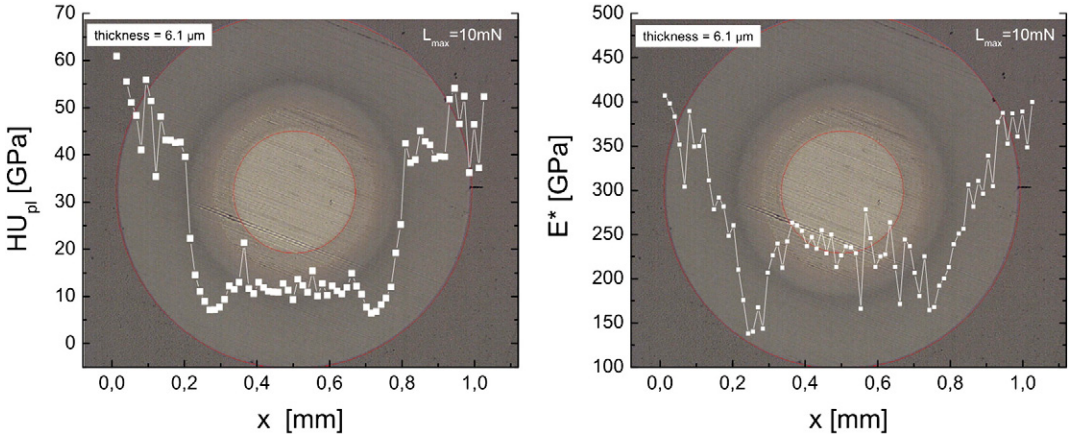

Fig. 4. Hardness and reduced Young's modulus measured through the calotte at the load of 10 mN.

volume) calculated according to Johnson's contact model [17]. It means that the hardness of the coating reached the value of 40 GPa, which corresponds well with the hardness measured from the top of the coating, even earlier, i.e. very fast during the coating growth, at the latest when the coating reaches the total thickness of ~1.5 μm.

In order to evaluate the sample composition, the EDX measurements were performed along the calotte diameter. The results in Fig. 5 were obtained with accelerating voltage of 15 kV. The absolute accuracy of EDX analyses across the calotte is however limited by the fact, that each 'point' analysis is averaged over the interaction volume (about 1 μm^3). On the other hand, the EDX analysis is a non-destructive method contrary to techniques based on ion milling. Its advantage lies in fact, that it enabled us to get the indentation response from the same place as the EDX line scan was done. This method of chemical composition analysis was applied mainly because the interaction volume of the EDX measurement is comparable with the plastically deformed zone around the indents in the nanoindentation measurements (estimated according to Johnson's contact model [17]) for applied loads of 10 and 20 mN. The film consisted of titanium and carbon; the substrate contained of iron, carbon, chromium and vanadium. Although the carbon content evaluation using EDX is rather qualitative, from the composition profile in Fig. 5 it is possible to deduce, that the titanium to carbon ratio slightly increases with coating thickness. This evolution of composition however does not significantly influence the mechanical properties of the coating as the measured hardness reaches steady state value as soon as the total thickness (Ti + nc-TiC/a-C:H) reaches ~1.5 μm. We can furthermore see that at the top of the coating a Ti/C ratio of about 45/55 was reached. The decrease in hardness values obtained from the measurements at 75 mN (Fig. 5) appears much earlier than in case of 10 mN, already when the n-TiC/a-C:H coating thickness decreased to approximately 2.2 μm, what again corresponded well with the estimated radius of the plastically deformed zone according to Johnson's contact model [17].

4. Conclusion

The nc-TiC/a-C:H coatings were prepared in the low ion bombardment conditions by the means of Ti target sputtering in acetylene containing atmosphere. In order to promote the adhesion, 700 nm Ti layer was deposited on stainless steel samples prior the deposition of the 5.5 μm nc-TiC/a-C:H layer. The adhesion of this layered system was HF 1 according to German standard DIN CEN/TS 1071-8. The hardness and Young's modulus measured from the top of the coating were 43 GPa and 380 GPa, respectively. Depth analyses of mechanical properties were performed by the nanoindentation measurements throughout the calotte. Hardness reached the value of 40 GPa, which corresponds well with the hardness measured from the top of the coating at the latest as the total thickness (Ti + nc-TiC/a-C:H) reached ~1.5 μm. Chemical composition was slightly evolving with thickness of the coating, however mechanical properties were not significantly affected by this evolution.

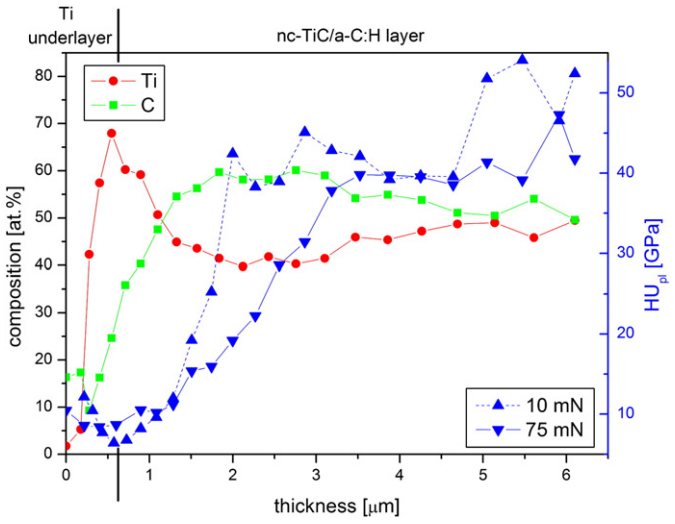

Fig. 5. Chemical composition measured by EDX and the hardness measured by nanoindentation at two different loads (10 and 75 mN) as a function of the coating thickness.

Acknowledgements

This research has been supported by the MSM contracts 0021622411, OP R&DI CZ.1.05/2.1.00/03.0086 and by GACR contracts 202/08/P038 and 104/09/H080. Pavel Souček is acknowledged as Holder of the Brno PhD Talent Financial Aid.

References

[1] A. Czyżniewski, W. Prechtl, J. Mater. Process. Technol. 157–158 (2004) 274.
[2] J.C. Sánchez-López, D. Martínez-Martínez, C. Lópes-Cartes, A. Fernández, Surf. Coat. Technol. 202 (2008) 4011.
[3] D.M. Cao, B. Feng, W.J. Meng, L.E. Rehn, P.M. Baldo, M.M. Khonsari, Appl. Phys. Lett. 79/3 (2001) 329.
[4] J. Musil, P. Novák, R. Čerstvý, Z. Soukup, J. Vac. Sci. Technol. A 28 (2010) 244.
[5] Y.T. Pei, D. Galvan, J.Th.M. De Hosson, A. Cavaleiro, Surf. Coat. Technol. 198 (2005) 44.
[6] D. Galvan, Y.T. Pei, J.Th.M. De Hosson, Acta Mater. 53 (2005) 3925.
[7] Y. Hu, L. Li, X. Cai, Q. Chen, P.K. Chu, Diamond Relat. Mater. 16 (2007) 181.
[8] D. Galvan, Y.T. Pei, J.Th.M. De Hosson, J. Vac. Sci. Technol. A 24 (4) (2006) 1441.
[9] W. Gulbinski, S. Mathur, H. Shen, T. Suszko, A. Gilewicz, B. Warcholinski, Appl. Surf. Sci. 239 (2005) 302.
[10] H. Wang, S. Zhang, Y. Li, D. Sun, Thin Solid Films 516 (2008) 5419.
[11] D. Martínez-Martínez, C. López-Cartes, A. Fernández, J.C. Sánchez-López, Thin Solid Films 517 (2009) 1662.
[12] A.A. El Mel, B. Angleraud, E. Gautron, A. Granier, P.Y. Tessier, Surf. Coat. Technol. 204 (2010) 1880.
[13] J. Hopwood, Phys. Plasmas 5 (1998) 1624.
[14] P. Vašina, T. Hytková, M. Eliáš, Plasma Sources Sci. Technol. 18 (2009) 025011, (8pp).
[15] W.C. Oliver, G.M. Pharr, J. Mater. Res. 19 (2004) 3.
[16] J. Goldstein, D.E. Newbury, D.C. Joy, C.E. Lyman, P. Echlin, E. Lifshin, L. Sawyer, J.R. Michael, Scanning Electron Microscopy and X-Ray Analysis, third ed., Kluwer, New York, 2003.
[17] K.L. Johnson, J. Mech. Phys. Solids 18 (1970) 115.

Surface & Coatings Technology 211 (2012) 111–116

Contents lists available at SciVerse ScienceDirect

Surface & Coatings Technology

journal homepage: www.elsevier.com/locate/surfcoat

Evaluation of composition, mechanical properties and structure of nc-TiC/a-C:H coatings prepared by balanced magnetron sputtering

Pavel Souček [a,*], Tereza Schmidtová [a], Lukáš Zábranský [a], Vilma Buršíková [a], Petr Vašina [a], Ondřej Caha [b], Mojmír Jílek [c], Abdelaziz El Mel [d], Pierre-Yves Tessier [d], Jan Schäfer [e], Jiří Buršík [f], Vratislav Peřina [g], Romana Mikšová [g]

[a] Department of Physical Electronics, Faculty of Science, Masaryk University, Kotlářská 2, CZ-61137, Brno, Czech Republic
[b] Department of Condensed Matter Physics, Faculty of Science, Masaryk University, Kotlářská 2, CZ-61137, Brno, Czech Republic
[c] SHM Šumperk, Průmyslová 3020/3, CZ-787 01, Šumperk, Czech Republic
[d] Université de Nantes, CNRS, Institut des Matériaux Jean Rouxel, UMR 6502, 2 rue de la Houssinière B.P. 32229-44322 Nantes cedex 3, France
[e] INP Greifswald e.V., Felix-Hausdorff-Str. 2, D-17489, Greifswald, Germany
[f] Institute of Physics of Materials, Academy of Sciences of the Czech Republic, Žižkova 22, CZ-61662, Brno, Czech Republic
[g] Nuclear Physics Institute, Academy of Sciences of the Czech Republic, v.v.i., Řež 130, CZ-25068, Řež, Czech Republic

ARTICLE INFO

Article history:
Received 6 May 2011
Accepted in revised form 8 September 2011
Available online 16 September 2011

Keywords:
Nanocomposite
Magnetron sputtering
Titanium
Carbon
Mechanical properties

ABSTRACT

Nanocomposites like nc-TiC/a-C:H show promising combinations of properties such as high hardness and Young's modulus combined with low friction and wear. These properties can be furthermore tailored to suit particular industrial needs. In this paper, we report on the preparation and analyses of several μm thick and well adherent nc-TiC/a-C:H coatings with different stoichiometry. These coatings were deposited in a relatively low ion bombardment environment using magnetron sputtering of titanium target operated in well-balanced magnetic field configuration on high speed steel and hardmetal substrates. Gaseous hydrocarbon (acetylene) was added to the deposition chamber as source of carbon. Hardness and Young's modulus of 46 GPa and 415 GPa respectively were reached.

1. Introduction

nc-TiC/a-C(:H) nanocomposite is composed of TiC nanocrystallites embedded in an amorphous (hydrogenated) carbon matrix. Depending on the amount of titanium atoms added to a-C and on the synthesis procedure the composition varies from pure titanium via TiC known since 1960s [1] to almost pure DLC film doped with Ti atoms. The properties of nc-TiC/a-C(:H) films can be tailored from very hard films with hardness reaching over 40 GPa and Young's modulus higher than 300 GPa respectively [2,3] to low friction films [4,5] with friction coefficient around 0.1 and wear rate lower than $2{\cdot}10^{-7}$ mm^3/Nm [6]. However the adhesion of nc-TiC/a-C(:H) films to industrially attractive substrates is often poor. An adhesion promoting interlayer is routinely introduced into the coating system to overcome this problem. Usually chromium [7,8], titanium [9] or graded [8] interlayers are employed. Usual synthesis procedures of these coatings are either co-sputtering of graphite and titanium targets [4,7,10-12] or sputtering of titanium target in an hydrocarbon (mostly methane or acetylene) containing environment [2,5,7,13]. Other methods of nc-TiC/a-C(:H) are also reported such as filtered vacuum arc [3], sputtering combined with pulsed laser deposition [14], carbon sputtering combined with titanium evaporation [1] etc. The coatings are deposited at wide range of ion bombardment conditions which are unfortunately not always completely specified. Reports on process using balanced [5,7], unbalanced magnetic field configuration sputtering [2,11], closed field unbalanced sputtering [7,8,16,17] or an IPVD concept [5,13,15] can be found. Biased [2,3,7-9,11,15-20] or floating [4,7,9,12,13] substrates are both used. The thicknesses of these coatings range typically from several hundred nanometers up to about 3 μm.

Sputtering of a titanium target in acetylene (C_2H_2) containing atmosphere was used in our experiments. In order to prepare nc-TiC/a-C:H coatings with thickness around 5 μm or more, thus coatings with low internal stress and good adhesion, a well-balanced magnetic field configuration, relatively low RF substrate bias power and deposition of Ti adhesion layer was employed. Acetylene flow was varied to obtain films with different chemical compositions. The structure and mechanical properties of these coatings were thoroughly analyzed to observe the dependencies of composition, structure and mechanical properties on the acetylene flow [2,6,7,9-15]. The composition of these coatings was optimized in order to obtain the highest possible hardness.

* Corresponding author. Tel.: +420 549 49 3062.
E-mail address: soucek@physics.muni.cz (P. Souček).

0257-8972/$ – see front matter © 2011 Elsevier B.V. All rights reserved.
doi:10.1016/j.surfcoat.2011.09.012

2. Experimental

The depositions were carried out using industrial sputtering system Alcatel SCM 650. A well balanced sputtering source equipped with titanium target (purity 99.99%, 20 cm in diameter) was driven by Huettinger TruPlasma Bipolar 4010 generator operated in DC mode. High speed steel and hardmetal (cemented tungsten carbide) samples were placed on a biasable (13.56 MHz RF) substrate holder located 6.5 cm from the target. The deposition chamber was evacuated by a turbomolecular pump backed by a Roots pump to the base pressure in the order of 10^{-4} Pa. Gas inlet was located between the target and the substrate at the distance of 2 cm from the target. Argon (purity 99.999%) and acetylene (purity 99.6%) gasses were dosed via a mass flow controller.

Prior the deposition the high speed steel (HSS), hardmetal (WC) and Si substrates were ultrasonically cleaned in a degreasing agent. The titanium target was cleaned by an abrasive to mechanically remove any carbon layer formed during previous depositions. After placing the samples into the chamber and separating them from the target by a shutter, both the target and the substrates were further cleaned by argon ion bombardment. This cleaning phase was performed until the discharge voltage stabilized indicating that the target was completely cleaned of carbon contaminants. The next day, after the target and the chamber cooled down to room temperature, the deposition procedure commenced with already cleaned target by a short pre-deposition cleaning. This was done for 35 min ensuring removal of any adsorbed contaminants over the night and the substrates were pre-heated at the same time by the ion bombardment. The conditions were as follows: 65 sccm Ar (~3 Pa), 1 kW DC, 500 W RF. Then the deposition took place. At first the shutter between the substrates and the target was opened and a pure titanium adhesion layer was deposited for 3 min (~700 nm thick Ti layer) at 20 sccm Ar, 2 kW DC, 225 W RF (~0.03 W/cm^2; ~−100 V bias). After that, the desired acetylene flow was set ranging from 8 to 14 sccm to obtain coatings with specific chemical compositions (corresponding to 30 at.%C to 68 at.%C respectively in the nc-TiC/a-C:H coating), all other parameters were kept constant, i.e. 20 sccm Ar, 2 kW DC, 225 W RF (~−100 V bias). After 45 min of deposition time, the discharge and gas supplies were turned off and the samples were let to cool down for several hours under vacuum.

Atomic composition was determined by Rutherford backscattering (RBS) and elastic recoil detection (ERDA) methods [21,22] using a Van de Graaff generator and TANDETRON with linear electrostatic accelerators. The contents of Ti, C and O were measured by RBS using 1.74 MeV and 2.2 MeV protons and 3.04 MeV alpha particles as projectiles. The ERDA with an incident beam of 2.75 MeV alpha particles at 75° to the surface normal was used for the measurement of the H content. Hydrogen atoms recoiled under 30° were detected with a surface barrier detector covered with a 12 μm thick mylar stopping foil which prevented detector from reflected alpha particles. The charge of impinging alpha particles was measured using beam chopper with Au layer and monitored by RBS with regard to precise live time. The accessible depth for ERDA is less than 1 μm. The H contend is compared with 11.9% H:Si standard. The RBS and ERDA measurements were evaluated by computer codes GISA 3 [23] and SIMNRA [24], using enhanced non-Rutherford cross-section values from a SigmaBase (also part of SIMNRA Code). Thickness measured in at/cm^3 compared with the thickness evaluated using a calotest Platit CT 50 leads to density (g/cm^3) estimation.

A Rockwell test was used to evaluate the adhesion of the films according to German DIN CEN/TS 1071-18 standards. This test was performed with a Rockwell C-scale diamond tipped indenter from Meopta. Fischerscope H100 depth sensing indenter equipped with a Berkovich tip was used to study the indentation response of the samples. The samples were polished before the nanoindentation tests (approximately 5% of the coating's thickness was removed) in order to eliminate the influence of the roughness. A large number of indentation tests (at least 60 indentations per sample) were performed at applied load of 75 mN on each sample. The hardness and the elastic modulus were evaluated using the standard procedure proposed by Oliver and Pharr [25]. In order to obtain reliable values of mechanical properties such testing condition were used in nanoindentation measurements under which the substrate did not influence the measured values. The maximum indentation depth did not exceed 500 nm, therefore the very often used “rule-of-thumbs” like “indentation to 10% of the film thickness samples the film alone” was fulfilled. Moreover, we estimated the radius of the plastically deformed zone (radius of irreversibly deformed volume of the coating) according to Johnson's contact model [26]. The calculated radius was in each case significantly lower, than the coating thickness, which confirms that the measured data were not influenced with the substrate. More details of the evaluation methods of the plastic hardness and Young's modulus can be found elsewhere [27].

Residual stress was calculated from curvature of rectangular silicon substrates before and after deposition. The curvature was determined using profilometer DEKTAK VEECO 8. The stress was calculated from the Stoney formula [28]. The vertical structure of hardmetal samples was analyzed on fracture surfaces by a field-emission Scanning Electron Microscope LYRA 3 XMU FEG/SEM × FIB by Tescan. Operating voltage of the SEM was 15 kV. A thin sheet for TEM measurement was cut out from hardmetal samples using a focused ion beam gun integrated in the same scanning electron microscope. Transmission electron microscope CM12 STEM Philips operating at accelerating voltage of 120 KV was used to image the microstructure of the coating. X-ray diffraction was measured using copper X-ray tube (wavelength 1.542 Å) in the parallel beam setup with a parabolic multilayer mirror as a collimator and monochromator of the primary beam and parallel plate collimator with secondary graphite monochromator as an analyzer. Grazing incidence detector scan was used for measurement of all samples. Additionally also θ-2θ scan was used for selected samples.

3. Results and discussion

Mechanical properties of nc-TiC/a-C:H coatings depend primarily on the carbon content [2,4,7,8] in the coating or more precisely on the amount of the soft a-C:H matrix embedding the nc-TiC grains [10]. In our research, the acetylene flux was varied from 8 sccm to 14 sccm to obtain coatings with different carbon contents. Summary of deposition conditions and resulting coating properties is provided in Table 1. The coating's thicknesses varied from 6 μm for films deposited with the lowest acetylene flux to about 4 μm for the samples deposited at the highest acetylene flux. Thus the deposition rate decreased from ~150 nm/min to ~100 nm/min The deposition rate of the titanium adhesion layer was ~230 nm/min. The deposition rate of nc-TiC/a-C:H is comparable to reported deposition rates, i.e. around 100 nm/min [2,11]. The observed decrease of deposition rate with increasing acetylene flux may be caused due to formation of a-C layer on the target (target poisoning) that prevents Ti sputtering. Within the range of the studied experimental conditions the Ti flux on the substrate is probably not compensated enough by the flux of carbon fragments.

Chemical composition of the nc-TiC/a-C:H coatings on hardmetal substrates determined by RBS and ERDA measurements as a function of acetylene supply is plotted in Fig. 1. The samples on HSS yielded similar composition. Titanium content is steadily decreasing from ~62 at.% for 8 sccm of acetylene to ~28 at.% for 14 sccm, while carbon content steadily increases from ~30 at.% to ~68 at.%. Oxygen contamination is less than 5 at.%. The main sources of oxygen are probably the post-deposition contamination and contaminations in low purity acetylene used in the deposition. Hydrogen content stays low around or less than 10 at.%. The ratio of Ti/C>1 is obtained for coatings deposited at acetylene fluxes of 10 sccm and lower and Ti/C<1 for coatings deposited at fluxes of 11 sccm or higher. The coating's density as determined from

Table 1
Summary of deposition conditions and resulting chemical composition and mechanical properties of nc-TiC/a-C:H coatings. All results except for the crystallite size are for hard-metal substrates. Crystallite size is determined for high speed steel substrates. The roughness was measured over 8 mm long line a thus represents roughness at macroscale.

C_2H_2 [sccm]	Chemical composition [at.%]		Thickness [μm]	Dep. rate [nm/min]	Density [g/cm^3]	R_a (macro) roughness [μm]	HU_{pl} [GPa]	E [GPa]	Mean crystallite size [nm]
	Ti	C							
8	62.2	29.8	6.1	151	4.7	0.12	13 ± 1	222 ± 5	13
9	60	27.5	5.8	144	4.3	0.15	22 ± 3	283 ± 20	15
10	55.4	35.6	6.0	149	4.2	0.17	24 ± 2	289 ± 12	42
11	41.4	54.1	4.3	111	3.8	0.07	35 ± 1	315 ± 6	15
12	40.6	55.2	5.0	127	4.2	0.07	46 ± 2	415 ± 7	19
13	30.1	59.1	3.4	91	3.7	0.1	37 ± 2	316 ± 10	5.3
14	27.5	62.5	4.5	116	3.3	0.05	23 ± 1	225 ± 5	4.5

Lattice parameter [Å]	Adhesion	Compressive stress [GPa]
4.326	HF 0	
4.349	HF 0	0.34
4.357	HF 1	
4.357	HF 0	0.37
4.354	HF 1	0.42
4.363	HF 1	0.45
4.356	HF 0	

RBS measurements using thickness evaluated from the calotest showed a monotonous decrease from 4.7 g/cm^3 for the coating with the highest amount of titanium to 3.3 g/cm^3 for the film with the least incorporated titanium. Density of stoichiometric TiC is 4.9 g/cm^3 [29] and the density of amorphous carbon is 2.0 g/cm^3 [30].

Nanoindentation measurements were performed to evaluate the plastic hardness and Young's modulus. The results for coatings deposited on hardmetal and the applied load of 75 mN are summarized in Table 1 and plotted in Fig. 2. Hardness lower than 20 GPa is typical for films with either too high or too low carbon content [2,4,5,7–12]. In our experiment, the maximal hardness and Young's modulus of 46 ± 2 GPa and 415 ± 7 GPa respectively are reached simultaneously at the acetylene flow of 12 sccm,[1] significantly exceeding the typical values in the literature [1–12,14]. The residual compressive stress, measured for selected samples only, stayed under 0.5 GPa for all coatings as can be seen in Table 1.

High values of hardness were also reached for up to 2.5 μm thick TiC/a-C:H coatings by Zehnder et al. [16,17] using closed field unbalanced magnetron sputtering configuration. They reached hardness up to ~35 GPa for samples prepared at −240 V bias. About the same hardness of ~35 GPa was also reached by Hu et al. [9] for coatings up to ~1 μm, preparation of thicker coatings was limited by high internal stress. Czyżniewski and Precht [2] reached hardness of ~42 GPa for nc-TiC/a-C:H coatings prepared at −100 V bias. Wiklund et al. [1] reached hardness over 40 GPa for up to 2.6 μm thick TiC/a-C coatings using combination of electron beam evaporation of Ti target together with magnetron sputtering of C target with rotating substrates. This way a thin titanium film and carbon film are deposited in succession and are mixed during the process. However this high hardness is coupled with high internal compressive stress of 6–8 GPa.

Acetylene flow of 12 sccm corresponds to 41 at.% titanium content and 55 at.% carbon content thus to the Ti/C ratio approximately 3/4. The highest values of hardness and Young's modulus in our research are reached only for narrow range of acetylene. Both quantities are significantly lowered for acetylene flow change of as little as 1 sccm. Similar sharp maximum of hardness can be found in Ref. [16], where the Ti concentration window for the hardest coatings was only about 5 at.% wide.

[1] In our previous paper [20] the maximal hardness and Young's modulus are obtained at lower acetylene flow of 10 sccm. This shift is caused by replacing of an old worn out DC generator by a new one providing now really 2 kW of DC power.

It has been shown [9,10,16,17], that the relative amount of TiC and a-C(:H) phases has more direct influence in determining the properties of the coatings rather than the amount of titanium and carbon. The content of TiC and a-C(:H) phases depends on the carbon content, but also on other deposition conditions such as applied bias. Hu et al. [9], Zehnder at al. [17] and Czyżniewski and Precht [2] observed highest hardness for samples with only about 10–20% of a-C:H phase content, on the other hand Martínez-Martínez et al. [10] and Zhang et al. [18] observed highest hardness for samples containing about 35–45% a-C phase content.

SEM and TEM imaging was performed for the sample with highest hardness (HU_{pl} = 46.2 GPa), i.e. prepared at 12 sccm of acetylene. Both SEM (Fig. 3) and TEM (Fig. 4) revealed presence of dense columnar structure. The width of the elongated TiC grains is about 15 nm. Selected area diffraction pattern (inset of Fig. 4) from circular area 0.5 μm in diameter confirms the face centered cubic structure of TiC with lattice parameter close to that of TiC in database [31]. Only very low a-C phase content compared to TiC phase is visible in the TEM image of the sample with highest hardness (Fig. 6), which is in accordance with literature [10,18].

Adhesion of the coatings on HSS substrates was measured using Rockwell C-scale test at the load of 1500 N according to DIN CEN/TS 1071-18. All films were viable according to the DIN CEN/TS 1071-18 industrial standards and showed very good adhesion in the HF0–HF1

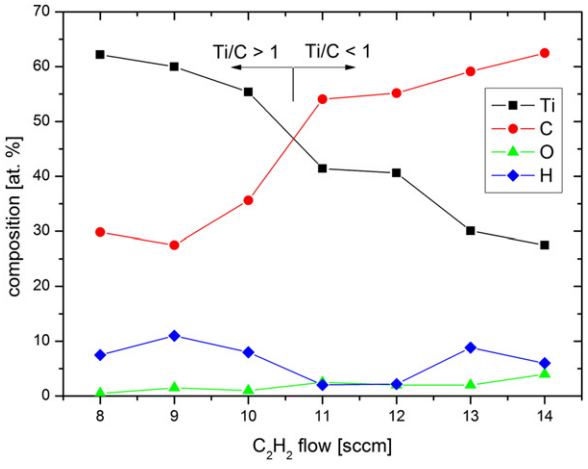

Fig. 1. Chemical composition of nc-TiC/a-C:H coatings as measured by RBS and ERDA.

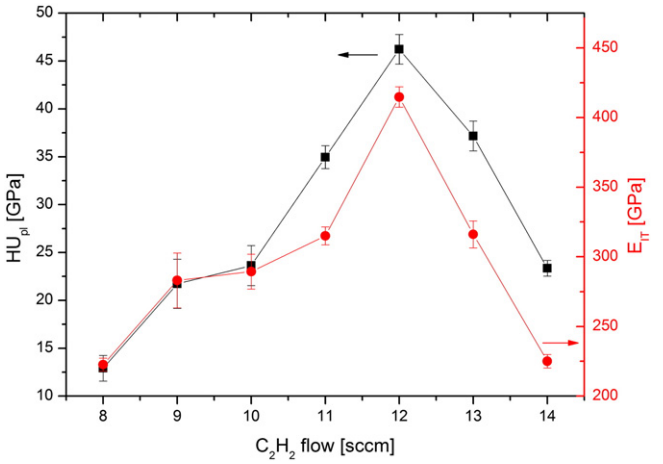

Fig. 2. Dependence of plastic hardness and Young's modulus on the acetylene flow. A sharp maximum in both dependencies at 12 sccm is observed.

range, as is shown in Table 1. Typical Rockwell indents are shown in Fig. 5. Macro-roughness of samples on hardmetal substrates was evaluated using a profilometer over length of 8 mm and summarized in Table 1. Roughness in the macroscale of the sample prepared at 8 sccm of acetylene is $R_a = 0.12$ μm and it increases with increasing acetylene supply (i.e. carbon content). A sharp decrease in the roughness from $R_a = 0.17$ to $R_a = 0.07$ was observed when the acetylene flux increases from 10 sccm to 11 sccm. Further increase of the acetylene supply results in roughness which doesn't significantly alter being 0.05 μm for samples with higher carbon content. The roughness of the uncoated hardmetal substrates was measured to be 0.05 μm.

X-ray diffraction measurements were performed on HSS samples to estimate the crystallite size and texture. The diffraction patterns show strong peaks corresponding to TiC along with weak peaks corresponding to substrate metal (iron) and adhesion interlayer (titanium). Fig. 6 shows the diffraction patterns for samples prepared at 8 sccm, 12 sccm and 14 sccm. The TiC crystallite size shown in Table 1 was calculated from the Scherrer formula attributing the total broadening of the (111) peak to the crystallite size only. Results in Table 1 thus report the smallest possible value of the mean crystallite size in the crystallographic direction [111]. Crystallite sizes in the in-plane direction are smaller than the determined size in the growth direction, as is shown by the TEM. More accurate values were obtained for samples prepared for the acetylene flux of 12 and 13 sccm using Williamson–Hall analysis of the diffraction maxima 111 and 222, which correspond to the same crystallographic plane.

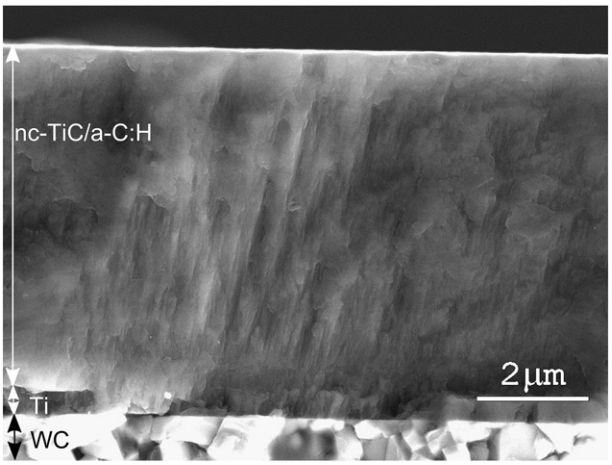

Fig. 3. SEM image of a nc-TiC/a-C:H coating prepared at 12 sccm of acetylene on a hardmetal substrate.

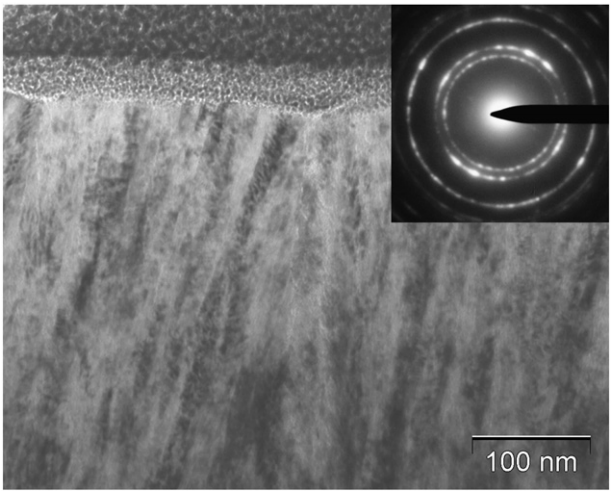

Fig. 4. TEM bright field image and selected area diffraction pattern of the nc-TiC/a-C:H coating prepared at 12 sccm of acetylene.

The mean crystallite size in these samples turned out to be about twice as big as the minimal values given in Table 1 and the mean deformation was about 0.5% to 1.5%. The TEM image of a lamella cut perpendicularly to the sample surface shows grains from about 5 nm to around 30 nm often forming larger clusters (see Fig. 6). The dependence of the crystallite size on the acetylene flux behaves similarly as the roughness. The crystallite size increases with increasing

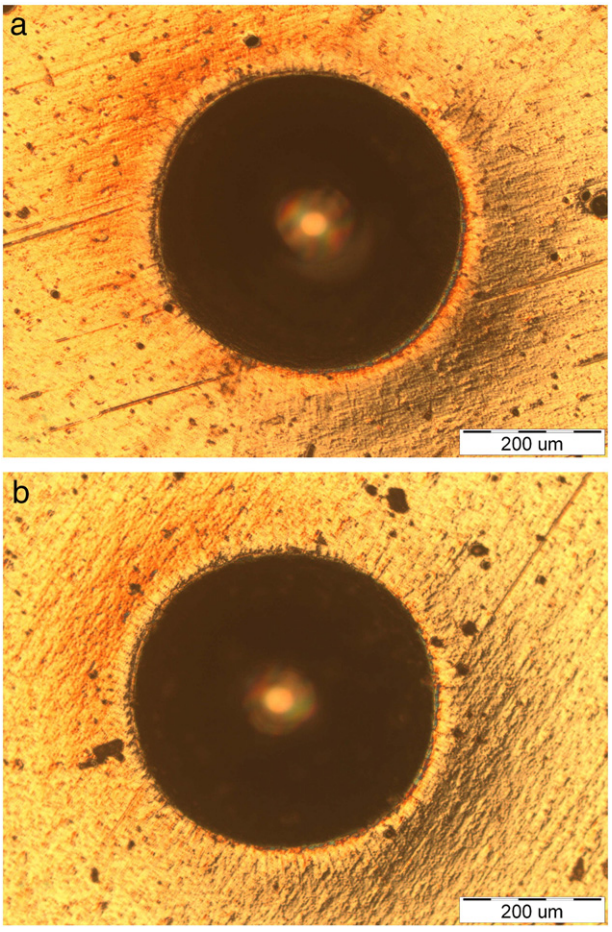

Fig. 5. Typical Rockwell indents showing a) adhesion level 0 for coating prepared at 10 sccm of acetylene b) adhesion level 1 for coating prepared at 11 sccm. Both indents show only very fine cracks around the edge of the crater.

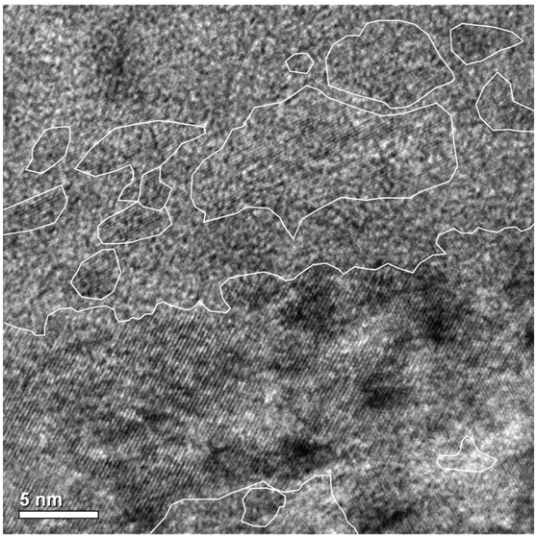

Fig. 6. HR-TEM image of a lamella cut perpendicularly to the sample surface shows grains from about 5 nm to around 30 nm often forming larger clusters.

acetylene supply from 15 nm for the smallest acetylene flow up to 42 nm for the acetylene flow of 10 sccm. Then a sudden drop to 15 nm at acetylene flow of 11 sccm and later well under 10 nm is observed. Similar, however less sharp maximum in the crystallite size at ~50 at.% titanium is reported in Ref. [11]. Also a significant decrease of grain size from more than 20 nm for samples with <4% a-C:H phase content to 3–5 nm for samples with >4% a-C:H phase content for samples prepared at −240 V bias is reported in Ref. [17]. The same but less pronounced behavior observed for samples prepared at −91 V bias in the same reference. Determined crystallite sizes in our research are in accordance with values reported in the literature — several nanometers for Ti contents up to 46 at.% [2,9].

Only very weak diffraction peaks corresponding to titanium were found in the XRD patterns of those samples deposited at higher supply of the acetylene gas. We attributed the presence of weak Ti peaks in these patterns to the Ti adhesive layer as the coatings deposited at higher acetylene supply are the thinnest in the series. The absence of titanium peaks together with no peaks corresponding to $Ti_{1.6}C$ phases [4] in the XRD patterns (see Fig. 7) for samples where Ti/C>1 indicates that a substoichiometric TiC was formed as can be deduced from a Ti–C phase diagram [32]. This is also confirmed by the lattice parameter

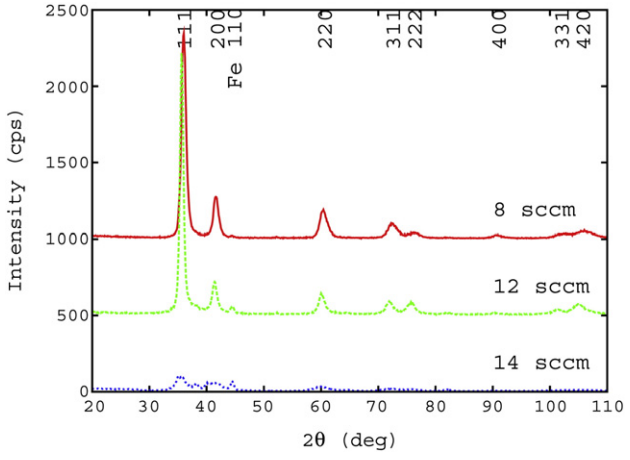

Fig. 7. XRD patterns for samples prepared at acetylene flow of 8 sccm, 12 sccm and 14 sccm. The curves for 8 sccm and 12 sccm are shifted to higher values for clarity. The positions of the TiC peaks are indicated by their Laue indices at the top of the graph.

evolution — see Table 1. Samples prepared at acetylene flows of 10 sccm or higher have lattice parameter around 4.36 Å (error for all measurements is around 0.005 Å). Sample prepared at 9 sccm C_2H_2 (~59 at.% Ti) shows lattice parameter reduced by 0.2% and sample prepared at 8 sccm (~63 at.% Ti) even by 0.8%. The lattice parameter according to PDF card #32-1383 is 4.3274 Å [33]. Only the sample prepared at 8 sccm of acetylene is close to this value, although lattice parameters larger than the reference value are quite often observed [19,20,34].

Also the texture of the crystallites was evaluated by the XRD measurements. The material is observed to be highly textured for the least carbon containing films and becomes more isotropic with increasing carbon content until 10 sccm of acetylene, where again preferential texture is observed. This sudden change in the texture correlates with decrease of crystallite size and the coating roughness. Increase of the acetylene supply over 12 sccm results in nearly isotropic coating prepared at 14 sccm of acetylene containing 62 at.% carbon.

4. Conclusions

Several μm thick nc-TiC/a-C:H coatings were prepared at relatively low ion bombardment environment using well-balanced magnetron sputtering of a titanium target in an acetylene containing atmosphere. High speed steel and hardmetal substrates were used. Acetylene flow was varied to obtain films with different chemical compositions ranging from 30 at.%C to 68 at.%C. Approximately 700 nm thick titanium layer was deposited prior the nc-TiC/a-C:H growth to promote the adhesion of the coating. Very good adhesion corresponding to HF0-HF1 was reached according to the German DIN CEN/TS 1071-8 standard. The highest hardness and Young's modulus of 46 GPa and 415 GPa respectively were reached for the nanoindentation measurements at 75 mN load at the Ti/C ratio approximately 3/4. SEM and TEM images of this sample show a dense columnar structure with elongated grains ~15 nm wide. XRD proves the presence of TiC grains of characteristic size ranging from several tens of nm to several nm depending of the carbon content in the coating. Shift in TiC peak position and the fact that no Ti peaks were detected in XRD patterns of the coatings, where Ti/C >1 indicates that a substoichiometric TiC was formed. The orientation of the TiC grains changes non-monotonously from highly preferential orientation for the coatings with the lowest carbon content to nearly uniform orientation distribution of TiC nanocrystallites in the coatings with highest carbon contents.

Acknowledgment

This research has been supported by the MSM contract 0021622411, by GACR contract 104/09/H080 and R&D center project for low-costplasma and nanotechnology surface modifications CZ.1.05/2.1.00/03.0086 funded by European Regional Development Fund. Pavel Souček acknowledges the Brno City Municipality as Holder of Brno PhD Talent Financial Aid.

References

[1] U. Wiklund, M. Nordin, O. Wänstrand, M. Larsson, Surf. Coat. Technol. 124 (2000) 154.
[2] A. Czyżniewski, W. Precht, J. Mater. Process. Technol. 157–158 (2004) 274.
[3] Y. Wang, X. Zhang, X. Wu, H. Zhang, X. Zhang, Appl. Surf. Sci. 255 (2008) 1801.
[4] J.C. Sánchez-López, D. Martínez-Martínez, C. Lópes-Cartes, A. Fernández, Surf. Coat. Technol. 202 (2008) 4011.
[5] D.M. Cao, B. Feng, W.J. Meng, L.E. Rehn, P.M. Baldo, M.M. Khonsari, Appl. Phys. Lett. 79/3 (2001) 329.
[6] J. Musil, P. Novák, R. Čerstvý, Z. Soukup, J. Vac. Sci. Technol. A 28 (2010) 244.
[7] Y.T. Pei, D. Galvan, J.Th.M. De Hosson, A. Cavaleiro, Surf. Coat. Technol. 198 (2005) 44.
[8] D. Galvan, Y.T. Pei, J.Th.M. De Hosson, Acta Mater. 53 (2005) 3925.
[9] Y. Hu, L. Li, X. Cai, Q. Chen, P.K. Chu, Diam. Relat. Mater. 16 (2007) 181.
[10] D. Martínez-Martínez, C. López-Cartes, A. Fernández, J.C. Sánchez-López, Thin Solid Films 517 (2009) 1662.

[11] W. Gulbinski, S. Mathur, H. Shen, T. Suszko, A. Gilewicz, B. Warcholinski, Appl. Surf. Sci. 239 (2005) 302.
[12] K. Polychronopoulou, C. Rebholz, M.A. Baker, L. Theodorou, N.G. Demas, S.J. Hinder, A.A. Polycarpou, C.C. Doumanidis, K. Böbel, Diamond Relat. Mater. 17 (2008) 2054.
[13] A.A. El Mel, B. Angleraud, E. Gautron, A. Granier, P.Y. Tessier, Surf. Coat. Technol. 204 (2010) 1880.
[14] A.A. Voevodin, J.S. Zabinski, J. Mater. Sci. 33 (1998) 319.
[15] W.J. Meng, R.C. Tittsworth, L.E. Rehn, Thin Solid Films 377–378 (2000) 222.
[16] T. Zehnder, J. Patscheider, Surf. Coat. Technol. 133–134 (2000) 138.
[17] T. Zehnder, P. Schwaller, F. Munnik, S. Mikhailov, J. Patscheider, J. Appl. Phys. 95 (8) (2004) 4327.
[18] S. Zhang, X.L. Bui, J. Jiang, X. Lim, Surf. Coat. Technol. 198 (2005) 206.
[19] G. Li, L.F. Xia, Thin Solid Films 396 (2001) 16.
[20] E. Lewin, E.O.Å. Persson, M. Lattemann, M. Stüber, M. Gorgoi, A. Sandell, C. Ziebert, F. Schäfers, W. Braun, J. Halbritter, S. Ulrich, W. Eberhardt, L. Hultman, H. Siegbahn, S. Svensson, U. Jansson, Surf. Coat. Technol. 202 (2008) 3563.
[21] W.K. Chu, J.W. Mayer, M.A. Nicolet, Back scattering Spectrometry, Acad. Press, New York, 1978.
[22] J.R. Tesmer, M. Nastasi, J.Ch. Barbour, in: C.J. Maggiore (Ed.), Handbook of Modern Ion Beam Materials Analysis, Material Research Society, Pitsburg, Pensylvania, 1995.
[23] J. Saarilahti, E. Rauhala, Nucl. Instrum. Methods Phys. Res. Sect. B 64 (1992) 734.
[24] M. Mayer, SIMNRA User's Guide, Technical Report IPP 9/113, Max-Planck-Institut fuer Plasmaphysick, Garching, Germany, 1997.
[25] W.C. Oliver, G.M. Pharr, J. Mater. Res. 19 (2004) 3.
[26] K.L. Johnson, J. Mech. Phys. Solids 18 (1970) 115.
[27] P. Vašina, P. Souček, T. Schmidtová, M. Eliáš, V. Buršíková, M. Jílek, M. Jílek Jr., J. Schäfer, J. Buršík, Surf. Coat. Technol. 205 (2011) S53.
[28] G.G. Stoney, Proc. R. Soc. Lond. Ser. A 82 (1909) 172.
[29] J.F. Shackelford, W. Alexander (Eds.), CRC Materials Science and Engineering handbook, 3 rd edition, CRC Press, Boca Raton, 2001.
[30] National Institute of Standards and Technology, www.nist.gov.
[31] P. Villars, K. Cenzual, Pearson's Crystal Data, Release 2009/10, ASM International, Ohio, USA, 2009.
[32] D.A. Andersson, P.A. Korzhavyi, N. Johansson, Calphad 32 (2008) 543.
[33] M.C. Morris, H.F. McMurdie, E.H. Evans, B. Paretzkin, H.S. Parker, N.C. Panagiotopoulos, C.R. Hubbard, NBS Monograph 25, Sec. 18, 1981.
[34] E. Lewin, M. Råsander, M. Klintenberg, A. Bergman, O. Eriksson, U. Jansson, Chem. Phys. Lett. 496 (2010) 95.

Surface & Coatings Technology 255 (2014) 8–14

Contents lists available at ScienceDirect

Surface & Coatings Technology

journal homepage: www.elsevier.com/locate/surfcoat

On the control of deposition process for enhanced mechanical properties of nc-TiC/a-C:H coatings with DC magnetron sputtering at low or high ion flux

Pavel Souček [a,*], Tereza Schmidtová [a], Lukáš Zábranský [a], Vilma Buršíková [a], Petr Vašina [a], Ondřej Caha [b], Jiří Buršík [c], Vratislav Peřina [d], Romana Mikšová [d], Y.T. Pei [a,e], J.Th.M. De Hosson [e]

[a] Department of Physical Electronics, Faculty of Science, Masaryk University, Kotlářská 2, CZ-61137 Brno, Czech Republic
[b] Department of Condensed Matter Physics, Faculty of Science, Masaryk University, Kotlářská 2, CZ-61137 Brno, Czech Republic
[c] Institute of Physics of Materials, Academy of Sciences of the Czech Republic, Žižkova 22, CZ-61662 Brno, Czech Republic
[d] Nuclear Physics Institute, Academy of Sciences of the Czech Republic, v.v.i., Řež 130, CZ-25068, Řež, Czech Republic
[e] Department of Applied Physics, Materials Innovation Institute M2i, University of Groningen, Nijenborgh 4, 9747 AG Groningen, The Netherlands

ARTICLE INFO

Available online 9 November 2013

Keywords:
Nanocomposite
Magnetron sputtering
Ion flux on the substrate
Titanium carbide
Enhanced mechanical properties

ABSTRACT

Nanocomposite coatings consisting of nanocrystallites embedded in an amorphous matrix can be tailored to exhibit unusual combination of properties such as high hardness and modulus combined with low friction and wear. The properties of the coatings are governed by parameters of the deposition plasma, which are a nontrivial function of the deposition process parameters. Energy flux onto the growing films provided by ionized species is one of the key parameters influencing the properties of coatings. This study is focused on the influence of ion flux on the properties of the growing nc-TiC/a-C:H thin film in order to achieve enhanced mechanical properties. Two different magnetic field configurations were used. The saturated ion current on the substrate was found to be seven times higher in the strongly unbalanced magnetic configuration as compared to well-balanced configuration. The deposition temperature was constant at ~320 °C, which is higher than the usual temperature for similar depositions of nc-TiC/a-C(:H) coatings. The structure and mechanical properties of the coatings prepared at low or high ion flux were studied and compared. It is concluded that the level of the impinging ion flux in DC magnetron sputtering is not a significant factor influencing the mechanical properties of the coatings in the presented setup.

1. Introduction

Nanocrystalline titanium carbide embedded in amorphous (hydrogenated) carbon matrix – nc-TiC/a-C(:H) – is a versatile material combining the properties of hard titanium carbide nanocrystallites and relatively soft hydrogenized carbon matrix. Depending on the content of the phases the properties of the nanocomposite can be tailored from hard films with hardness reaching over 40 GPa and Young's modulus higher than 300 GPa [1–3] to low friction films [4,5] with friction coefficient around 0.1 and wear rate lower than 2×10^{-7} mm^3/Nm [6,7]. In order to improve the adhesion of nc-TiC/a-C(:H) films an adhesion-promoting interlayer is introduced into the coating system. Chromium [8,9], titanium [10] or graded [9] interlayers are most often employed.

The synthesis of hydrogenated nc-TiC/a-C:H composite is mostly performed by sputtering of titanium target in hydrocarbon containing plasma by a hybrid PVD–PECVD process [11]. Methane [12] and acetylene [3,5,7,8,13] are most often used. Hydrogen free nc-TiC/a-C nanocomposites are usually deposited by co-sputtering of graphite and titanium targets [4,8,14–16].

The properties of nc-TiC/a-C(:H) nanocomposite coatings are largely determined by the volumetric fraction and size distribution of TiC nanocrystallites [10,14,21] or by the concentration of titanium and carbon [1,3,7–10,15,17–21]. It was reported that hardness of the nanocomposites with similar chemical composition can vary significantly among different authors showing that in addition to coating composition, deposition temperature or the ion impingement during the deposition should have impact. Typically, the deposition temperatures are below or around 200 °C [1,3,4,7–10,14,16,18–21], i.e. low compared to the melting temperature of TiC (3067 °C) [1] and also below the temperature where the amorphous carbon matrix starts to deteriorate (<350 °C) [22]. The variance of coating hardness from some of the authors can be seen in Fig. 1. Comparing the hardness of nc-TiC/a-C(:H) coatings of Gulbinski et al. [15] (substrate temperature of 450 °C and −10 V substrate bias voltage) with those of Martínez-Martínez et al. [14] (150–250 °C, floating substrate) both deposited at low or floating substrate bias voltage at distinctively different temperatures, similar hardness for similar composition is found. Therefore, the deposition temperature by itself does not explain differences in hardness. Flux of impinging ions and the ion energy distribution function (or average

* Corresponding author. Tel.: + 420 549 49 2587.
E-mail address: soucek@physics.muni.cz (P. Souček).

0257-8972/$ – see front matter © 2013 Elsevier B.V. All rights reserved.
http://dx.doi.org/10.1016/j.surfcoat.2013.11.001

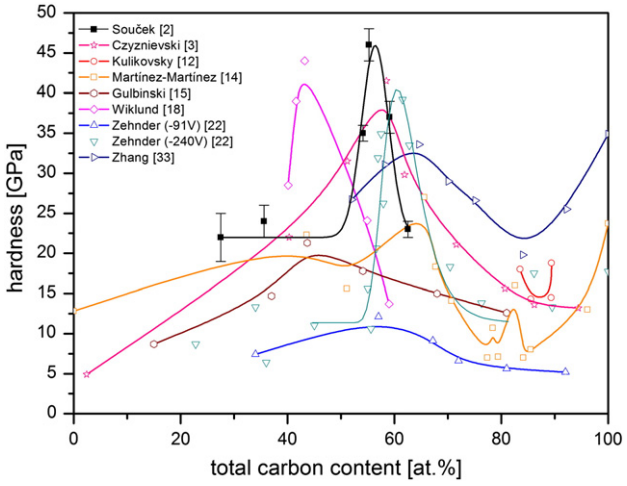

Fig. 1. Hardness comparison of nc-TiC/C(:H) coatings from selected authors.

energy per ion) have both influence on the coating properties. The ion energy can be tuned by applying various substrate bias voltage levels or by using different waveforms of voltage applied on the magnetron cathode. The effect of applying various bias levels on coating hardness was shown by Kulikovsky et al. [12], who observed a maximum hardness at −100 V bias and lower hardness at other bias voltages, although in his work higher bias voltage was linked with higher deposition temperature. Zehnder and Patscheider [21] showed a distinct increase in hardness when substrate bias voltage increased from −91 V to −240 V. Also the structure can be altered by applying substrate bias [18]. Pei et al. [19] showed the influence of pulsed DC (p-DC) frequency on the microstructure of nc-TiC/a-C(:H) nanocomposite coatings. The p-DC frequency influenced both the energy distribution and the flux of argon ions in the plasma. The microstructure changed from columnar at 100 kHz to column-free microstructure at 300 and 350 kHz. This microstructure evolution was attributed to the effect of ion impingement of higher energy input as proven by the measurement of ion energy distribution function on substrate. p-DC substrate bias also leads to higher ion current on the substrate [23].

Nevertheless, it is difficult to conclude from the published work the influence of impinging ion flux on the properties of resulting coatings because not all the experimental details were always fully presented (i.e. substrate bias voltage, magnetic field configuration, target size and target to substrate distance). Depending on the target–substrate distance, unbalanced magnetron does not necessarily lead to a considerable plasma immersion of the substrates. For instance, a distance of 100–150 mm between substrates and 2 in. magnetrons (not uncommon in research systems) gives very low plasma densities at the substrates (no visible plasma) even for highly unbalanced magnetrons. The aim of this work is to single out the effect of the impinging ion flux on the microstructure and properties of nc-TiC/a-C:H nanocomposite coatings with changing magnetron strength in order to pinpoint optimal deposition conditions for production of hard and adherent coatings. Two different magnetic field configurations, well balanced and strongly unbalanced, were employed.

2. Experimental procedures

Depositions were carried out using industrial sputtering system Alcatel SCM 650. DC magnetron sputtering was employed to sputter a titanium target Ø 200 mm in argon/acetylene atmosphere. High speed steel (Ø 20 mm × 4.7 mm) and tungsten carbide cermet substrates (20 mm equilateral triangle base × 4.7 mm) were used. Further details about the equipment can be found in [2].

In order to achieve different ion fluxes on the growing film, two different sets of magnets were used to configure well-balanced and strongly unbalanced magnetic field, respectively. The magnetic field structure was measured by a Hall probe and is depicted in Fig. 2. In this measurement, the Hall probe was fixed and the magnets were placed on a movable tray. The radial- and the z-component of the magnetic field were measured in an array 125 mm long (from the center of the magnet to the edge of the magnet and further 25 mm beyond) and 110 mm high with 5 mm steps in both axes. The magnetic field structure was then calculated numerically from this data. The substrates were placed at the position directly facing the racetrack on the target, as indicated by the red lines in Fig. 2. The balanced magnetic field configuration resulted in a saturated ion current of 0.3 mA/cm^2 measured at the substrate position, while the unbalanced magnetic field resulted in an ion current of 2.1 mA/cm^2. The probe was biased during the measurement with −60 V DC, which is enough to shield the bulk electrons in the plasma from the probe and achieve ion current saturation [24].

A titanium adhesion layer ~700 nm thick was deposited directly before the deposition of the coating. After that, the desired acetylene flow was set to obtain coatings with specific chemical compositions, all other parameters were kept constant, i.e. 20 sccm Ar flow, −100 V substrate bias voltage. The DC power supplied to the cathode was chosen to sustain stable deposition temperature ~320 °C for both magnetic field configurations used in this work. The power necessary to achieve the desired substrate temperature was 2–2.5 kW. Relatively high magnetron power corresponding to the deposition temperature of ~320 °C

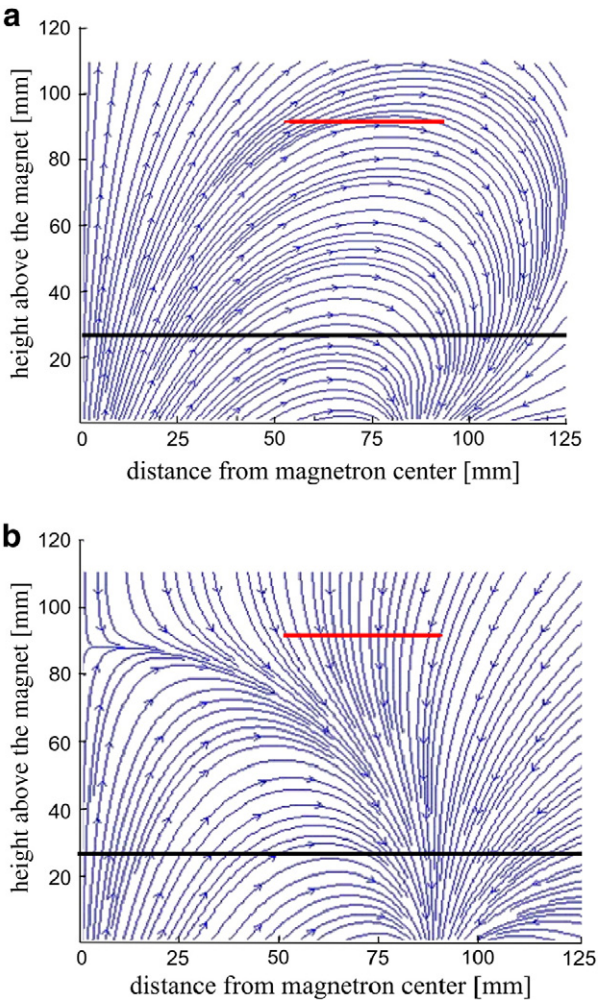

Fig. 2. Magnetic field structure of the magnetrons used in the experiments: (a) well balanced magnetron and (b) strongly unbalanced magnetron. The red line indicates the approximate position of the substrates. The black line indicates the target surface.

was chosen to achieve high deposition rates of the coatings. The deposition was carried out for 45 min. Further details about the deposition procedure can be found in [2]. The two series of coatings deposited are thus named according to the magnetron configurations as BAL-xxC and UNB-xxC, where BAL and UNB mean well-balanced and strongly unbalanced, respectively, and xx stands for the carbon concentration of a coating in atomic percentage. Depositions with unbalanced magnetic field configurations were carried out to higher acetylene fluxes (i.e. higher carbon concentration of the coating), acetylene flux during the balanced series was limited due to excessive arcing.

Chemical composition of the coatings was determined by Rutherford backscattering (RBS) and elastic recoil detection analysis (ERDA) using a Van der Graaff generator and TANDETRON linear electrostatic accelerators. The contents of Ti, C and O were measured by RBS using 1.74 MeV and 2.2 MeV protons and 3.04 MeV alpha particles as projectiles. The ERDA with an incident beam of 2.75 MeV alpha particles at 75° to the surface normal was used for the measurement of the H content. Hydrogen atoms recoiled under 30° were detected with a surface barrier detector covered with a 12 μm thick mylar stopping foil which blocked the detector from reflected alpha particles. The charge of impinging alpha particles was measured using beam chopper with golden layer and monitored by RBS with regard to precise live time. The accessible depth for ERDA is less than 1 μm. The H content is compared with 11.9% H:Si standard. The RBS and ERDA measurements were evaluated by computer codes GISA 3 [25] and SIMNRA [26], using enhanced non-Rutherford cross-section values from SigmaBase (also part of SIMNRA Code).

Fischerscope H100 depth sensing indenter equipped with a Berkovich tip was used to study the indentation response of the coating samples. A large number of indentation tests (at least 60 indentations per sample) were performed at the applied load on each sample. The hardness and the elastic modulus were evaluated using the standard procedure proposed by Oliver and Pharr [27]. In order to obtain reliable values of mechanical properties such testing conditions were used in nanoindentation measurements under which the substrate did not influence the measured values. The maximum indentation depth did not exceed 500 nm, therefore, the very often used "rule-of-thumb" — "indentation to 10% of the film thickness" was fulfilled. Moreover, the radius of the plastically deformed zone (radius of irreversibly deformed volume of the coating) was estimated according to Johnson's contact model [28]. The calculated radius was in each case significantly lower than the coating thickness, which confirmed that the measured data were not influenced by the substrate.

The microstructure of nc-TiC/a-C:H coatings was characterized on fracture cross section with a field-emission scanning electron microscope (SEM) (LYRA 3 XMU FIB-FESEM, Tescan, CZ). The operating voltage of the SEM was 15 kV. Transmission electron microscope (TEM) CM12 STEM Philips operating at accelerating voltage of 120 kV was used for TEM imaging. Grazing incidence X-ray diffraction using copper X-ray tube (wavelength 1.542 Å) was employed to measure the size and lattice parameter of TiC nanocrystallites.

3. Results and discussion

In order to keep the desired substrate temperature at the same bias voltage for both balanced and strongly unbalanced magnetron configurations, different magnetron power was applied. According to our expectation that higher power applied on the magnetron cathode will result in higher sputtering rate of titanium, it was necessary to inject more hydrocarbon gas to deposit nanocomposite coatings of similar composition. Therefore, the acetylene supply was normalized to the magnetron power in order to compensate for the sputtering rate difference. Dependence of the chemical composition on the normalized acetylene flow is plotted in Fig. 3. Titanium composition steadily decreased from ~65 at.% to ~10 at.% and carbon composition steadily increased from ~30 at.% to ~70 at.% with higher acetylene flow to magnetron

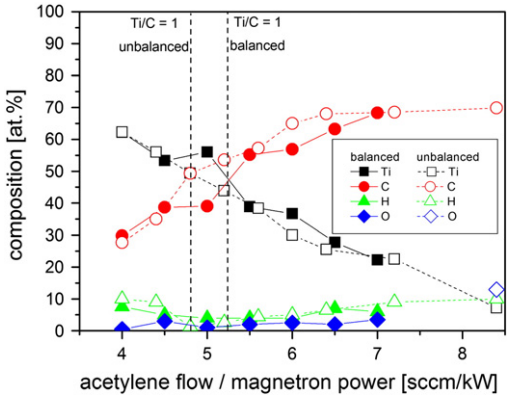

Fig. 3. Dependence of the chemical composition on the normalized acetylene flow.

power ratio. Saturation of carbon concentration in UNB-xxC coating series was observed at high acetylene supply to magnetron power ratio. Hydrogen concentration stayed around 10 at.% for the depositions with acetylene flow to magnetron power ratio <6.5 sccm·kW^{-1} and then somewhat increased with further increasing the acetylene flow at the expense of carbon concentration so that the aforementioned carbon saturation is observed. Oxygen contamination stayed <4 at.% at the whole deposition range. Matrix-assisted laser desorption/ionization analyses of our coatings proved that hydrogen in the nc-TiC/a-C:H coating was bonded not only in the a-C:H matrix but also in TiH compound [29], which can explain presence of hydrogen in coatings where no matrix should be formed. The Ti/C concentration ratio of unity was reached at the acetylene flow to magnetron power ratio of 4.8 sccm·kW^{-1} for the UNB-xxC series deposited with unbalanced magnetron at high flux of impinging Ar ions and at 5.2 sccm·kW^{-1} for the BAL-xxC series deposited with the balanced magnetron, respectively, as indicated in Fig. 3. In unbalanced magnetron, the magnetized plasma is less confined close to the magnetron target which leads to less intensive sputtering of titanium from the target at the same applied power than in the case of the balanced magnetron. Thus, lower acetylene supply is required in unbalanced magnetron sputtering to achieve the same composition of the nanocomposite coatings as in balanced magnetron reactive sputtering and the stoichiometric point is reached at lower normalized acetylene flow. The rate of the carbon content increase for coatings of around 50 at.% C was similar for both series unlike in the work of Samuelsson et al. [17], who showed much slower evolution of C/Ti ratio in the case of High-Power Impulse Magnetron Sputtering (HiPIMS) with very high ion fluxes compared with DC magnetron sputtering.

It has been shown [10,14,21,30], that the relative amount of TiC and a-C(:H) phases can be used to determine the properties of the coatings as well as the amount of titanium and carbon. Zhang et al. [30] employing co-sputtering of titanium and graphite targets at −150 V substrate bias voltage reported on 19% of a-C matrix at 58 at.% C and an increase to 98% of a-C matrix with total carbon content of 92 at.%. Hu et al. [10] employing Ti target sputtering in acetylene containing atmosphere reported on a linear increase of a-C matrix content form ~10% at 54 at.% C to ~90% at 96 at.% C. The linear increase was the same for unbiased substrates and substrates biased with −100 V. Gulbiński et al. [15] used a pulsed DC (100 kHz) unbalanced Ti sputtering (1–3 mA/cm^2 ion current) in Ar/C_2H_2 atmosphere and reported on an increase of a-C matrix content in even sub-stoichiometric coatings (~20% a-C:H matrix at 40 at.% C content) with a fast increase to ~70% of a-C:H matrix at 60 at.% C with further though slower increase of a-C:H matrix content with total carbon content to ~97% of a-C:H at 85 at.% C. The content of TiC and a-C(:H) phases depends on the carbon content, but also on other deposition conditions such as applied substrate bias. Thus, data in Fig. 3 can not be simply transformed to phase composition.

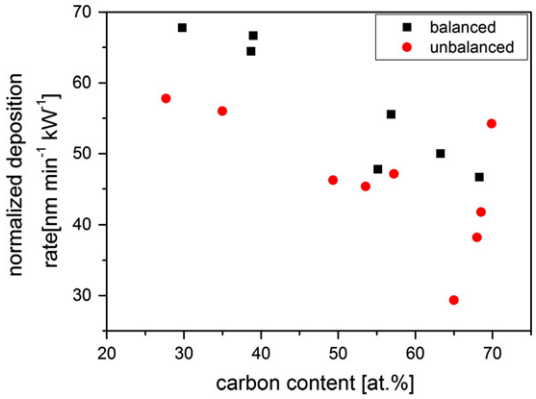

Fig. 4. Evolution of the normalized deposition rate of nc-TiC/a-C:H nanocomposite coatings.

Thick coatings were prepared. The thickness ranges from approximately 3 μm to 6.5 μm depending on the carbon content. Fig. 4 shows the plot of the deposition rate normalized to magnetron power versus the carbon content of the coatings. With balanced sputtering, the normalized deposition rate shows a steady decrease with increasing carbon content of the coating. This is attributed to evolution of target state as is discussed in Schmidtová et al. [31]. Similar trend of normalized deposition rate decrease is also observed with unbalanced configuration up to carbon content of ~65 at.%. Up to ~68 at.% C lower thickness and deposition rate is observed for the unbalanced series of similar carbon content. This can be explained by lower titanium sputtering rate at unbalanced magnetron compared to the balanced one. Furthermore, the plasma sustained at higher discharge voltage but lower current in unbalanced magnetic field configuration is less dense in the volume and lower dissociation rate of acetylene can be expected than in the plasma driven at comparable power in balanced magnetic field configuration at lower voltage and higher current, i.e. higher plasma density. In the unbalanced configuration the plasma is spread more to the substrate so that the acetylene can be dissociated closer to the substrate and more carbon can be incorporated into the growing film as well. A sharp increase in the normalized deposition rate from ~33 $nm \cdot min^{-1} \cdot kW^{-1}$ at 65 at.% C to ~50 $nm \cdot min^{-1} \cdot kW^{-1}$ at 69.9 at.% C is then observed. Similar increase of the deposition rate of nc-TiC/a-C:H with carbon carrying gas can be seen in the literature [3,16,17].

Fig. 5 shows the cross-section of BAL-55C and UNB-57C. Both exhibit columnar microstructure with columns ~200 nm thick. The columns are slightly tilted from vertical growth by ~15° because the cross sections were fractured near the sample edge that was slanted from the racetrack of the target. The presence of the columnar structure can be also indicated by a cauliflower surface pattern of the coatings. Within the studied composition range of both series, coatings with similar chemical composition show similar structure for both the series, i.e. a clear columnar structure with column thickness in the order of few hundred nanometers. Fig. 6 shows the microstructure of UNB-68C and UNB-70C with high carbon content deposited with the strongly unbalanced magnetron on cermet substrates. UNB-68C (Ti/C = 0.45[1]) shows a fine columnar structure. In contrast, UNB-70C (Ti/C = 0.10) is of column-free microstructure. The high difference in Ti/C ratios with similar carbon content is due to high hydrogen content in the most carbon-containing coating. These results are in accordance with the trend observed previously. Pei et al. [7,8] show pronounced columnar structure in coatings with 66.6 at.% C (Ti/C = 0.48), almost invisible columns in the coating of 81 at.% C (Ti/C = 0.22) and glassy structure in the coating containing 87.2 at.% C (Ti/C = 0.14), all the coating samples were prepared with −100 V bias as in our experiment. Lin et al. showed similar result, namely pronounced columns in coatings of low carbon content and a shift to glassy structure at 80.5 at.% C concentration (Ti/C = 0.24 assuming only Ti and C concentrations measured). A Transmission electron microscope (TEM) imaging of sample BAL-55C (lying in the composition interval, where hard coatings can be prepared) from the balanced series was performed in order to see the structure more clearly (see Fig. 7). This imaging clearly revealed the presence of the dense columnar structure with TiC grains ranging from about 5 nm to around 30 nm in size and often forming larger clusters, relatively large distance between the clusters separated by the a-C:H matrix can be seen.

The grain size and lattice parameter of TiC nanocrystallites were investigated using grazing angle X-ray diffraction (XRD). The grain size was calculated using Scherrer equation attributing the total broadening of the (111) peak to the crystallite size only and is plotted in Fig. 8a. Scherrer formula thus reports the smallest possible value of the mean crystallite size in the crystallographic direction [111]. Crystallite sizes from the Scherrer formula in the in-plane direction given by XRD were smaller than the determined size in the growth direction, as was shown by the TEM. More accurate values of the crystallite size were obtained for selected samples using Williamson–Hall analysis of the diffraction maxima 111 and 222, which correspond to the same crystallographic plane. The mean crystallite size in these samples turned out to be about twice as big as the minimal values given by the Scherrer equation. The crystallite size remains stable around ~15 nm for carbon content of <60 at.%, including the hypostoichiometric TiC_x ($x < 1$) region (C content < 50 at.%). Then a drop of the grain size to ~5 nm is observed in the coatings with carbon content > 60 at.%. This is attributed to the competition between grain nucleation and grain growth, i.e. the nanocrystallites grow rather in number than in size at high carbon content [19]. The evolution of the crystallite size with carbon content is identical for both series regardless of the flux of ions bombarding the

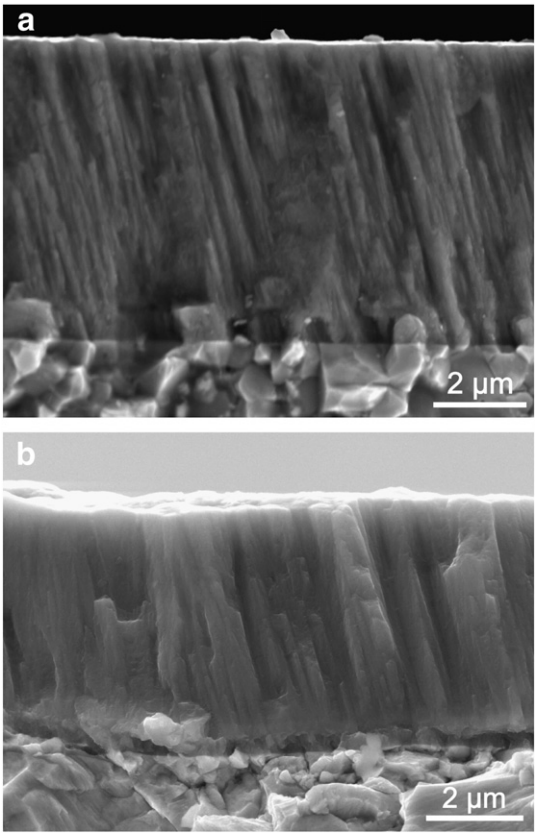

Fig. 5. SEM images revealing the microstructure of nc-TiC/a-C:H nanocomposite coatings of similar composition on cermet substrates: (a) BAL-55C and (b) UNB-57C coating.

[1] Ti/C ratio in the text is presented where coatings with similar carbon content show very different titanium content or vice versa.

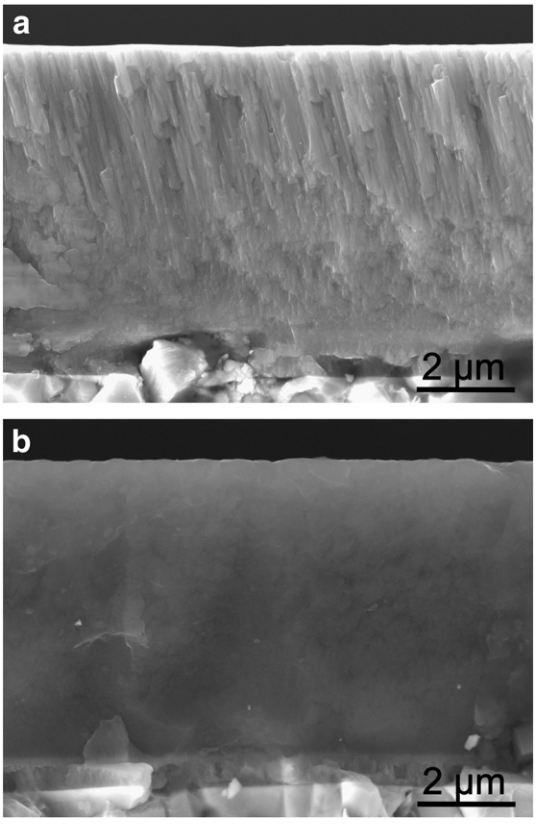

Fig. 6. SEM micrographs showing the fracture cross section of coatings deposited on cermet substrates with a strongly unbalanced magnetron: (a) columnar structure of UNB-68C coating (Ti/C = 0.45) and (b) column-free microstructure of UNB-70C coating (Ti/C = 0.1).

growing coating. Similar trend in the grain size can be also found in literature. Martínez-Martínez et al. [14] showed an increase in TiC crystallite size from 6 nm to 30 nm when titanium concentration reached 49 at.%. Zehnder and Patscheider [21] demonstrated a sharp increase from ~5 nm to over 20 nm with increasing titanium concentration from 40 at.% to 55 at.%. Gulbinsky et al. [15], on the other hand, showed

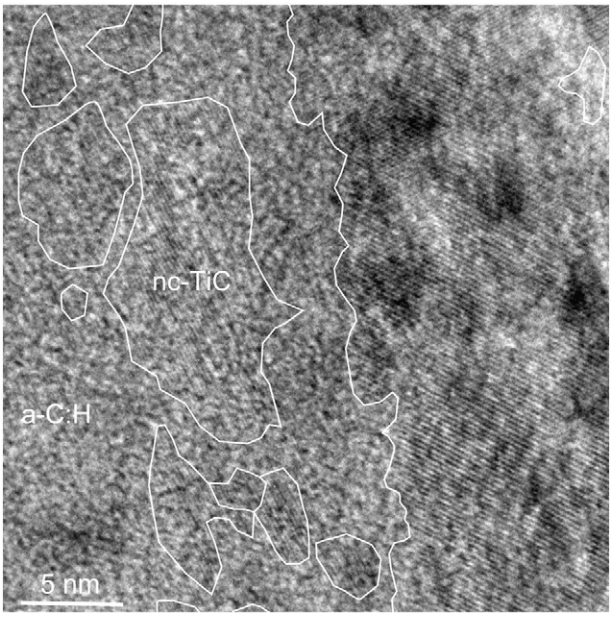

Fig. 7. TEM image showing TiC grains in a-C:H matrix of BAL-55C.

a maximal TiC crystallite size of 75 nm at nearly stoichiometric TiC composition and a decrease in TiC crystallite size for both higher and lower concentration of titanium. The evolution of lattice parameter of TiC nanocrystallites in both series is plotted in Fig. 8b. A clear increase in the lattice parameter from ~4.259 Å at highly substoichiometric TiC composition (28 at.% C) to 4.375 Å at nearly stoichiometric TiC composition (48 at.% C). This increase of the lattice parameter can be explained by reduced vacancies in the substoichiometric TiC lattice with increasing C content. The lattice parameter remained around 4.375 Å with further increasing the C content up to 70 at.% C. The lattice parameter of TiC phase formed under equilibrium condition is 4.3274 Å [32], although the lattice parameter larger than the reference value is quite often observed in sputtered coatings [33,34]. Lewin et al. reported that expansion of the lattice parameter was connected to charge transfer at the interface from the carbide phase to the more electronegative carbon matrix phase [35,36]. It is concluded that the evolution of the grain size and of the lattice parameter is identical for both series of coatings regardless of the flux of bombarding ions.

The mechanical properties were evaluated using nanoindentation. The maximal hardness of 46 ± 2 GPa and indentation modulus of 415 ± 7 GPa were achieved at 55 at.% C in the case of BAL-55C deposited with the well balanced magnetron configuration (see Fig. 9). In the case of unbalanced magnetron sputtered coatings, the maximal hardness and modulus were 45 ± 2 GPa and 420 ± 20 GPa, respectively, measured at the carbon content of 53.5 at.% (UNB-54C). The maximal hardness and modulus were reached at nearly the same composition and are almost identical in value. No broadening of the optimal composition range to reach high hardness and modulus was observed even with strongly unbalanced magnetron sputtering, different from the result reported by Samuelsson et al. [17] in HiPIMS deposition, in which ionized species are delivered onto substrate and thus, may

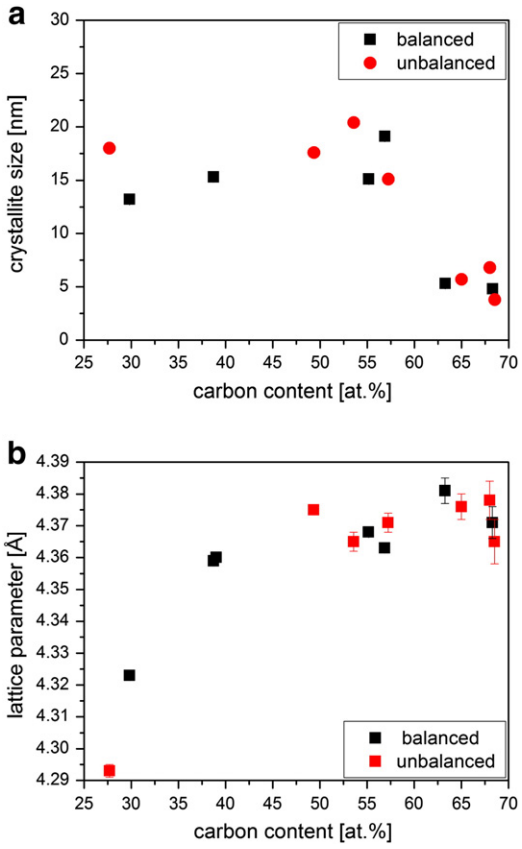

Fig. 8. Dependence of (a) crystallite size and (b) lattice parameter of TiC nanocrystallites on the carbon content of the coatings as measured by GI-XRD.

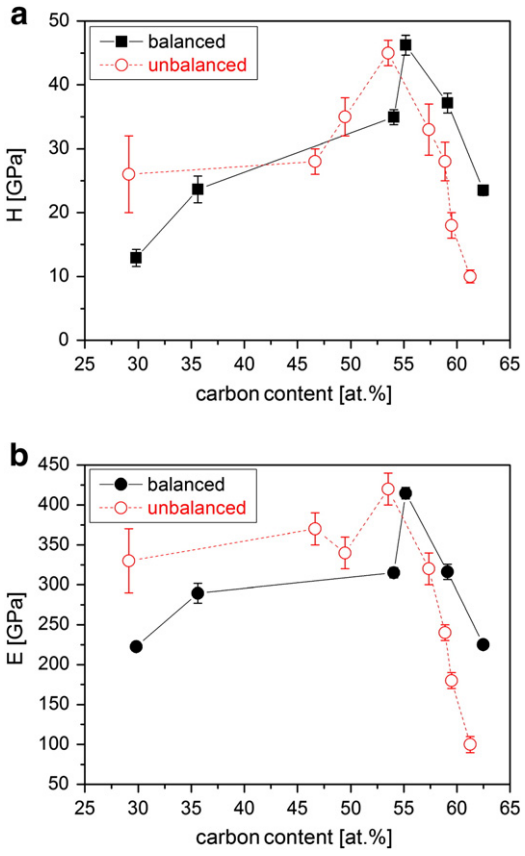

Fig. 9. (a) Hardness and (b) modulus of nc-TiC/a-C:H nanocomposite coatings showing a pronounced maximum at ~55 at.% C for both series of coatings.

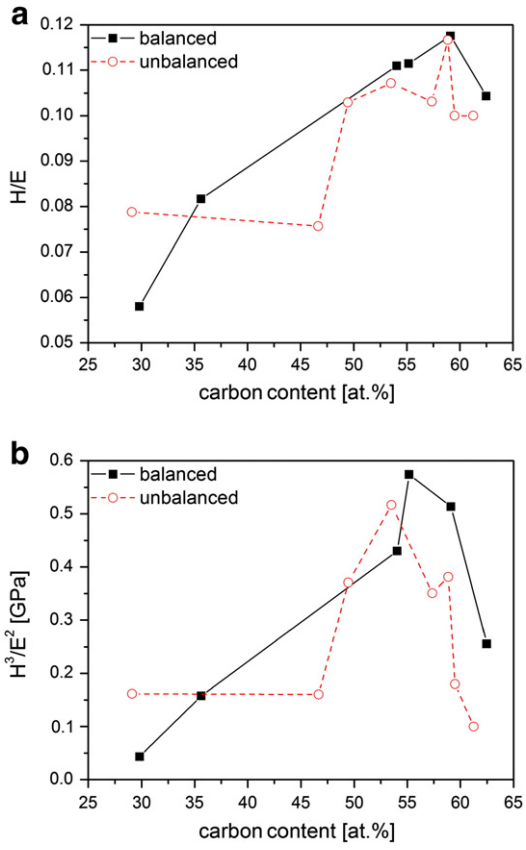

Fig. 10. Dependence of (a) H/E and (b) H^3/E^2 on carbon content.

change the microstructure and property of the coatings. A report on the indentation response of the coatings can be found in [37].

The hardest samples from both series exhibited larger grains ~18 nm, which is contrary to the Hall–Petch theory in poly-crystallites [38–40] which shows that the hardness is inversely proportional to the crystal size. TEM image of the hardest coating from the balanced series revealed the presence of non-negligible amount (much more than a few atomic layers between grains) of a-C:H matrix and grain sliding may occur at higher C/Ti ratios (see Fig. 7). Further optimization of deposition parameters may lead to grain refining at similar composition thus mechanical properties may be enhanced as was proposed in [36,41]. A similar trend, that is hardest coating with large TiC crystallite size, was reported by Gulbiński et al. [15].

Also other parameters like toughness and resilience of the coating play an important role in industrial applications of protective coatings. Toughness can be defined as the ability of a material to absorb energy during deformation up to rupture. It has been proposed that the toughness depends on the hardness to Young's modulus ratio H/E [8,14,42]. The prediction of the wear of the coatings can be based on the resilience of the coating, which is defined as the resistance of a material against plastic deformation and relates to the ratio of H^3/E^2. Fig. 10 shows the plot of H/E and H^3/E^2 on the total carbon content. The H/E parameter varies from 0.06 to 0.12 for the balanced series and from 0.08 to 0.12 for the unbalanced series (see Fig. 8). Both series show similar trends, i.e. a low H/E (<0.1) in the coatings with a high Ti content and a high H/E (~0.11–0.12) achieved in coatings with high carbon content. The maximum H/E ratio of 0.12 is reached in coatings BAL-59C and UNB-59C of the same carbon content. Both maxima of H/E lie in the region with a higher C concentration than corresponds to the maximum hardness. The values of H/E are in good accordance with Pei et al. [8], where H/E ranges from 0.87 to 0.123 and the maximum achieved in the coating of 87 at.% C and with Martínez-Martínez et al. [14] where H/E ranges from 0.05 for pure titanium coating to 0.11 for nc-TiC/a-C coating with 79% of a-C matrix. For comparison the highest H/E values achievable with heat-treated tool steel is ~0.04, for ceramics like Al_2O_3, ZrO_2, Si_3N_4 or SiC ~0.06 and nitride based coatings like TiN and CrN ~0.08 [43]. The composition of the coatings for the maximum H^3/E^2 corresponds with that for the maximum hardness for both series. BAL-55C with a hardness of 46 GPa shows H^3/E^2 of 0.57 GPa and UNB-54C with hardness of 45 GPa shows H^3/E^2 of 0.52 GPa. Martínez-Martínez et al. [14] reported a maximum H^3/E^2 ratio of 0.31 for the coating with 47 mol% of a-C matrix (66% C and 34% Ti).

Good mechanical performance of the nc-TiC/a-C:H coatings is illustrated in Fig. 11 that shows residual indents made with a 1 N load for the unbalanced series. No cracks were propagating from the tips of the

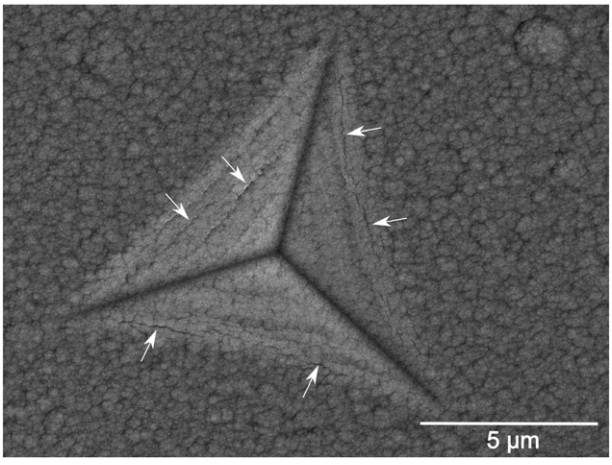

Fig. 11. SEM image of an indent at 1 N on coating UNB-55C (Ti/C = 0.74).

indent, only some minor cracks parallel to the indenter edges within the indent itself were visible (marked with white arrows) for coatings with high hardness. No cracks were visible for other coatings in the series. The trend was the same in the balanced series. This was an indication of high toughness. Pei et al. [44] observed distinct cracks propagating in the coatings of columnar microstructure from the corners of indents made with a cube-corner indenter at lower load of 190 mN.

4. Conclusions

Thick adherent nc-TiC/a-C:H nanocomposite coatings were prepared with magnetron sputtering at high deposition rates with −100 V substrate bias at low and high flux of impinging Ar ions using well balanced and strongly unbalanced magnetic field configuration at elevated deposition temperature of ~320 °C. Super-hard coatings were prepared at both magnetic configurations with maximal hardness and modulus of 45 GPa and 420 GPa. The coating structure, grain size, lattice parameter and mechanical properties were governed primarily by the composition of the coatings. The level of the ion flux did not play a significant role in the deposition process in the presented setup, though it cannot be ruled out that the effect of the ion flux would be more noticeable for coatings deposited at ambient temperatures as higher deposition temperature associated with high deposition rate can partially negate these effects. It can be concluded that at elevated temperatures superhard coatings were prepared by optimizing the chemical composition as the ion flux played only a minor role in the determining of the mechanical properties.

Acknowledgment

This research has been supported by GACR contracts 104/09/H080 and 205/12/0407 and R&D center project for low-cost plasma and nanotechnology surface modifications CZ.1.05/2.1.00/03.0086 funded by European Regional Development Fund. This work was also supported by RVO61389005. Pavel Souček acknowledges the Brno City Municipality as recipient of Brno PhD Talent Financial Aid.

References

[1] Y. Wang, X. Zhang, X. Wu, H. Zhang, X. Zhang, Appl. Surf. Sci. 255 (2008) 1801–1805.
[2] P. Souček, T. Schmidtová, L. Zábranský, V. Buršíková, P. Vašina, O. Caha, M. Jílek, A.A. El Mel, P.Y. Tessier, J. Schäfer, J. Buršík, V. Peřina, R. Mikšová, Surf. Coat. Technol. 211 (2012) 111–115.
[3] A. Czyżniewski, W. Prechtl, J. Mater. Process. Technol. 157-158 (2004) 274–283.
[4] J.C. Sánchez-López, D. Martínez-Martínez, C. Lópes-Cartes, A. Fernández, Surf. Coat. Technol. 202 (2008) 4011–4018.
[5] D.M. Cao, B. Feng, W.J. Meng, L.E. Rehn, P.M. Baldo, M.M. Khonsari, Appl. Phys. Lett. 79 (3) (2001) 329–331.
[6] J. Musil, P. Novák, R. Čerstvý, Z. Soukup, J. Vac. Sci. Technol. A 28 (2010) 244–249.
[7] Y.T. Pei, D. Galvan, J.Th.M. De Hosson, C. Strondl, J. Eur. Ceram. Soc. 26 (2006) 565–570.
[8] Y.T. Pei, D. Galvan, J.Th.M. De Hosson, A. Cavaleiro, Surf. Coat. Technol. 198 (2005) 44–50.
[9] D. Galvan, Y.T. Pei, J.Th.M. De Hosson, Acta Mater. 53 (2005) 3925–3934.
[10] Y. Hu, L. Li, X. Cai, Q. Chen, P.K. Chu, Diamond Relat. Mater. 16 (2007) 181–186.
[11] T. Schmidtová, P. Souček, P. Vašina, Surf. Coat. Technol. 205 (2011) S299–S303.
[12] V. Kulikovsky, A. Tarasenko, F. Fendrych, L. Jastrabik, D. Chvostova, F. Franc, L. Soukup, Diamond Relat. Mater. 7 (1998) 774–778.
[13] A.A. El Mel, B. Angleraud, E. Gautron, A. Granier, P.Y. Tessier, Surf. Coat. Technol. 204 (2010) 1880–1883.
[14] D. Martínez-Martínez, C. López-Cartes, A. Fernández, J.C. Sánchez-López, Thin Solid Films 517 (2009) 1662–1671.
[15] W. Gulbinski, S. Mathur, H. Shen, T. Suszko, A. Gilewicz, B. Warcholinski, Appl. Surf. Sci. 239 (2005) 302–310.
[16] K. Polychronopoulou, C. Rebholz, M.A. Baker, L. Theodorou, N.G. Demas, S.J. Hinder, A.A. Polycarpou, C.C. Doumanidis, K. Böbel, Diamond Relat. Mater. 17 (2008) 2054–2061.
[17] M. Samuelsson, K. Sarakinos, H. Högberg, E. Lewin, U. Jansson, B. Wälivaara, H. Ljungcrantz, U. Helmersson, Surf. Coat. Technol. 206 (2012) 2396–2402.
[18] D. Galvan, Y.T. Pei, J.Th.M. De Hosson, Surf. Coat. Technol. 201 (2006) 590–598.
[19] Y.T. Pei, C.Q. Chen, K.P. Shaha, J.Th.M. De Hosson, J.W. Bradley, S.A. Voronin, M. Čada, Acta Mater. 56 (2008) 696–709.
[20] J. Lin, J.J. Moore, B. Mishra, M. Pinkas, W.D. Sproul, Thin Solid Films 517 (2008) 1131–1135.
[21] T. Zehnder, J. Patscheider, Surf. Coat. Technol. 133–134 (2000) 138–144.
[22] A. Grill, Diamond Relat. Mater. 8 (1999) 428–434.
[23] K.E. Cooke, J. Hampshire, W. Southwall, D.G. Teer, Surf. Coat. Technol. 177–178 (2004) 789–794.
[24] M.A. Lieberman, A.J. Lichtenberg, Principles of Plasma Discharges and Materials Processing, second ed. John Wiley & sons, Hoboken, 2005.
[25] J. Saarilahti, E. Rauhala, Nucl. Instrum. Meth. Phys. Res. Sect. B 64 (1992) 734–741.
[26] M. Mayer, SIMNRA User's Guide, Technical Report IPP 9/113, Max-Planck-Institut fuer Plasmaphysick, Garching, Germany, 1997.
[27] W.C. Oliver, G.M. Pharr, J. Mater. Res. 19 (2004) 3–20.
[28] K.L. Johnson, J. Mech. Phys. Solid 18 (1970) 115–126.
[29] F. Amato, N.R. Panyala, P. Vašina, P. Souček, J. Havel, Rapid Commun. Mass Spectrom. 27 (2013) 1196–1202.
[30] S. Zhang, X.L. Bui, J. Jiang, X. Li, Surf. Coat. Technol. 198 (2005) 206–211.
[31] T. Schmidtová, P. Souček, V. Kudrle, P. Vašina, Surf. Coat. Technol. (2013), http://dx.doi.org/10.1016/j.surfcoat.2013.05.014.
[32] M.C. Morris, H.F. McMurdie, E.H. Evans, B. Paretzkin, H.S. Parker, N.C. Panagiotopoulos, C.R. Hubbard, Standard X-ray Diffraction Powder Patterns: Section 18 — Data for 58 Substances, NBS, Washington, 1981.
[33] G. Li, L.F. Xia, Thin Solid Films 396 (2001) 16–22.
[34] E. Lewin, E.O.Å. Persson, M. Lattemann, M. Stüber, M. Gorgoi, A. Sandell, C. Ziebert, F. Schäfers, W. Braun, J. Halbritter, S. Ulrich, W. Eberhardt, L. Hultman, H. Siegbahn, S. Svensson, U. Jansson, Surf. Coat. Technol. 202 (2008) 3563–3570.
[35] E. Lewin, M. Rasender, M. Klintenberg, A. Bergman, O. Eriksson, U. Jansson, Chem. Phys. Lett. 496 (1–3) (2010) 95–99.
[36] U. Jansson, E. Lewin, Thin Solid Films 536 (2013) 1–24.
[37] L. Zábranský, V. Buršíková, J. Buršík, P. Vašina, P. Souček, O. Caha, M. Jílek, V. Peřina, Chem. List. 106 (2012) s1508–s1511.
[38] E.O. Hall, Proc. Phys. Soc. Lond. Sect. B 64 (1951) 747–753.
[39] N.J. Petch, J. Iron Steel Inst. 174 (1953) 25–28.
[40] P.H. Mayrhofer, C. Mitterer, L. Hultman, H. Clemens, Prog. Mater. Sci. 51 (2006) 1032–1114.
[41] U. Jansson, E. Lewin, M. Rasander, O. Eriksson, B. André, U. Wiklund, Surf. Coat. Technol. 206 (2011) 583–590.
[42] A. Leyland, A. Matthews, Wear 246 (2000) 1–11.
[43] In: C. Donnet, A. Erdemir (Eds.), Tribology of Diamond-like Carbon Films, Springer, New York, 2008.
[44] Y.T. Pei, D. Galvan, J.Th.M. De Hosson, Acta Mater. 53 (2005) 4505–4521.

Surface & Coatings Technology 315 (2017) 17–23

Contents lists available at ScienceDirect

Surface & Coatings Technology

journal homepage: www.elsevier.com/locate/surfcoat

On the significance of running-in of hard nc-TiC/a-C:H coating for short-term repeating machining

Radek Žemlička [a], Pavel Souček [a,*], Petr Vogl [b], Mojmír Jílek [a,b], Vilma Buršíková [a], Petr Vašina [a], Y.T. Pei [a,c]

[a] Department of Physical Electronics, Faculty of Science, Masaryk University, Kotlářská 2, CZ–61137, Brno, Czech Republic
[b] Platit a.s., Průmyslová 3, CZ-78701 Šu3mperk, Czech Republic
[c] Advanced Production Engineering, Engineering and Technology Institute Groningen, University of Groningen, Nijenborgh 4, 9747 AG Groningen, The Netherlands

ARTICLE INFO

Article history:
Received 26 September 2016
Revised 14 January 2017
Accepted in revised form 7 February 2017
Available online 09 February 2017

Keywords:
TiC
Tribology
Run-in period
Machining

ABSTRACT

The importance of the often omitted running-in phase of tribological testing was studied on hard nc-TiC/a-C:H coating system selected as a representative of protective tribological coatings. The tribological measurements were periodically interrupted and the counterpart ball was replaced by a new one after every interrupted test to simulate machining applications, where the coatings are repeatedly in contact with a new material. The changes in the coefficient of friction and the wear rate of the counterpart ball were found to be dependent mainly on the roughness of the coating at any stage. It was found out that after substantial smoothening of the wear track of the measured coating, the coefficient of friction stabilized at the steady-state value attained in an uninterrupted long tribotest. This steady state value was reached at the very beginning of the test and initial instabilities in the coefficient of friction were no longer observed. It was also concluded that only after the nc-TiC/a-C:H coating gets smoothened enough within the wear track, the steady-state coefficient of friction can describe even applications where the counterpart is being periodically replaced by a new one.

1. Introduction

Tribological studies are usually focused on the long term evolution of the wear behavior and friction of a sliding couple [1], and the so-called running-in stage that is the initial phase of sliding contact between fresh, unworn solid surfaces is rarely studied and is often omitted [2]. The running-in period is usually a short transition phase and significantly differs from the steady-state of sliding contact that is generally studied and quantified [1]. The running-in stage usually takes much less time than the rest of the measurement and the value of the coefficient of friction (CoF) is often unstable in this initial measurement phase.

The omitting of the initial running-in period is easily justifiable if the tested coating is designed for the applications where the same parts of the machine are in constant contact with each other during their whole life time, typically in car engines. On the other hand, there are applications such that the coating gets in contact with a new counterpart over and over again, such as drilling, milling, forming etc. For example, a drill makes a hole usually just for several seconds and then it starts to drill a new hole in a different place or a different workpiece. If there is a transfer film created between the contact surfaces of the drill and one hole, this transfer film does not play a role in drilling another hole. What coefficient of friction is more relevant for such applications? Is it the one measured in the running-in phase or the steady-state coefficient of friction? To answer this question, the running-in stage was studied in detail in both continuous and interrupted tribotests.

Hard nc-TiC/a-C:H nanocomposite coatings consisting of TiC nanocrystallites embedded in amorphous carbon matrix have lately been the focus of many studies for an unusual combination of high hardness [3–5] and low friction [6–9]. The tribological properties of these coatings have been widely studied and are well understood [10–14]. The CoF was reported to depend on several coating parameters with the most important being the content of carbon and the coating structure [7,8,15]. In general, initially high CoF usually decreases to a lower stable value at a long sliding distance. The achievement of a low and stable CoF is typically explained by creation of a carbon rich transfer film in between the counterpart ball and the testing coating [16].

In this study we investigated the significance of the running-in stage and if the value of the coefficient of friction measured after the initial stabilization is even relevant for short-term repeated applications such as drilling. Furthermore, we studied the influence of the coating surface roughness on the evolution of the CoF to investigate the origin of the running-in aspect.

2. Experimental

Hybrid PVD-PECVD technique was used for the deposition of nc-TiC/a-C:H coating with carbon content of approximately 90 at.%. The deposition

* Corresponding author.
E-mail address: soucek@physics.muni.cz (P. Souček).

http://dx.doi.org/10.1016/j.surfcoat.2017.02.020
0257-8972/

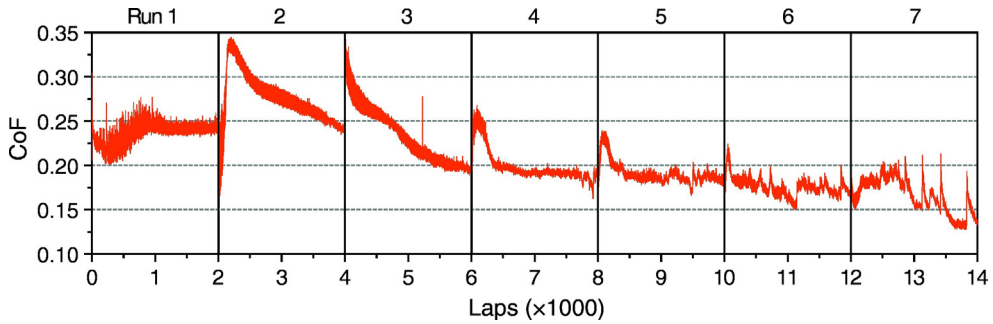

Fig. 1. Evolution of the coefficient of friction in an interrupted tribo-test carried out at the sliding speed of 0.3 m/s and normal load of 5 N. The test was repeatedly interrupted after every 2000 laps. The wear track was ultrasonically cleaned by each interruption.

was carried out in an industrial coating machine Pi 411 from Platit. A single central rotating cylindrical titanium cathode (Ø110 × 510 mm, 20 mm thick, impurities max. 0.17 mass %) was sputtered in argon (purity > 99.999%) and acetylene (purity 99.8%) atmosphere. Hardened M2 steel substrates (Ø30 × 6 mm) were pre-cleaned in a chemical bath and then ultrasonicated in a degreasing agent. The pre-cleaned samples were put into the chamber and placed in substrate holders around the central cathode.

The chamber was first evacuated to the base pressure of 1×10^{-3} Pa and subsequently heated to 450 °C. Then the samples were cleaned by argon ion bombardment. The deposition was then carried out with the following deposition parameters: 20 kW of magnetron power, −100 V bias, 25 sccm of Ar (~0.42 Pa) and a substrate temperature of 450 °C. The samples performed a 3 axes planetary rotation to ensure good coating homogeneity. Firstly, a titanium nitride layer ~1 μm thick was deposited using sputtering of titanium target in argon/nitrogen atmosphere. The TiN initial layer was followed by a hard interlayer of nc-TiC/a-C:H coating 0.5 μm thick with a hardness of 38 GPa and carbon content of 50 at.%. This layer was created using sputtering of titanium target in argon/acetylene atmosphere as described in [17]. A nc-TiC/a-C:H top coat with ~90 at.% carbon and thickness of 1 μm was finally deposited by increasing the flow of acetylene. Thus, the total thickness of the deposited coating system was 2.5 μm with the tribological top-coat thickness of 1 μm.

Tribotests were done using a CSM high temperature tribometer in a ball-on-disc configuration and in circular mode at sliding speeds of 0.1 and 0.3 m/s and normal loads of 5 N and 10 N, respectively, against uncoated Ø6 mm 100Cr6 steel ball (hardness of 7 GPa). The tribotests were always carried out for a specific number of laps (10,000 laps–sliding distance of approximately 180 m). The tests were carried out at humidity of 50% and at room temperature of 20 ± 1 °C. The roughness and wear were quantified using a laser confocal optical microscope OLYMPUS OLS 4000. The morphology of nc-TiC/a-C:H coatings was further characterized using DektakXT 3D profilometer and Philips XL30 ESEM scanning electron microscope operating at acceleration voltage of 10 kV.

3. Results

Fig. 1 shows the evolution of the coefficient of friction in dry sliding, where the test was repeatedly interrupted after every 2000 laps. The experiment was carried out at sliding speed of 0.3 m/s and normal load of 5 N. The counterpart ball was changed for each new run and the wear track was ultrasonically cleaned by each interruption to remove any debris and also possible carbon rich transfer film formed in the wear track. It was observed that during the first run the CoF remained ~0.25 in the whole test of 2000 laps (7 min). At the start of the second run the CoF first increased to 0.3 and then slowly decreased to 0.2. The third run started again with a high value of CoF of 0.3 and this value gradually decreased to 0.17. The CoF was 0.25 at the start of the fourth run and stabilized at 0.15 after ~500 laps. The fifth run was similar to the fourth run with a less pronounced initial CoF increase. The runs 6 and 7 exhibited a relatively stable value of CoF of ~0.18 with no pronounced initial CoF evolution during the first laps of each run. Small peaks in the CoF curve followed by gradual decrease are typical manifestation of the tearing off of the transfer film and its gradual building up thereafter. For the few first interrupted runs, the initial CoF measured at the beginning of the successive run was higher than the steady-state value of the CoF measured at the end of the previous run. It was concluded that until the fifth run, the replacement of a new counterpart ball by the interruption played a role in the evolution of the CoF during the running-in period. These measurements were repeated several times and the same behavior was always observed such that the initial increase of the coefficient of friction typically disappeared in the fourth or fifth run.

In order to investigate the role of possible carbon rich transfer film a similar experiment was performed with the wear track not being cleaned by the individual interruptions but only the counterpart ball

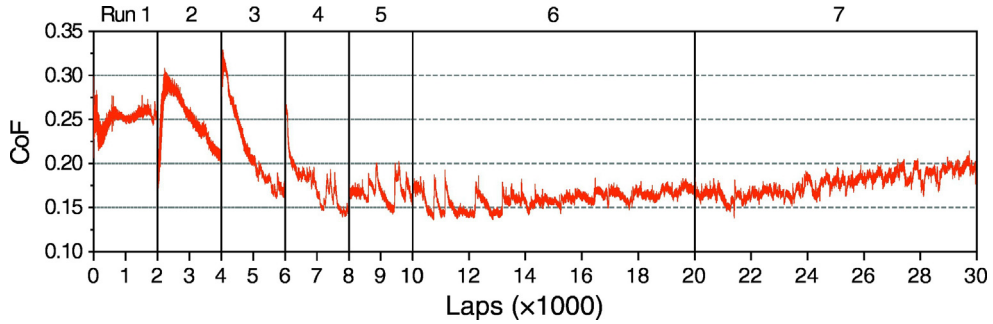

Fig. 2. Evolution of the coefficient of friction in an interrupted tribo-test carried out at the sliding speed of 0.3 m/s and normal load of 5 N. The test was repeatedly interrupted after every 2000 laps. The wear track was not cleaned by each interruption.

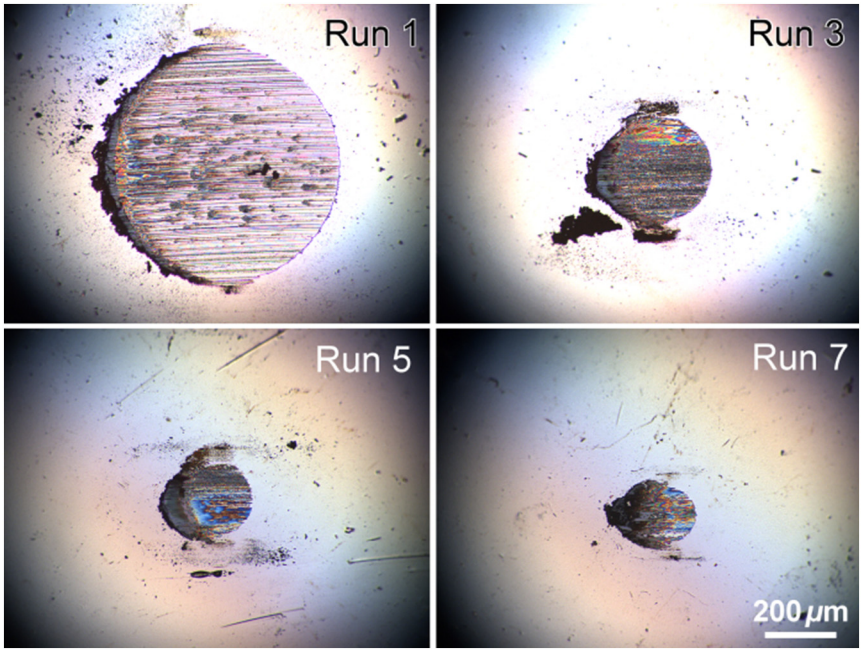

Fig. 3. Optical image of the wear scar of counterpart balls from the interrupted tribo-test corresponding to the CoF curves plotted in Fig. 1. Seven runs of equal sliding length of 2000 laps were performed with the wear track being cleaned after each run.

was replaced with a new one every interruption. The measured evolution of the CoF is plotted in Fig. 2. There was no appreciable difference from the previous group of experiments where the wear track was cleaned after every interruption. Again the CoF was high and stable (~0.25) in the first run. The CoF was initially high and gradually decreased in the second to fourth run, and the value of the CoF was relatively stable (~0.15–0.2) during all the subsequent runs. One can thus conclude that the cleaning of the wear track did not play a significant role in the measured evolution of the CoF during the running-in phase of the measurement. The debris that remained on the surface of the tested sample did not affect the friction and possible formation of the transfer film. This is highly advantageous for the transfer of laboratory results to industrial applications, where the cutting tools are not usually cleaned during work. The runs six and seven as seen in Fig. 2 were further prolonged from 2000 to 10,000 laps in order to test a long term stability of the CoF. The slight gradual increase of the CoF during the run sixth and seventh can be attributed to a gradual wear and roughening of the steel ball with the transfer film being thinner or even missing at the edges of the contact area of the ball and the coating [18].

Fig. 3 depicts the wear scar of counterpart balls taken after each run corresponding to the CoF plotted in Fig. 1. The wear volume of the steel ball decreased at every consecutive run with most pronounced changes

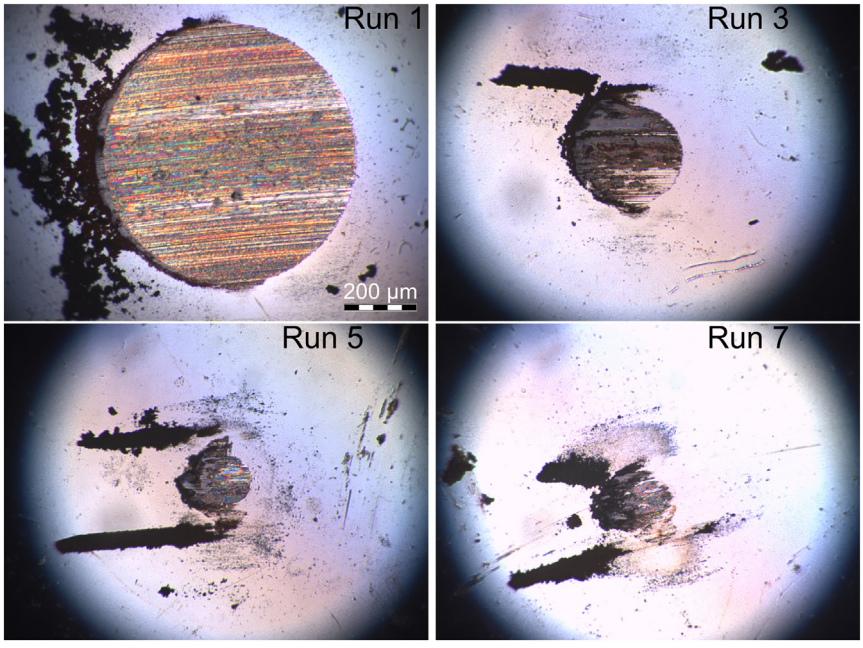

Fig. 4. Optical image of the wear scar of counterpart balls from the interrupted tribo-test corresponding to the CoF curves plotted in Fig. 2. Five runs of equal sliding length of 2000 laps and two runs of 10,000 laps were performed with the wear track not being cleaned after each run.

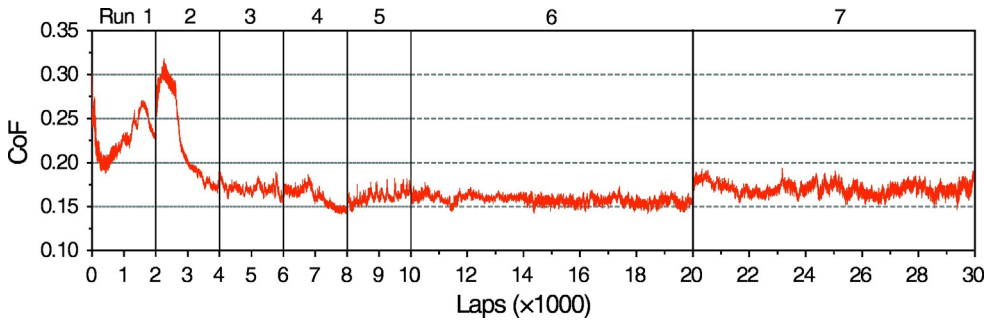

Fig. 5. Evolution of the coefficient of friction measured at the applied load of 10 N and sliding speed of 0.3 m/s. The test was repeatedly interrupted. The wear track was not cleaned by each interruption.

between the first several runs. Typically, the runs where higher CoF was measured resulted in several times larger wear volume of the steel ball. It was also found out that the wear scars on the counterpart ball observed after testing both with and without cleaning of the racetrack yielded were of similar size after the same number of laps, as is illustrated in Fig. 4, where the wear scars of the balls used in the experiment in Fig. 2 are shown. Furthermore, even if the sixth and seventh runs were prolonged from 2000 laps (experiment in Fig. 1) to 10,000 laps (experiment in Fig. 2) the wear scars were still comparable in size (see images of wear scars from the seventh run in Figs. 3 and 4) This indicates that the wear of the counterpart ball is most pronounced at the start of the measurement and is minor during the later stages of the test, as prolonging the sliding distance five times in the last two runs led to a little increase of counterpart ball wear.

The length and the character of the running-in period were further studied for different normal loads and sliding speeds. The normal load in the previous experiments with repeated interruptions was always set to 5 N. Fig. 5 shows the CoF evolution with a normal load of 10 N. The wear track was not cleaned in this test. The comparison of the experimental results between 5 N load and 10 N load showed that increasing the applied load led to shortening of the initial high CoF running-in phase. A low and stable CoF was achieved by the fifth run with 5 N load, while the same was achieved by third run when the load was doubled to 10 N.

Furthermore, a repeatedly interrupted tribo-test for comparison was carried out where the wear track was cleaned by each interruption but the ball was kept unchanged for all the runs. The CoF evolution (not shown) exhibited similar behavior as in the case where the ball was changed after every interruption. The CoF exhibited low and stable value from the fourth run onwards, although a very short running-in period can be now detected in all runs. The apparent size of the wear scar on the ball was almost identical after the first run of 2000 laps till the end of the experiment at 30000 laps.

The evolution of the CoF plotted in Fig. 6 compares two experiments with different sliding speeds without any interruptions. Fig. 6a shows the CoF measured at load of 5 N and sliding speed of 30 cm/s as used in previous experiments, while Fig. 6b shows the CoF measured at lower sliding speed of 10 cm/s and 5 N load. The number of laps needed to achieve a stable CoF was very close in both cases. As the sliding speed was significantly faster in Fig. 6a, the running-in period took markedly shorter time – approximately 15 min at sliding speed of 30 cm/s as compared to approximately 48 min with sliding speed of 10 cm/s.

The evolution of wear morphology of the coating was studied on the same area of a wear track by each run. Fig. 7 shows the CoF evolution in the interrupted test performed under the same sliding conditions as shown in Fig. 2. The sample was not cleaned between the interruptions and the same area on the wear track was examined by scanning electron microscopy before the test and after selected runs in order to correlate the evolution of the wear morphology and the CoF. The O symbol denotes the original status of as-deposited coating before the tribotest, letter A indicates the second group of micrographs taken after run 2. The B group and C group, of micrographs were taken after the fourth run and the final seventh run, respectively. Fig. 8 depicts the micrographs of the wear track taken at different moments as described previously. The surface of the as-deposited coating was covered by typical cauliflower patterns that result in a high roughness R_a of about 0.18 μm. As the tribotest progressed, the asperities were being polished and the CoF was decreasing at the same time. When the asperities

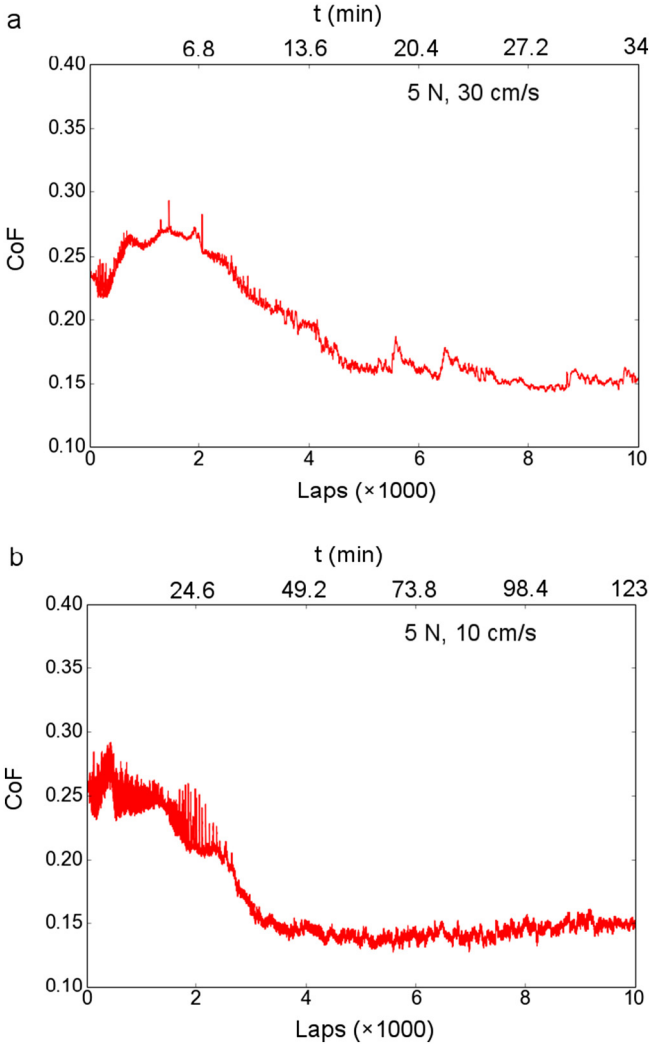

Fig. 6. CoF curve measured at 5 N normal load and different sliding speeds: (a) 0.3 m/s and (b) 0.1 m/s. The tests were not interrupted.

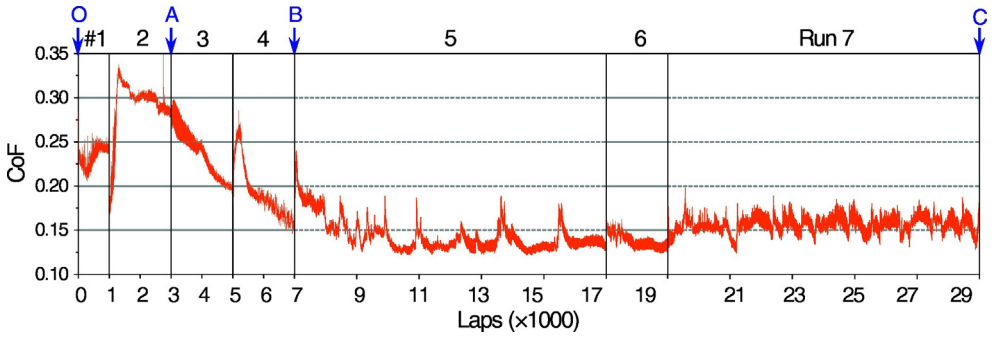

Fig. 7. Evolution of the CoF in an interrupted tribo-test performed at 0.3 m/s sliding speed and 5 N load. The indexes O, A, B and C indicate SEM observations of the wear morphology of the coating as shown in Fig. 8.

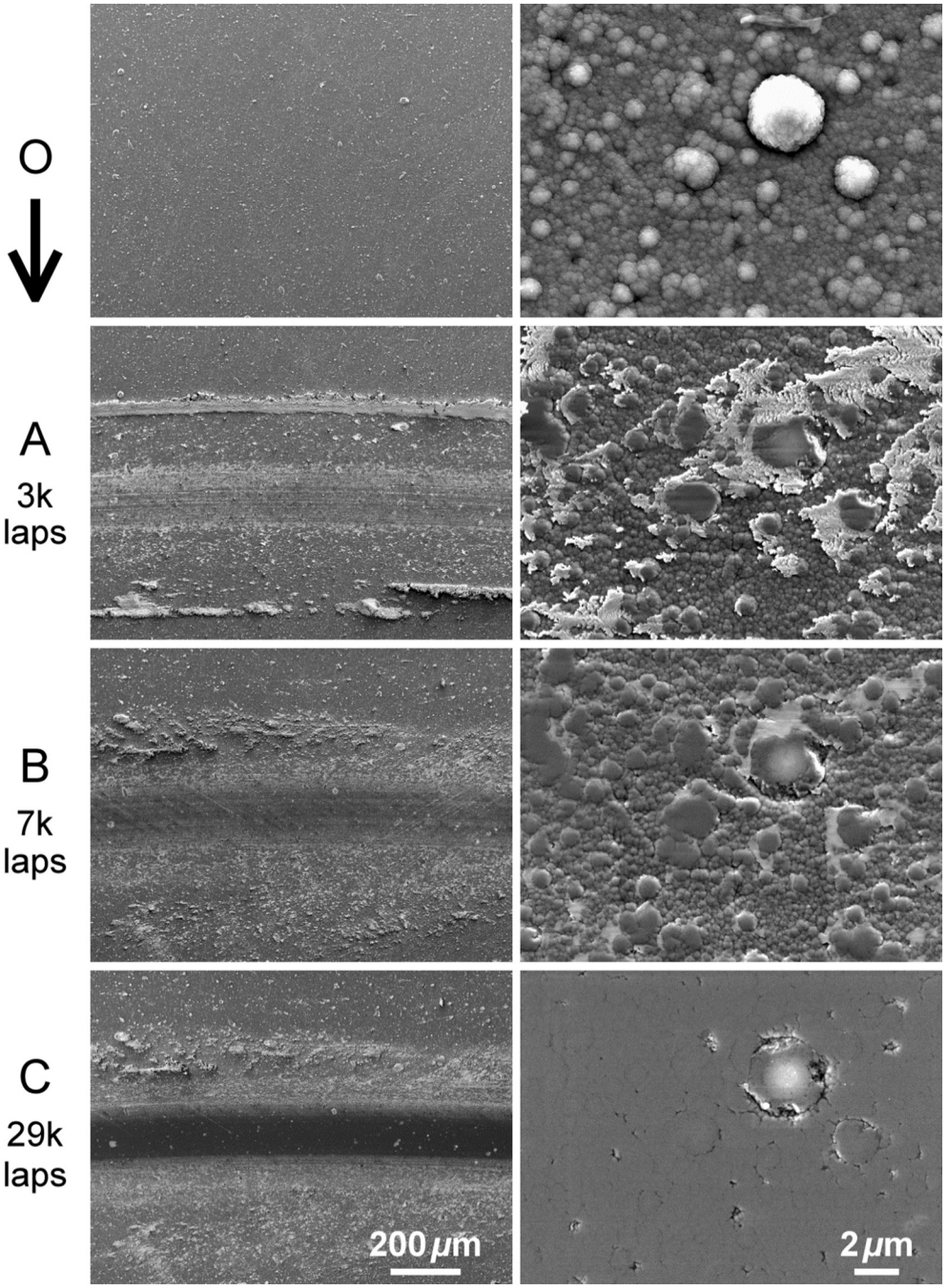

Fig. 8. SEM images showing the evolution of wear morphology of the same area in the wear track taken during consecutive runs indicated in Fig. 7.

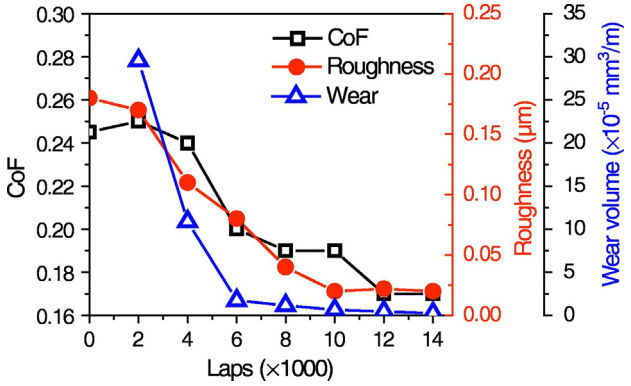

Fig. 9. Evolution of CoF against the roughness of the wear track formed on the coating and the wear volume of the ball counterpart after each run of 2000 laps.

appeared to be almost completely polished after four runs - resulting in much smoother contact with the counterpart ball as seen in the C group of micrographs - the CoF decreased to a low steady-state value.

The decrease of the surface roughness is closely correlated with the decrease of the CoF and of the wear rate of the ball counterpart, as shown in Fig. 9. The gradual polishing of the wear track by the ball during sliding leads to a significant decrease in the surface roughness of the wear track, which in turn leads to considerable decrease of the coefficient of friction. When the coating was polished enough, the CoF stayed stable at the same level even after the interruption so that the change of the counterpart did not play a significant role in the value of the CoF during the studied running-in phase.

4. Discussion

The influence of the initial roughness on the tribological properties of titanium carbon coatings was investigated by Shaha et al. [16]. The time needed for the initial decrease and stabilization of the CoF was correlated with the initial surface roughness. The initial decrease of the CoF was explained by the formation of carbon-rich transfer film between the wear track and the counterpart. It was found out that a higher initial coating roughness correlated with longer time needed to achieve a stable CoF value. It was concluded that high initial roughness of the coating impedes the creation of the transfer film and the drop and the stabilization of the CoF takes longer time in the case of rough coatings [16].

Similar explanation can be also used to describe the behavior of the CoF in this work. The high initial roughness of the as-deposited coatings (Ra ~ 0.18 μm) caused an initial roughening of the ball counterpart and high wear of the ball. In this case the carbon-rich transfer film did not sufficiently cover the contact area and therefore the CoF value was high. As the counterpart was changed to a new one for the next run, the CoF increased at the beginning of the second run because of the roughening of the surface of the new counterpart. During the second run, the CoF started to decrease as the carbon rich transfer film started to form when the roughening of the contact area was less significant due to lower roughness of the coating wear track as compared to the very first run. As the coating got smoother after the very first runs, the time needed for the formation of a new transfer film got shorter. Finally, when the surface of the coating wear track was smoothed enough the change of the counterpart ceased to influence the value of the CoF and the CoF value was low and stable from the beginning of the run. The formation of the carbon rich transfer layer in our experiments can be deduced from the behavior of the CoF observed in the later runs of all tests. A sudden increase in the CoF followed by a slower gradual decrease to the steady-state value is a typical for a sudden breakdown and gradual rebuilding of a carbon rich transfer layer between the sliding bodies [18,19]. Also the steady state value of the CoF is consistent to that of nc-TiC/a-C(:H) coatings with high carbon content that are characterized by creation of the carbon transfer film [7]. Moreover, residual carbon debris was detected in and around the wear track after the tribotests.

No significant change in the CoF evolution was observed in the case where the ball was kept unchanged for all the interrupted tests but the wear track was cleaned after each interruption. This indicates that the roughness of the much softer counterpart ball plays only a little role in affecting the CoF behavior. Also as the low value of the CoF was achieved at the very beginning of the later runs regardless of the experiment type, no effect of chemical aging of the wear track and repeated creation of disadvantageous contaminated and oxidized layer on the coating as proposed by Rani et al. [20] was observed. Thus the CoF behavior can be attributed only to the coating roughness.

The counterpart ball in tests with the significantly smoothened coating exhibited such a small wear rate that the size of its wear scar was nearly unchanged with the length of sliding. The apparent wear volume of the ball achieved in the last two runs of 10,000 laps each depicted in Fig. 4 was very close to those depicted in Fig. 3 where the sliding distance was only 2000 laps. Apart from the prolonged runs, moreover, the wear track was not cleaned after every interruption in this case. As the CoF was low and stable even at the start of the last two runs for both cleaned and uncleaned wear track, the transfer film was assumed to form fast at the start of the measurement even when the wear track was cleaned.

The ever rapidly reached low and stable CoF in the test with doubled load 10 N can be explained by a faster polishing of the coating due to higher applied load. The same explanation holds for the experiments verifying the influence of sliding speed. Although the time needed to smoothen the coating and thus reach the low and stable CoF was different at sliding speed of 0.3 m/s versus 0.1 m/s, the total number of laps needed to reach such a regime was nearly the same. It implies that sliding at lower speed leads to corresponding increase of running-in period necessary to achieve low enough roughness for fast formation of transfer film that helps to reduce friction and wear.

5. Conclusions

Nanocomposite nc-TiC/a-C:H coating with high carbon content of ~90 at.% was deposited by a hybrid PVD-PECVD process in industrial conditions. The running-in phase of ball-on-disc tribotests was analyzed in detail in order to establish the validity of omitting the running-in phase for short term repeated applications such as drilling, milling, forming, etc.

The roughness of the nc-TiC/a-C:H coating was found to be the primary cause of the instabilities of the initial part of the tribo-testing. The initial unstable CoF was identified to be caused by the initial decrease of the roughness of the as-deposited coating. High initial roughness of the coating led to slow or no formation of a carbon rich transfer film needed for achieving of low coefficient of friction. After the roughness of the hard coating decreased to a certain value, transfer film could form within a short time and the resulting CoF was stable. Roughness of the softer steel ball and possible oxidation of the wear track were found out to be of little influence.

When the CoF had stabilized, the interruption of sliding test and the change of counterpart had no effect on further CoF evolution. Furthermore, the steady-state CoF measured in the standard long uninterrupted tests was identical to the one measured in interrupted short tests after the coating became smoothened. Therefore, the standard CoF analysis procedure involving quantification of the value of CoF measured in the steady state region after the running-in period is relevant even for short term repeating applications such as drilling, milling or forming.

Acknowledgment

This research has been supported by GACR contract 205/12/0407, by project CZ.1.05/2.1.00/03.0086 funded by European Regional Development Fund, and project LO1411 (NPU I) funded by Ministry of Education, Youth and Sports of Czech Republic.

References

[1] B. Bhushan, Principles and Applications of Tribology, John Wiley & Sons, 2013 321–401.
[2] P.J. Blau, On the nature of running-in, Tribol. Int. 38 (2005) 1007.
[3] Y. Wang, X. Zhang, X. Wu, H. Zhang, X. Zhang, Compositional, structural and mechanical characteristics of nc-TiC/aC: H nanocomposite films, Appl. Surf. Sci. 255 (5) (2008) 1801–1805.
[4] P. Souček, T. Schmidtová, L. Zábranský, V. Buršíková, P. Vašina, O. Caha, M. Jílek, A.A. El Mel, P.Y. Tessier, J. Schäfer, J. Buršík, V. Peřina, R. Mikšová, Evaluation of composition, mechanical properties and structure of nc-TiC/aC: H coatings prepared by balanced magnetron sputtering, Surf. Coat. Technol. 211 (2012) 111–116.
[5] A. Czyżniewski, W. Precht, Deposition and some properties of nanocrystalline, nanocomposite and amorphous carbon-based coatings for tribological applications, J. Mater. Process. Technol. 157 (2004) 274–283.
[6] F.S. James, F. Shackelford, W. Alexander, Materials Science and Engineering Handbook, CRC Press, LLC, 2001 471.
[7] J.C. Sánchez-López, D. Martínez-Martínez, C. López-Cartes, A. Fernández, Tribological behaviour of titanium carbide/amorphous carbon nanocomposite coatings: from macro to the micro-scale, Surf. Coat. Technol. 202 (16) (2008) 4011–4018.
[8] D.M. Cao, B. Feng, W.J. Meng, L.E. Rehn, P.M. Baldo, M.M. Khonsari, Friction and wear characteristics of ceramic nanocomposite coatings: titanium carbide/amorphous hydrocarbon, Appl. Phys. Lett. 79 (3) (2001) 329–331.
[9] J. Musil, P. Novák, R. Čerstvý, Z. Soukup, Tribological and mechanical properties of nanocrystalline-TiC/aC nanocomposite thin films, J. Vac. Sci. Technol. A 28 (2) (2010) 244.
[10] Y.T. Pei, D. Galvan, J.Th.M. De Hosson, A. Cavaleiro, Nanostructured TiC/aC coatings for low friction and wear resistant applications, Surf. Coat. Technol. 198 (1) (2005) 44–50.
[11] K.P. Shaha, Y.T. Pei, D. Martínez-Martínez, J.C. Sánchez-López, J.Th.M. De Hosson, Effect of process parameters on mechanical and tribological performance of pulsed-DC sputtered TiC/a-C:H nanocomposite films, Surf. Coat. Technol. 205 (7) (2010) 2633–2642.
[12] Y.T. Pei, D. Galvan, J.Th.M. De Hosson, C. Strondl, Advanced TiC/aC: H nanocomposite coatings deposited by magnetron sputtering, J. Eur. Ceram. Soc. 26 (4) (2006) 565–570.
[13] K. Polychronopoulou, C. Rebholz, M.A. Baker, L. Theodorou, N.G. Demas, S.J. Hinder, A.A. Polycarpou, C.C. Doumanidis, K. Böbel, Nanostructure, mechanical and tribological properties of reactive magnetron sputtered TiC_x coatings, Diam. Relat. Mater. 17 (12) (2008) 2054–2061.
[14] T. Zehnder, P. Schwaller, F. Munnik, S. Mikhailov, J. Patscheider, Nanostructural and mechanical properties of nanocomposite nc-TiC/aC: H films deposited by reactive unbalanced magnetron sputtering, J. Appl. Phys. 95 (8) (2004) 4327–4334.
[15] D. Martínez-Martínez, C. López-Cartes, A. Fernández, J.C. Sánchez-López, Influence of the microstructure on the mechanical and tribological behavior of TiC/aC nanocomposite coatings, Thin Solid Films 517 (5) (2009) 1662–1671.
[16] K.P. Shaha, Y.T. Pei, D. Martínez-Martínez, J.Th.M. De Hosson, Influence of surface roughness on the transfer film formation and frictional behavior of TiC/aC nanocomposite coatings, Tribol. Lett. 41 (1) (2011) 97–101.
[17] R. Žemlička, M. Jílek, P. Vogl, P. Souček, V. Buršíková, J. Buršík, P. Vašina, Understanding of hybrid PVD-PECVD process with the aim of growing hard nc-TiC/a-C: H coatings using industrial devices with a rotating cylindrical magnetron, Surf. Coat. Technol. 255 (2014) 118–123.
[18] Y.T. Pei, D. Galvan, J.Th.M. De Hosson, Nanostructure and properties of TiC/aC: H composite coatings, Acta Mater. 53 (17) (2005) 4505–4521.
[19] K.P. Shaha, Y.T. Pei, D. Martinez-Martinez, J.Th.M. De Hosson, Influence of hardness and roughness on the tribological performance of TiC/a-C nanocomposite coatings, Surf. Coat. Technol. 205 (2010) 2624–2632.
[20] R. Rani, N. Kumar, A.T. Kozakov, K.A. Googlev, K.J. Sankaran, P.Kr. Das, S. Dash, A.K. Tyagi, I.- Nan Lin, Superlubrication properties of ultrananocrystalline diamond film sliding against a zirconia ball, RSC Adv. 5 (2015) 100663–100673.

Surface & Coatings Technology 311 (2017) 257–267

Contents lists available at ScienceDirect

Surface & Coatings Technology

journal homepage: www.elsevier.com/locate/surfcoat

Superhard nanocomposite nc-TiC/a-C:H coatings: The effect of HiPIMS on coating microstructure and mechanical properties

Pavel Souček *, Josef Daniel, Jaroslav Hnilica, Katarína Bernátová, Lukáš Zábranský, Vilma Buršíková, Monika Stupavská, Petr Vašina

Department of Physical Electronics, Faculty of Science, Masaryk University, Kotlářská 2, CZ-61137 Brno, Czech Republic

ARTICLE INFO

Article history:
Received 1 July 2016
Revised 5 January 2017
Accepted in revised form 7 January 2017
Available online 09 January 2017

Keywords:
Nanocomposite
TiC
HiPIMS
Structure
Mechanical properties

ABSTRACT

Nanocomposite coatings consisting of titanium carbide crystallites embedded in amorphous carbon matrix were deposited utilizing direct current magnetron sputtering (DCMS) and high power impulse magnetron sputtering (HiPIMS) of titanium target in argon/acetylene atmosphere. DC driven depositions of coatings with high amount of carbon were accompanied by significant arcing during the deposition. HiPIMS utilization made reliable arc-free deposition of coatings with high carbon content possible. Analyses of the coating structure revealed that utilization of HiPIMS favours carbon incorporation into the TiC_x grains rather than to the matrix. HiPIMS deposited coatings exhibited stoichiometry of the TiC_x grains closer to unity with grains exhibiting lower lattice parameter and a lower fraction of the a-C matrix. This led to a smaller mean TiC_x grain separation by the a-C:H matrix. Also the surface structure of the HiPIMS deposited coatings was much finer. The structure refinement resulted in overall higher hardness of HiPIMS deposited coatings with the hardest coatings reaching the superhard region of >40 GPa and in 40% increase of H/E ratio and nearly threefold increase of H^3/E^2 ratio.

1. Introduction

Coatings consisting of nanocrystalline titanium carbide grains embedded in amorphous (hydrogenated) carbon matrix – nc-TiC/a-C(:H) can be tailored from super-hard coatings [1,2,3] with hardness reaching up to 46 GPa [4] to low friction coatings [5,6,7] by varying the phase composition. Such a wide range of functional properties can be achieved owing to nanocomposite nature of such coatings.

Hydrogen free nc-TiC/a-C coatings are usually deposited by employing co-sputtering of carbon and titanium targets [8,9,10,11,12,13,14], although other PVD methods such as electron beam titanium evaporation with carbon magnetron sputtering [15], titanium magnetron sputtering with carbon pulsed laser deposition [16,17], compound TiC target sputtering with possible carbon target co-sputtering [5,18,19,20], ICP assisted PVD/CVD [21] or combination of IPVD/PECVD [22]. Hydrogenated nc-TiC/a-C:H coatings are most often deposited by sputtering of titanium target in hydrocarbon containing plasma by a hybrid PVD–PECVD process with methane [23,24] or acetylene [1,3,4,6,25,26,27,28,29,30,31] as carbon precursors. If hydrogenated nc-TiC/a-C:H coatings are deposited by direct-current (DC) magnetron sputtering with argon/acetylene atmosphere, TiH phase can also be present in the coating [32]. Typically, DC [3,4,5,6,7,21,22,23,24,25,26,28,30] or mid-frequency pulsed DC (p-DC) [1,10,11,12,33] magnetron sputtering is employed and the resulting deposited coatings have been thoroughly studied in recent years. However, significantly fewer reports dedicated to nc-TiC/a-C:H coatings deposited by High Power Impulse Magnetron Sputtering (HiPIMS) can be found [34,35]. Thus the HiPIMS deposition process is much less described and the employment of HiPIMS on the structure and mechanical properties of the deposited nc-TiC/a-C:H coatings is not fully understood yet.

HiPIMS employs short intense power pulses on the sputtered target with a typical duty cycle of a few percent [36,37,38,39]. This power time distribution leads to plasma several orders of magnitude denser during the pulse than it is for a DC magnetron sputter deposition process. Denser plasma generally leads to high fraction of ionized sputtered species [39,40,41]. Correspondingly, such deposition process usually leads to total ion flux on the substrate several orders of magnitude higher during the pulse than it is in DC magnetron sputtering [36,42]. Furthermore, the much denser plasma can enhance the plasma chemistry [43] which can alter the dissociation of acetylene in the hybrid PVD-PECVD process of nc-TiC/a-C:H deposition using acetylene gas as carbon source for the coating. Such a high level of ion bombardment of the growing coating and altered plasma chemistry can affect the structure and overall properties of the resulting coating [44].

The present paper explores possibilities of nc-TiC/a-C:H deposition by a hybrid PVD-PECVD process of Ti target sputtering in argon/acetylene atmosphere. Coatings were deposited with DC and HiPIMS at the same mean power. The conditions for HiPIMS were chosen in a way to achieve high and stable current in the pulse for at least half of the

* Corresponding author.
E-mail address: soucek@physics.muni.cz (P. Souček).

http://dx.doi.org/10.1016/j.surfcoat.2017.01.021
0257-8972/

pulse duration. In addition, biasing conditions were chosen to attain similar grain microstrain in DCMS and HiPIMS. This allows us to focus only on the differences in the structure of the deposited coatings and its effects on the mechanical properties without introducing further stress induced hardening effects.

The evolution of the discharge state with acetylene flow is described. The possibilities of carbon rich coating deposition by DCMS and HiPIMS will be discussed. Coatings deposited with DC, HiPIMS are mutually compared, and the differences of the coatings properties are discussed. Structural parameters leading to mechanical properties enhancement for HiPIMS depositions are identified and the advantages and disadvantages of HiPIMS depositions process to synthesize nc-TiC/a-C:H coatings are shown.

2. Experimental setup

All depositions were carried out using industrial sputtering system Alcatel SCM 650 with a cylindrical vacuum chamber ∅ 65 × 35 cm. The deposition chamber was evacuated by a turbomolecular pump backed by a Roots pump to the base pressure in the order of 10^{-4} Pa. A well balanced magnetron source (see ref. [4] for specific magnetic field structure measurements) was equipped with a 99.95% purity ∅ 20 cm Ti target. For direct current (DC) deposition the target was driven by a Hüttinger TruPlasma Bipolar 4010 generator operated in DC mode. Melec SIPP 2000 USB generator was used for High Power Impulse Magnetron Sputtering (HiPIMS) experiments. Voltage and current waveforms for HiPIMS discharge were measured using integrated Melec measuring system containing voltage and current transducers using Tektronix TDS 2014C digital oscilloscope.

Cemented tungsten carbide (hardmetal) substrates were placed on a biasable (13.56 MHz RF) substrate holder located 6.5 cm from the target above the target racetrack. Argon (purity 99.999%) was used as the working gas and acetylene (purity 99.6%) was used as a carbon source. Gasses were dosed via mass flow controllers. The gas inlet was located between the target and the substrate at a distance of 2 cm from the target.

First, the hardmetal substrates were ultrasonically cleaned in a degreasing agent. The titanium target was mechanically cleaned. Then the vacuum chamber was evacuated. The target and the substrates were further simultaneously cleaned by argon ion bombardment after being separated by a shutter. The cleaning was performed until the discharge voltage stabilized indicating that the target was completely cleaned. This usually took 1–2 h. After the target and the chamber cooled down to room temperature during the night, the deposition procedure commenced by a short pre-deposition cleaning. This was done for 35 min ensuring removal of any contaminants adsorbed during the night. The substrates were pre-heated to ~150 °C at the same time by the ion bombardment. The cleaning phase conditions were as follows: 65 sccm Ar (~3 Pa), 1 kW DC on the Ti target, 500 W RF on the substrate holder.

Then the shutter between the substrate and the target was opened and the argon flow was set to 20 sccm (~1.1 Pa). For DCMS depositions the power on the titanium target was set to 1.25 kW and the self-bias on the RF driven substrate was set to − 100 V. A pure titanium ~500 nm interlayer was deposited before the nc-TiC/a-C:H coating in order to promote adhesion. The acetylene flow was then set to the desired value. Coatings in DCMS conditions were deposited for 60 min in order to prepare at least two micrometres thick films. Although no intentional heating was applied, the temperature on the substrate during the deposition was measured to be ~300 °C due to close proximity of the substrate and the target. For HiPIMS experiments, the sample holder was disconnected after the cleaning phase and was left at floating potential. The potential time averaged through the pulse was measured to be ~− 3 V during the deposition. HiPIMS depositions were performed similarly to DCMS depositions at the same mean power of 1.25 kW with several exceptions - thinner ~100 nm Ti interlayer was deposited due to lower deposition rate of HiPIMS, 400 μs long pulse with repetition frequency of 30 Hz (1.2% duty cycle) was used instead of DC, the deposition time was doubled to 120 min to again achieve at least ~2 μm thin film and floating substrate was used instead of RF biasing. In DCMS the power of 1.25 kW corresponded to the discharge voltage of ~− 360 V and discharge current of ~3.5 A for a clean Ti target. The temperature of the substrates during the deposition was measured also to be ~300 °C.

The surface of nc-TiC/a-C:H coatings was imaged using a Tescan MIRA 3 field-emission scanning electron microscope (SEM) with electron accelerating voltage of 10 kV. The thickness was determined by abrading a spherical cap by a calotester and consecutive imaging of the spherical cap by LEXT OLS4000 3D Laser Measuring Confocal Microscope. The chemical composition was measured using Oxford Instruments EDX attached to the SEM. The quantification of the elemental composition was made using internal standards library supplied by Oxford Instruments within AZtec Software. The chemical composition referred to throughout the text was always evaluated by EDX. Grazing angle of incidence X-ray diffraction (GIXRD) utilizing RIGAKU SmartLab diffractometer was performed to analyse the crystalline structure. The angle of incidence of the copper K_α X-ray ($\lambda = 1.54056$ Å) source was set to 0.5°. GIXRD was chosen to eliminate WC diffraction peaks from the cemented tungsten carbide substrate as WC and TiC diffraction peaks overlap. After correction for the instrumental broadening, the grain size was calculated from the most intensive TiC diffraction peak corresponding to (111)diffraction using the Scherrer formula attributing the total broadening of the peak to the crystallite size only (neglecting the strain broadening). The Scherrer formula thus reports the smallest possible value of the mean crystallite size. The microstrain of the crystallites was estimated by thy Williamson-Hall plot. XPS analysis were performed to analyse the bonding state of the carbon atoms, to calculate the amount of the a-C:H phase, the grain stoichiometry factor and the mean grain separation. The XPS data were recorded using a Thermo Scientific K-Alpha XPS system equipped with a micro-focused, monochromatic Al K_α X-ray source (1486.6 eV). High resolution spectra were recorded with pass energy of 50 eV. The samples were cleaned by 0.5 keV Ar ion bombardment for 30 min before every XPS measurement. Low ion energy ensured that the coating itself was not affected by the cleaning and a long time of cleaning ensured removal of all surface contaminants. The recorded spectra were calibrated by setting the C1 s peak to 285 eV. Horriba LabRAM HR Evolution microraman spectrometer with 532 nm laser was used to analyse the bonding state of the a-C:H matrix. The acquired Raman spectra were fitted with four peaks – the D peak located ~1350 cm^{-1}, the G peak located ~1570 cm^{-1} and the D_1 and G_1 peaks located ~1220 and 1350 cm^{-1}, respectively - similarly to [30,45,46,47]. The G and D peaks arise due to stretching or breathing of the sp^2 carbon sites [47]. D_1 and G_1 peaks (alternatively can be found denoted as ν_1 and ν_2) can be attributed to trans-polyacetylene chains [46,47]. Fischerscope H100 depth sensing indenter equipped with a Berkovich tip was used to study the indentation response of the coated samples. At least 12 indents were made at each load on every sample. The hardness and the elastic modulus were evaluated using the standard procedure proposed by Oliver and Pharr [48]. Such testing conditions were used in nanoindentation measurements under which the substrate did not influence the measured values of the hardness and the effective elastic modulus ($E_{eff} = E / (1 - \nu^2)$, where E is the Young's modulus and ν is the Poisson ratio).

3. Results

A typical waveform of the discharge current and cathode voltage acquired for a clean Ti target during the HiPIMS pulse is plotted in Fig. 1. The pulse voltage in this case was ~− 525 V. The discharge current was increasing for the first 175 μs and saturated at a nearly steady state value of ~260 A for the remaining 225 μs. This means that a high discharge current density of 3 A/cm^2 of the racetrack surface was

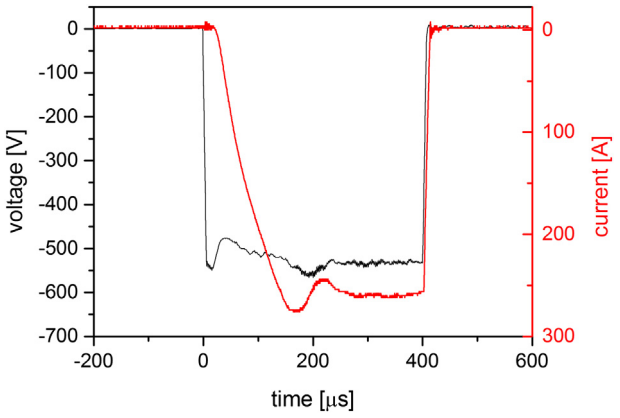

Fig. 1. Voltage and current waveform of the HiPIMS pulse for a clean Ti target.

achieved for ~50% of each pulse. The values of the discharge current and cathode voltage were evolving slightly after the addition of acetylene and were stabilized in approximately 15 min for both the DCMS and the HiPIMS process signifying that the coatings were grown in stabilized conditions for 75% of the deposition time for DCMS and 88% of the deposition time for HiPIMS. In the DCMS the voltage shifted from ~−360 V for no acetylene supply to −370–−470 V for acetylene flow range used. The voltage shift in HiPIMS case was from −525 V for no acetylene to −480 V to −580 V for process with acetylene. These conditions resulted in a nearly homogeneous depth profile of coating composition and mechanical properties. This was verified by a technique described in [49], where EDX and nanoindentation measurements in an abraded crater (calotte) throughout the coating are proposed for in-depth analysis of chemical composition and mechanical properties. Achieving a homogeneous depth profile of the coating properties simplifies evaluation of the EDX and indentation measurements performed from the top of the coating.

Fig. 2a depicts the plot of the acetylene supply needed to achieve a specific carbon content in the deposited coatings and Fig. 2b depicts the deposition rate of the corresponding coatings. The carbon content on the x-axis for Fig. 2 as well as all other graphs is derived from EDX analyses. The specific values of the carbon content as well as other coating parameters are also summarized in Table 1. For both the DCMS and HiPIMS processes, coatings with carbon content lower than ~55 at.% exhibited approximately linear increase of the carbon content with increasing acetylene supply and a nearly stable deposition rate. However, approximately 2–3 times higher acetylene flow was required to deposit coatings with the same composition in DCMS as in HiPIMS. The deposition rate of HiPIMS deposited samples was ~20 nm/min, whereas it was ~40 nm/min for DCMS depositions. Significantly lower deposition rate of coatings with the same carbon content deposited in HiPIMS conditions together with higher acetylene supply needed to achieve the same coating composition in DCMS was explained by lower titanium flux onto the coating in HiPIMS depositions compared to DCMS case. Because high discharge current density was reached and maintained for a significant part of the pulse, high ionization of sputtered titanium atoms and their back-attraction to the target can be expected [50]. This agrees well with the available literature, as the deposition rate of metals in HiPIMS is often decidedly lower than in DCMS [34,51,52]. A small reduction of the deposition rate of HiPIMS deposited coatings around 55 at.% of C was observed, similarly as in [34]. Samuelsson et al. [34] also observed that for depositions of TiC/C:H coatings the Ti/C ratio ~ 1 could have been reached at much broader interval of acetylene supplies in HiPIMS than was possible in DCMS process, however opposite behaviour was observed in this work. In our case a much smaller change of the acetylene gas supply was needed to alter the composition of the deposited coating in the HiPIMS process compared to DCMS. Thus such a convenient broadening of the acetylene

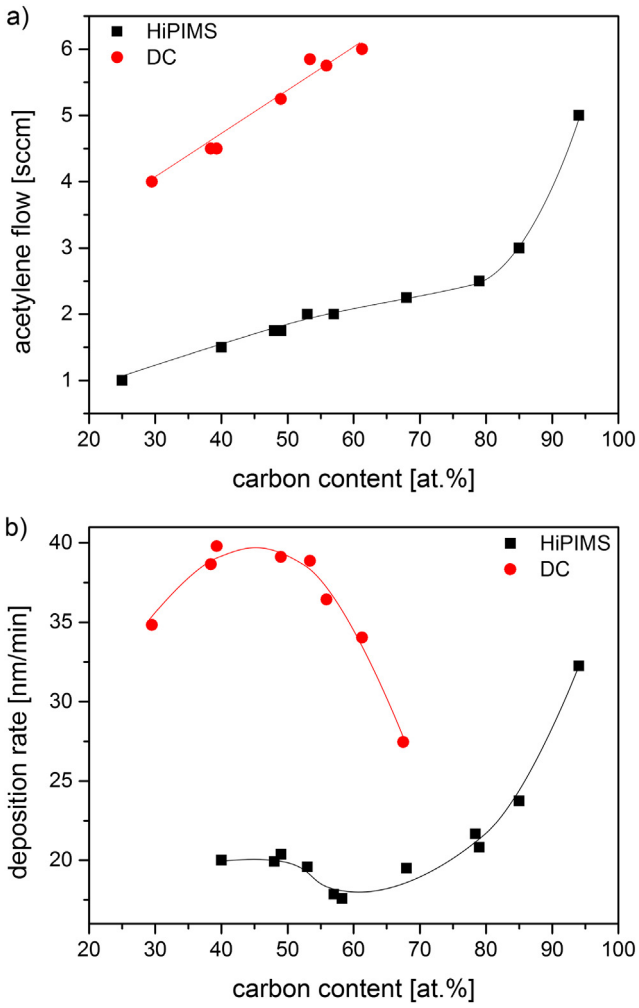

Fig. 2. a) Acetylene flux needed to deposit coatings with specific composition b) Deposition rate of corresponding coatings. Lines are added as guides for the eye.

supply interval as described by Samuelsson et al. [34] is not universal for HiPIMS sputtering of Ti target in argon/acetylene mixture and that such a trend was rather specific for the employed experimental setup and conditions.

Coatings with carbon content higher than ~55 at.% deposited by DCMS also showed a pronounced decrease of the deposition rate with increasing carbon content. In case of reactive magnetron sputtering, similar drop of the deposition rate is being explained by changes of the target state [53,54] which are usually reflected in the evolution of the discharge voltage [55]. Fig. 3 shows the corresponding dependence of the discharge voltage on the carbon content in the coating deposited using hybrid PVD-PECVD process with both the DC and HiPIMS plasma excitation. Whereas the discharge voltage in DCMS is nearly constant for coatings with carbon content lower than 50 at.%, a very shallow minimum at carbon content of ~50 at.% was observed. The hybrid deposition process behaviour and the existence of the local voltage minimum in DC driven process was studied in detail in our previous work and was attributed to the formation of the TiC on the target racetrack [56]. The shallow local minimum was followed by a steep increase of the discharge voltage that was attributed to the formation of the carbon rich layer at the target racetrack [56]. The decrease of the deposition rate at higher carbon contents in the DCMS deposited coatings can be explained by lower flux of the sputtered titanium from the target as the target racetrack got covered by carbon residue which prevented the titanium sputtering. The effect of lower sputtering rate was probably not sufficiently compensated by the increase of carbon flux on the

Table 1
Overview of the deposited coatings.

C [at.%]	Grain size [nm]	Lattice parameter [Å]	a-C phase [%]	Stoichiometry	H [GPa]	E_{eff} [GPa]
DCMS						
30	16	4.276	17.2	0.35	11 ± 1	238 ± 16
38	13	4.293			21 ± 2	261 ± 12
39	14	4.323	26.4	0.48	21 ± 2	279 ± 11
48	15	4.348			28 ± 3	386 ± 18
49	19	4.358	29	0.68	24 ± 2	339 ± 15
53	14	4.363			33 ± 4	326 ± 13
56	15	4.355	25.7	0.94	27 ± 1	254 ± 8
61	8	4.337			33 ± 3	268 ± 27
61	11	4.348	34.8	1.03	27 ± 3	227 ± 13
61	6				29 ± 1	236 ± 6
65	4	4.339			21 ± 3	183 ± 17
68			66.5	0.69		
HiPIMS						
25	20	4.251			12 ± 2	242 ± 20
40	17	4.295	5.8	0.63	32 ± 3	392 ± 12
48	25	4.319			39 ± 3	428 ± 17
49	20	4.318	14.1	0.83	38 ± 3	343 ± 18
53	17	4.322	16.6	0.94	40 ± 3	378 ± 30
57	9	4.313	25.2	0.99	45 ± 4	309 ± 12
68	4		55.4	0.95	32 ± 4	230 ± 12
79	2	4.311	85.3	0.55	20 ± 1	186 ± 6
85	1	4.313	91.9	0.46	20 ± 1	167 ± 3
94					20 ± 1	143 ± 3

coating. Furthermore, with DCMS sputtering it was not possible to prepare coatings with carbon content higher than ~72 at.% because the racetrack got almost completely covered with black carbon residue and significant arcing occurred during the deposition at these conditions. A photograph of the target surface after deposition of coating with 72 at.% is depicted in Fig. 4a. It shows the racetrack to be almost entirely covered by black carbon rich layer.

Fig. 4b shows the target racetrack after HiPIMS deposition process leading to deposition of a coating with 94 at.% C. The whole target exhibited significantly lower amount of carbon contamination than in the case of DCMS. We supposed that strong back attraction of the sputtered and ionized metallic atoms to the target in HiPIMS conditions kept the target surface more metallic and clean of carbon contaminates as compared to DCMS case, where the number of titanium ions is low. This led to postponement of the discharge voltage rise until depositions leading to coatings with ~80 at.% C in HiPIMS were carried out as compared to ~50 at.% for DCMS (see Fig. 3). Before the onset of the voltage rise, the HiPIMS discharge voltage exhibited a decrease when the carbon content was increased from ~55 at.% to 80 at.%. This can be again explained by formation of the TiC on the target racetrack as in the DCMS case, although shifted to higher carbon contents of the coatings.

Using HiPIMS it was possible to perform controlled arc-free depositions of coatings with much higher carbon content than in the DCMS case. Furthermore, the deposition rate in HiPIMS increased for coatings with high carbon content. Similar though less pronounced increase of the deposition rate in HiPIMS sputtering of Ti in argon/acetylene atmosphere was shown by Samuelsson et al. [34]. The increase of the deposition rate at high acetylene fluxes with HiPIMS can be explained by the enhanced chemistry in the plasma utilized by HiPIMS, as the deposition rate of carbon coatings was shown to increase with the number of active carbon species generated in the plasma [57,58].

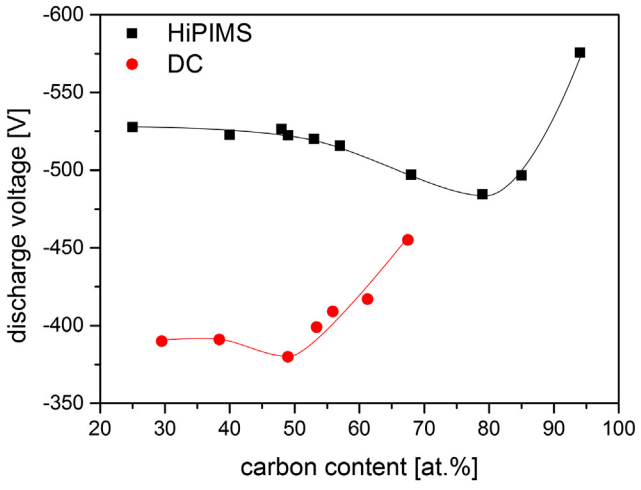

Fig. 3. Steady state discharge voltage for HiPIMS and DC depositions. The onset of the voltage increase is shifted to higher carbon contents for HiPIMS depositions. Lines are added as guides for the eye.

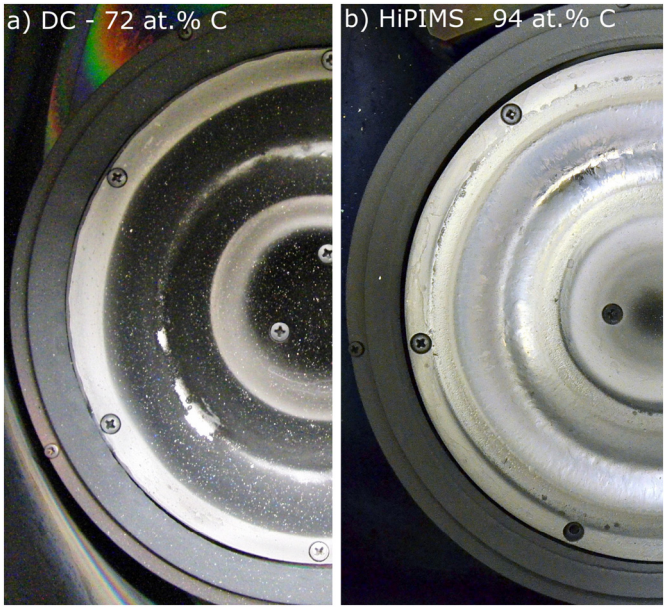

Fig. 4. Target racetrack after deposition for processes leading to coatings with high carbon content a) DC b) HiPIMS. Black carbon residue in the case of DC is present.

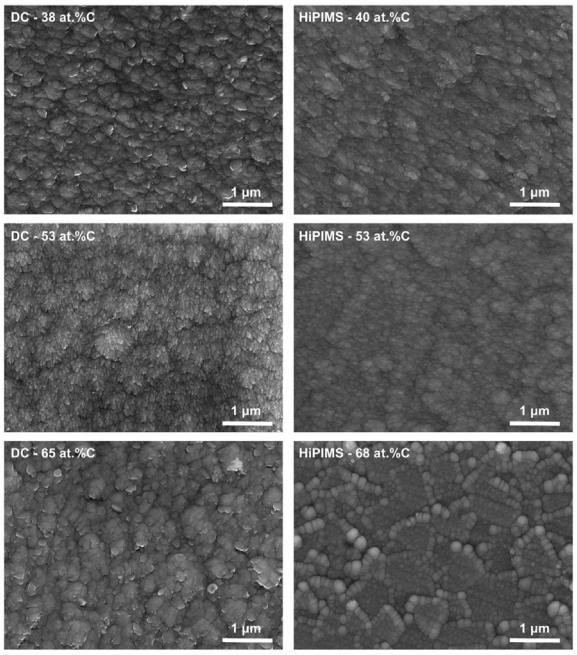

Fig. 5. SEM images of coating surface of coatings with similar composition for DC (left column) and HiPIMS (right column). Surface feature refinement was observed for coatings deposited using HiPIMS.

SEM images of deposited coating surfaces are shown in Fig. 5. DCMS deposited samples are shown in the left column and HiPIMS deposited samples in the right column. Samples with similar carbon content are always compared. Coatings with ~40 at.% C, coatings with ~53 at.% C and coatings with ~65–70 at.% C were selected to demonstrate the evolution of the coating surface morphology. All images were taken with identical magnification of 50 kx and view field of 5.54 μm. There was no appreciable difference between DCMS and HiPIMS deposited coatings with ~40 at.% of carbon. Both exhibited patterned structure with surface features several hundred nanometres in size. DCMS deposited coating with 53 at.% of carbon exhibited larger clusters with the size in the order of hundreds of nanometres with secondary smaller structures with dimensions in the order of tens of nanometres. HiPIMS deposited coating with the same carbon content exhibited significantly more refined structure indicating a denser coating structure. The biggest difference between the DCMS and HiPIMS deposited coatings was observed for coatings with carbon content of ~65 at.%. DCMS deposited coating with 65 at.% carbon content exhibited patterned scaly surface with scales several hundred nanometres in size. HiPIMS deposited coating with 68 at.% C exhibited a very significant refinement of the surface structure size in parts of the substrate surface, but the surface was not homogenous. Larger plains and narrower ledges were present on the sample surface. The size and shape of such plains corresponded well with the size and shape of tungsten carbide grains in the hardmetal substrate and the ledges corresponded with the WC grain boundary filled by a cobalt based matrix. The thickness of the HiPIMS deposited coating was measured to be 2.4 ± 0.2 μm. Thus, the coating surface was significantly affected by the substrate inhomogeneity even for a very thick coating. The inhomogeneous substrate surface profile was probably caused by the preceding mechanical polishing and/or preferential sputtering of the cobalt matrix in the substrate during pre-deposition plasma cleaning. Utilizing of HiPIMS thus led to surface structure refinement especially in samples with higher carbon content, however, the coating surface was affected by the substrate surface inhomogeneity even for >2 μm thick coating.

Comparison of the XRD diffraction patterns for coatings with similar carbon content deposited by DC and HiPIMS is plotted in Fig. 6a and b, respectively. The observed TiC diffractions are labelled with their Miller

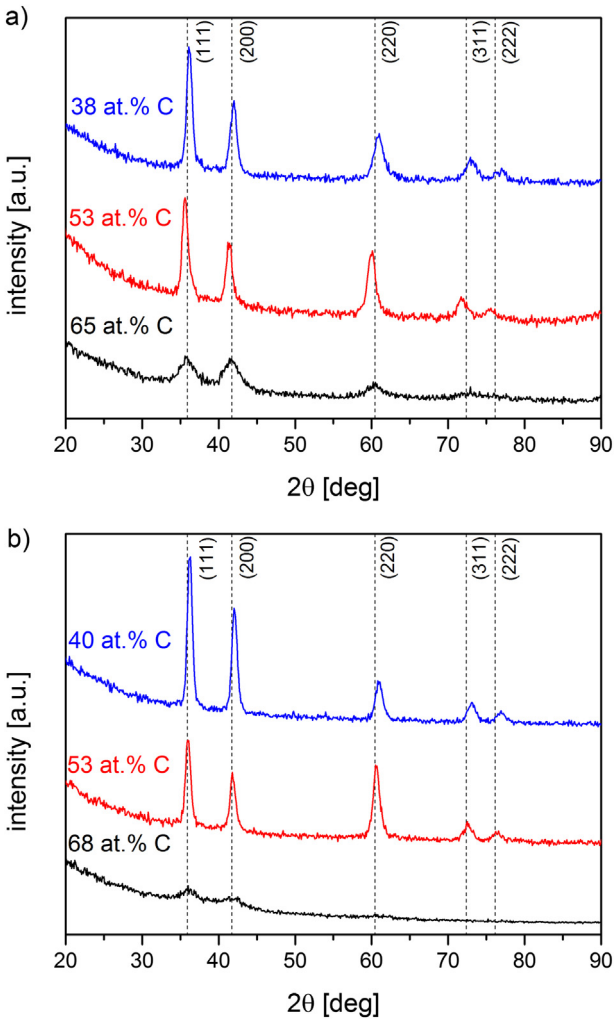

Fig. 6. Comparison of the XRD data for coatings with similar carbon content deposited by a) DC and b) HiPIMS. Reference positions of the TiC diffractions as per PDF card no. 00-032-1383 are plotted as dashed vertical lines.

indices. Reference positions of the TiC diffractions as per PDF card no. 00-032-1383 are plotted as dashed vertical lines. All the measured data exhibited only peaks corresponding to TiC, no diffractions corresponding to metallic hcp Ti were observed in any of the XRD patterns even for coatings with low carbon content. The XRD results are plotted in Fig. 7. The mean TiC crystallite size calculated from the (111) diffraction peak is plotted in Fig. 7a and the lattice parameter in Fig. 7b. The DCMS and HiPIMS deposited samples exhibited similar trends in the mean crystallite size. Coatings with ≤55 at.% C exhibited relatively large TiC grains (10–20 nm). The mean crystallite size was somewhat higher for HiPIMS deposited coatings containing ≤55 at.% C (~18 nm) compared to DC deposited samples (~14 nm). The mean TiC crystallite size decreased with increasing carbon content for the HiPIMS as well as the DCMS deposited coatings with carbon content ≥ 55 at.% C. A decrease of crystallite size with increasing carbon content is typical for nc-TiC/a-C:H coatings prepared by DC magnetron sputtering with carbon content ≥ 50 at.% C [3,9,13,27,28,29], as high amounts of carbon act as crystallite boundary sealant preventing further crystallite growth and instead promote nucleation of higher number of smaller TiC crystallites [3]. Samuelsson et al. [34] observed sharpening of TiC diffraction peaks with increasing carbon content and suggested that in contrast to the DCMS process, the increase of C content in the films did not hinder, but even promoted the TiC grain growth in HiPIMS deposited coatings. Such an effect was not seen in our work as the trends for DCMS and HiPIMS depositions both showed a marked decrease of the crystallite

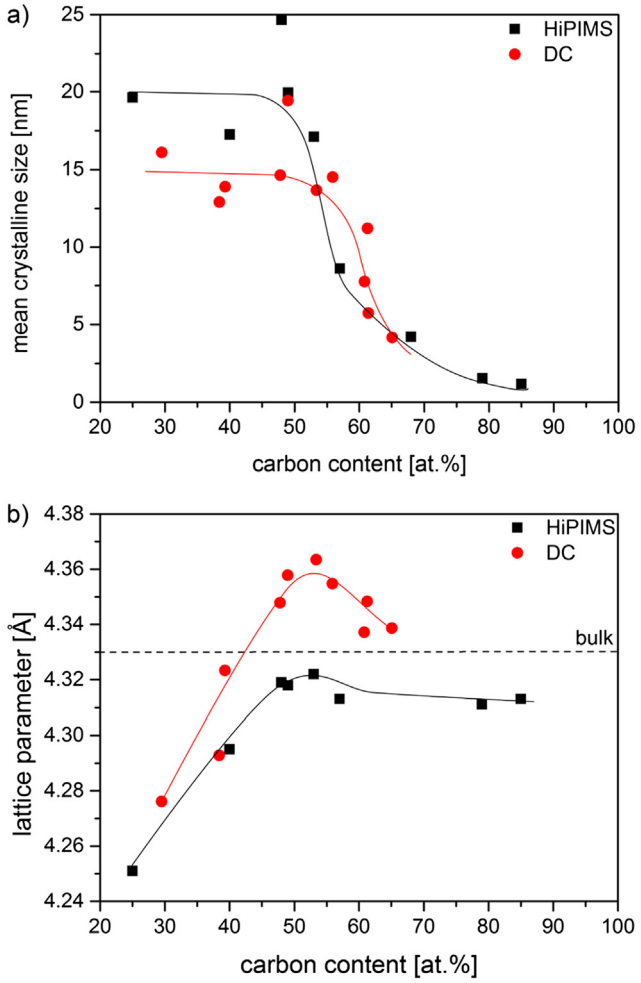

Fig. 7. XRD results: a) mean crystallite size, b) lattice parameter of HiPIMS and DC deposited coatings. Lines are added as guides for the eye.

size with increasing carbon content. The microstrain of the crystallites was analysed by Williamson-Hall plot and it was found out that the DCMS deposited as well as HiPIMS deposited nc-TiC/a-C:H coatings exhibited similar strain of 0.4–0.8%. Thus the grain size calculated by the Scherrer equation is not systematically shifted between the DCMS and HiPIMS samples.

The lattice parameter of the TiC crystallites calculated from the X-ray diffractograms is plotted in Fig. 7b. The value of the lattice parameter of bulk TiC (4.33 Å) was taken from PDF card no.00-031-1400 [59] and is plotted in the graph as a horizontal dashed line for comparison. The lattice parameter was smaller than the bulk value for both the HiPIMS and DCMS depositions for samples with carbon content ≤ 50 at.% probably due to carbon vacancies in the lattice. The lattice parameter increased with increasing carbon content for both DCMS and HiPIMS deposited coatings as the vacancies in the TiC grains were filled with carbon atoms until carbon content of ~55 at.%. When this composition was reached, the lattice parameter stopped to increase for both DCMS and HiPIMS deposited samples. DCMS deposited coatings moreover always exhibited higher lattice parameter than HiPIMS deposited coatings with similar composition. The lower lattice parameter of the TiC grains in nc-TiC/a-C:H coatings deposited using HiPIMS can be correlated to a densification of the crystal structure [60] suggesting a stronger ion bombardment in HiPIMS conditions.

XPS studies were performed to analyse the phase composition of the coatings. An example of a fitted spectra (DCMS deposited coating with 65 at.% C) is plotted in Fig. 8 and shows the C1s peak fitted by its C—C, C—Ti and C—Ti* components [22,34]. C—C bonds corresponded

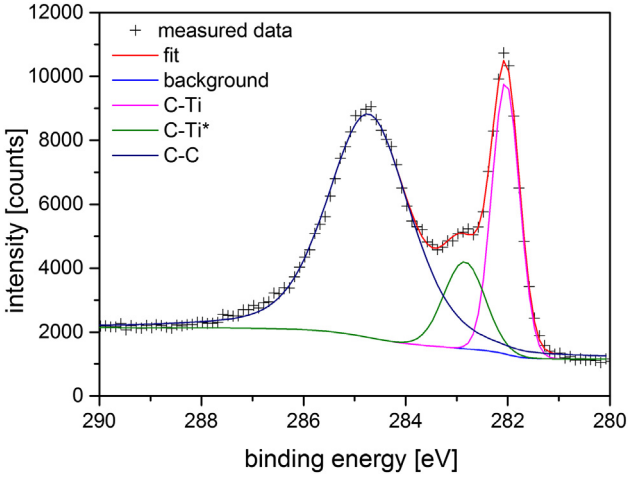

Fig. 8. XPS C1s peak of DC deposited sample with 65 at.% of carbon fitted by its C—C, C—Ti and C—Ti* components.

to peak centred at 285 eV, Ti—C bonds corresponded to the peak located ~282 eV. The middle peak located at ~283 eV corresponded to the so called C—Ti* bonds located on the edge of the TiC grains and the matrix [61]. Fig. 9a and b shows the comparison of the XPS spectra of coatings deposited by DCMS and HiPIMS, respectively. DCMS as well as HiPIMS deposited coatings exhibit increase of the intensity of the C—C peak as

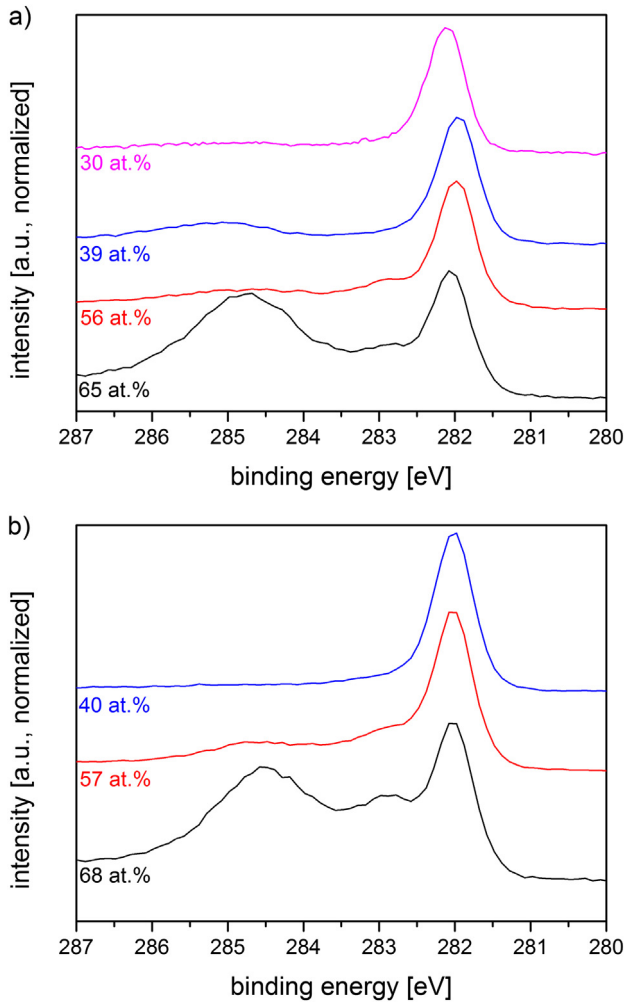

Fig. 9. Comparison of XPS C1s peaks of coatings prepared by a) DC b) HiPIMS.

the carbon content increases, indicating forming of increasing amounts of the a-C:H matrix. Furthermore, the HiPIMS deposited coatings exhibit comparatively less prominent C—C peak corresponding to DCMS deposited coatings with similar carbon content, particularly at lower carbon contents. Fig. 10 shows the plot of the a-C phase content on the total carbon content DC deposited coatings always contained a significant amount of the a-C:H matrix, even for coatings with ≤50 at.% C. The amount of the a-C:H phase slowly increased from ~15 to ~30% with carbon content increase from 29 at.% to 56 at.%. The amount of the a-C matrix was significantly lower for HiPIMS coatings with carbon content ≤ 60 at.%. The amount of the a-C phase was even nearing zero at the lowest carbon contents. For coatings with carbon content ≥ 60 at.%, the amount of a-C matrix significantly increased with increasing carbon content for both the DCMS and HiPIMS deposited coatings. Lower amount of a-C matrix, although in contrast in the whole studied composition range up to ~70 at.% of carbon, was also shown by Samuelsson [62]. The amount of the a-C phase in HiPIMS deposited coatings in the present study is also close to the amount predicted by thermodynamic equations for deposition under thermodynamic equilibrium [62].

The thickness of the matrix separating the individual TiC crystallites (i.e. the mean grain separation) was estimated from the phase ratios and the grain size using a model assuming cube shaped grains [14,30,63] and the density of the a-C:H phase of 2.2 $g \cdot cm^{-3}$ [30]. The resulting mean grain separation as a function of the total carbon content is plotted in Fig.11. Even though the grain size in DCMS deposited coatings was slightly smaller, the DCMS deposited coatings generally exhibited higher mean grain separation, especially for samples with lower carbon content. This was due to much higher fraction of the a-C phase in DCMS deposited coatings. The mean grain separation was increasing only slightly with increasing carbon content for DCMS deposited coatings and was in the interval of 0.75–1.1 nm. The mean grain separation evolved much more for HiPIMS deposited coatings. The mean grain separation was lower than 0.25 nm for sample with 40 at.% C and rose up to 1 nm for sample with 85 at.% C with a much steeper slope than was observed for DCMS deposited samples.

The stoichiometry factor x in TiC_x was estimated from the total carbon and titanium content evaluated by EDX and the TiC and the a-C:H phase ratio acquired by XPS measurements according to equation.

$x = \frac{C\ (at.\%)}{Ti\ (at.\%)} \cdot \frac{A_{C-Ti}}{A_{C-C}+A_{C-Ti}}$, where C (at.%), Ti (at.%) denote the total concentration of carbon and titanium, respectively, A_{C-Ti} denotes the area of the C—Ti and C—Ti* peaks fitted in the C1s XPS spectrum and A_{C-C} denotes the area of the C—C peak in the C1s XPS spectrum. The stoichiometry factor as a function of the total carbon content is plotted in Fig. 12. The stoichiometry factor increased with increasing total carbon content for both the DCMS and HiPIMS cases for coatings with ≤60 at.% of carbon. When the carbon content was lower than the titanium content there was not enough carbon atoms present in the coatings for formation of stoichiometric TiC crystals. Moreover, the amorphous carbon matrix was formed even when the coating contained low amount of carbon (see Fig. 10). Thus, highly sub-stoichiometric TiC_x crystals are formed in coatings with low carbon content. The stoichiometry improved with increasing carbon content as more carbon is available to fill the vacancies in the TiC lattice. Lower amount of amorphous carbon matrix was formed when HiPIMS was utilized for coatings with ≤60 at.% carbon. This resulted in HiPIMS deposited TiC_x crystallites stoichiometry generally exhibiting closer to unity. The TiC_x crystallites reached the highest stoichiometry factor at around 55–60 at.% C for both DCMS and HiPIMS cases. If the total carbon content further increased, the stoichiometry factor of the TiC_x grains decreased. This indicates that for coatings with high amount of carbon, the carbon rather formed the a-C:H matrix phase than the TiC_x phase.

The Raman spectra of the deposited coatings are plotted in Fig. 13. The sp^3/sp^2 hybridization of carbon in the a-C:H matrix was qualitatively estimated from the position of the G peak and intensity ratio of I(D)/I(G) as proposed for a-C films by Ferrari [64] and extended to a-C:H films by Casiraghi et al. [65]. The position of the G peak for all coatings regardless of their carbon content or method of plasma excitation was in the interval of 1555–1575 cm^{-1} and the I(D)/I(G) ratio was within the

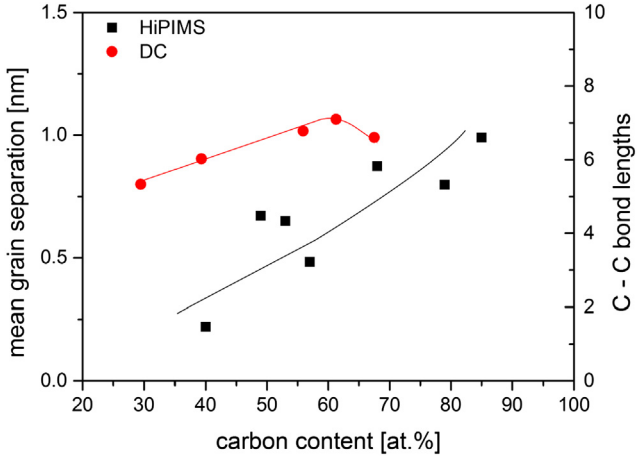

Fig. 11. Mean grain separation in HiPIMS and DC deposited coatings. Lines are added as guides for the eye.

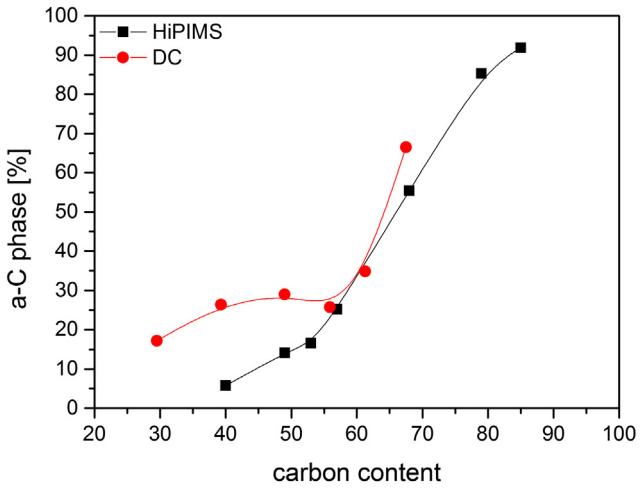

Fig. 10. The a-C phase fraction in HiPIMS and DC deposited coatings. Lines are added as guides for the eye.

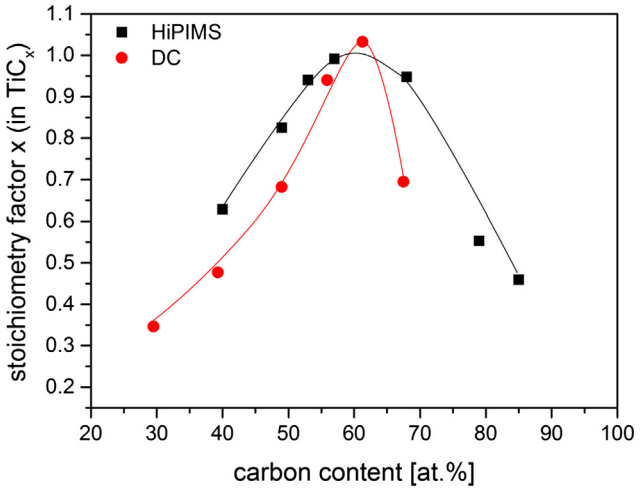

Fig. 12. Stoichiometry of TiC crystallites in HiPIMS and DC deposited coatings. Lines are added as guides for the eye.

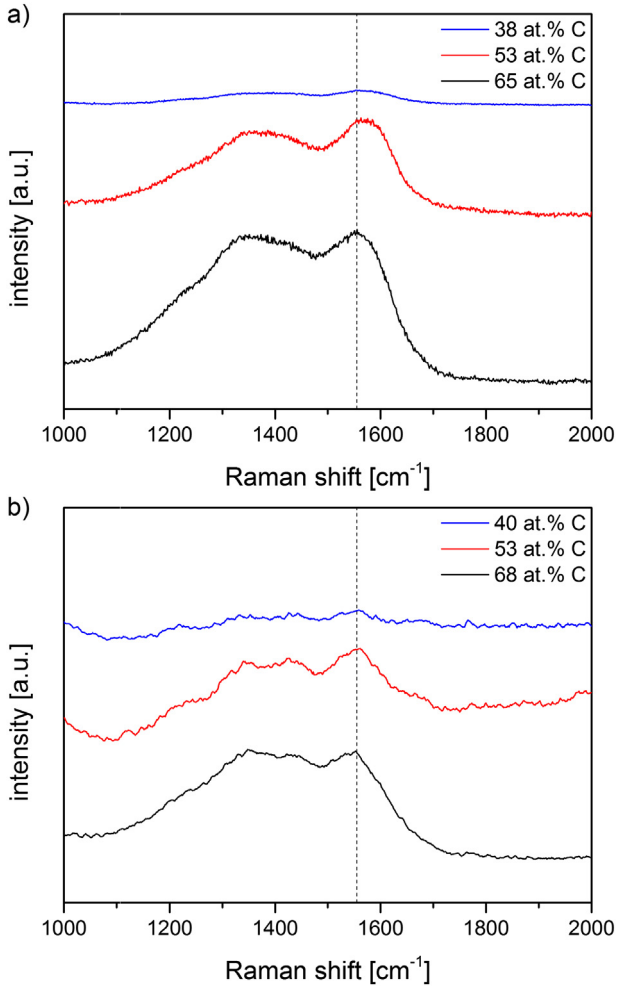

Fig. 13. Comparison of Raman spectra of coatings with similar carbon content prepared by a) DC and b) HiPIMS.

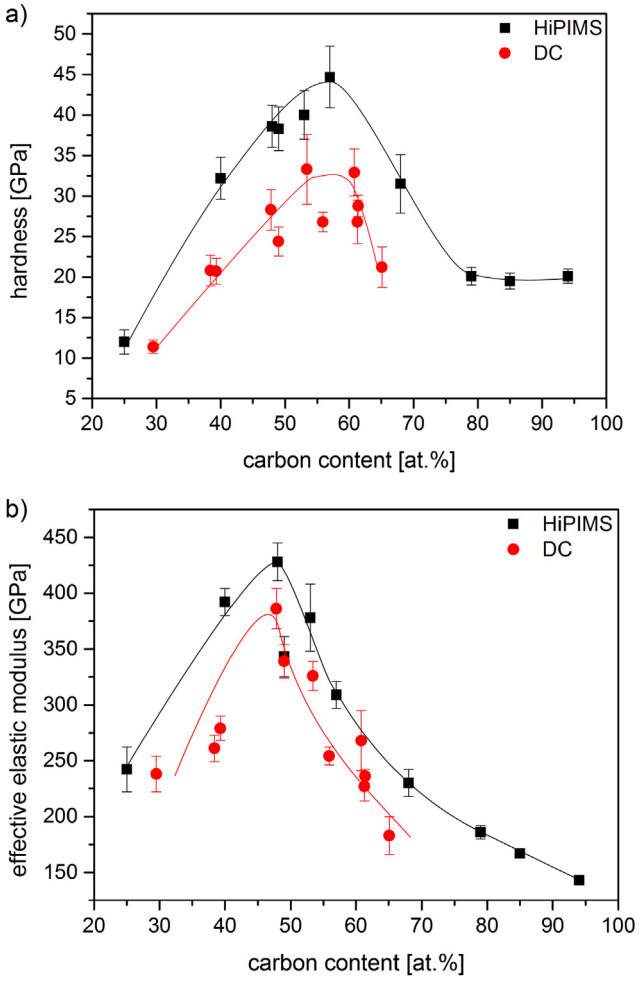

Fig. 14. a) Hardness and b) elastic modulus of HiPIMS and DC deposited coatings. Lines are added as guides for the eye.

interval of 0.6–0.8. Thus, the sp^3 carbon hybridization was estimated to always be lower than ~10%.

The hardness and the effective elastic modulus of the coatings are plotted in Fig. 14a and b, respectively. The trends in hardness were similar for coatings prepared by both DCMS and HiPIMS. The hardness was low for samples with very low carbon content (<15 GPa). As the carbon content increased, the hardness increased correspondingly. This continued up to ~55 at.% carbon, where the hardness was the highest. The highest hardness of 33 ± 4 GPa was achieved in the case of DCMS deposited coatings, whereas the hardness of 45 ± 4 GPa was achieved in the case of HiPIMS deposited coatings. If the amount of carbon was increased even more above 55 at.%, the hardness again significantly decreased. The hardness of coatings with high amount of carbon was 15–20 GPa which is in good accordance with hardness of magnetron sputtered DLC or Ti-DLC coatings [66,67,68]. Although the trend is the same for DCMS and HiPIMS deposited coatings, the hardness of the HiPIMS coatings was shifted to higher values compared to coatings prepared by DCMS in all cases. The elastic modulus exhibited similar trends as the hardness – that is low the relatively values at the lowest carbon content followed by an increase up to ~425 GPa with increasing carbon content continued by a decrease with further carbon increase in carbon content. The highest elastic modulus was obtained for coatings with slightly sub-stoichiometric chemical composition (~48 at.% C). The elastic modulus was generally higher for coatings prepared by HiPIMS, albeit the difference was less pronounced than in the hardness. It has been proposed that the toughness of the material depends on the hardness to elastic modulus ratio H/E, and that the prediction of the wear of the coatings can be based on the resilience of the coating which is defined as the resistance of the material against plastic deformation and relates to the ratio of H^3/E^2 [11,18,69]. Because of significantly higher hardness and only slightly higher elastic modulus, the HiPIMS deposited coatings exhibited also higher values of H/E and H^3/E^2 ratios. The hardest HiPIMS coating with 57 at.% C exhibited H/E ratio of 0.14 and H^3/E^2 ratio of 0.94 GPa, while the hardest DCMS deposited coating with 53 at.% C exhibited lower values of 0.10 and 0.35 GPa, respectively. The highest values of the H/E ratio for nc-TiC/a-C(:H) reported in the literature are usually in the interval of 0.1–0.12 [1,10,26,70]. HiPIMS deposited coatings presented in this work thus exhibited high hardness > 40 GPa, H/E ratio was 30% higher than the highest literature value for coatings with similar composition [71]. The H^3/E^2 ratio was even trebled compared to the highest reported value [10]. Thus superior toughness and resistance to plastic deformation of the HiPIMS deposited nc-TiC/a-C:H coatings are strongly implied.

4. Discussion

The hardness of a nanocomposite coating is given by the properties of the phases forming the nanocomposite and by the properties of the phase interface. In the case of nc-TiC/a-C:H coatings it is the coating structure, the crystallite stoichiometry and size, the mean grain separation, matrix properties and anchoring of the grains in the matrix. The mechanical properties of a nanocomposite can be enhanced due the so-called grain boundary strengthening, i.e. effect similar to the so-called Hall-Petch effect described in polycrystalline materials [72,73].

For this effect to take place, the grain size should be in the size range of 5–10 nm. Furthermore, the grains should be separated by only a single or at most a few monolayers of the matrix. It was shown that a single monolayer of the matrix was optimal for reaching the highest hardness of nanocomposite nc-TiN/a-SiN_x system [74]. The sp^3/sp^2 bonding in the matrix might also play a role as carbon based coatings with higher sp^3 content generally exhibit higher hardness [75,76]. The macrostructure of the coatings influences the mechanical properties of the coatings as well, as it has been shown that coatings with glassy structure exhibit higher hardness and elastic modulus than coatings with columnar structure [6,71].

The properties of the hardest coatings deposited by DCMS and HiPIMS are compared in Table 2. Two samples in the DCMS experiments are listed as both exhibited the same hardness within the margin of error. One of the DCMS prepared samples contained 53 at.% C and the other 61 at.% C. The surface topography of the coating with carbon content of 53 at.% and hardness of 33.3 GPa was coarse, indicating columnar macrostructure with column width of 600–700 nm. The lattice parameter was 0.7% larger than the equilibrium value, indicating less dense structure of the grains. The TiC_x grains were ~14 nm large, the stoichiometric factor was 0.9 and the grains were separated by ~1 nm of the matrix phase. Considering that the average C—C bond length in amorphous carbon is in the range of 0.143–0.152 nm [75], the mean grain separation corresponded to ~5–6 bond lengths, approximately corresponding to the same number monolayers of the matrix. The grain strain was similar in DCMS and HiPIMS deposited coatings. The content of the sp^3 C—C bonding in the a-C:H matrix was approximately 5–10%. The mean grain separation, the macrostructure and the sp^3/sp^2 bond ratio in the matrix were similar in both hardest samples. However, the grain size in the sample containing 61 at.% C decreased to 8 nm and the lattice parameter was only 0.2% larger than the equilibrium value. Also the stoichiometry factor was increased to 0.95. Despite this, the hardness was not significantly affected. Thus the mean grain separation, the macrostructure and low sp^3 bond content in the matrix seem to be the limiting factors for achieving higher hardness in DC driven process.

Decreasing the amount of carbon in the DCMS deposited coatings below the optimum interval, i.e. below 53 at.% C, led to no significant change of the surface topography and the grain size also stayed approximately the same. The sp^3/sp^2 ratio of the C—C bonds in the matrix was not significantly changed. The mean grain separation decreased to ~4–5 monolayers. However, the stoichiometry factor of the TiC_x grains decidedly decreased. The hardness decreased as the effect of smaller mean grain separation was overshadowed by the loss of TiC_x grain stoichiometry. On the other hand, carbon content increase above 61 at.% led to a fast drop of the TiC_x grain size below the value optimal for grain boundary strengthening. The stoichiometry factor of the grains decreased and the mean grain separation notably increased. Consequently, the hardness of the coatings decreased due to adverse effects of bad stoichiometry, possible inverse Hall-Petch effect [77] and grain sliding [78,79].

Thus in order to reach higher hardness, the macrostructure should be refined, the crystals should be made denser and should be separated by lower number of a-C:H matrix layers. The stoichiometry of the TiC_x grains should be maintained or increased. Using DC driven plasma deposition process it is not possible to optimize the structure of the nc-TiC/a-C:H coatings for achieving hardness higher than 33 GPa.

The hardest coating prepared by HiPIMS contained 57 at.% of C and thus exhibited similar carbon content as the hardest samples prepared by DCMS. The TiC_x grain size is comparable to that of the samples prepared by DCMS and the sp^3 bond ratio also did not significantly change. However, the stoichiometry factor was slightly increased to 0.99, the lattice parameter was 0.7% smaller than the equilibrium bulk value, indicating denser structure of the crystals, the mean grain separation decreased to 3–4 monolayers of the a-C:H matrix and the surface topography was decidedly refined indicating a denser macrostructure. This structure refinement led to the hardness of 44.7 GPa which is an increase of 33%. As the grain size was not refined compared to DCMS case and the grain stoichiometry was improved only very slightly, the crystallite density, the mean grain separation and the macrostructure were the most important parameters responsible for the hardness enhancement.

Decreasing the carbon content below 53 at.% as well as increasing it above 57 at.% had similar effects on the coating structure as in DCMS case. However, the HiPIMS deposited coatings always exhibited grain stoichiometry closer to unity, lower mean grain separation, finer macrostructure and lower lattice parameter than their DCMS deposited counterparts. This resulted in overall higher hardness of the HiPIMS deposited nc-TiC/a-C:H coatings.

5. Conclusion

Nanocomposite nc-TiC/a-C:H coatings were deposited with the same mean power utilizing DC magnetron sputtering and HiPIMS in argon/acetylene atmosphere. The deposition rate was lower in HiPIMS, however it increased at higher acetylene flows where DCMS process was unstable. Significantly lower acetylene flow was needed to produce coatings with similar total carbon content in HiPIMS compared to DCMS. It was also shown that HiPIMS employment was highly advantageous for controlled and repeatable deposition of nc-TiC/a-C:H coatings with high carbon content. Even though HiPIMS discharge with a relatively long pulse length is generally prone to arc occurrence due to impurities or debris on the cathode, no such behaviour was observed. Whereas the total carbon content in DCMS deposited samples was limited to ≲70 at.% due to poisoning processes on the titanium target, coatings with carbon contents of ≳90 at.% were possible to be deposited by HiPIMS.

HiPIMS deposited coatings exhibited similar sized grains as DCMS but with exhibited lower lattice parameter and a finer surface structure. Utilization of HiPIMS also favoured carbon incorporation into the TiC_x grains as HiPIMS deposited coatings exhibited stoichiometry factor of the TiC_x grains closer to unity and lower fraction of the a-C matrix. This corresponded to a smaller mean grain separation of the TiC_x grains by the a-C matrix in HiPIMS deposited coatings. This was attributed to higher ion bombardment and thus higher energy influx to the growing film inherent to the HiPIMS process. TiC_x grain stoichiometry factor closer to density and higher grain density combined with lower mean grain separation and macrostructure refinement led to overall higher hardness of HiPIMS deposited coatings. The mean grain separation, TiC_x grain density and the macrostructure were found to play the key role in hardness enhancement of the HiPIMS deposited nc-TiC/a-C:H coatings. H/E and H^3/E^2 ratios were substantially higher for HiPIMS deposited coatings indicating enhanced toughness and tribological properties. Thus HiPIMS can be successfully used to influence the growth conditions of nc-TiC/a-C:H coatings in order to alter the microstructure in a way favourable for achieving enhanced mechanical properties.

Table 2
Comparison of the hardest coatings deposited by DC and HiPIMS.

	H [GPa]	C [at.%]	Crystallite size [nm]	Lattice parameter [Å]	Stoichiometry	Mean grain separation [nm]	Macrostructure
DC	33 ± 4	53	14 ± 2	4.363 ± 0.001	0.90	1	Coarse
	32.9 ± 3	61	8 ± 1	4.337 ± 0.001	0.95	1	Coarse
HiPIMS	45 ± 4	57	9 ± 1	4.313 ± 0.001	0.99	0.5	Fine

Acknowledgment

This research has been supported by project LO1411 (NPU I) funded by Ministry of Education, Youth and Sports of Czech Republic.

References

[1] A. Czyzniewski, W. Precht, Deposition and some properties of nanocrystalline, nanocomposite and amorphous carbon-based coatings for tribological applications, J. Mater. Process. Technol. 157–158 (2004) 274–283.
[2] Y. Wang, X. Zhang, X. Wu, H. Zhang, X. Zhang, Compositional, structural and mechanical characteristics of nc-TiC/a-C:H nanocomposite films, Appl. Surf. Sci. 255 (2008) 1801–1805.
[3] T. Zehnder, J. Patscheider, Nanocomposite TiC/a-C:H hard coatings deposited by reactive PVD, Surf. Coat. Technol. 133–134 (2000) 138–144.
[4] P. Souček, T. Schmidtová, L. Zábranský, V. Buršíková, P. Vašina, O. Caha, J. Buršík, V. Peřina, R. Mikšová, Y.T. Pei, J.T.M. De Hosson, On the control of deposition process for enhanced mechanical properties of nc-TiC/a-C:H coatings with DC magnetron sputtering at low or high ion flux, Surf. Coat. Technol. 255 (2014) 8–14.
[5] J. Musil, P. Novák, R. Čerstvý, Z. Soukup, Tribological and mechanical properties of nanocrystalline-TiC/a-C nanocomposite thin films, J. Vac. Sci. Technol. A 28 (2010) 244–249.
[6] Y.T. Pei, D. Galvan, J.T.M. De Hosson, C. Strondl, Advanced TiC/a-C:H nanocomposite coatings deposited by magnetron sputtering, J. Eur. Ceram. Soc. 26 (2006) 565–570.
[7] P. Souček, T. Schmidtová, V. Buršíková, P. Vašina, Y.T. Pei, J.T.M. De Hosson, O. Caha, V. Peřina, R. Mikšová, P. Malinský, Tribological properties of nc-TiC/a-C:H coatings prepared by magnetron sputtering at low and high ion bombardment of the growing film, Surf. Coat. Technol. 241 (2014) 64–73.
[8] J.C. Sánchez-López, D. Martínez-Martínez, C. López-Cartes, A. Fernández, Tribological behaviour of titanium carbide/amorphous carbon nanocomposite coatings: from macro to the micro-scale, Surf. Coat. Technol. 202 (2008) 4011–4018.
[9] D. Martínez-Martínez, C. López-Cartes, A. Fernández, J.C. Sánchez-López, Influence of the microstructure on the mechanical and tribological behavior of TiC/a-C nanocomposite coatings, Thin Solid Films 517 (2009) 1662–1671.
[10] C.Q. Chen, Y.T. Pei, K.P. Shaha, J.T.M. De Hosson, Nanoscale deformation mechanism of TiC/a-C nanocomposite thin films, J. Appl. Phys. 105 (2009) 114314.
[11] J. Lin, J.J. Moore, B. Mishra, M. Pinkas, W.D. Sproul, Syntheses and characterization of TiC/a:C composite coatings using pulsed closed field unbalanced magnetron sputtering (P-CFUBMS), Thin Solid Films 517 (2008) 1131–1135.
[12] Y.T. Pei, C.Q. Chen, K.P. Shaha, J.T.M. De Hosson, J.W. Bradley, S.A. Voronin, M. Čada, Microstructural control of TiC/a-C nanocomposite coatings with pulsed magnetron sputtering, Acta Mater. 52 (2008) 696–709.
[13] S. Zhang, X.L. Bui, J. Jiang, X. Li, Microstructure and tribological properties of magnetron sputtered nc-TiC/a-C nanocomposite, Surf. Coat. Technol. 198 (2005) 206–211.
[14] E. Lewin, O. Wilhelmsson, U. Jansson, Nanocomposite nc-TiC/aC thin films for electrical contact applications, J. Appl. Phys. 100 (2006), 054303.
[15] U. Wiklund, M. Nordin, O. Wänstrand, M. Larsson, Evaluation of a flexible physical vapor deposited TiC–C coating system, Surf. Coat. Technol. 124 (2000) 154–161.
[16] A.A. Voevodin, J.S. Zabinski, Load-adaptive crystalline–amorphous nanocomposites, J. Mater. Sci. 33 (1998) 319–327.
[17] A.A. Voevodin, S.V. Prasad, J.S. Zabinski, Nanocrystalline carbide/amorphous carbon composites, J. Appl. Phys. 82 (1997) 855–858.
[18] Y.T. Pei, D. Galvan, J.T.M. De Hosson, A. Cavaleiro, Nanostructured TiC/a-C coatings for low friction and wear resistant applications, Surf. Coat. Technol. 198 (2005) 44–50.
[19] M. Stüber, H. Leiste, S. Ulrich, H. Holleck, D. Schild, Microstructure and properties of low friction TiC–C nanocomposite coatings deposited by magnetron sputtering, Surf. Coat. Technol. 150 (2002) 218–226.
[20] A. Mani, P. Aubert, F. Mercier, H. Khodja, C. Berthier, P. Houdy, Effects of residual stress on the mechanical and structural properties of TiC thin films grown by RF sputtering, Surf. Coat. Technol. 194 (2005) 190–195.
[21] W.J. Meng, R.C. Tittsworth, L.E. Rehn, Mechanical properties and microstructure of TiC/amorphous hydrocarbon nanocomposite coatings, Thin Solid Films 377–378 (2000) 222–232.
[22] A.A. El Mel, B. Angleraud, E. Gautron, A. Granier, P.Y. Tessier, Microstructure and composition of TiC/a-C:H nanocomposite thin films deposited by a hybrid IPVD/PECVD process, Surf. Coat. Technol. 204 (2010) 1880–1883.
[23] V. Kulikovsky, A. Tarasenko, F. Fendrych, L. Jastrabik, D. Chvostova, F. Franc, L. Soukup, The mechanical, tribological and optical properties of Ti-C:H coatings, prepared by DC magnetron sputtering, Diam. Relat. Mater. 7 (1998) 774–778.
[24] V. Kulikovsky, P. Bohac, F. Franc, D. Chvostova, A. Deineka, V. Vorlicek, L. Jastrabik, Degradation and stress evolution in a-C, a-C:H and Ti-C:H films, Surf. Coat. Technol. 142-144 (2001) 702–706.
[25] D. Galvan, Y.T. Pei, J.T.M. De Hosson, Reactive magnetron sputtering deposition and columnar growth of nc-TiC/a-C:H nanocomposite coatings, J. Vac. Sci. Technol. A 24 (2006) 1441–1447.
[26] Y.T. Pei, D. Galvan, J.T.M. De Hosson, Nanostructure and properties of TiC/a-C:H composite coatings, Acta Mater. 53 (2005) 4505–4521.
[27] W. Gulbiński, S. Mathurb, H. Shen, T. Suszko, A. Gilewicz, B. Warcholiński, Evaluation of phase, composition, microstructure and properties in TiC/a-C:H thin films deposited by magnetron sputtering, Appl. Surf. Sci. 239 (2005) 302–310.
[28] D. Galvan, Y.T. Pei, J.T.M. De Hosson, Influence of deposition parameters on the structure and mechanical properties of nanocomposite coatings, Surf. Coat. Technol. 201 (2006) 590–598.
[29] Y. Hu, L. Li, X. Cai, Q. Chen, P.K. Chu, Mechanical and tribological properties of TiC/amorphous hydrogenated carbon composite coatings fabricated by DC magnetron sputtering with and without sample bias, Diam. Relat. Mater. 16 (2007) 181–186.
[30] T. Zehnder, P. Schwaller, F. Munnik, S. Mikhailov, J. Patscheider, Nanostructural and mechanical properties of nanocomposite nc-TiC/a-C:H films deposited by reactive unbalanced magnetron sputtering, J. Appl. Phys. 95 (8) (2004) 4327–4334.
[31] P. Souček, T. Schmidtová, L. Zábranský, V. Buršíková, P. Vašina, O. Caha, M. Jílek, A.A. El Mel, P.Y. Tessier, J. Schäfer, J. Buršík, V. Peřina, R. Mikšová, Evaluation of composition, mechanical properties and structure of nc-TiC/a-C:H coatings prepared by balanced magnetron sputtering, Surf. Coat. Technol. 211 (2012) 111–116.
[32] F. Amato, N.R. Panyala, P. Vašina, P. Souček, J. Havel, Laser desorption ionisation quadrupole ion trap time-of-flight mass spectrometry of titanium-carbon thin films, Rapid Commun. Mass Spectrom. 27 (2013) 1196–1202.
[33] Y.T. Pei, K.P. Shaha, C.Q. Chen, R. van der Hulst, A.A. Turkin, D.I. Vainsthein, J.T.M. De Hosson, Growth of nanocomposite films: from dynamic roughening to dynamic smoothening, Acta Mater. 57 (2009) 5156–5164.
[34] M. Samuelsson, K. Sarakinos, H. Högberg, E. Lewin, U. Jansson, B. Wälivaara, H. Ljungcrantz, U. Helmersson, Growth of Ti-C nanocomposite films by reactive high power impulse magnetron sputtering under industrial conditions, Surf. Coat. Technol. 206 (2012) 2396–2402.
[35] M. Balzer, M. Fenker, Three-dimensional thickness and property distribution of TiC films deposited by DC magnetron sputtering and HIPIMS, Surf. Coat. Technol. 250 (2014) 37–43.
[36] V. Kouznetsov, K. Macak, J.M. Schneider, U. Helmersson, I. Petrov, A novel pulsed magnetron sputter technique utilizing very high target power densities, Surf. Coat. Technol. 122 (1999) 290–293.
[37] U. Helmersson, M. Lattemann, J. Bohlmark, A.P. Ehiasarian, J.T. Gudmundsson, Ionized physical vapor deposition (IPVD): a review of technology and applications, Thin Solid Films 513 (2006) 1–24.
[38] K. Sarakinos, J. Alami, S. Konstantinidis, High power pulsed magnetron sputtering: a review on scientific and engineering state of the art, Surf. Coat. Technol. 204 (2010) 1661–1684.
[39] A. Anders, Discharge physics of high power impulse magnetron sputtering, Surf. Coat. Technol. 205 (2011) S1–S9.
[40] D.V. Mozgrin, I.K. Fetisov, G.V. Khodachenko, High-current low-pressure quasi-stationary discharge in a magnetic field: experimental research, Plasma Phys. Rep. 21 (5) (1995) 400–409.
[41] K. Macák, V. Kouznetsov, J. Schneider, U. Helmersson, I. Petrov, Ionized sputter deposition using an extremely high plasma density pulsed magnetron discharge, J. Vac. Sci. Technol. A 18 (2000) 1533–1537.
[42] J. Bohlmark, M. Lattemann, J. Gudmundsson, A. Ehiasarian, Y. Arandagonzalvo, N. Brenning, U. Helmersson, The ion energy distributions and ion flux composition from a high power impulse magnetron sputtering discharge, Thin Solid Films 515 (2006) 1522–1526.
[43] J. Benedikt, R.V. Woen, S.L.M. van Mensfoort, V. Perina, J. Hong, M.C.M. van de Sanden, Plasma chemistry during the deposition of a-C:H films and its influence on film properties, Diam. Relat. Mater. 12 (2003) 90–97.
[44] J. Musil, S. Kadlec, J. Vyskočil, V. Poulek, Reactive deposition of hard coatings, Surf. Coat. Technol. 39–40 (1989) 301–314.
[45] J. Patscheider, T. Zehnder, M. Diserens, Structure-performance relations in nanocomposite coatings, Surf. Coat. Technol. 146–147 (2001) 201–208.
[46] F. Piazza, A. Golanski, S. Schulze, G. Relihan, Transpolyacetylene chains in hydrogenated amorphous carbon films free of nanocrystalline diamond, Appl. Phys. Lett. 3 (2003) 358–360.
[47] A.C. Ferrari, J. Robertson, Resonant Raman spectroscopy of disordered, amorphous, and diamondlike carbon, Phys. Rev. B 64 (2001), 075414.
[48] W.C. Oliver, G.M. Pharr, Measurement of hardness and elastic modulus by instrumented indentation: advances in understanding and refinements to methodology, J. Mater. Res. 19 (2004) 3–20.
[49] P. Vašina, P. Souček, T. Schmidtová, M. Eliáš, V. Buršíková, M. Jílek, M. Jílek Jr., J. Schäfer, J. Buršík, Depth profile analyses of nc-TiC/a-C:H coating prepared by balanced magnetron sputtering, Surf. Coat. Technol. 205 (2011) S53–S56.
[50] D.J. Christie, Target material pathways model for high power pulsed magnetron sputtering, J. Vac. Sci. Technol. A 23 (2005) 330–335.
[51] A. Anders, Deposition rates of high power impulse magnetron sputtering: physics and economics, J. Vac. Sci. Technol. A 28 (2010) 783–790.
[52] J. Čapek, M. Hála, O. Zabeida, J.E. Klemberg-Sapieha, L. Martinů, Deposition rate enhancement in HiPIMS without compromising the ionized fraction of the deposition flux, J. Phys. D. Appl. Phys. 46 (2013), 205205. (10 pp.).
[53] S. Berg, H.-O. Blom, T. Larsson, C. Nender, Modeling of reactive sputtering of compound materials, J. Vac. Sci. Technol. A 5 (1987) 202–207.
[54] S. Berg, T. Nyberg, Fundamental understanding and modeling of reactive sputtering processes, Thin Solid Films 476 (2005) 215–230.
[55] D. Depla, G. Buyle, J. Haemer, R. DeGryse, Discharge voltage measurements during magnetron sputtering, Surf. Coat. Technol. 200 (2006) 4329–4338.
[56] T. Schmidtová, P. Souček, V. Kudrle, P. Vašina, Non-monotonous evolution of hybrid PVD–PECVD process characteristics on hydrocarbon supply, Surf. Coat. Technol. 232 (2013) 283–289.
[57] G. Fedosenko, A. Schwabedissen, J. Engemann, E. Braca, L. Valentini, J.M. Kenny, Pulsed PECVD deposition of diamond-like carbon films, Diam. Relat. Mater. 11 (2002) 1047–1052.
[58] N. Ravi, V.L. Bukhovets, I.G. Varshavskaya, G. Sundararajan, Deposition of diamond-like carbon films on aluminium substrates by RF-PECVD technique: influence of process parameters, Diam. Relat. Mater. 16 (2007) 90–97.

[59] M.C. Morris, H.F. McMurdie, E.H. Evans, B. Paretzkin, H.S. Parker, N.C. Panagiotopoulos, C.R. Hubbard, Standard X-ray Diffraction Powder Patterns: Section 18 — Data for 58 Substances, NBS, Washington, 1981.
[60] D. Binder, W.J. Sturm, Equivalence of X-ray lattice parameter and density changes in neutron-irradiated LiF, Phys. Rev. 96 (1954) 1519–1522.
[61] E. Lewin, P.O.Å. Persson, M. Lattemann, M. Stüber, M. Gorgoi, A. Sandell, C. Ziebert, F. Schäfers, W. Braun, J. Hallbirter, S. Ulrich, W. Eberhardt, L. Hultman, H. Siegbahn, S. Svensson, U. Jansson, On the origin of a third spectral component of C1s XPS-spectra for nc-TiC/a-C nanocomposite thin films, Surf. Coat. Technol. 202 (2008) 3563–3570.
[62] M. Samuelsson, Fundamental Aspects of HiPIMS Under Industrial Conditions(Dissertation No. 1461) Linköping University, Sweden, 2012.
[63] U. Jansson, E. Lewin, Sputter deposition of transition-metal carbide films — a critical review from a chemical perspective, Thin Solid Films 536 (2013) 1–24.
[64] A.C. Ferrari, Determination of bonding in diamond-like carbon by Raman spectroscopy, Diam. Relat. Mater. 11 (2002) 1053–1061.
[65] C. Casiraghi, A.C. Ferrari, J. Robertson, Raman spectroscopy of hydrogenated amorphous carbons, Phys. Rev. B 72 (2005), 085401.
[66] X.L. Bui, Y.T. Pei, J.T.M. De Hosson, Magnetron reactively sputtered Ti-DLC coatings on HNBR rubber: the influence of substrate bias, Surf. Coat. Technol. 202 (2008) 4939–4944.
[67] K. Yamamoto, K. Matsukado, Effect of hydrogenated DLC coating hardness on the tribological properties under water lubrication, Tribol. Int. 39 (2006) 1609–1614.
[68] S. Zhang, X.L. Bui, Y. Fu, Magnetron sputtered hard a-C coatings of very high toughness, Surf. Coat. Technol. 167 (2003) 137–142.
[69] A. Leyland, A. Matthews, On the significance of the H/E ratio in wear control: a nanocomposite coating approach to optimised tribological behaviour, Wear 246 (2000) 1–11.
[70] D.M. Cao, B. Feng, W.J. Meng, L.E. Rehn, P.M. Baldo, M.M. Khonsari, Friction and wear characteristics of ceramic nanocomposite coatings: titanium carbide/amorphous hydrocarbon, Appl. Phys. Lett. 3 (2001) 329–331.
[71] K.P. Shaha, Y.T. Pei, D. Martínez-MArtínez, J.C. Sánchez-López, J.T.M. De Hosson, Effect of process parameters on mechanical and tribological performance of pulsed-DC sputtered TiC/a-C:H nanocomposite films, Surf. Coat. Technol. 205 (2010) 2633–2642.
[72] E.O. Hall, The deformation and aging of mild steel: III discussion of results, Proc. Phys. Soc. London B 64 (1951) 747–753.
[73] N.J. Petch, The cleavage strength of polycrystals, J. Iron Steel Inst 174 (1953) 25–28.
[74] S. Veprek, R.F. Zhang, M.G.J. Veprek-Heijman, S.H. Sheng, A.S. Argon, Superhard nanocomposites: origin of hardness enhancement, properties and applications, Surf. Coat. Technol. 204 (2010) 1898–1906.
[75] J. Robertson, Diamond-like amorphous carbon, Mater. Sci. Eng. R 37 (2002) (2002) 129–137.
[76] P. Písařík, M. Jelínek, T. Kocourek, J. Remsa, J. Zemek, J. Lukeš, J. Šepitka, Influence of diamond and graphite bonds on mechanical properties of DLC thin films, J. Phys. Conf. Ser. 594 (2015), 012008. (6 pp.).
[77] C.E. Carlton, P.J. Ferreira, What is behind the inverse Hall–Petch effect in nanocrystalline materials? Acta Mater. 55 (2007) 3749–3756.
[78] J. Schiotz, F.D. Di Tolla, K.W. Jacobsen, Softening of nanocrystalline metals at very small grain sizes, Nature 391 (1998) 561–563.
[79] Z.W. Shan, E.A. Stach, J.M.K. Wiezorek, J.A. Knapp, D.M. Follstaedt, S.X. Mao, Grain boundary-mediated plasticity in nanocrystalline nickel, Science 305 (2004) 654–657.

Hindawi
Journal of Nanomaterials
Volume 2017, Article ID 6368927, 13 pages
https://doi.org/10.1155/2017/6368927

Research Article

Investigation of the Influence of Ni Doping on the Structure and Hardness of Ti-Ni-C Coatings

J. Daniel, P. Souček, K. Bernátová, L. Zábranský, M. Stupavská, V. Buršíková, and P. Vašina

Department of Physical Electronics, Faculty of Science, Masaryk University, Kotlarska 2, 611 37 Brno, Czech Republic

Correspondence should be addressed to P. Vašina; vasina@physics.muni.cz

Received 31 January 2017; Revised 16 April 2017; Accepted 30 May 2017; Published 6 July 2017

Academic Editor: Albano Cavaleiro

Nanocomposite nc-TiC/a-C:H thin films exhibit unique combination of mechanical properties, high hardness, low friction, and wear. Selective doping by weak-carbide forming element can be used in order to specifically design the physical and chemical properties of nc-TiC/a-C:H coatings. In this paper we report on an effect of nickel addition on structure and hardness of the nc-TiC/a-C:H coatings. The effect of Ni alloying on the coating structure under conditions of DCMS and HiPIMS depositions was studied. The coating structure was correlated with the coating hardness. The grain size, the grain carbon vacancy concentration, and the mean grain separation were found to be the key parameters determining the coating hardness. Ni doping proved to have a significant effect on the coating microstructure which resulted in changes of the hardness of the deposited coatings.

1. Introduction

Nanocomposite transition metal carbide based coating systems have been systematically studied because of advantageous combination of their physical, chemical, and mechanical properties such as high hardness, high wear resistance, low friction coefficient, and good thermal stability. This nanocomposite structure consists of hard nanocrystalline metal carbide grains surrounded by amorphous carbon phase. One of the most widely studied transition metal carbide nanocomposite systems, denoted as nc-TiC/a-C:H, consists of nanocrystalline TiC grains embedded in an amorphous hydrogenated carbon matrix [1]. The nc-TiC/a-C:H coatings with high hardness [2–15] or with low coefficient of friction and wear [16–19] were described in the literature. The synthesis of hydrogenated nc-TiC/a-C:H nanocomposites is generally performed utilizing a hybrid PVD-PECVD process of sputtering of titanium target in hydrocarbon containing plasma. This process was described in detail in [20].

To further enhance the mechanical properties of titanium and carbon based coatings, a strategy utilizing doping of the coatings by a non-carbine forming element such as nickel was proposed [21]. If nickel is introduced in specific quantities under specific deposition conditions, nickel can be incorporated into the Ti-C grains and therefore metastable Ti-Ni-C grains embedded in carbon matrix can be formed [22]. It was calculated that Ti-Ni-C/a-C system with ≥25% of Ni can transit to a more thermodynamically favorable state: the metastable grains will release carbon to the amorphous phase. This effect can result in changes of the coatings structure and thus in their mechanical properties [22]. Jansson et al. prepared nanocomposite Ti-Ni-C coatings with constant [Ni]/[Ti] ratio and different carbon contents by DC cosputtering of Ti, C, and Ni targets and compared them with nickel-free nc-TiC/a-C coatings prepared using the same deposition techniques [22]. Addition of ~25 at. % of Ni led to the grain size decrease and increase of the amount of the amorphous carbon phase. Also, a moderate hardening of the coatings was observed. This effect was attributed to the nanocomposite hardening effect described by Zehnder et al. [3, 12]. Furthermore, if the Ti-Ni-C system contains <25 at. % of Ni, application of external forces, for example, via indentation of friction, can lead to overcoming the thermodynamical barrier and releasing of carbon from the grain to the matrix. Therefore, nc-Ti-Ni-C/a-C:H system could be used as a smart lubricating coating.

In this work hybrid PVD-PECVD process consisting of sputtering of a metallic target in reactive hydrocarbon atmosphere [4, 23–26] is used to synthesize nanocomposite hydrogenated nc-Ti-Ni-C/a-C:H coatings. The hybrid process instead of cosputtering was used to further expand the concept proposed for hydrogen free coatings [22]. Also, the hybrid process has a better future applicability as it is already industrially used [23] exhibiting higher deposition rates. Significantly lower amounts of Ni (less than ~10 at. %) than in the case of Jansson et al. [22] were used to purposely synthesize coatings with metastable Ti-Ni-C grains. To study the influence of the plasma excitation on the possibilities of synthesis of the metastable grains, Direct Current Magnetron Sputtering (DCMS) and High Power Impulse Magnetron Sputtering (HiPIMS) processes were used. HiPIMS process is characterized by enhanced adatom diffusion, enhanced ion and energy fluxes, and higher thin film forming ion concentration compared to DCMS [26–28]. The influence of Ni doping on the chemical composition, phase composition, microstructure, and mechanical properties of nc-Ti-Ni-C/a-C:H coatings prepared by both DCMS and HiPIMS will be discussed.

2. Experimental Details

Samples were deposited in a semi-industrial Alcatel SCM 650 sputtering system. Sputtering target (⌀ 20 cm) was driven by a Hüttinger TruPlasma Bipolar 4010 generator operated in DC mode in the DCMS case or by Melec SIPP 2000 generator in the HiPIMS case. A well balanced magnetic field configuration was used; for more details of the magnetic field configuration see [4]. The substrates were mounted onto a biasable (13.56 MHz RF) substrate holder 6.5 cm above the racetrack of the target. Titanium target with purity of 99.7% was used for preparation of the Ni-free samples. A compound target with 87.5% of Ti and 12.5% of Ni and purity of 99.95% was used for the Ni-doped coating preparation. The deposition chamber was evacuated by a turbomolecular pump backed by a Roots pump to the base pressure in the order of 10^{-4} Pa. Gas inlet was located between the substrate holder and the target at the distance of 2 cm from the target. Acetylene with purity of 99.6% was used as a source of carbon and hydrogen; argon with purity of 99.999% was used as a buffer gas. Gases were dosed via mass-flow controllers.

Cemented tungsten-carbide substrates (R_a = 3 nm) were precleaned in a chemical bath and ultrasonicated in a degreasing agent. Both the target and the substrates were further cleaned by Ar ion bombardment. During this cleaning phase, the substrate was preheated prior to the deposition to a temperature of ~150°C. After the cleaning phase, the argon flow rate was set to 20 sccm (~1.1 Pa) and the deposition of ~750 nm thick adhesion interlayer took place. Then the acetylene was introduced into the chamber. The coating's depositions were performed with deposition parameters summarized in Table 1. Longer deposition time in HiPIMS was used due to generally lower deposition rates [29]. For DCMS depositions the bias of –100 V was used; for HiPIMS deposition a substrate was left on floating potential. Substrate temperature of ~300°C was reached in both the DCMS and the HiPIMS cases after approximately 15 minutes from the start of the deposition. After the deposition the samples were left to cool down for two hours under vacuum.

Table 1: Parameters of the coatings deposition.

	DCMS	HiPIMS
Mean power (kW)	1.25	1.25
Pulse length (μs)	—	400
Pulse frequency (Hz)	—	30
Maximal current (A)	~2.5	~400
Substrate bias (V)	–100	—
Argon flow rate (sccm)	20	20
Deposition duration (min)	60	120

Spherical abrasions prepared by a calotester and measured by laser confocal microscope LEXT OLS4000 3D were used for determination of coating's thickness. Energy-dispersive X-ray spectroscopy (EDX) analyses using Tescan MIRA FEG SEM equipped with an EDX detector from Oxford Instruments were performed to determine the chemical composition of the coatings. Internal library of standards included in the Aztec software by Oxford Instruments was used for quantitative evaluation of the composition. X-ray diffraction (XRD) utilizing Rigaku SmartLab Type F diffractometer was used to determine the mean grain size and the lattice parameter. The diffractometer operated with $Cu_{K\alpha}$ radiation (λ = 0.1541 nm). Grazing angle of incidence (GIXRD) configuration with the angle of 0.5° was used for the measurement. X-ray photoelectron spectroscopy (XPS) was used to obtain information about the phase composition: content of the amorphous phase and the nanocrystalline phase. The XPS signals were recorded using a Thermo Fischer Scientific K-Alpha XPS. This system equipped with a microfocused monochromatic $Al_{K\alpha}$ X-ray source (1486.6 eV) was used for determination of phase composition of coatings. An X-ray beam with 200 W power (650 microns spot size) was used for determination of the lattice parameter as well as the mean grain size. The mean size of the TiC grains was calculated from the most intensive diffractogram peak corresponding to the (111) crystallographic direction using the Scherrer equation neglecting the effect of the grain strain [30]. The lattice parameter was always calculated from the three first intensive TiC diffraction peaks: (111), (200), and (311). Survey and high resolution spectra were collected with pass energy of 50 and 20 eV, respectively. The charge shift of the spectra was then corrected by setting the C1s peak to 284.8 eV. Fischerscope H100 depth sensing indenter (DSI) equipped with a Berkovich tip was used to measure the coating's hardness. The load applied on the tip and the corresponding indentation depths were recorded simultaneously for both the loading and the unloading parts. Hardness was determined using standard Oliver and Pharr method [31]. The indentation load of 40 mN was chosen in order to keep the radius of the deformed volume (estimated according to Johnson's contact model [32]) sufficiently low to avoid influence of the substrate. The tip area function was calibrated using fused silica and hard metal standards.

Typically, 32 indents were performed in different places on the sample for hardness analysis.

Stoichiometry of TiC grains was calculated in a simplified qualitative model, where all titanium atoms are assumed to be forming Ti-C bonds in the titanium carbide grains. Coefficient of stoichiometry of TiC grains in the Ni-free coatings was calculated as

$$x = \frac{[\mathrm{C}] \cdot A_{\mathrm{C\text{-}Ti}}}{[\mathrm{Ti}] \cdot A_{\mathrm{C1s}}}, \quad (1)$$

where [C] and [Ti] denote the atomic composition of the sample taken from EDX, $A_{\mathrm{C\text{-}Ti}}$ denotes the area under (C-Ti + C-Ti*) peak, and A_{C1s} denotes the area of the whole XPS C1s peak [26]. Two extreme cases were calculated. The first case assumed that there were no Ni-C bonds in the grain. In this case the coefficient of stoichiometry could be calculated directly from (1). The second case assumed that all the titanium as well as the nickel atoms created bonds with C atoms. In this case the coefficient of stoichiometry was calculated using a modification of (1):

$$x = \frac{[\mathrm{C}] \cdot \left(A_{\mathrm{C\text{-}Ti}} + A_{\mathrm{C\text{-}Ni}}\right)}{([\mathrm{Ti}] + [\mathrm{Ni}]) \cdot A_{\mathrm{C1s}}}, \quad (2)$$

where $A_{\mathrm{C\text{-}Ni}}$ denotes area under (C-Ni) peak in XPS C1s spectrum. The actual coefficient of stoichiometry should therefore lie between those of the extreme cases.

The mean grain separation (MGS) was calculated using information about the chemical composition, the mean grain size, and the phase composition. For calculation of the MGS a model assuming cubic grains uniformly distributed in the matrix was utilized [12, 21]. The equation used for calculation of the nc-TiC/a-C mean grain separation was adopted from [21] and adapted for nc-(Ti,Ni)C/a-C:H coatings assuming that Ni is included in TiC grains not forming regular carbide:

$$\mathrm{MGS} = c\left(\sqrt[3]{1 + r_{\mathrm{vol}}} - 1\right), \quad (3)$$

$$r_{\mathrm{vol}} = \frac{A_{\mathrm{C\text{-}C}}}{A_{\mathrm{C\text{-}Ti}} + A_{\mathrm{C\text{-}Ni}}} \frac{M_{\mathrm{a\text{-}C}}}{xM_{\mathrm{TiC}} + yM_{\mathrm{Ni}}} \frac{x\rho_{\mathrm{TiC}} + y\rho_{\mathrm{Ni}}}{\rho_{\mathrm{a\text{-}C}}}, \quad (4)$$

where c denotes the mean grain size, $A_{\mathrm{C\text{-}C}}$, $A_{\mathrm{C\text{-}Ti}}$, and $A_{\mathrm{C\text{-}Ni}}$ denote areas under (C-C), (C-Ti + C-Ti*), and (C-Ni) peaks in XPS C1s spectrum, $M_{\mathrm{a\text{-}C}}$, M_{TiC}, and M_{Ni} denote atomic weights of amorphous carbon, titanium carbide, and nickel, and $\rho_{\mathrm{a\text{-}C}}$, ρ_{TiC}, and ρ_{Ni} denote mass densities of amorphous carbon, titanium carbide, and nickel. The atomic weights were taken as $M_{\mathrm{a\text{-}C}} = 12.0$ amu [12], $M_{\mathrm{TiC}} = 59.5$ amu [12], and $M_{\mathrm{Ni}} = 58.7$ amu [33]. Mass densities $\rho_{\mathrm{a\text{-}C}} = 2.20\,\mathrm{g{\cdot}cm^{-3}}$ [12], $\rho_{\mathrm{TiC}} = 4.91\,\mathrm{g{\cdot}cm^{-3}}$ [12], and $\rho_{\mathrm{Ni}} = 8.91\,\mathrm{g{\cdot}cm^{-3}}$ [34] were used. Symbols x and y in (4) denote the weighted average of titanium and nickel content:

$$x = \frac{[\mathrm{Ti}]}{[\mathrm{Ti}] + [\mathrm{Ni}]}, \quad (5)$$

$$y = \frac{[\mathrm{Ni}]}{[\mathrm{Ti}] + [\mathrm{Ni}]}, \quad (6)$$

where [Ti] and [Ni] denote content of titanium and nickel in the coating.

3. Results

Series of Ni-free nc-TiC/a-C:H as well as Ni-doped nc-(Ti, Ni)C/a-C:H coatings were prepared by HiPIMS and DCMS processes. The thickness of the DCMS prepared coatings was in the range of 3.8–4.2 μm for coatings with ~30%–~70% of carbon. The thickness of the HiPIMS prepared coatings deposited for twice as long as the DCMS deposited coatings was in the range of 2.5–3.0 μm for coatings with ~20%–~75% of carbon. Deposition rate of the DCMS prepared coatings was thus approximately three times higher than the deposition rate of HiPIMS prepared coatings. This agrees well with finding that the deposition rate is generally significantly lower in HiPIMS compared to DCMS, mostly due to the titanium ion back-attraction to the target [27, 29, 35]. No influence of nickel addition on coating's thickness and deposition rate was observed.

As the total carbon content in the Ni-free as well as the Ni-doped coating increased, a total content of metallic elements, that is, Ti in the Ni-free coatings and Ti and Ni in the Ni-doped coatings, linearly decreased. Figure 1 shows linear decrease of the total content of titanium and nickel in the case of the Ni-doped coatings prepared by DCMS (Figure 1(a)) and HiPIMS (Figure 1(b)).

An example of diffraction patterns of the Ni-free coating with [C]/[Ti] ratio of ~0.33 (black line) and the coating containing ~10% Ni with the same [C]/[Ti] ratio (red line) is depicted in Figure 2. Only peaks corresponding to the TiC phase were observed in the diffraction pattern; no diffraction peaks corresponding to nickel or titanium phase were observed. The same, that is, only peaks corresponding to the TiC phase, were observed in case of all studied coatings. The lattice parameter calculated from the most intense peak of X-ray diffractograms is plotted in Figure 3. The bulk TiC lattice parameter of 4.33 Å [36] is plotted as a horizontal line for comparison. Figure 3(a) shows the comparison of the lattice parameter of the Ni-free and the Ni-doped coatings prepared by the DCMS; Figure 3(b) shows the same comparison in the HiPIMS case. The lattice parameter increased with increasing carbon content for all the coatings with less than ~50% of C. This was followed by a decrease of the lattice parameter for the DCMS and the Ni-free HiPIMS coatings. The Ni-doped HiPIMS deposited coatings with carbon content ≳50% exhibited lattice parameter independent of the total carbon content. The HiPIMS prepared coatings always exhibited lattice parameter lower than the DCMS prepared coatings and also lower than lattice parameter of bulk TiC. The lattice parameter of the Ni-doped coatings with ≤50% C was always higher than the lattice parameter of the corresponding Ni-free coatings.

The comparison of the mean grain size of the Ni-free and the Ni-doped coatings prepared by DCMS is shown in Figure 4(a). The mean grain size of the Ni-free coatings did not significantly change with increasing total carbon content up to ~50% and was ~25 nm. Ni-doped coatings exhibited pronounced increase of the grain size from ~5 nm to ~24 nm as the carbon content increased from ~30% to ~50%. As the carbon content increased further, the grain size decreased both for the Ni-free and for the Ni-doped coatings and

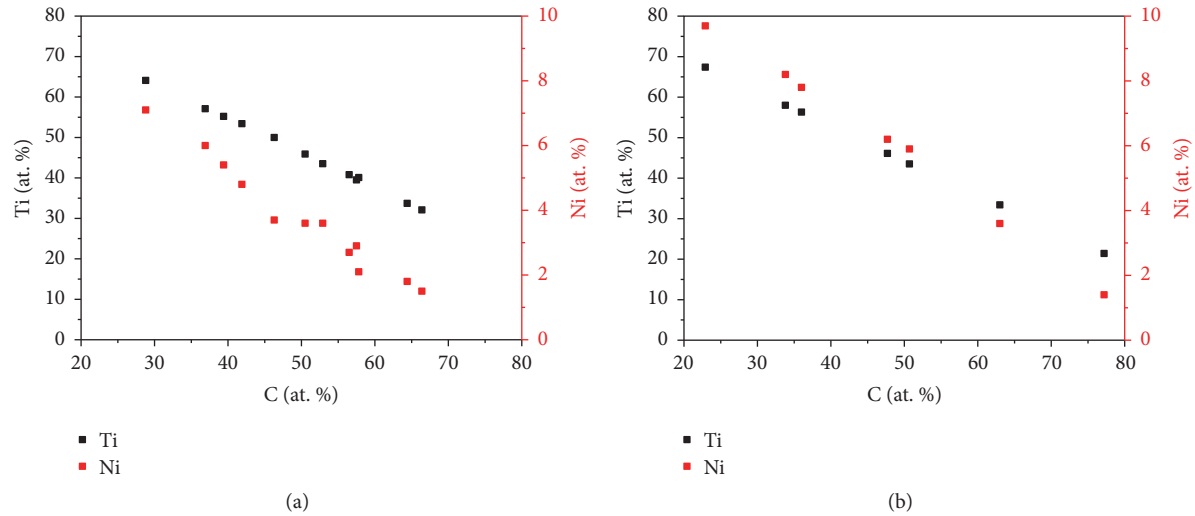

Figure 1: Dependence of titanium and nickel content on the total content of carbon. Comparison of (a) the DCMS and (b) the HiPIMS prepared coatings.

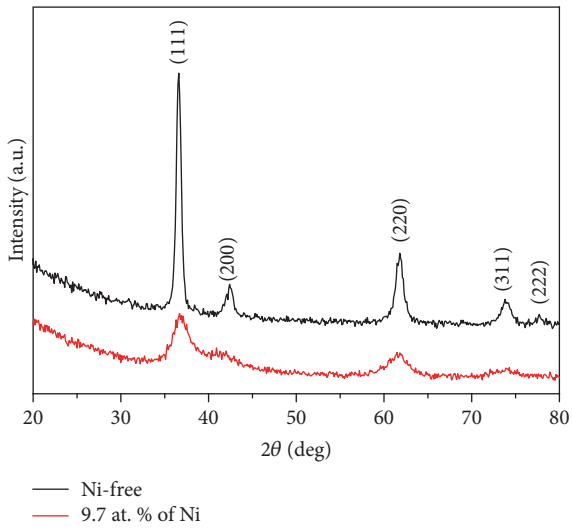

Figure 2: Diffraction patterns of the HiPIMS prepared Ni-free (black line) coating with [C]/[Ti] ratio ~0.33 and the HiPIMS prepared Ni-doped coating with 9.7% of Ni (red line) with [C]/[Ti] ratio ~0.34. Crystallographic direction of the TiC peaks is denoted above certain peaks.

the coating with the highest amount of carbon exhibited grain size of ~4 nm. The mean grain size of the HiPIMS prepared coatings is plotted in Figure 4(b). The mean grain size in the Ni-free coatings decreased with the increasing total carbon content from ~37 nm for coating with ~25% of carbon down to ~5 nm for coating with ~68% of carbon. The grain size in the Ni-doped coatings increased from ~4 nm for coating with the lowest amount of carbon up to ~15 nm for coating with carbon amount of ~48%. As the carbon content increased further, the grain size decreased down to ~2 nm and remained constant for the rest of the carbon rich coatings. Ni-doped coatings showed generally smaller grains compared to Ni-free coatings which was more pronounced in the HiPIMS series. The grain size reduction effect was also more pronounced in coatings with low amount of carbon.

High resolution XPS measurements were carried out on the C1s, Ti2p, and Ni2p peak regions. Comparison of Ti2p peaks of coatings with similar carbon content without and with Ni prepared at both the DCMS and HiPIMS is plotted in Figure 5. Samples with the lowest amount of carbon and thus the highest amount of nickel are shown to illustrate the highest possible effect of Ni doping on the measures Ti2p peaks. The Ti2p peaks exhibit minimal differences between the samples. The binding energy of the maximum intensity of the $Ti2p_{3/2}$ of 449.6–449.9 eV as well as that of the $Ti2p_{1/2}$ peak of 460.9–461.3 eV agrees with the position of the Ti-C bond [3, 10, 37] indicating majority of Ti being bonded to carbon. Ti-O bonding is also present in the coating as a minor component. No Ti-Ti bonding was detected. This was true for all of the analyzed samples independently of their carbon content, nickel presence, or the method of deposition. The Ni2p peaks of the DCMS and HiPIMS deposited coatings with the highest amount of nickel together with a reference spectrum Ni (99.999% purity, Goodfellow) are presented in Figure 6. The positions of the $Ni2p_{3/2}$ as well as the $Ni2p_{1/2}$ peaks in the deposited coatings are shifted by 0.8 eV to higher energies compared to the Ni reference. The positions of the Ni2p peaks are in good agreement with the literature value for Ni-C bonds [37]. Further, no Ni-Ni bonds were detected, which was in good agreement with findings from XRD showing no presence of Ni crystallites. The amount of the a-C:H phase was quantified using the curve deconvolution of the C1s peak [15, 22, 37]. An example of deconvoluted high resolution C1s peak of Ni-free (~61% of carbon) and Ni-doped (~58% of carbon) coatings prepared by DCMS is shown in Figure 7. An amount of the a-C:H phase was estimated by comparison of C-C bond area to sum of C-Ti, C-Ti* and C-Ni bond areas.

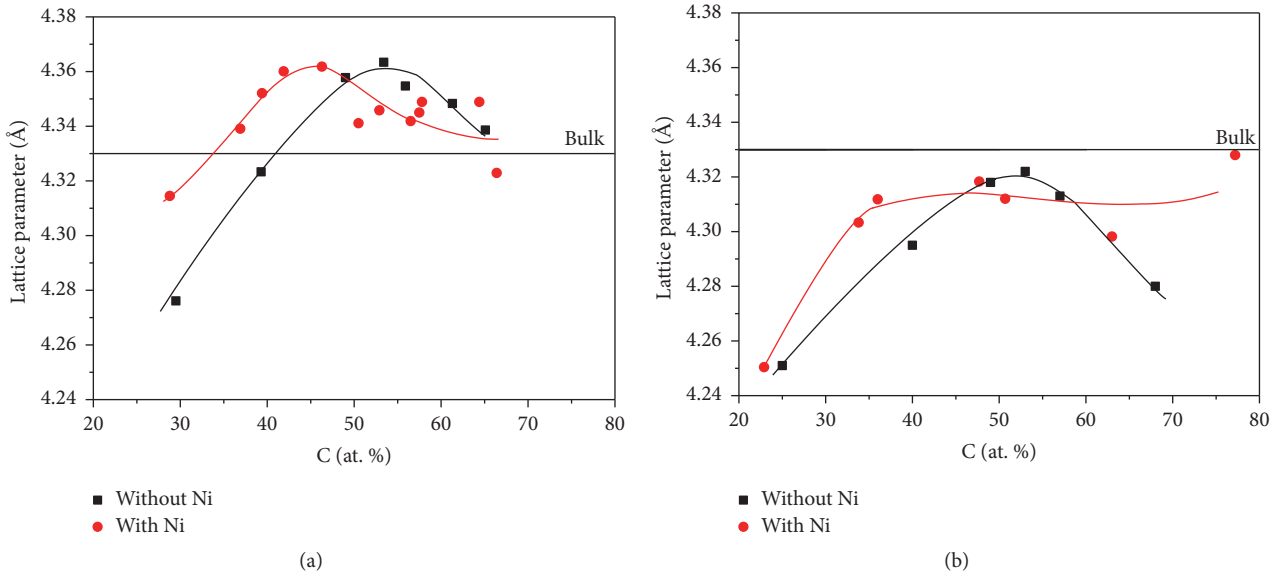

FIGURE 3: The lattice parameter of the Ni-free (black marks) and the Ni-doped (red marks) coatings. Comparison of (a) the DCMS prepared coatings with (b) the HiPIMS prepared coatings. Line at 4.33 Å denoted the bulk TiC lattice parameter [36]. Lines are added as guides for the eye.

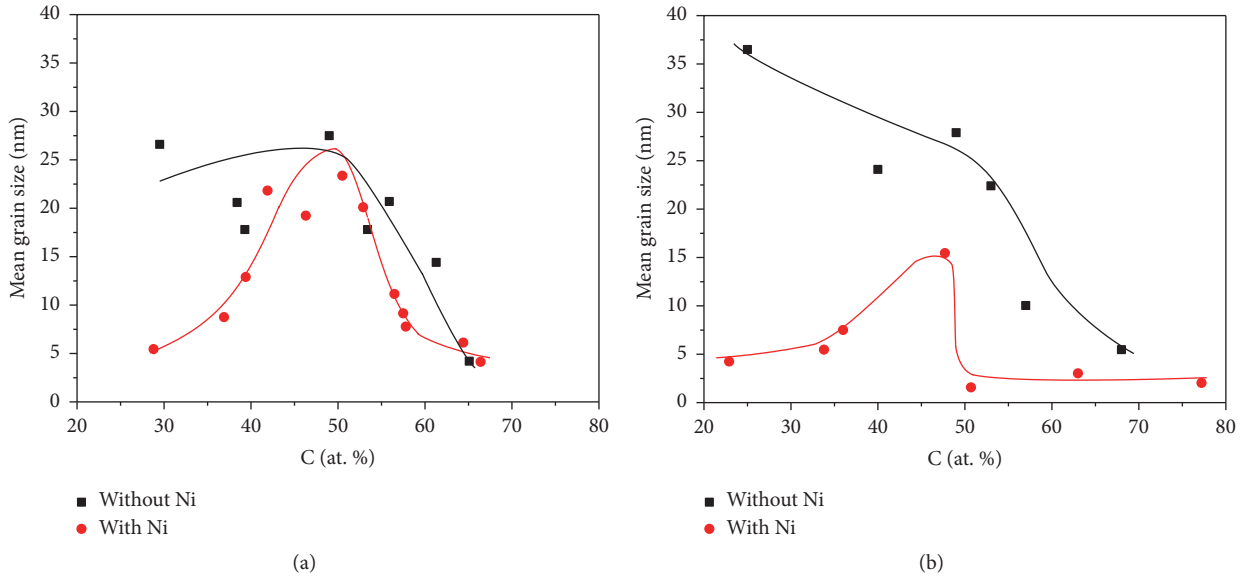

FIGURE 4: The mean grain size of the Ni-free (black marks) coatings compared with the Ni-doped (red marks) coatings. Comparison of (a) the DCMS prepared coatings and (b) the HiPIMS prepared coatings. Lines are added as guides for the eye.

Figures 8(a) and 8(b) show the comparison of the amount of the a-C:H phase of the Ni-free and the Ni-doped coatings prepared by DCMS and HiPIMS, respectively. Rapid increase of amount of the a-C:H phase was observed in the DCMS deposited coatings. However, the Ni-free coatings with ≲50% exhibited significantly higher amount of the a-C:H phase compared to corresponding Ni-doped coatings. This effect is the most pronounced in the coatings with the lowest amount of carbon where the Ni-free coatings exhibited significantly higher amount of the a-C:H phase than the Ni-doped coatings. No effect of Ni addition on the total a-C:H amount was observed in the HiPIMS deposited coatings. Both the Ni-free and the Ni-doped coatings exhibited slight increase of the amount of the a-C:H phase in the coatings with total carbon content ≲50% followed by rapid increase up to ~70% for coatings with the high amount of carbon.

Coefficient of stoichiometry in the DCMS prepared coatings is plotted in Figure 9(a). The Ni-free coatings with

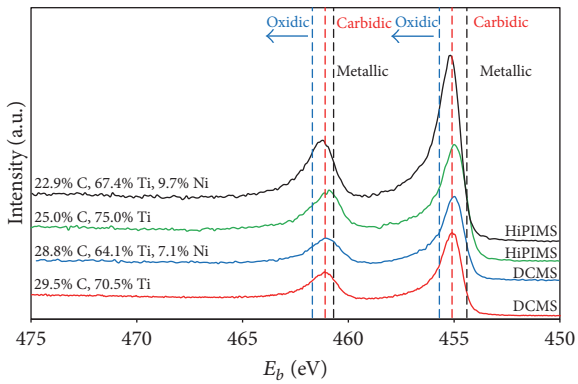

Figure 5: Comparison of high resolution XPS spectra of the Ti2p peaks.

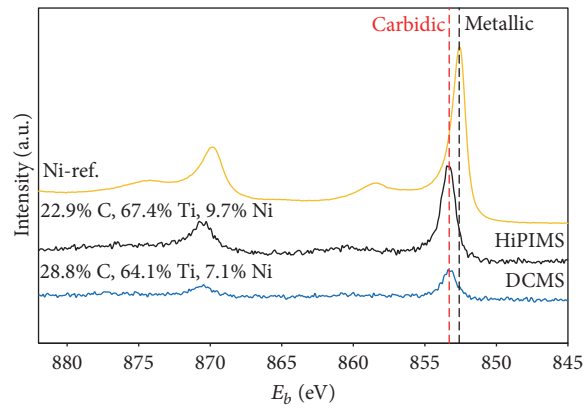

Figure 6: Comparison of high resolution XPS spectra of the Ni2p peaks.

carbon content ≲50% exhibited increase of coefficient of stoichiometry with increasing carbon content. When ≲50% of carbon was reached, coefficient of stoichiometry of ~1 was attained. As the carbon content increased further, the coefficient of stoichiometry decreased. In the case of the Ni-doped coatings the stoichiometry coefficient was calculated for two extreme cases. In both cases the Ni-doped coatings exhibited a monotonous increase of the coefficient of stoichiometry with increasing carbon content; stoichiometry coefficient ~1 was reached for coatings with ≳60% of carbon. The coefficient of stoichiometry was higher for the Ni-doped coatings with ≲45% of carbon. The Ni-doped coatings with carbon content of ~45–65% exhibited lower coefficient of stoichiometry, as the increase of the coefficient of stoichiometry was slower than in the case of the Ni-free coatings. The coefficient of stoichiometry of the Ni-doped coatings was higher for coatings with carbon content ≳60% as the Ni-free coatings already exhibited a decrease of the coefficient of stoichiometry. Coefficient of stoichiometry in the Ni-free coatings prepared by HiPIMS (see Figure 9(b)) with ≲50% of C also increased with increasing carbon content. Similarly to the DCMS case, the HiPIMS coatings with ~50% of C exhibited coefficient of stoichiometry ~1. The Ni-doped coatings with ≲50% of carbon exhibited increasing of the stoichiometry coefficient with increasing carbon content. The coefficient of stoichiometry in the Ni-doped coatings reached maximum value ~1 for coatings with 50–60% of carbon and it decreased with further carbon content increase. The coefficient of stoichiometry was lower for the HiPIMS deposited Ni-doped coatings with ≲50% of carbon.

The mean grain separation is plotted in Figure 10. The number of carbon monolayers separating the grains corresponding to the calculated MGS is plotted on the right axis in case of both graphs [38]. Increase of the MGS with increasing carbon content was observed in all series of coatings. This increase is, however, for coating with carbon content ≳50% less pronounced than the increase of the amount of a-C:H phase because of simultaneous decrease of the grain size. The DCMS prepared Ni-free coatings exhibited higher MGS compared to corresponding Ni-doped coatings (see Figure 10(a)). The most pronounced difference of the MGS was observed in coatings with the lowest amount of carbon. While MGS of the Ni-free coating was ~0.8 nm, which corresponded to ~6 carbon monolayers, grains in the Ni-doped coating were separated only by 1 carbon monolayer which corresponded to MGS ≲ 0.1 nm. As the carbon content increased the difference in MGS of the Ni-doped and the Ni-free coatings decreased. In the case of the HiPIMS prepared coatings (Figure 10(b)), the Ni-doped coatings exhibited lower MGS than the corresponding Ni-free coatings. Employing the HiPIMS, the MGS was reduced compared to DCMS which was the most pronounced particularly for Ni-free coatings at low carbon contents.

Figure 11 shows the hardness of the DCMS (Figure 11(a)) and the HiPIMS (Figure 11(b)) prepared coatings. In the DCMS case the hardness of the Ni-free coatings increased from ~11 GPa up to ~30 GPa with increasing content of carbon up to ~55%. As the carbon content increased further, the hardness of the Ni-free coatings decreased. Hardness of the Ni-doped coatings increased from ~20 GPa up to ~29 GPa with increasing total carbon content up to ~45%. Then the hardness was not significantly influenced by the total carbon content and remained ~25 GPa for coatings with ≳45% of carbon. The Ni-free coatings prepared by HiPIMS exhibited increase of hardness from ~15 GPa up to ~45 GPa with increasing content of carbon up to ~57%. The hardness decreased down to 30 GPa with further carbon increase up to 70%. Hardness of the Ni-doped coatings prepared by HiPIMS behaved similarly to the case of the Ni-free up to ~48% of carbon where the Ni-doped coatings exhibited maximum hardness of ~38 GPa. The hardness then decreased with increasing carbon content down to 20 GPa for coatings with 75% of carbon. HiPIMS prepared coatings exhibited higher hardness than the DCMS prepared coatings for both Ni-free and Ni-doped coatings. The maxima of the hardness for HiPIMS prepared coatings were shifted to lower amount of carbon for Ni-doped coatings with respect to the Ni-free case.

All the results presented in previous chapter are summarized in Table 2 (DCMS prepared coatings) and Table 3 (HiPIMS prepared coatings). Some parameters could not be determined due to problems, for example, coating delamination. Visibly erroneous data was discarded.

Table 2: Overview of the coatings prepared by DCMS.

C (at. %)	Lattice parameter (Å)	Grain size (nm)	a-C:H phase (%)	MGS (nm)	Hardness (GPa)
Ni-free					
29.5	4.2761	26.6	17.2	0.799	11.4 ± 0.8
38.4		20.6			
39.3	4.3233	17.8	26.4	0.904	20.7 ± 1.6
49.0	4.3578	27.5	29.0		24.4 ± 1.8
53.4	4.3634	17.8	13.7		33.3 ± 4.3
55.9	4.3547	20.7	25.7	1.016	26.8 ± 1.2
61.3	4.3483	14.4	34.8	1.065	26.8 ± 2.7
65.1	4.3405	4.2	66.5	0.991	21.2 ± 2.5
Ni-doped					
28.8	4.3010	5.5	2.6	0.025	20.0 ± 1.1
36.9	4.3391	8.8	14.2	0.248	19.0 ± 1.9
39.4	4.3521	12.9	3.8	0.088	23.4 ± 2.3
41.9	4.3601	21.8	13.3	0.562	29.1 ± 3.1
46.3	4.3678	19.2	11.3	0.404	25.8 ± 2.3
50.5	4.3411	23.4	32.9		24.2 ± 2.2
52.4	4.3472				
52.9		20.1	14.3	0.556	23.9 ± 2.6
56.5	4.3419	11.2	41.4		30.6 ± 1.8
57.5	4.3450	9.2	39.7		29.9 ± 2.0
57.8	4.3489	7.8	44.8		22.6 ± 3.5
64.4	4.3432	6.1	40.2	0.609	21.4 ± 1.9
66.4	4.3229	4.1	54.8	0.688	27.5 ± 2.3

Table 3: Overview of the coatings prepared by HiPIMS.

C (at. %)	Lattice parameter (Å)	Grain size (nm)	a-C:H phase (%)	MGS (nm)	Hardness (GPa)
Ni-free					
25.0	4.2502	36.5			15.1 ± 1.3
40.0	4.2950	24.1	5.8	0.221	34.5 ± 2.5
49.0	4.3180	27.9	14.1	0.671	38.3 ± 2.7
53.0	4.3216	22.4	16.6	0.650	40.0 ± 3.0
57.0	4.3130	10.0	25.2	0.483	44.7 ± 3.8
68.0	4.2890	5.5	55.4	0.873	31.5 ± 3.6
Ni-doped					
22.9	4.2600	4.3	5.7	0.043	17.3 ± 0.8
33.8	4.3033	5.5	8.6	0.084	26.8 ± 2.1
36	4.3118	7.5			33.8 ± 1.5
47.7	4.3185	15.5	12.1	0.341	38.2 ± 4.1
50.7	4.3120	1.6	13.9	0.041	33.6 ± 4.4
63	4.2982	3.0	37.0	0.264	24.6 ± 4.1
77.2	4.2930	2.0	70.2	0.576	20.4 ± 1.7

4. Discussion

The observed dependencies of the crystalline phase from XRD analyses (Figures 2–4) can be summarized and explained as follows. Only diffractions corresponding to fcc TiC lattice were observed (see Figure 2) for both Ni-free and Ni-doped coatings. Thus, Ni did not form independent crystallites. It was incorporated in TiC grains or it was dispersed in the carbon matrix. As the lattice parameter of the Ni-doped coatings was influenced by Ni being always larger than that of the Ni-free coatings (Figure 3) the nickel incorporation in the grains can be presumed. The increase

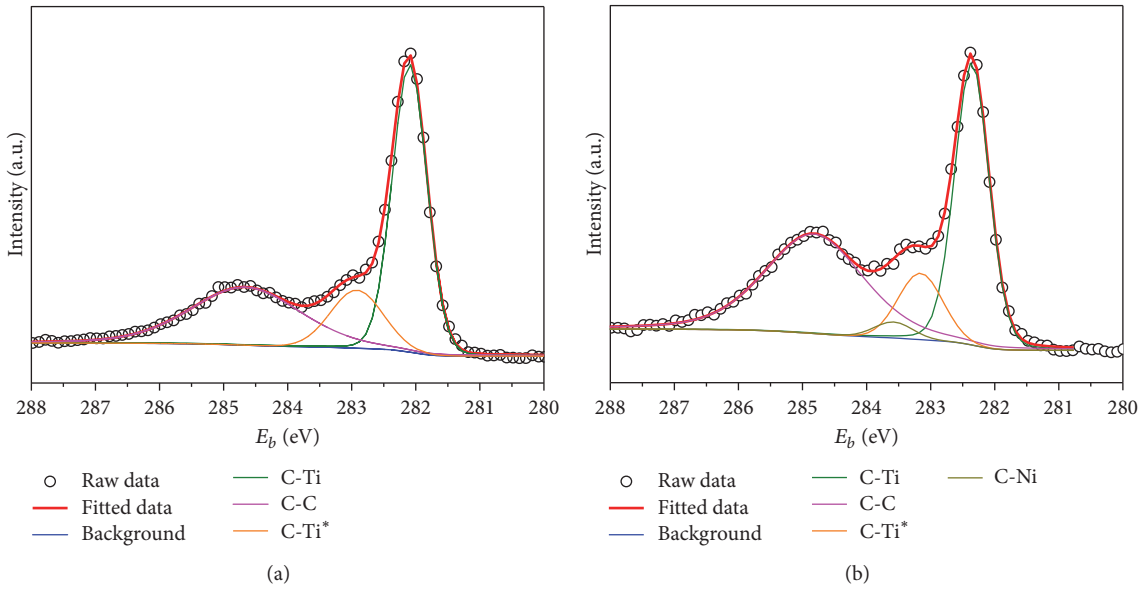

Figure 7: Fitted XPS spectra of C1s peak of (a) Ni-free coating and (b) Ni/doped coating with similar carbon content of ~60%.

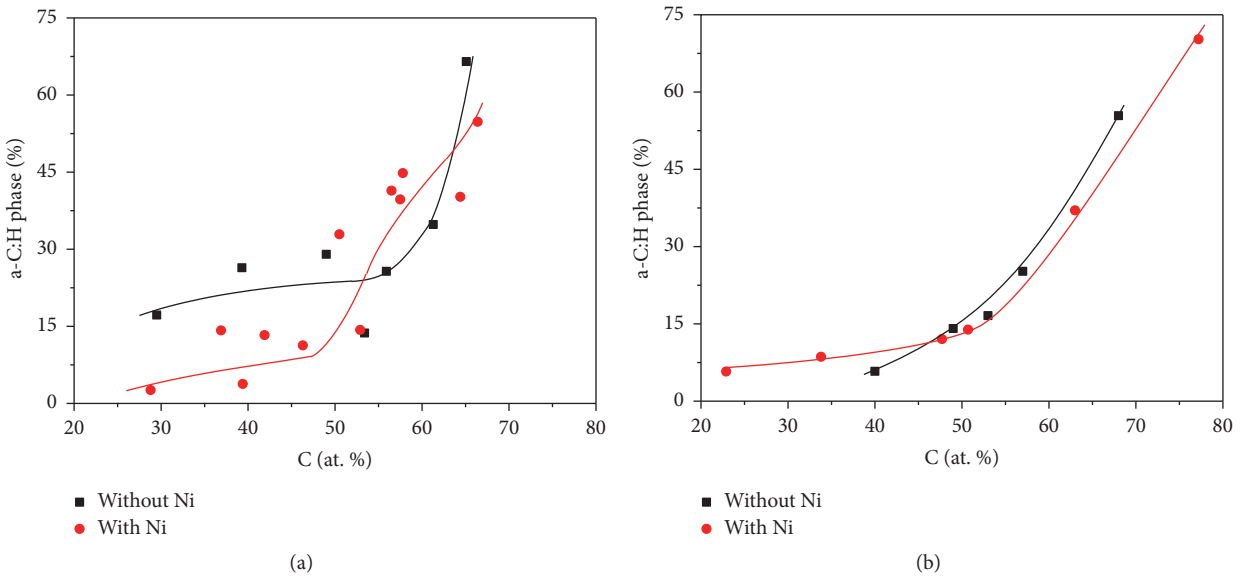

Figure 8: The relative amount of the amorphous hydrogenated carbon (a-C:H) phase. Comparison of the Ni-free (black marks) and the Ni-doped (red marks) coatings prepared by (a) the DCMS and (b) the HiPIMS. Lines are added as guides for the eye.

of the lattice parameter of the coatings with increasing total carbon content in coatings with $\lesssim$50% can be explained by vacancy filling [34]. The number of vacancies in the TiC crystal lattice decreased with increasing carbon content. The carbon atoms occupied the vacancies and the lattice parameter increased accordingly. The DCMS prepared coatings with $\gtrsim$50% of carbon exhibited higher lattice parameter than bulk value [36]. Similar effect, that is, higher value of the lattice parameter of DCMS deposited TiC/C coatings than the bulk lattice parameter of TiC, was observed by several authors [3, 26, 39–41]. The lattice parameter of the HiPIMS prepared coatings (Figure 3(b)) was always lower than the lattice parameter of the DCMS (Figure 3(a)) prepared coatings. This was due to the generally higher kinetic energy of the particles impinging the surface of the growing coatings in HiPIMS [42]. Higher energy influx promoted the surface diffusion of the adatoms and enabled them to reach energetically more favorable position. Higher energy influx and promoted surface diffusion resulted in denser crystallites as indicated by the lower lattice parameter in the HiPIMS case [29].

A decrease of the grain size with increasing carbon content was observed in DCMS as well as in HiPIMS prepared coatings with carbon content $\gtrsim$ 50% regardless of Ni doping. This is due to a rapid increase of the a-C:H

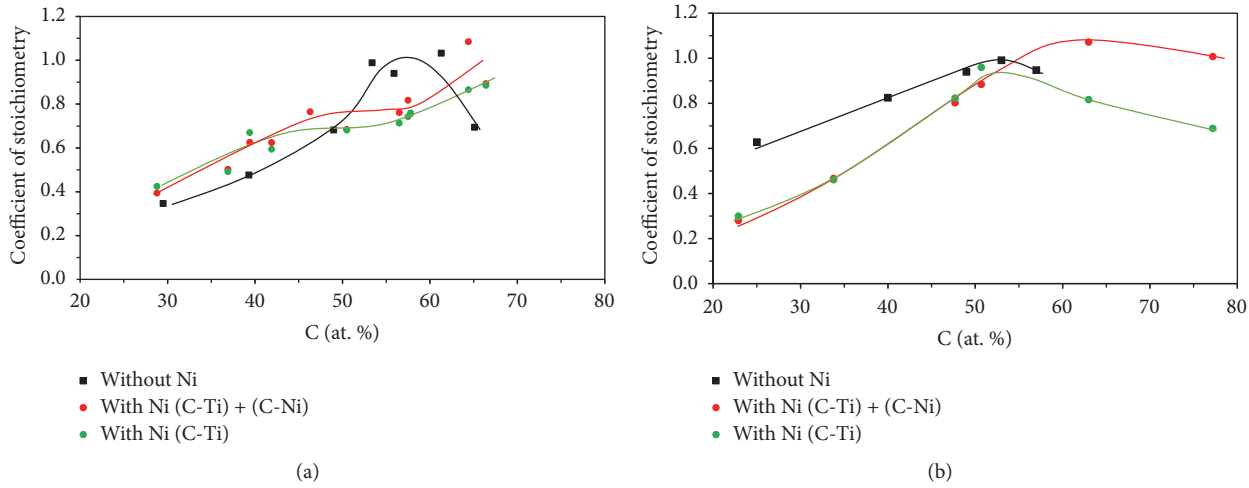

FIGURE 9: Stoichiometry in TiC crystallites of the Ni-free (black marks) and of the Ni-doped (red and green marks) coating. Comparison of (a) the DCMS and (b) the HiPIMS prepared sets of coatings. Lines are added as guides for the eye.

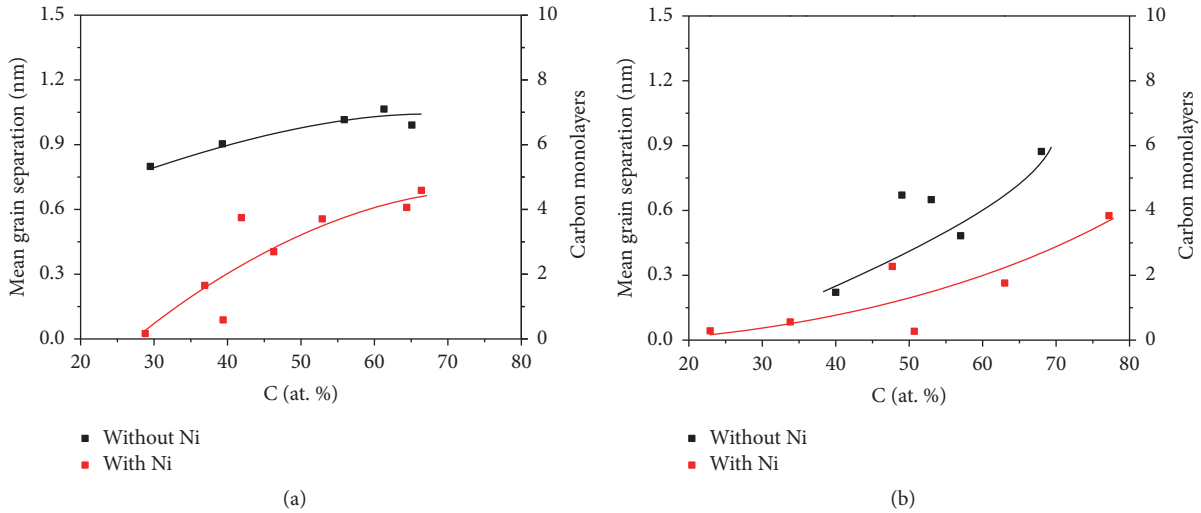

FIGURE 10: The mean grain separation of the Ni-free (black marks) and of the Ni-doped (red marks) coating. Comparison of (a) the DCMS and (b) the HiPIMS prepared sets of coatings. Lines are added as guides for the eye.

phase content in coatings with carbon content $\gtrsim 50\%$ (see Figure 5). Thus the a-C:H phase covered the growing grains and hindered their growth [29]. This led to formation of higher number of smaller grains. Ni-doped coatings with carbon content $\lesssim 50\%$ exhibited smaller grains than the Ni-free coatings with similar carbon content (see Figure 4). This effect was more pronounced in the coatings with low amount of carbon and high amount of nickel. A similar phenomenon of grain size decrease initiated by third-element doping was observed in other carbide systems [21, 37, 43, 44]. Råsander et. al. calculated that nickel presence in the TiC lattice leads to lowering of the formation energy and the migration energy barriers of the carbon vacancies in comparison with the Ni-free TiC lattice [45]. High concentration of crystal defects, for example, vacancies, leads to the formation of planar defects acting as grain boundaries which resulted in smaller grains compared to a system with lower number of vacancies [34]. Thus, we formulate a hypothesis that nickel incorporation into the nc-TiC/a-C:H coatings modified the vacancy distribution in the TiC_x grains which resulted in arrangement of planar defects leading to formation of grain boundaries and thus to the reduction of the grain size.

Jansson et al. [22] proposed that Ni addition should lead to releasing of the carbon from the TiC grains into the a-C phase. Thus, Ni-doped coatings with the same amount of carbon as Ni-free coatings should exhibit a higher amount of a-C phase. However, in our study, no influence of nickel addition on the amount of amorphous carbon phase was observed for the HiPIMS prepared coatings (see Figure 6(b)). In the case of the DCMS prepared coatings, the Ni-doped coatings with $\lesssim 50\%$ of carbon exhibited even lower amount of the a-C(:H) phase than the Ni-free coatings (Figure 8(a)).

It has been observed that the a-C(:H) phase was formed even for coatings with $\lesssim 50\%$ of carbon [10, 16]. So the

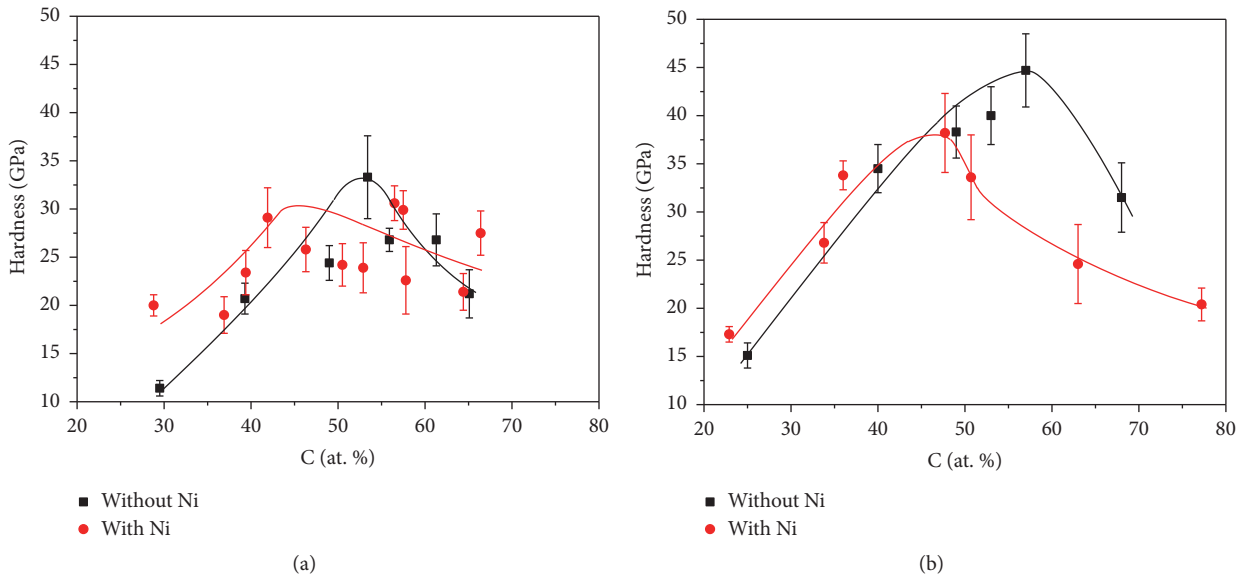

Figure 11: The hardness of the Ni-free (black marks) and the Ni-doped (red marks) coatings. Comparison of (a) the DCMS and (b) the HiPIMS prepared coatings. Lines are added as guides for the eye.

coatings are composed of TiC grains with strong deficit of carbon surrounded by small amount of amorphous carbon. High temperature or strong ion bombardment may force the carbon to pass from the a-C:H phase near the grain surface to the grain itself. The Ni-doped coatings with ≲50% C prepared by DCMS exhibited significantly smaller grains (see Figure 4(a)) and lower amount of the a-C:H phase (see Figure 8(a)) than the corresponding Ni-free coatings. The lower amount of the a-C:H phase in case of the Ni-doped coatings can be explained by presence of smaller grains with higher surface/volume ratio, facilitating the effect of the carbon transfer from the matrix to the grains. In the case of HiPIMS the ion bombardment was so intense that enough energy is supplied where carbon was incorporated into the grains independently of their size. The nickel induced grain size reduction thus did not significantly affect the amount of the a-C:H phase in HiPIMS deposited coatings. Furthermore, in strongly substoichiometric TiC grains the nickel addition may not lead to complete releasing of carbon atoms from a grain, but rather to carbon atom relocation within a TiC grain. The carbon atom could be trapped in a nearby vacancy instead of being removed from the grain to the amorphous phase.

The evolution of the mean grain size and the mean grain separation of the Ni-free and the Ni-doped coatings prepared by DCMS is schematically depicted in Figure 12. Analogous scheme for the HiPIMS prepared coatings is depicted in Figure 13. For simplicity, we can divide all the range of carbon content into three zones. This division into three zones illustrates the changes of the microstructure of the deposited coatings affecting the mechanical properties.

In the case of the DCMS deposited coatings an increase of the hardness was observed up to carbon content of ~50% (Zone 1 in Figures 12(a) and 12(b)). This increase was

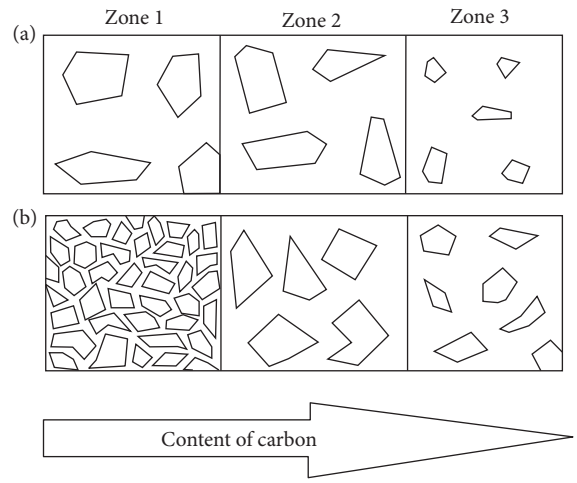

Figure 12: Scheme of the mean grain size and the mean grain separation of (a) the Ni-free and (b) the Ni-doped coatings prepared by DCMS. Zone 1 denoted coatings with low amount of carbon, Zone 2 denoted medium amount of carbon, and Zone 3 denoted high amount of carbon.

attributed to lowering of the grain vacancy concentration similarly to [26], because only low vacancy concentration is favorable for achieving a high hardness [46, 47]. Increase of the initially low grain size in the case of the Ni-doped coatings was also an important factor in the hardness enhancement because of effects analogical to the Hall-Petch effect [48–53]. The initial hardness increase with increasing carbon content was observed despite a slight increase of the MGS as high MGS facilitates the grain sliding [54]. The DCMS prepared Ni-doped coatings with carbon content ≲ 50% also

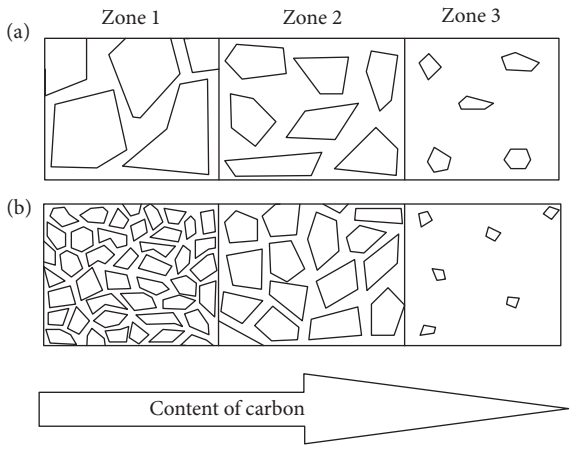

Figure 13: Scheme of the mean grain size and the mean grain separation of (a) the Ni-free and (b) the Ni-doped coatings prepared by HiPIMS. Zone 1 denoted coatings with low amount of carbon, Zone 2 denoted medium amount of carbon, and Zone 3 denoted high amount of carbon.

exhibited higher hardness than the Ni-free coatings. This hardening was attributed to lower grain size as well as the lower amount of a-C:H phase corresponding to lower MGS. Also the Ni-doped coatings exhibited lower amount of the a-C:H phase for the same total carbon content and thus lower carbon vacancy concentration in the grains can be expected. The hardness of the DCMS deposited coatings with carbon content $\gtrsim 50\%$ was similar for the Ni-doped and the Ni-free coatings due to comparable grain size as well as comparable amount of the a-C:H phase (see Zone 3 in Figures 11(a) and 11(b)). Some slight differences in the grain size and in the a-C:H phase content led to differences in the MGS; however, generally high MGS ($\gg$1 monolayer) had no appreciable effect on the measured hardness as only 1 monolayer is optimal for the effect of nanocomposite hardening [51, 52, 55].

The coating microstructure governed also the hardness of the coatings prepared by HiPIMS. The initial hardness increase up to 50% of carbon was mainly caused by lowering of the grain vacancy concentration and the grain size evolution (Zone 1 in Figure 13). The initial TiC grain size of ~5 nm observed in the Ni-doped coatings was low and the effect analogical to the inverse Hall-Petch effect in polycrystalline films could occur [51–53, 55]. As the TiC grain size increased, the hardness increased accordingly. The maximum grain size of ~15 nm was reached at 45% of carbon (Zone 2 in Figure 13). The grains still contained lattice vacancies because of carbon deficiency and preferential formation of the a-C:H matrix phase. The individual grains were on average separated by ~2 monolayers of the matrix. This combination of parameters resulted in hardness of ~37 GPa. On the other hand, the Ni-free coatings initially exhibited large grains with the size of ~35 nm that is too high for achieving high hardness due the effect analogous to the Hall-Petch effect in polycrystallites [51–53]. The grain size steadily decreased while the hardness increased with the carbon content increase (see Zone 3 in Figures 13(a) and 13(b)). The combination of the grain size, low vacancy concentration, and low mean grain separation which was optimal for the highest hardness was reached in coating with ~55% of C. This coating exhibited ~10 nm grains separated by ~3 monolayers of the matrix. Low vacancy concentration can be expected as the carbon content is >50% unlike in the case of the hardest Ni-doped coating. This combination of parameters resulted in maximal hardness of ~45 GPa.

The hardness of the coatings deposited by HiPIMS was generally higher than that of the corresponding DCMS deposited coatings. This can be partially attributed to grain size decrease, but also to the lower amount of the a-C:H phase formed under HiPIMS conditions. This led to a lower mean grain separation as well as reduction of grain vacancy concentration in the grains due to HiPIMS induced carbon transfer from the matrix to the grains.

5. Conclusion

Ni-free and Ni-doped nc-TiC/a-C:H coatings were prepared by a hybrid PVD-PECVD process of titanium and titanium-nickel compound target sputtering in argon/acetylene atmosphere. DCMS as well as the HiPIMS was used for the depositions in order to study the influence of the plasma excitation on the structure and hardness of the deposited coatings.

Nickel was found to be incorporated into the grains. Nickel addition also led to decrease of the grain size. This effect was more pronounced for the coatings with carbon content $\lesssim 50\%$. The grain size reduction was attributed to grain boundary formation due to formation of lattice defects induced by nickel incorporation into the grains. Smaller grains in the Ni-doped coatings prepared by DCMS exhibited higher surface to volume ratio than that exhibited by the larger grains in the Ni-free coatings. This led to decrease of the amount of the a-C:H phase in the Ni-free coatings as higher surface area of the grains led to enhanced carbon transfer from the matrix to the grains. The HiPIMS prepared coatings exhibited no influence of nickel addition on the a-C:H amount, due the high ion bombardment energy promoting the carbon incorporation even into the bulk of the larger grains. The resulting hardness of the deposited coatings was shown to be governed primarily by the grain size, vacancy concentration in the grains, and their mean grain separation. Ni doping had a significant effect on the hardness of the coatings. For DCMS deposited coatings with $\lesssim$50% of carbon the hardness increased with Ni doping due to favorable structure changes. The structure was not significantly changed and the hardness was not changed. The effect of the Ni doping was less pronounced for HiPIMS deposited coatings with $\lesssim$50% of carbon. However, the hardness of the Ni-doped coatings was strongly reduced for coatings with higher carbon content primarily due to unfavorable grain size lowering induced by Ni doping.

Conflicts of Interest

The authors declare that they have no conflicts of interest.

Acknowledgments

This research has been supported by Project LO1411 (NPU I) funded by Ministry of Education, Youth and Sports of Czech Republic and the Czech Science Foundation (Project 15-17875S).

References

[1] J.-E. Sundgren, B.-O. Johansson, and S.-E. Karlsson, "Mechanisms of reactive sputtering of titanium nitride and titanium carbide I: influence of process parameters on film composition," *Thin Solid Films*, vol. 105, no. 4, pp. 353–366, 1983.

[2] D. Martínez-Martínez, C. López-Cartes, A. Fernández, and J. C. Sánchez-López, "Influence of the microstructure on the mechanical and tribological behavior of TiC/a-C nanocomposite coatings," *Thin Solid Films*, vol. 517, no. 5, pp. 1662–1671, 2009.

[3] T. Zehnder and J. Patscheider, "Nanocomposite TiC/a-C:H hard coatings deposited by reactive PVD," *Surface and Coatings Technology*, vol. 133, no. 134, pp. 138–144, 2000.

[4] Pavel Souček, T. Schmidtová, L. Zábranský et al., "On the control of deposition process for enhanced mechanical properties of nc-TiC/a-C:H coatings with DC magnetron sputtering at low or high ion flux," *Surface and Coatings Technology*, vol. 255, pp. 8–14, 2014.

[5] Y. T. Pei, D. Galvan, J. T. M. De Hosson, and A. Cavaleiro, "Nanostructured TiC/a-C coatings for low friction and wear resistant applications," *Surface and Coatings Technology*, vol. 198, no. 1–3, pp. 44–50, 2005.

[6] D. Galvan, Y. T. Pei, and J. T. M. De Hosson, "TEM characterization of a Cr/Ti/TiC graded interlayer for magnetron-sputtered TiC/a-C:H nanocomposite coatings," *Acta Materialia*, vol. 53, no. 14, pp. 3925–3934, 2005.

[7] Y. Wang, X. Zhang, X. Wu, H. Zhang, and X. Zhang, "Compositional, structural and mechanical characteristics of nc-TiC/a-C:H nanocomposite films," *Applied Surface Science*, vol. 255, no. 5, pp. 1801–1805, 2008.

[8] W. K. Chu, J. W. Mayer, and M. A. Nicolet, *Back Scattering Spectrometry*, Academic Press, New York, NY, USA, 1978.

[9] U. Wiklund, M. Nordin, O. Wänstrand, and M. Larsson, "Evaluation of a flexible physical vapor deposited TiC-C coating system," *Surface and Coatings Technology*, vol. 124, no. 2-3, pp. 154–161, 2000.

[10] Y. Hu, L. Li, X. Cai, Q. Chen, and P. K. Chu, "Mechanical and tribological properties of TiC/amorphous hydrogenated carbon composite coatings fabricated by DC magnetron sputtering with and without sample bias," *Diamond and Related Materials*, vol. 16, no. 1, pp. 181–186, 2007.

[11] W. J. Meng, R. C. Tittsworth, and L. E. Rehn, "Mechanical properties and microstructure of TiC/amorphous hydrocarbon nanocomposite coatings," *Thin Solid Films*, vol. 377-378, pp. 222–232, 2000.

[12] T. Zehnder, P. Schwaller, F. Munnik, S. Mikhailov, and J. Patscheider, "Nanostructural and mechanical properties of nanocomposite nc-TiC/a-C:H films deposited by reactive unbalanced magnetron sputtering," *Journal of Applied Physics*, vol. 95, no. 8, pp. 4327–4334, 2004.

[13] S. Zhang, X. L. Bui, J. Jiang, and X. Li, "Microstructure and tribological properties of magnetron sputtered nc-TiC/ a-C nanocomposite," *Surface and Coatings Technology*, vol. 198, no. 1-3, pp. 206–211, 2005.

[14] G. Li and L. F. Xia, "Structural characterization of TiC_x films prepared by plasma based ion implantation," *Thin Solid Films*, vol. 396, no. 1-2, pp. 16–22, 2001.

[15] E. Lewin, P. O. Å. Persson, M. Lattemann et al., "On the origin of a third spectral component of C1s XPS-spectra for nc-TiC/a-C nanocomposite thin films," *Surface and Coatings Technology*, vol. 202, no. 15, pp. 3563–3570, 2008.

[16] D. M. Cao, B. Feng, W. J. Meng, L. E. Rehn, P. M. Baldo, and M. M. Khonsari, "Friction and wear characteristics of ceramic nanocomposite coatings: Titanium carbide/amorphous hydrocarbon," *Applied Physics Letters*, vol. 79, no. 3, pp. 329–331, 2001.

[17] J. C. Sánchez-López, D. Martínez-Martínez, C. López-Cartes, C. Fernández-Ramos, and A. Fernández, "A nanoscale approach for the characterization of amorphous carbon-based lubricant coatings," *Surface and Coatings Technology*, vol. 200, no. 1-4, pp. 40–45, 2005.

[18] J. Musil, P. Novák, R. Čerstvý, and Z. Soukup, "Tribological and mechanical properties of nanocrystalline-TiC/a-C nanocomposite thin films," *Journal of Vacuum Science & Technology A*, vol. 28, no. 2, pp. 244–249, 2010.

[19] Y. T. Pei, D. Galvan, J. T. M. De Hosson, and C. Strondl, "Advanced TiC/a-C:H nanocomposite coatings deposited by magnetron sputtering," *Journal of the European Ceramic Society*, vol. 26, no. 4-5, pp. 565–570, 2006.

[20] T. Schmidtová, P. Souček, V. Kudrle, and P. Vašina, "Non-monotonous evolution of hybrid PVD-PECVD process characteristics on hydrocarbon supply," *Surface and Coatings Technology*, vol. 232, pp. 283–289, 2013.

[21] U. Jansson and E. Lewin, "Sputter deposition of transition-metal carbide films—a critical review from a chemical perspective," *Thin Solid Films*, vol. 536, pp. 1–24, 2013.

[22] U. Jansson, E. Lewin, M. Råsander, O. Eriksson, B. André, and U. Wiklund, "Design of carbide-based nanocomposite thin films by selective alloying," *Surface and Coatings Technology*, vol. 206, no. 4, pp. 583–590, 2011.

[23] R. Žemlička, M. Jílek, P. Vogl et al., "Understanding of hybrid PVD-PECVD process with the aim of growing hard nc-TiC/a-C: H COATINGS using industrial devices with a rotating cylindrical magnetron," *Surface and Coatings Technology*, vol. 255, pp. 118–123, 2014.

[24] P. Souček, T. Schmidtová, L. Zábranský et al., "Evaluation of composition, mechanical properties and structure of nc-TiC/a-C:H coatings prepared by balanced magnetron sputtering," *Surface and Coatings Technology*, vol. 211, pp. 111–116, 2012.

[25] P. Souček, T. Schmidtová, V. Buršíková et al., "Tribological properties of nc-TiC/a-C: H coatings prepared by magnetron sputtering at low and high ion bombardment of the growing film," *Surface and Coatings Technology*, vol. 241, pp. 64–73, 2014.

[26] P. Souček, J. Daniel, J. Hnilica et al., "Superhard nanocomposite nc-TiC/a-C:H coatings: the effect of HiPIMS on coating microstructure and mechanical properties," *Surface and Coatings Technology*, vol. 311, pp. 257–267, 2017.

[27] U. Helmersson, M. Lattemann, J. Bohlmark, A. P. Ehiasarian, and J. T. Gudmundsson, "Ionized physical vapor deposition (IPVD): a review of technology and applications," *Thin Solid Films*, vol. 513, no. 1-2, pp. 1–24, 2006.

[28] K. Sarakinos, J. Alami, and S. Konstantinidis, "High power pulsed magnetron sputtering: a review on scientific and engineering state of the art," *Surface and Coatings Technology*, vol. 204, no. 11, pp. 1661–1684, 2010.

[29] M. Samuelsson, D. Lundin, J. Jensen, M. A. Raadu, J. T. Gudmundsson, and U. Helmersson, "On the film density using high

power impulse magnetron sputtering," *Surface and Coatings Technology*, vol. 205, no. 2, pp. 591–596, 2010.

[30] P. Scherrer, "Estimation of the size and internal structure of colloidal particles by means of röntgen," *Nachrichten von der Gesellschaft der Wissenschaften zu Göttingen*, vol. 2, pp. 96–100, 1918.

[31] W. C. Oliver and G. M. Pharr, "Measurement of hardness and elastic modulus by instrumented indentation: advances in understanding and refinements to methodology," *Journal of Materials Research*, vol. 19, no. 1, pp. 3–20, 2004.

[32] K. L. Johnson, "The correlation of indentation experiments," *Journal of the Mechanics and Physics of Solids*, vol. 18, no. 2, pp. 115–126, 1970.

[33] N. N. Greenwood and A. Earnshaw, *Chemistry of the Elements*, Elsevier, 2012.

[34] A. I. Gusev, A. A. Rempel, A. Magerl, and J., *Disorder and Order in Strongly Nonstoichiometric Compounds: Transition Metal Carbides, Nitrides and Oxides*, vol. 47, Springer Science & Business Media, 2013.

[35] J. Vlček, P. Kudláček, K. Burcalová, and J. Musil, "High-power pulsed sputtering using a magnetron with enhanced plasma confinement," *Journal of Vacuum Science and Technology A: Vacuum, Surfaces and Films*, vol. 25, no. 1, pp. 42–47, 2007.

[36] L. Toth, Ed., *Transition Metal Carbides and Nitrides*, Elsevier, 2014.

[37] E. Lewin, B. André, S. Urbonaite, U. Wiklund, and U. Jansson, "Synthesis, structure and properties of Ni-alloyed TiC_x-based thin films," *Journal of Materials Chemistry*, vol. 20, no. 28, pp. 5950–5960, 2010.

[38] J. Robertson, "Diamond-like amorphous carbon," *Materials Science and Engineering: R: Reports*, vol. 37, pp. 129–282, 2002.

[39] E. Lewin, M. Rsander, M. Klintenberg, A. Bergman, O. Eriksson, and U. Jansson, "Design of the lattice parameter of embedded nanoparticles," *Chemical Physics Letters*, vol. 496, no. 1–3, pp. 95–99, 2010.

[40] E. Lewin, O. Wilhelmsson, and U. Jansson, "Nanocomposite nc-TiC/a-C thin films for electrical contact applications," *Journal of Applied Physics*, vol. 100, no. 5, Article ID 054303, 2006.

[41] E. Lewin, M. Gorgoi, F. Schäfers, S. Svensson, and U. Jansson, "Influence of sputter damage on the XPS analysis of metastable nanocomposite coatings," *Surface and Coatings Technology*, vol. 204, no. 4, pp. 455–462, 2009.

[42] D. Binder and W. J. Sturm, "Equivalence of X-ray lattice parameter and density changes in neutron-irradiated LiF," *Physical Review*, vol. 96, no. 6, pp. 1519–1522, 1954.

[43] O. Wilhelmsson, S. Bijelovic, M. Lindquist et al., "Deposition and characterization of magnetic Ti-Fe-C nanocomposite thin films," *Thin Solid Films*, vol. 518, no. 10, pp. 2607–2616, 2010.

[44] E. Lewin, K. Buchholt, J. Lu, L. Hultman, A. L. Spetz, and U. Jansson, "Carbide and nanocomposite thin films in the Ti-Pt-C system," *Thin Solid Films*, vol. 518, no. 18, pp. 5104–5109, 2010.

[45] M. Råsander, B. Sanyal, U. Jansson, and O. Eriksson, "A first principles study of the stability and mobility of defects in titanium carbide," 2013, https://arxiv.org/abs/1303.2848.

[46] H. W. Hugosson, P. Korzhavyi, U. Jansson, B. Johansson, and O. Eriksson, "Phase stabilities and structural relaxations in substoichiometric TiC_{1-x}," *Physical Review B*, vol. 63, no. 16, 2001.

[47] X.-X. Yu, G. B. Thompson, and C. R. Weinberger, "Influence of carbon vacancy formation on the elastic constants and hardening mechanisms in transition metal carbides," *Journal of the European Ceramic Society*, vol. 35, no. 1, pp. 95–103, 2015.

[48] J. Musil, "Hard nanocomposite coatings: thermal stability, oxidation resistance and toughness," *Surface and Coatings Technology*, vol. 207, pp. 50–65, 2012.

[49] E. O. Hall, "The deformation and ageing of mild steel: III discussion of results," *Proceedings of the Physical Society Section B*, vol. 64, no. 9, pp. 747–752, 1951.

[50] N. J. Petch, "The cleavage strength of polycrystals," *Journal of the Iron and Steel Institute*, vol. 174, pp. 25–28, 1953.

[51] S. Zhang, H. L. Wang, S.-E. Ong, D. Sun, and X. L. Bui, "Hard yet tough nanocomposite coatings—present status and future trends," *Plasma Processes and Polymers*, vol. 4, no. 3, pp. 219–228, 2007.

[52] S. Vepřek and S. Reiprich, "A concept for the design of novel superhard coatings," *Journal of Thin Solid Films*, vol. 268, no. 1-2, pp. 64–71, 1995.

[53] J. Musil and J. Vlček, "Magnetron sputtering of hard nanocomposite coatings and their properties," *Surface and Coatings Technology*, vol. 142-144, pp. 557–566, 2001.

[54] J. Schiøtz, F. D. Di Tolla, and K. W. Jacobsen, "Softening of nanocrystalline metals at very small grain sizes," *Nature*, vol. 391, no. 6667, pp. 561–563, 1998.

[55] C. E. Carlton and P. J. Ferreira, "What is behind the inverse Hall-Petch effect in nanocrystalline materials?" *Acta Materialia*, vol. 55, no. 11, pp. 3749–3756, 2007.

EPJ AP
Applied Physics
EPJ.org
your physics journal

Eur. Phys. J. Appl. Phys. (2016) 75: 24716 DOI: 10.1051/epjap/2016150591

On the study of the mechanical properties of Mo-B-C coatings

Lukáš Zábranský, Vilma Buršíková, Pavel Souček, Petr Vašina, and Jiří Buršík

edp sciences

The title “The European Physical Journal” is a joint property
of EDP Sciences, Società Italiana di Fisica (SIF) and Springer

Eur. Phys. J. Appl. Phys. (2016) 75: 24716
DOI: 10.1051/epjap/2016150591

THE EUROPEAN PHYSICAL JOURNAL APPLIED PHYSICS

Regular Article

On the study of the mechanical properties of Mo-B-C coatings*

Lukáš Zábranský[1,a], Vilma Buršíková[1], Pavel Souček[1], Petr Vašina[1], and Jiří Buršík[2]

[1]Department of Physical Electronics, Faculty of Science, Masaryk University, Kotlářská 2, 61137 Brno, Czech Republic
[2]Institute of Physics of Materials, Academy of Sciences of the Czech Republic, Žižkova 22, 61662 Brno, Czech Republic

Received: 1 December 2015 / Received in final form: 14 April 2016 / Accepted: 21 April 2016

Abstract. Mo_2BC thin films show a favourable combination of high stiffness, hardness and elastic modulus together with moderate ductility. In this study we focused on the comparison of mechanical properties of Mo-B-C thin films with different structures (nanocrystalline or amorphous). The thin films were deposited on steel, hard metal and silicon substrates using DC magnetron sputtering. The mechanical properties of Mo-B-C films were studied using indentation techniques under both quasistatic and dynamic conditions using a wide range of loads from 50 μN up to 1 N. The results showed that even amorphous Mo-B-C thin films had high hardness of 19.5 ± 0.5 GPa and elastic modulus of 276 ± 5 GPa. Their hardness is comparable with the common amorphous diamond-like carbon coatings. Moreover, their fracture toughness is significantly higher. The results of mechanical tests were correlated with microstructure observations carried out using scanning and transmission electron microscopy. The images of the deformed area under the residual indentation imprints showed no cracking even after high loads or after indentation with sharp cube corner indenter.

1 Introduction

Hard and wear resistant coatings employed for protection of cutting tools exhibit high hardness and stiffness which are often accompanied with brittle deformation behaviour. Cracking can consequently lead to coating failure and thus reduces the lifetime of the coated tool. It is therefore favourable to combine high stiffness, hardness and elastic modulus with moderate ductility to reduce crack initiation and propagation. There are two criteria which are generally used for determination if the material is brittle or ductile. Pugh [1] showed that if the ratio of bulk modulus to shear modulus B/G is greater than 1.75, the material exhibits ductile metal-like behaviour. Otherwise, the material is considered brittle. Pettifor [2] showed that the value of the Cauchy pressure can also give information about ductility. Cauchy pressure is determined as the difference between elastic constants C_{12}–C_{44}. If it is negative, material is brittle. Positive Cauchy pressure, on the other hand, implies ductile behaviour.

Based on previous ab initio calculations [3,4], the material Mo_2BC has a desired combination of high Young modulus of 470 GPa and moderate ductility with $B/G = 1.74$ and Cauchy pressure of +43 GPa [3]. The Mo_2BC material belongs to nanolaminates exhibiting similar structure as the well known MAX phases [5,6] (M = transition metal, A is a group A element and X is either boron or carbon). Emmerlich et al. [3] prepared thin films of this material on Al_2O_3 substrate (temperature of 900 °C) using DC magnetron sputtering. The surface roughness measured by scanning probe microscope (SPM) was in the order of nm. The chemical composition was determined by Rutheford backscattering spectroscopy (RBS) and elastic recoil detection analysis (ERDA) as 49 at.% Mo, 27 at.% B and 24 at.% C. The Young modulus of 460 ± 21 GPa and hardness of 29 ± 2 GPa were measured by nanoindentation using the load of 5 mN. 80% of the deformation energy was dissipated during plastic deformation. The maximum depth was 290 nm and the pile-up around residual imprints was 20–50 nm high.

Bolvardi et al. [4] simulated properties of M_2BC phases for M = Ti, V, Zr, Nb, Mo, Hf, Ta, W. The highest density of valence electrons and the highest Young modulus were obtained for M = Mo, W or Ta. In another paper Bolvardi et al. [7] managed to prepare crystalline Mo_2BC thin films using high power pulsed magnetron sputtering (HPPMS) with synthesis temperature of 380 °C while the synthesis temperature in case of standard DC magnetron sputtering was found to be 550 °C. Because the crystallization temperature of as deposited amorphous Mo_2BC powder was measured by differential scanning calorimetry as 820 °C, the ion bombardment induced surface diffusion was considered as the main reason for the lower synthesis temperature.

[a] e-mail: zerafel@mail.muni.cz

* Contribution to the topical issue "6th Central European Symposium on Plasma Chemistry (CESPC-6)", edited by Nicolas Gherardi, Ester Marotta and Cristina Paradisi

Table 1. Summarized deposition conditions, "(p)" means that the power was pulsed with frequency 350 kHz and duty cycle 65%. Otherwise, the power was DC.

Sample name	Power on a target [W]				Bias voltage [V]	Deposition time [min]	Temperature [°C]
	B_4C	C	Mo	Mo_2BC			
A1	–	–	–	250 (p)	–	180	No heating
A2	–	–	–	250 (p)	−200	420	No heating
C1	128	278 (p)	91	–	−200	480	350
C2	128	250 (p)	110	–	–	480	500
C3	104	281	84	–	−200	300	No heating

In this work the mechanical properties of nanocrystalline (partially crystallized) and amorphous Mo-B-C thin films were compared. The films were deposited on steel, hard metal and silicon substrates using DC magnetron sputtering. Even the amorphous films showed relatively high hardness and elastic modulus which could be compared to common diamond-like carbon (DLC) material discussed see for example in [8]. The study of residual indentation imprints for the loads up to 1 N revealed that no cracking occurred even after the indentation depth exceeded the film thickness. This implies very good fracture toughness of the studied material.

2 Experimental

Several samples were prepared using magnetron sputtering of (i) a single Mo_2BC target (Mo-B-C coatings marked with A) or (ii) three targets: B_4C, C and Mo (Mo-B-C coatings marked with C) in order to better control the stoichiometry. The hard-metal (cemented tungsten carbide, WC-Co), high speed steel (HSS) and silicon substrates were ultrasonically cleaned in a degreasing agent and then placed in the chamber using load-lock system. Prior to the deposition process all substrates were cleaned in argon plasma for 20 min. The deposition pressure was 0.3 Pa. The deposition conditions are summarized in Table 1. In case of HSS substrate an 80 nm thick molybdenum interlayer was deposited prior the deposition of Mo-B-C film. The temperature on the substrate holder for sample C1 and C2 was 350 °C and 500 °C, respectively. The RF bias −200 V was used in some cases (see Tab. 1). The thickness of all coatings was in the range from 1 to 2 μm.

The hardness and elastic modulus were measured and evaluated by depth sensing nanoindentation technique performed on a Hysitron TI950 Triboindenter equipped with a Berkovich tip. The tip diameter was less than 50 nm. The nanoscale measuring head with resolution of 1 nN and load noise floor less than 30 nN was used for this study. Several testing modes were used in the range of indentation loads from 0.1 to 10 mN, namely quasistatic nanoindentation test, quasistatic nanoindentation with several unloading segments and nanodynamic mechanical analysis (nanoDMA) in the range from 0.1 to 300 Hz. The quasistatic indentation tests were carried out in load controlled regime using constant loading rate of 0.2 mN/s. Both the partial unload regime and the nanodynamical analysis were carried out in constant strain rate regime. The pre-load of 2 μN was set to ensure good contact between the tip and the surface. The indenter tip calibration was carried out for low loads (indentation depths <100 nm). The depth profiles of the hardness and elastic modulus were carried out in the load range from 0.25 to 10 mN. The standard procedure proposed by Oliver and Pharr [9] was used for the evaluation of the hardness and elastic modulus.

Further, the cube-corner indenter with tip radius of about 30 nm and with centerline-to-face angle of 34.3° was used to study the prepared films. This very sharp indenter is commonly used to produce well-defined cracks around indentation prints in order to estimate the fracture toughness of thin films at very small scales.

Moreover, several quasistatic indentation test were performed using a Fisherscope H100 instrumented indentation tester at maximum load of 1 N in order to study the differential hardness [10,11] and the fracture resistance of the coating/substrate system. Berkovich indenter with tip radius of 200 nm was used for these tests. The load increase was controlled according to function $L = Ct^2$, where L is the load, t is the time and $C = 2.5$ mNs^{-2}. The differential hardness was calculated as the derivative of the indentation load according to the contact area. The differential hardness dependence on the indentation depth is used to visualize the defect creation in the tested materials.

X-ray diffraction was used in order to determine whether the material is crystalline, nanocrystalline or amorphous. Measurements of X-ray diffraction were performed on Rigaku Smartlab X-ray diffractometer with a fixed angle of incidence. The grazing incidence configuration was used. The details of microstructure in the vicinity of indentation prints made with indentation load of 1 N were studied by means of electron microscopy. Thin lamellas were prepared using a focused ion beam (FIB) technique in a scanning electron microscope (SEM) LYRA 3 XMU FEG/SEM×FIB by Tescan. The lamellas were further studied using transmission electron microscopes (TEM) Philips CM12 STEM (thermoemission source, accelerating voltage 120 kV) and JEOL JEM-2100F (FEG, accelerating voltage 200 kV). The surface morphology was analyzed by an atomic force microscope Ntegra Prima NT-MDT in a semi-contact mode. The area of 10×10 μm was studied using a 20 μm/s scan rate.

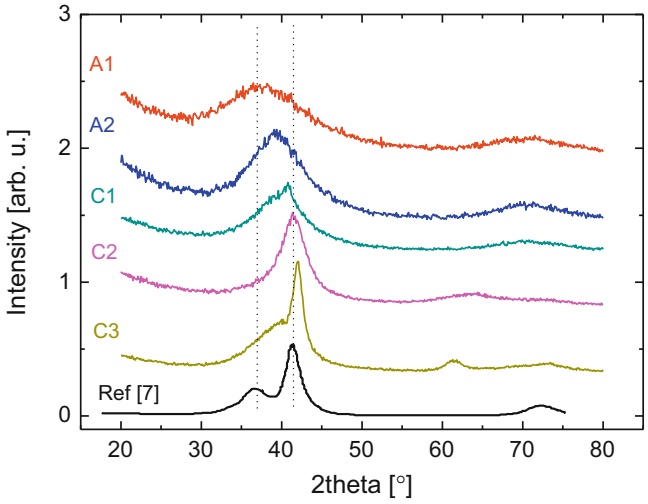

Fig. 1. The diffraction patterns of five films compared with Ref. [7].

3 Results and discussion

The microstructure of Mo-B-C films deposited on WC substrates was studied by both, X-ray diffraction and TEM. The diffractograms presented in Figure 1 are compared with results obtained by Bolvardi et al. [7] on Mo_2BC film prepared using high power pulsed magnetron sputtering (HPPMS) at substrate temperature of 480 °C. According to [7], the appearance of two distinctive peaks at around 36° and 42° indicates the crystalline character of the films. The peak around 42° becomes stronger for films with increasing crystalline content in Mo-B-C films and it originates mainly from Mo_2BC (1 1 1) signal, however, it may be overlapped by Mo_2BC (0 8 0). The wide band at around 36° is an overlap of several peaks instead of signal arisen from amorphous Mo-B-C matrix. The diffractogram presented at the top in Figure 1 shows only a wide band at around 36° suggesting the formation of an amorphous structure for coating marked as A1. The diffractogram of sample A2 contains one wide band situated between 36° and 42° which may represent some transition between amorphous and nanocrystalline state. The combined Rutheford backscattering spectroscopy (RBS) and the elastic recoil detection analysis (ERDA) showed that all coatings prepared using sputtering of one Mo_2BC target were far from the stoichiometric composition (the atomic percentage of Mo differed from the stoichiometric one by more than 10%). The sample group C was prepared using sputtering of three targets (see Tab. 1). What dominates in the diffractograms of this group is a more or less asymmetric broad peak between 36° and 42°, which arises from an overlap of several peaks including an amorphous band. This peak suggests partially crystalline (nanocomposite) structure for samples C1, C2 and C3, which was also proven by TEM study. Moreover, the diffractogram of sample C3 exhibits a significant increase in Mo_2BC (1 1 1) signal indicating substantial increase in volume fraction of Mo_2BC crystallites. The sputtering of three targets (see Tab. 1) enabled a better control of the film stoichiometry, therefore the C samples prepared using this method exhibit a partial crystallinity even without any sample heating as it is proven in case of sample C3.

The microstructure of amorphous coating A1 deposited on hard metal substrate is depicted on TEM micrographs in Figure 2. A wavy coating/substrate interface and heavily deformed grains of hard metal, but no cracks or marks of adhesive failure are observed (Fig. 2a). Both the high resolution image and the selected area diffraction (SAD) pattern (Fig. 2b) confirm the amorphous character of the deposited layer.

The microstructure of nanocrystalline coating C3 deposited on an HSS substrate is shown in Figure 3. The thin lamella prepared by FIB in SEM (Fig. 3a) represents the central vertical section of an indentation print. Global TEM view (Fig. 3b) shows the deformed structure free of any cracks and interfacial failures. A detailed view (Fig. 3c and a high resolution image in Fig. 3d) shows nanosized columnar grains with amorphous material in between.

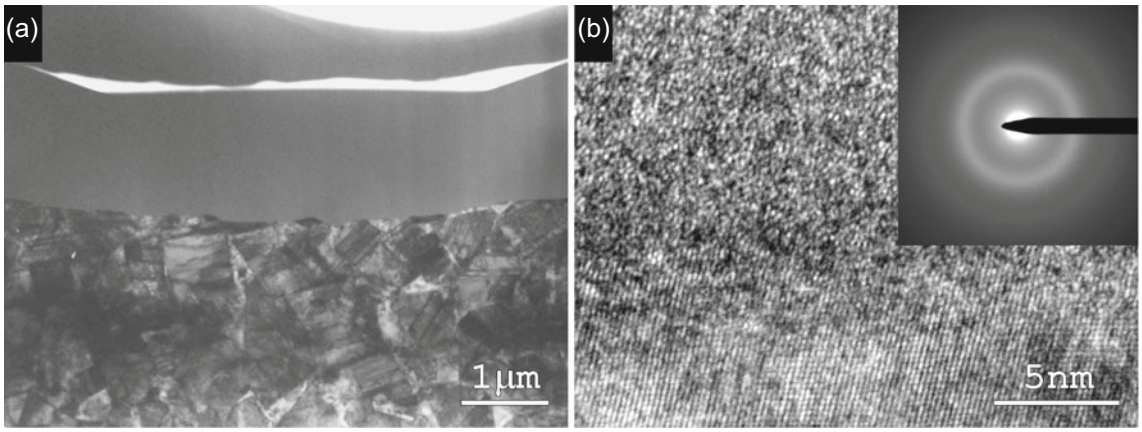

Fig. 2. The microstructure of amorphous coating A1 deposited on hard metal substrate. A global TEM view of the volume under indentation print (a) and a high resolution TEM micrograph of WC grain at the bottom part and an amorphous layer above with SAD pattern (b).

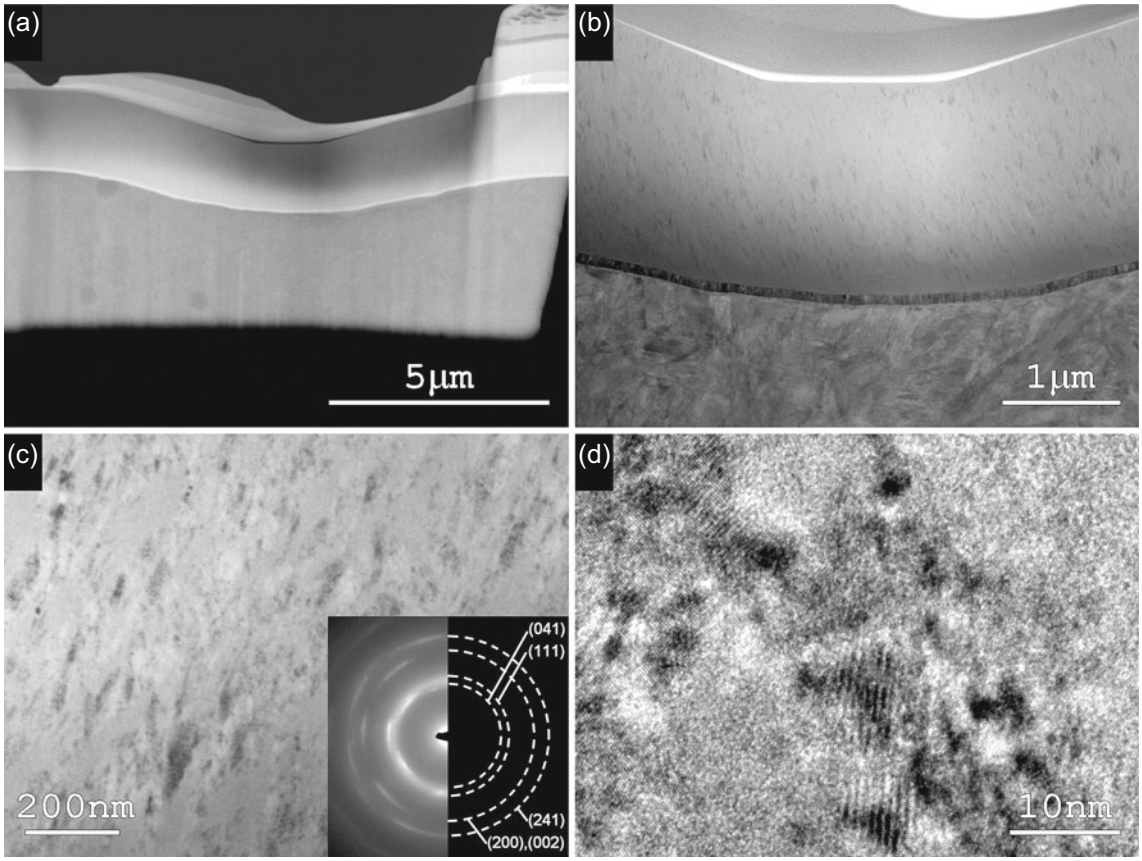

Fig. 3. The microstructure of the coating C3 deposited on an HSS substrate. The final stage of lamella preparation using a FIB in SEM, signal of backscattered electrons (a), a global TEM view of the volume under indentation print (b), a detail of the columnar microstructure with inserted SAD pattern (c) and a high resolution TEM micrograph (d).

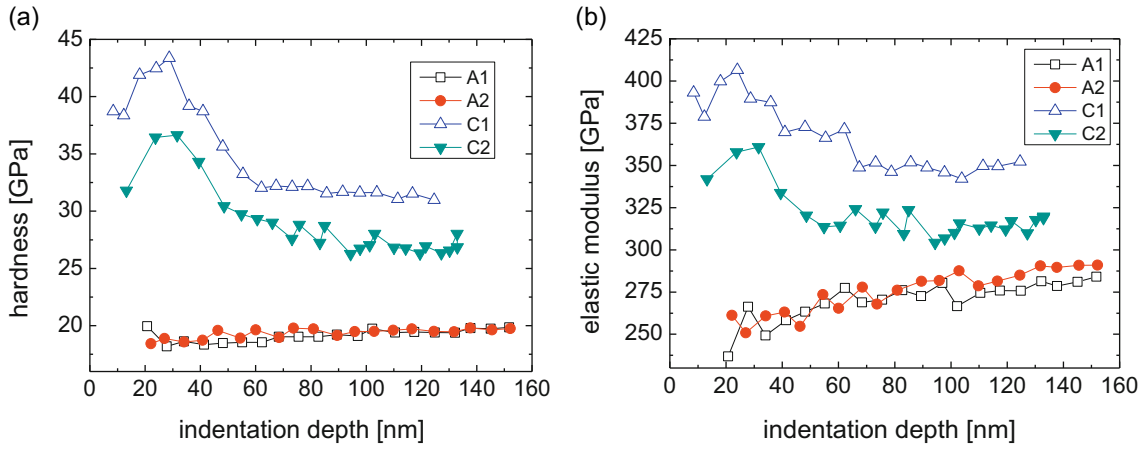

Fig. 4. The evolution of (a) hardness and (b) elastic modulus as functions of maximum indentation depth. The behaviour of these parameters differed with depth for amorphous and nanocrystalline coatings due to different intrinsic stress and microstructure.

The SAD pattern in Figure 3c confirms the Mo_2BC orthorhombic lattice (ICSD entry no. 043318, [12]). The diffraction patterns are assigned to (0 4 1), (1 1 1), (2 0 0), (0 0 2) and (2 4 1) planes of the Mo_2BC structure. The structure of SAD pattern indicates the presence of preferential orientation for Mo_2BC nanocrystallites.

The evolution of hardness and elastic modulus for all four samples deposited on hardmetal substrates is presented in Figure 4 as a function of maximum indentation depth. The error of these measurements was always <10%. Because the thickness of the coatings was larger than 1.0 μm, the values of hardness and elastic modulus taken from depths $<$ 100 nm should not be influenced by the substrate. However, in case of partially crystalline coatings C1 and C2 there is a significant increase in the hardness as well as elastic modulus at

Table 2. Calculated hardness H, elastic modulus E and their ratios H/E and H^3/E^2 for all five films.

Sample name	H [GPa]	E [GPa]	H/E	H^3/E^2 [GPa]
A1	19.4 ± 0.5	272 ± 5	0.071	0.099
A2	19.6 ± 0.5	280 ± 5	0.070	0.096
C1	27.2 ± 0.9	313 ± 11	0.087	0.205
C2	31.6 ± 0.8	345 ± 9	0.091	0.259
C3	20.6 ± 2.0	275 ± 16	0.075	0.116

the sample surface. The tip was carefully calibrated in the region of low indentation depths (between 20 nm and 100 nm) on certificated fused silica standard, therefore this increase does not arise from artefacts connected with imperfect indenter tip. The increased surface hardness compared to the bulk part of samples C1 and C2 is probably caused by internal stress evolution during the growth and due to nonhomogeneous microstucture through depth profile of the nanocomposite films. For comparison of the material parameters in Table 2, the values from greater depths were taken. The optimum depth for bulk hardness and elastic modulus evaluation was considered for the maximum indentation depth of 100 nm. This indentation depth is less than 10% of the film thickness.

The measured and calculated hardness H, elastic modulus E and their ratios H/E (measure of toughness) and H^3/E^2 (resilience) are presented in Table 2. The highest hardness of 31.6 ± 0.8 GPa was found for nanocrystalline sample C1, the highest elastic modulus was 345 ± 9 GPa for the same sample. The average hardness for amorphous samples was 19.5 ± 0.5 GPa and elastic modulus 276 ± 5 GPa.

The cube corner indenter was used and several imprints with maximum load of 10 mN were performed in order to study the crack resistance. The load-displacement curves revealed no sudden pop-in events in any of the samples. There was no cracking induced by the indentation up to 10 mN which indicated very good crack resistance [3]. In Figure 5a, there is a typical load-displacement curve, here for sample C1. Several measurements of differential hardness for sample C1 are plotted in Figure 5b. Differential hardness is calculated numerically from the loading curves for the maximum load of 1 N and it describes the instantaneous resistance of the material to deformation. It is important to state that the initial part (about first 200 nm) of the differential hardness curves strongly depends on the local structure, and is therefore very sensitive to any inhomogeneities such as grain boundaries. No large sudden drops in evolution of differential hardness also implied no cracking events, even for the load of 1 N. Here the maximum indentation depth exceeded the coating thickness and indentation induced plastic

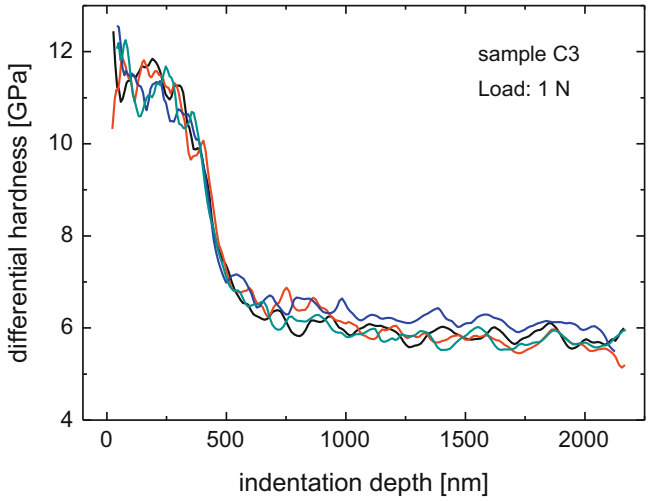

Fig. 6. The differential hardness dependence on the indentation depth for sample C3. The sudden differential hardness decrease from indentation depth of about 0.25 μm is caused by the expansion of the deformation zone into the substrate. The indentation response of the studied sample is fully controlled by plastic deformation of the HSS substrate from indentation depths of about 0.5 μm. Although the maximum indentation depth exceeded the coating thickness, indentation induced cracking was not observed.

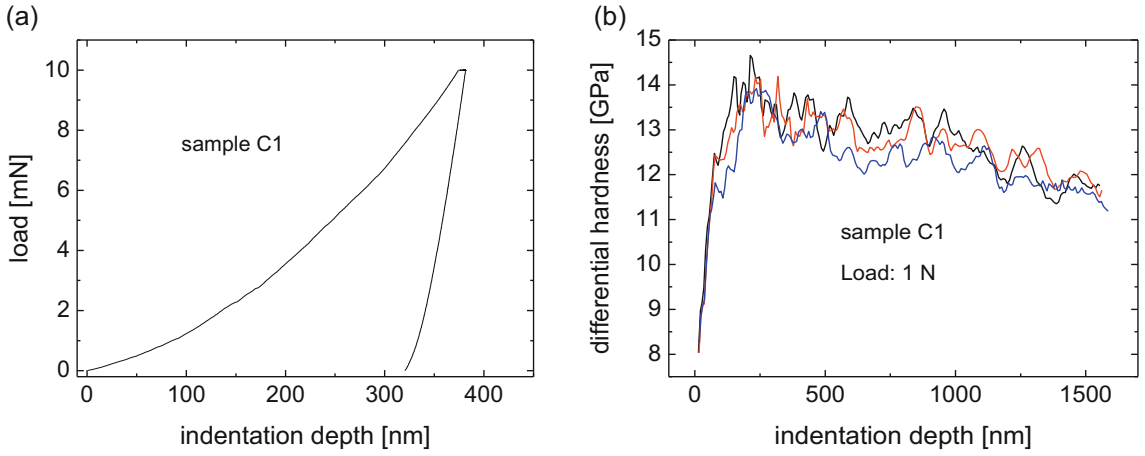

Fig. 5. (a) The example of load/displacement curve for maximum load of 10 mN performed using a cube corner indenter, and (b) three curves of differential hardness dependence on the indentation depth. No pop-in events in load-displacement curve or sudden drops in differential hardness indicated no cracking inside. The film C1 was deposited on hard metal substrate (WC).

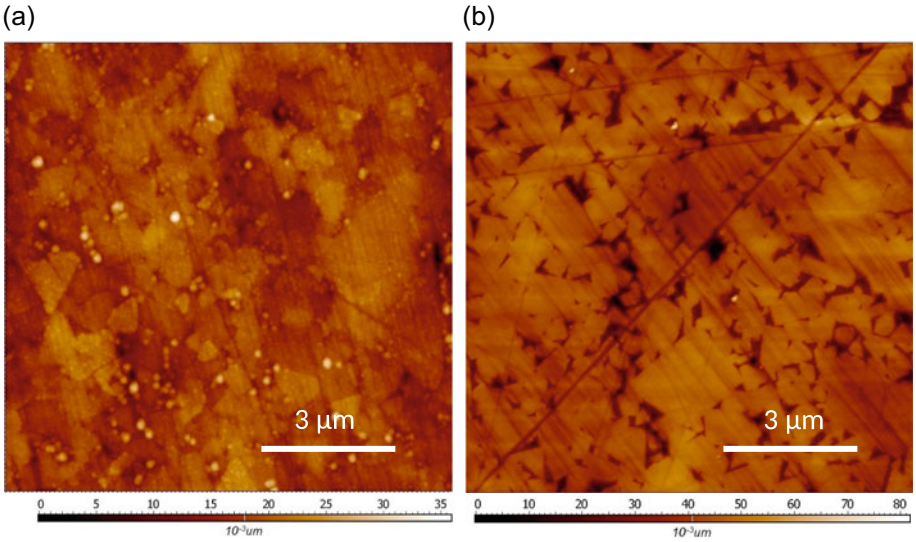

Fig. 7. The AFM images of (a) surface of the sample C2 and (b) uncoated hardmetal substrate.

deformation was controlled by the plastic behaviour of the substrate.

The hardness of amorphous Mo-B-C coatings is comparable with the hardness of most often used amorphous diamond-like carbon coatings [8,13–16]. However, the elastic modulus is significantly higher. Moreover, the crack resistance of the coatings is also substantially enhanced. Even though the maximum indentation depth exceeded the thickness of the coating, only plastic deformation of the coating and the substrate occurred. There were no pop-in events on the loading curve suggesting that no cracks occurred during the indentation (see Fig. 5a). This was also confirmed by the TEM results (see Figs. 2a, 3a and 3b) as well as by depth profiles of differential hardness (see Figs. 5b and 6) where sudden drops indicating cracking were not detected. The sudden differential hardness decrease from indentation depth around 0.25 μm was caused by the expansion of the deformation zone into the softer HSS substrate. The indentation response of the studied sample was fully controlled by plastic deformation of the HSS substrate from indentation depths around 0.5 μm. The hardness and elastic modulus of nanocrystalline Mo-B-C coatings are comparable with common hard coatings used for protective applications [17,18], for example nc-TiC/a-C:H [11,19–24]. However, fracture toughness is generally better for Mo-B-C coatings, especially when compared to nc-TiC/a-C:H that contains more carbon. The nc-TiC/a-C:H coatings with higher titanium content have excellent fracture toughness but, on the other hand, their hardness is generally lower [11,21]. The excellent resistance against brittle failure during tensile testing of Mo_2BC film on copper substrate was also reported [25].

The surface was studied by atomic force microscopy and the results for the nanocrystalline sample C2 are depicted in Figure 7a. The surface of uncoated polished and plasma cleaned hardmetal is in Figure 7b. From Figure 7b it is clear that the uncoated hardmetal contains deeper holes. The peak-to-valley height of hardmetal was 81 nm and the average roughness R_a = 5.1 nm. On the other hand, the calculated peak-to-valley height of the sample C2 was smaller and equaled approximately 36 nm. The average surface roughness of sample C2 was $R_a = 2.1$ nm. The coating obviously filled the holes during its growth and generally smoothed the surface.

4 Conclusion

Magnetron sputtering process was used for the preparation of five Mo-B-C coatings with different microstructures. The correct methodology for hardness and elastic modulus evaluation was developed. Different evolutions of hardness and elastic modulus depending on maximum indentation depth for amorphous and nanocrystalline samples were carried out. This was caused by different inner stress evolution during growth and by different inner structures. The Mo-B-C coating showed very favorable combination of high hardness and elastic modulus together with high fracture toughness. The average hardness of Mo-B-C coatings with amorphous structure was found as 19.5 GPa and their elastic modulus was around 276 GPa. The nanocrystalline Mo-B-C coatings have approximately the same hardness and elastic modulus as the typical nc-TiC/a-C:H coatings. However, the fracture toughness is generally higher for Mo-B-C films. The differential hardness curves and TEM images from the area under the indentation imprint proved that there was no crack formation in the vicinity of the imprints. Also the adhesion after indentation up to 1 N remained sufficient and no delamination occurred. The surface of the samples was studied using AFM. From the presented images and calculated surface roughness it was proven that the Mo-B-C coating smoothed the surface, surface roughness decreased from 5.1 nm for uncoated hardmetal to 2.1 nm.

This research has been supported by the project CZ.1.05/2.1.00/03.0086 funded by European Regional Development

Fund and project LO1411 (NPU I) funded by Ministry of Education Youth and Sports of Czech Republic and The Czech Science Foundation (Project 15-17875S).

References

1. S.F. Pugh, Phil. Mag. **45**, 823 (1954)
2. D.G. Pettifor, Mater. Sci. Technol. **8**, 345 (1992)
3. J. Emmerlich, D. Music, M. Braun, P. Fayek, F. Munnik, J.M. Schneider, J. Phys. D: Appl. Phys. **42**, 185406 (2009)
4. H. Bolvardi, J. Emmerlich, M. to Baben, D. Music, J. von Appen, R. Dronskowski, J.M. Schneider, J. Phys.: Condens. Matter **25**, 045501 (2013)
5. D. Music, J.M. Schneider, JOM **59**, 60 (2007)
6. M.W. Barsoum, T. El-Raghy, Am. Sci. **89**, 334 (2001)
7. H. Bolvardi, J. Emmerlich, S. Mráz, M. Arndt, H. Rudigier, J.M. Schneider, Thin Solid Films **542**, 5 (2013)
8. J. Robertson, Mat. Sci. Eng. R **37**, 129 (2002)
9. W.C. Oliver, G.M. Pharr, J. Mater. Res. **19**, 3 (2004)
10. B. Wolf, Phil. Mag. Phil. Mag. Lett. **86**, 5251 (2006)
11. L. Zábranský, V. Buršíková, J. Daniel, P. Souček, P. Vašina, J. Dugáček, P. St'ahel, O. Caha, J. Buršík, V. Peřina, Surf. Coat. Technol. **267**, 32 (2015)
12. G. Bergerhoff, I.D. Brown, in "*Crystallographic Databases*", edited by F.H. Allen et al. (International Union of Crystallography, Chester, England, 1987)
13. A. Grill, Diam. Relat. Mater. **8**, 428 (1999)
14. D. Franta, V. Buršíková, I. Ohlídal, P. St'ahel, M. Ohlídal, D. Nečas, Diam. Relat. Mater. **16**, 1331 (2007)
15. S. Neuville, A. Matthews, Thin Solid Films **515**, 6619 (2007)
16. S. Neuville, Surf. Coat. Technol. **206**, 703 (2011)
17. A.A. Voevodin et al., in *Nanostructured Thin Films and Nanodispersion Strengthened Coatings*, edited by A.A.Voevodin, D.V. Shtansky, E.A. Levashov, J.J. Moore (NATO Science Series II. Vol. 155, Kluwer Academic Sciences, Dordrecht, 2004)
18. J. Musil, Surf. Coat. Technol. **207**, 50 (2012)
19. A. Czyżniewski, W. Prechtl, J. Mater. Proc. Technol. **157–158**, 274 (2004)
20. P. Souček, T. Schmidtová, L. Zábranský, V. Buršíková, P. Vašina, O. Caha, M. Jílek, A.E. Mel, P.Y. Tessier, J. Schäfer, J. Buršík, V. Peřina, R. Mikšová, Surf. Coat. Technol. **211**, 111 (2012)
21. L. Zábranský, V. Buršíková, P. Souček, P. Vašina, T. Gardelka, P. St'ahel, O. Caha, V. Peřina, J. Buršík, Surf. Coat. Technol. **242**, 62 (2014)
22. Y.T. Pei, D. Galvan, J.Th.M. De Hosson, C. Strondl, J. Eur. Ceram. Soc. **26**, 565 (2006)
23. Y.T. Pei, D. Galvan, J.Th.M. De Hosson, A. Cavaleiro, Surf. Coat. Technol. **198**, 44 (2005)
24. P. Vašina, P. Souček, T. Schmidtová, M. Eliáš, V. Buršíková, M. Jílek, M. Jílek Jr., J. Schäfer, J. Buršík, Surf. Coat. Technol. **205**, s53 (2011)
25. S. Djaziri, S. Gleich, H. Bolvardi, C. Kirchlechner, M. Hans, C. Scheu, J.M. Schneider, G. Dehm, Surf. Coat. Technol. **289**, 213 (2016)

Vacuum 138 (2017) 199–204

Contents lists available at ScienceDirect

Vacuum

journal homepage: www.elsevier.com/locate/vacuum

Thermal stability of hard nanocomposite Mo-B-C coatings

L. Zábranský [a, *], V. Buršíková [a], P. Souček [a], P. Vašina [a], J. Dugáček [a], P. Sťahel [a], J. Buršík [b], M. Svoboda [b], V. Peřina [c]

[a] Department of Physical Electronics, Faculty of Science, Masaryk University, Kotlářská 2, Brno, CZ–61137, Czech Republic
[b] Institute of Physics of Materials, Academy of Sciences of the Czech Republic, Žižkova 22, Brno, CZ–61662, Czech Republic
[c] Nuclear Physics Institute, Academy of Sciences of the Czech Republic, v.v.i., Řež 130, CZ–25068, Czech Republic

ARTICLE INFO

Article history:
Received 15 July 2016
Received in revised form
1 December 2016
Accepted 13 December 2016
Available online 14 December 2016

Keywords:
Thermal stability
Mo_2BC coatings
Hardness
Fracture resistance

ABSTRACT

In the present work, nanocomposite Mo-B-C coatings were deposited on high speed steel and hard metal substrates by magnetron sputtering of three targets. These coatings were subjected to annealing to final temperatures in the range from 500 °C to 1000 °C. It was found that the as deposited Mo-B-C coatings exhibited hardness of ~20 GPa, nanocomposite microstructure with very fine grains (~2 nm) and low degree of crystallinity. The X-ray diffraction and transmission electron microscopy together with selective area electron diffraction were used to study the temperature induced changes of the microstructure of the coating and its crystallinity. The annealing process significantly improved the hardness (from ~20 GPa to ~30 GPa) and effective elastic modulus (from initial 330 GPa–500 GPa) of coatings while their resistance to fracture was kept sufficiently high.

1. Introduction

Recently, there has been an increased interest in boron and carbon based nanolaminate coatings such as Mo_2BC with similar structure to the so-called MAX phases [1,2] (M = transition metal, A is a group A element and X is either boron or carbon). The Mo_2BC material exhibits orthorhombic structure with the *Cmcm* space group (unit cell with large ratio of $b/a = 5.6$) and consists of face-sharing Mo_6B trigonal prismatic and Mo_6C octahedral (cubic rock-salt coordination) building blocks. Previous *ab initio* calculations [3,4] and subsequent experimental work [3,5,6] proved that Mo_2BC coatings exhibit a highly demanded combination of high hardness and Young's modulus which is accompanied by moderate ductility. These properties enable to reduce the crack initiation and propagation in the coating. Emmerlich et al. [3] synthesized crystalline Mo_2BC thin films on Al_2O_3 substrate using DC (direct current) magnetron sputtering with the deposition temperature of 900 °C. The Young's modulus of 460 ± 21 GPa and hardness of 29 ± 2 GPa were measured by nanoindentation using a load of 5 mN. Bolvardi et al. [7] managed to prepare crystalline Mo_2BC thin films using high power pulsed magnetron sputtering (HPPMS) with synthesis temperature of 380 °C while the synthesis temperature in case of standard DC magnetron sputtering was found to be at least 550 °C. In our previous papers [5,8], we reported on a low temperature deposition of Mo-B-C coatings using HPPMS and DC magnetron sputtering of either one Mo_2BC target or three targets: B_4C, C and Mo with or without additional substrate heating. In case of Mo_2BC target it was difficult to control the stoichiometry of the deposited samples, most of the coatings prepared by employing only the Mo_2BC target showed amorphous microstructure. Using sputtering of three targets we were able to control better the stoichiometry and the related microstructure of growing coatings. In general, the synthesized coatings exhibited different mechanical properties: their hardness ranged from ~19 GPa for amorphous coatings to ~32 GPa for nanocomposite coatings. According to our previous TEM study [5], the nanocomposite coatings consisted of nanosized Mo_2BC grains (2–10 nm) embedded in amorphous matrix. The as deposited coatings showed very good resistance against fracture due to their moderate ductility, predicted and calculated in previous studies [3,4]. It was concluded that these coatings have potential application as protective coatings for cutting tools.

However, for cutting tool applications the hardness and toughness are not the only important characteristics. The tools protected by hard coatings often operate at elevated temperatures and thus their thermal stability is also crucial. In general, the thermal activation can lead to the enhancement of diffusion, e.g. outward diffusion of hydrogen in case of hydrogenated DLC coatings [9–12] or inter-diffusion at the interface [13], changes in size, shape or

* Corresponding author.
E-mail address: zerafel@mail.muni.cz (L. Zábranský).

http://dx.doi.org/10.1016/j.vacuum.2016.12.016
0042-207X/

composition of grains such as recrystallization, segregation or grain growth processes [14,15], phase transitions [16] or stress relaxations [17]. These undesired effects often act as limiting factors in applications of protective coatings and, moreover, the mismatched coefficients of thermal expansion (CTE) of the substrate and the coating can often lead to adhesive failure. On the other hand, the thermal treatment can also improve some of the mechanical properties, e.g. age hardening of TiAlN due to phase decomposition [16].

Although Mo_2BC material in its bulk form is known from 1960s [18], only few research papers have been published so far in the area of thermal stability of Mo-B-C coatings. Bolvardi et al. [7] discussed the thermal annealing of amorphous Mo_2BC powder which was studied by differential scanning calorimetry and X-ray diffraction. It was shown that from 820 °C the bulk diffusion induced crystallization occurred which resulted in several distinguished Mo_2BC and Mo_2C diffraction peaks. However, the crystallization temperature was significantly lower for HPPMS or DC sputtering where the surface diffusion induced by ion bombardment was reported to be the main reason for this decrease of the crystallization temperature.

As it was shown by Bolvardi et al. [7], the annealing of the Mo_2BC powder resulted in the increase of the degree of crystallization. One of the goals of the present work was to determine whether the crystallization mechanism is performed in the same way in the case of thin Mo-B-C coatings. In order to study the influence of the annealing temperature on the degree of crystallization and the subsequent changes in the mechanical properties, several Mo-B-C coatings were prepared using HPPMS and DC magnetron sputtering. The deposition conditions were chosen in order to prepare coatings with similar initial properties and microstructures as in our previous study [5], i.e. coatings with nanocomposite microstructure, lower degree of crystallinity and hardness of ~20 GPa. In order to study the thermally induced changes the samples were measured using nanoindentation, scanning electron microscopy (SEM) to study the potential fracture around the residual imprints made by nanoindentation and GI-XRD to study the crystallinity changes after the annealing process.

2. Experimental

All discussed Mo-B-C thin films were prepared using magnetron co-sputtering of three targets: B_4C, Mo and C using sputtering system with a cylindrical chamber ø 50 cm × 50 cm. The hard metal (cemented tungsten carbide WC-Co, with [Co] = 10 at.%) and high speed steel (HSS) were ultrasonically cleaned in a degreasing agent and then placed in the chamber using a load-lock system. Prior to the deposition process all substrates were cleaned in argon plasma (pressure 0.3 Pa) for 20 min, here the radiofrequency (RF, 13.56 MHz) power of 100 W was applied on the substrate holder. After the cleaning of the substrate, the deposition commenced. The biasable substrate holder was located 28 cm below the targets and its rotation was set to 5 rpm during the whole deposition process in order to ensure good homogeneity of the growing films. The deposition conditions were: 128 W DC power on the B_4C target, 110 W DC on the Mo target and pulsed power of 250 W with repetition frequency of 350 kHz and off-time of 1 μs (duty cycle of 45%) applied on the C target. The deposition pressure was 0.1 Pa and the duration 480 min. Neither additional external heating on the substrate nor bias voltage were used during the deposition of the studied coatings as well as no interlayer enhancing the adhesion to above mentioned substrates was introduced.

The thermal stability of the films was investigated as a function of thermal annealing under UHV conditions. The furnace chamber was evacuated to the base pressure of about 10^{-5} Pa. The films were annealed in the resistively heated laboratory furnace Classic Clare 4.0 to several different final temperatures depending on the substrate material. The studied samples were subjected to annealing with constant heating rate of 10 °C/min. The coatings on hard metal substrate were annealed up to 1000 °C and in case of the HSS substrate, because of its lower thermal stability [15], the coatings underwent annealing up to 500 °C, 600 °C and 700 °C. After achieving the desired temperature, it was kept constant for 30 min in case of all experiments. Then the samples cooled down in vacuum for approximately 12 h. Afterwards, the nanoindentation measurements, X-ray diffraction, SEM and TEM studies were performed in order to determine changes in microstructure and mechanical properties.

The hardness and reduced elastic modulus were measured and evaluated using a depth sensing indentation method performed on a Hysitron TI950 Triboindenter equipped with a Berkovich tip. The mounted nanoscale measuring head with resolution of 1 nN and load noise floor lower than 30 nN allow to measure in the load range from 50 μN to 11 mN. Several testing methods were used, e.g. classic quasistatic test or quasistatic test with several partially unloading segments. The quasistatic indentation tests were carried out in load controlled regime using a constant loading rate of 0.2 mN/s. The indenter tip calibration was carried out for low loads (indentation depths < 100 nm). For the evaluation of the measured data, the standard procedure proposed by Oliver and Pharr [19] was used. The differential hardness H_{dif} [20,21], calculated as $H_{dif} = k\partial L/\partial(h^2)$, where L is the applied load, k is a constant depending on the indenter and h is the indentation depth, was measured using Fischerscope H100 microindentation tester equipped with a Berkovich tip. The quasistatic test with the load of 1 N was used in order to determine the loads or depths where the substrate starts to influence the measurement of the hardness or to detect cracking possibly emerging during deformation. The residual imprints after microindentation tests with the Fischerscope H100 and the surface of coatings as deposited and after annealing were analyzed on scanning electron microscope MIRA 3 FEG SEM with the accelerating voltage of 15 kV.

The coating microstructure was studied by means of electron microscopy using a Tescan LYRA 3XMU SEM × FIB scanning electron microscope (SEM), a Philips CM12 STEM transmission electron microscope (TEM) operating at 120 kV and a JEOL 2100F high resolution TEM. Thin lamellar cross sections for TEM observations were prepared using a focussed ion beam (FIB) in SEM.

Scratch tests were carried out with a Revetest Scratch Tester (Anton Paar) equipped with a 200 μm diamond Rockwell indenter. A progressive scratch of load with loading rate of 15 N/min from 1 N to 16 N on a 8 mm path was applied to all samples. X-ray diffraction was used in order to determine the inner structure and level of crystallinity of coatings. The measurements were performed on Rigaku Smartlab X-ray diffractometer with a grazing angle of incidence configuration with an incidence angle of 0.5°. The Rutheford backscattering spectroscopy (RBS) using ion beam provided by the tandem accelerator Tandetron MC 4130 was applied to determine the atomic composition of the studied samples. For this purpose, the proton projectiles with energies of 1740 (higher sensitivity to C content) and 2700 keV (higher sensitivity to B content) impinging vertically on the samples were utilized. The backscattered protons were analyzed at the scattering angle of 170°.

3. Results and discussion

The atomic composition of Mo-B-C coatings on carbon substrates was determined using RBS. The deposition conditions resulting in coatings with composition near to stoichiometric Mo_2BC ([Mo] = 49.9 at.%, [B] = 23.2 at.%, [C] = 23.2 at.%,

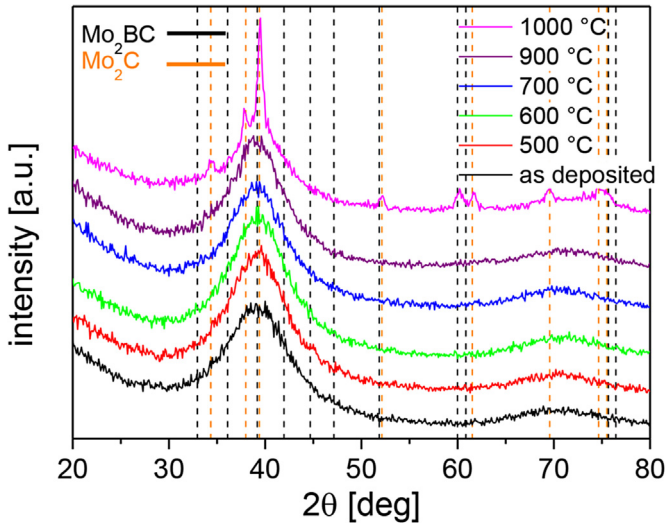

Fig. 1. The comparison of diffractograms for Mo_2BC coatings as deposited and annealed to 500 °C, 600 °C, 700 °C and 1000 °C.

[Ar] = 3.3 at.%, [O] = 0.4 at.%) were chosen for preparation of the set of coatings for the thermal stability studies. The RBS data obtained on Mo-B-C coating deposited on steel substrate showed of approximately 10% higher amount of Mo and of 10% lower amount of carbon as in the case of coating on carbon substrate, however, in case of steel substrate the sensitivity of B and C estimation is limited by overlapping their signals in spectra by signal of the steel substrate.

The influence of the annealing temperature on the degree of crystallization of the selected Mo-B-C coating was studied using X-ray diffraction technique. If we compare the X-ray diffractograms for Mo_2BC coatings as deposited and annealed to 500 °C, 600 °C, 700 °C, 900 °C and 1000 °C, one can see that there is no indication for any microstructural change (see Fig. 1) up to 900 °C. All diffractograms up to 900 °C are almost identical which means that the thermally induced microstructural changes are very fine and subtle. However, the diffraction region between 35° and 45 consists of many possible diffraction peaks from Mo_2BC and Mo_2C phases. Taking into account the fact that the coating is composed of very fine grains of nanometer size, the particular diffraction peaks could be wide and, therefore, their signals can be overlapped by each other forming such broad band. This broad band can hinder the observation of any small scale microstructural changes. This effect was also observed in our previous work [5] where the studied coatings also exhibited the fine-grained microstructure. Significant change in the diffractogram occurred after annealing to 1000 °C where several sharp peaks emerged. The main cause of their origin is the presence of the β-Mo_2C phase with additional contribution of the Mo_2BC phase. The β-Mo_2C peaks are sharp suggesting that a pronounced grain growth occurred.

A Philips CM12 STEM transmission electron microscope (TEM) was used to study the microstructure of as deposited coating and the coating annealed to 1000 °C. Although the TEM bright field image showed no contrast, the dark field image (Fig. 2a) reveals small crystalline objects ~2 nm in size. The respective selected area electron diffraction (SAED) pattern indicates a nanocrystalline material. Diffuse diffraction rings may point to Mo_2C structure in an amorphous MoBC matrix. The nanocrystalline character of the annealed coating is apparent in a TEM bright field image (Fig. 2b). The layer consists of nanocrystals up to 10 nm in size. SAED pattern with several diffuse rings and a week texture indicates Mo_2BC structure.

The as deposited Mo_2BC coatings on HSS and hard metal substrates exhibited a relatively high hardness of 20.5 ± 0.3 GPa, comparable with the hardness of commonly used amorphous diamond-like carbon protective coatings [9–12]. Their effective elastic modulus E_{eff}, expressed as $E_{eff} = E/(1-\nu^2)$ where E is Young's modulus of the coating and ν is Poisson's ratio of the coating, was 330 ± 5 GPa. The film thickness was around 1.5 μm.

The coatings on HSS substrates could withstand annealing up to 600 °C without any significant change in their adhesion. However,

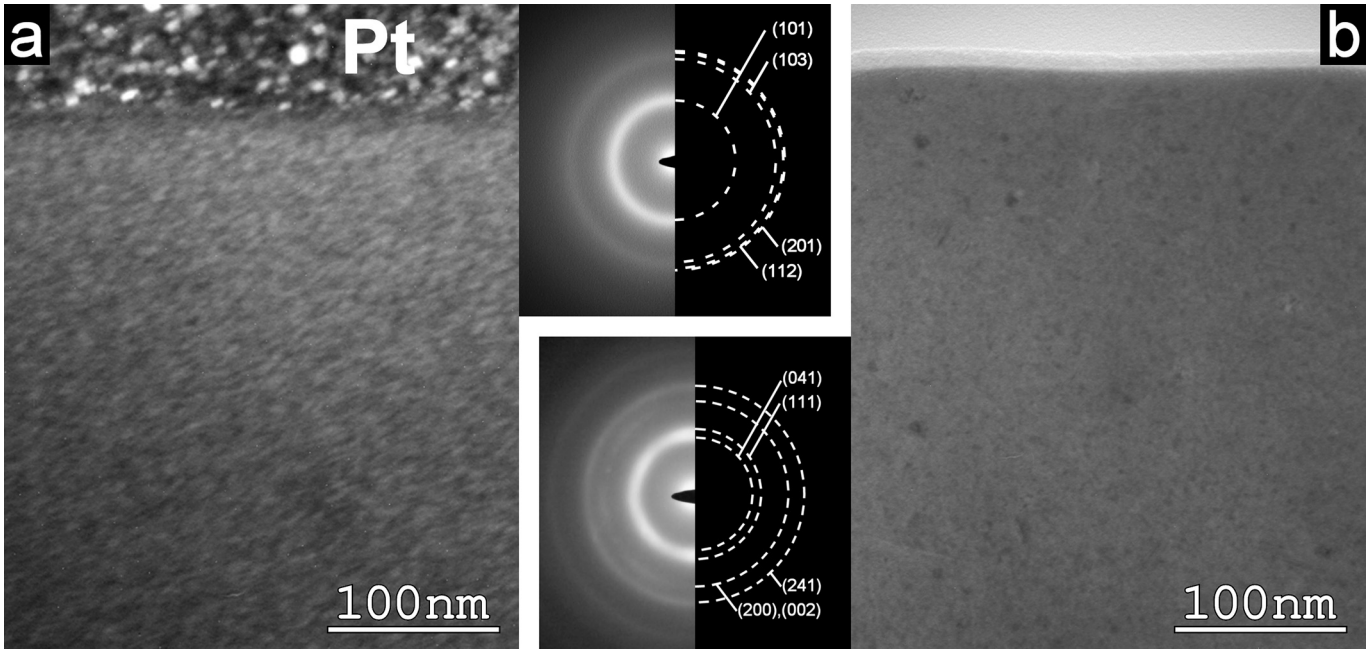

Fig. 2. TEM micrographs and respective SAED patterns: a) as deposited sample, dark field image and SAED pattern with rings of Mo_2C lattice; b) sample annealed to 1000 °C, bright field image and SAED pattern with rings of Mo_2BC lattice.

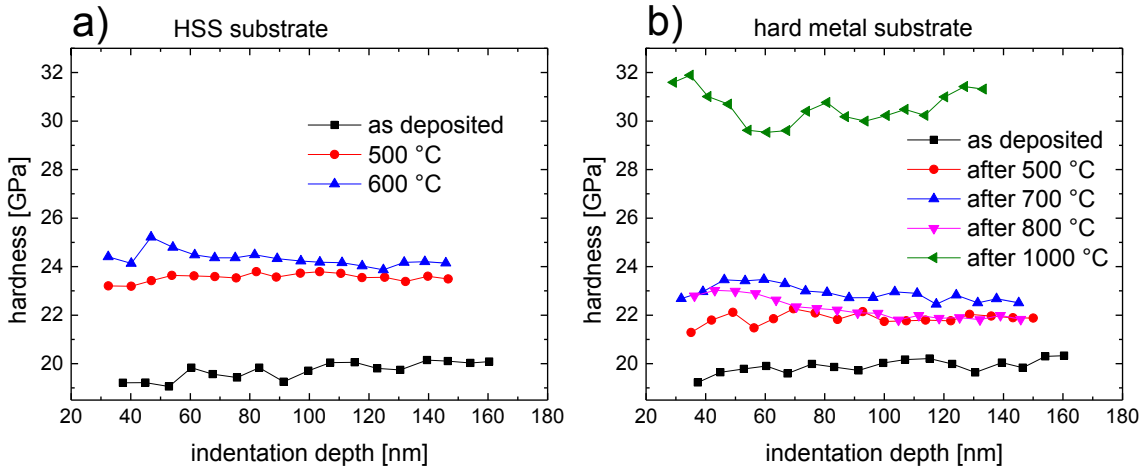

Fig. 3. The dependency of the hardness of coatings on a) HSS and b) hard metal substrates on indentation depth and its evolution induced by annealing.

during annealing to 700 °C the coating delaminated. On the other hand, the adhesion of all coatings on hard metal substrates remained sufficient even after annealing to 1000 °C. The reason for this dissimilarity lies in different coefficients of thermal expansion for HSS (CTE of ~13 μm/mK) and hard metal (CTE of ~6 μm/mK) substrates and the coating (estimated as ~ 8 μm/mK, based on known CTE of Mo_2C phase). If we assume that the intrinsic stress from the deposition process is relaxed during the annealing process, the estimated thermal stresses induced after cooling down from 700 °C are −1.4 GPa (compressive) in case of the coating on HSS substrate and 0.6 GPa (tensile) in case of the coating on hard metal.

The depth profiles of hardness and effective elastic modulus obtained for as-deposited and annealed coatings on HSS and hard metal substrates are presented in Fig. 3 and Fig. 4, respectively. Each point in the graphs represents an averaged value from 16 measurements performed by the quasistatic indentation test with 20 unloading segments in a load range from 0.5 to 11 mN. The error of these measurements is <8%. In order to eliminate the size effect and the influence of the indenter tip calibration for very low loads (<20 nm), the hardness and elastic modulus data were taken into account from indentation depths > 60 nm. As it can be seen, from 60 nm up to 160 nm both parameters are constant in the frame of the experimental errors indicating both, that the coatings are homogeneous and that the influence of the substrate on the measured data is negligible up to indentation depths of 160 nm. There is an increase of the hardness and effective elastic modulus measured after annealing to 500 °C, and in case of samples on HSS the hardness increased from the former 20.5 ± 0.3 GPa to 23.5 ± 0.5 GPa (see Fig. 3a) and the effective elastic modulus increased from 330 ± 5 GPa to 390 ± 7 GPa (see Fig. 4a). Annealing to 600 °C did not improve the hardness or, the effective elastic modulus significantly and all changes are within the experimental error from Figs. 3b and 4b we can see that similar behaviour is achieved also for annealed coatings on hard metal, however, here the increase of the hardness and effective elastic modulus is slightly smaller. The reason for this discrepancy is the different nature of thermal stress that arose from different CTEs of both substrates. The hardness improved to 22.0 ± 0.4 GPa and remained approximately constant after further annealing up to 800 °C. Although the crystallization temperature [7] had not been achieved, the increase of both mechanical properties upon annealing up to 800 °C is evident and appropriate discussion concerning several possible factors influencing the mechanical properties is needed and provided in paragraphs below. Further annealing of the Mo_2BC coating on hard metal substrate to final temperature of 1000 °C revealed considerable increase of hardness to 29.4 ± 0.6 GPa and the effective elastic modulus to 500 GPa. Here the temperature was high enough to induce the formation and growth of Mo_2BC crystallites. Moreover, the acquired values of the hardness and the effective elastic modulus are typical for crystalline Mo_2BC coatings [3].

There is a question that arose from nanoindentation and XRD data presented in Figs. 1, 3 and 4 – what is the main reason for the hardness increase at annealing temperatures starting from 500 °C where, according to XRD diffractograms, no significant crystallization occurred? The different thermal stress evolution may explain

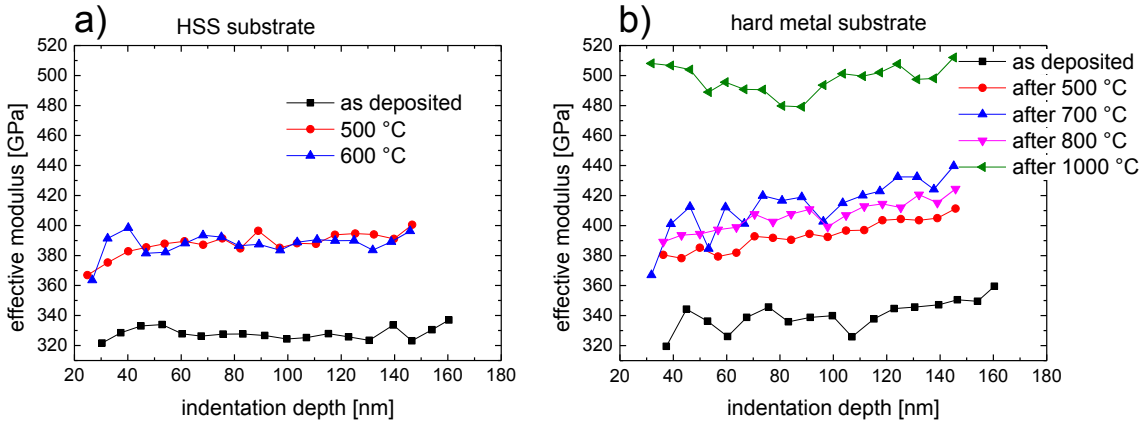

Fig. 4. The dependency of the effective elastic modulus of coatings on a) HSS and b) hard metal substrates on indentation depth and its evolution upon annealing.

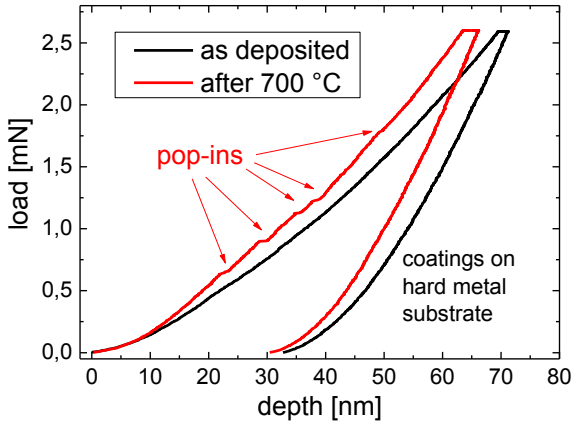

Fig. 5. The comparison of load-displacement curves for as deposited and annealed coatings on hard metal substrates with marked pop-ins.

the slightly different hardness and elastic modulus observed for HSS and hard metal substrates at 500 and 600 °C, what we see from Figs. 3 and 4, however, it does not provide explanation of step increase of hardness for these temperatures. The load/displacement curves obtained on as deposited and annealed coatings (see Fig. 5) showed that the hardness increase after annealing to 500 °C was also accompanied by structural changes. The as deposited coating exhibited smooth displacement response to loading and unloading without any pop-ins or pop-outs. However, after annealing several pop-ins, characteristic for crystalline materials, occurred for coatings on both substrates. These pop-in events are most probably caused by a grain boundary sliding mechanism [22,23] which means that during annealing to 500 °C additional crystallization of amorphous matrix occurred. However, the newly formed grains are too small to be distinguished in diffractograms presented in Fig. 3. It means that the nanocomposite strengthening effect is most probably the main reason for the hardness and effective elastic modulus increase of coatings after annealing to 500 °C.

The fracture resistance changes were studied using SEM imaging of residual imprints caused by the microindentation test. The as deposited samples showed no cracking around or inside the imprint even if the load of 1 N was used. With this load, the plastic zone already over-passed the coating-substrate interface which resulted in the plastic deformation of the substrate. This deformation of the substrate can induce cracking in the coating which is usually visible on SEM as cracks inside the imprint [14,15]. Using the differential hardness study it is possible to detect when this substrate deformation occurred as well as the presence of the subsequent cracking represented as distinct sudden drops in differential hardness curves. Fig. 6a shows the SEM image of the

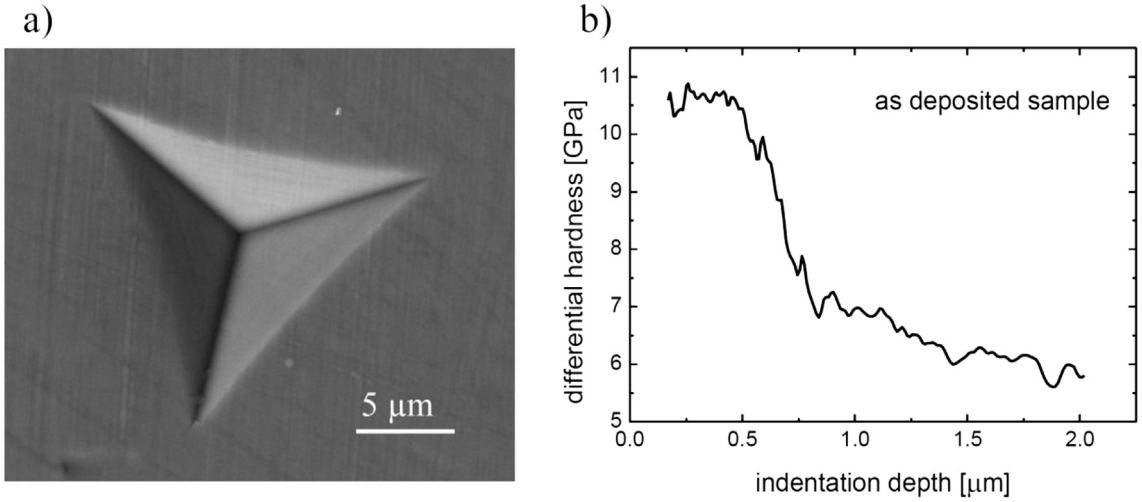

Fig. 6. a) The SEM image of the typical residual 1 N imprint made in as deposited sample on HSS substrate and b) the corresponding measurements of the differential hardness.

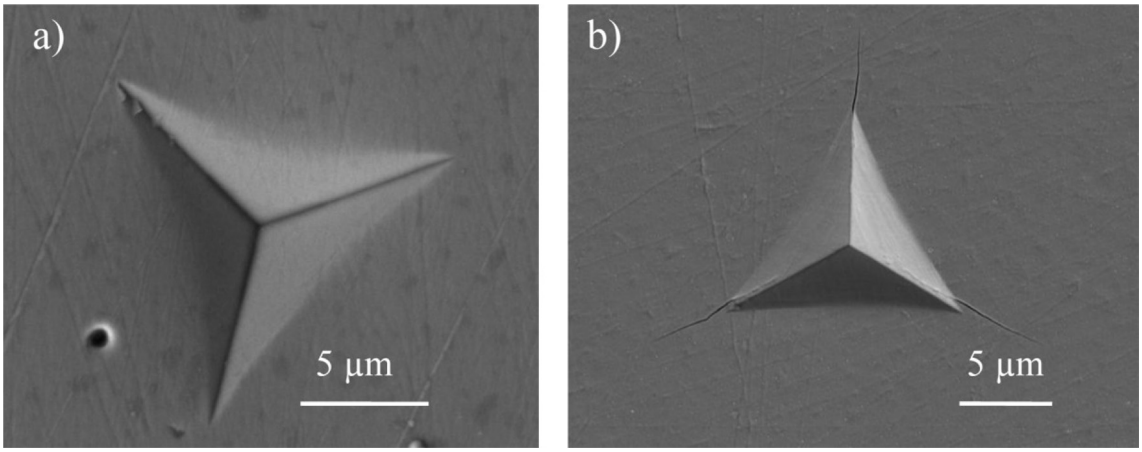

Fig. 7. SEM images of a) the sample on HSS substrate after annealing to 600 °C showing no cracking inside or around the imprint, b) the sample on hard metal after 1000 °C where cracks spreading from corners of the imprint are visible.

typical residual 1 N imprint made in as deposited sample on HSS substrate, and Fig. 6b presents the corresponding measurements of the differential hardness. No cracks are observed by SEM imaging, as well as no sudden drops are present in differential hardness curves meaning that, most probably, no indentation induced cracking occurred. The decrease of differential hardness from indentation depth of 0.5 μm in Fig. 6b was caused by influence of the HSS substrate. The coatings kept their desired ductile properties up to 600 °C – see Fig. 7a. However, the indentation tests after annealing to 1000 °C induced cracks spreading from corners of the imprints – see Fig. 7b. The decrease of ductility of the coating-substrate system (see Fig. 7b) is caused mainly by a growth of crystalline phase to the detriment of the amorphous phase which was indicated by pop-ins emerging after annealing and which may play an important role in the overall ductile properties of the coating.

4. Conclusion

Nanocomposite Mo-B-C coatings, exhibiting fine-grained structure, were prepared employing magnetron sputtering of three targets: B_4C, C and Mo. Two different substrates were used – high speed steel and hard metal (cemented tungsten carbide). The samples were subjected to annealing in temperature range from 500 to 1000 °C which in all cases significantly improved their hardness and elastic modulus. The hardness increased from original ~20 GPa to almost 30 GPa while annealed to 1000 °C, the effective elastic modulus increased from 330 GPa to about 500 GPa. Even though the crystallization temperature of the amorphous Mo_2BC material was found to be 820 °C, the fine grains existing in as deposited state could play the role of crystallization centers and may induce nanometer scale grain growth even below 500 °C. Exceeding the temperature above 900 °C additional growth of β-Mo_2C grains occurred according to X-ray diffractograms. According to the selective area electron diffraction patterns and X-ray diffraction technique the films annealed at 1000 °C consist of mixture of nanoscale Mo_2BC and β-Mo_2C grains. The coatings kept their desired ductile properties up to 600 °C. However, the indentation tests after annealing to 1000 °C induced cracks spreading from corners of the imprints.

Acknowledgement

This research has been supported by the project CZ.1.05/2.1.00/03.0086 funded by European Regional Development Fund and project LO1411 (NPU I) funded by Ministry of Education Youth and Sports of Czech Republic and the Czech Science Foundation (Project GACR 15-17875S).

References

[1] M.W. Barsoum, T. El-Raghy, Am. Sci. 89 (2001) 334–343.
[2] D. Music, J.M. Schneider, JOM 59 (2007) 60–64.
[3] J. Emmerlich, D. Music, M. Braun, P. Fayek, F. Munnik, J.M. Schneider, J. Phys. D. Appl. Phys. 42 (2009) 185406.
[4] H. Bolvardi, J. Emmerlich, M. to Baben, D. Music, J. von Appen, R. Dronskowski, J.M. Schneider, J. Phys. – Condens. Mat. 25 (2013) 045501.
[5] L. Zábranský, V. Buršíková, P. Souček, P. Vašina, J. Buršík, Eur. Phys. J. Appl. Phys. 75 (2016) 24716.
[6] S. Djaziri, S. Gleich, H. Bolvardi, C. Kirchlechner, M. Hans, C. Scheu, J.M. Schneider, G. Dehm, Surf. Coat. Tech. 289 (2016) 213–218.
[7] H. Bolvardi, J. Emmerlich, S. Mráz, M. Arndt, H. Rudigier, J.M. Schneider, Thin Solid Films 542 (2013) 5.
[8] J. Buršík, V. Buršíková, P. Souček, L. Zábranský, P. Vašina, Rom. Rep. Phys. 68 (2016) 1069–1075.
[9] J. Robertson, Mat. Sci. Eng. R37 (2002) 129, 281.
[10] D.R. Tallant, J.E. Parmeter, M.P. Siegal, R.L. Simpson, Diam. Relat. Mater 4 (1995) 191–199.
[11] M. Benlahsen, B. Racine, K. Zellama, G. Turban, J. Non-Cryst. Solids 283 (2001) 47–55.
[12] R.K.Y. Fu, Y.F. Mei, M.Y. Fu, X.Y. Liu, P.K. Chu, Diam. Relat. Mater 14 (2005) 1489–1493.
[13] H.C. Barshilia, A. Jain, K.S. Rajam, Vacuum 72 (2004) 241–248.
[14] L. Zábranský, V. Buršíková, P. Souček, P. Vašina, T. Gardelka, P. Sťahel, O. Caha, V. Peřina, J. Buršík, Surf. Coat. Tech. 242 (2014) 62–67.
[15] L. Zábranský, V. Buršíková, J. Daniel, P. Souček, P. Vašina, J. Dugáček, P. Sťahel, O. Caha, J. Buršík, V. Peřina, Surf. Coat. Tech. 267 (2015) 32–39.
[16] I.A. Abrikosov, A. Knutsson, B. Alling, F. Tasnádi, H. Lind, L. Hultman, M. Odén, Materials 4 (2011) 1599–1618.
[17] C. Fitz, A. Kolitsch, W. Fukarek, Thin Solid Films 389 (2001) 173–179.
[18] W. Jeitschko, H. Nowotny, F. Benesovsky, Monatsh. Chem. 94 (1963) 565–568.
[19] W.C. Oliver, G.M. Pharr, J. Mat. Res. 19 (2004) 3–20.
[20] B. Wolf, A. Richter, New J. Phys. 5 (2003) 15, 1-15.17.
[21] B. Wolf, Phil. Mag. Phil. Mag. Lett. 86 (2006) 5251–5264.
[22] E.N. Borodin, A.E. Mayer, Mat. Sci. Eng. A 532 (2012) 245–248.
[23] J. Shi, M.A. Zikry, Mat. Sci. Eng. A 520 (2009) 121–133.